

HIGH
PRESSURE
SCIENCE
AND
TECHNOLOGY

PROCEEDINGS

XI AIRAPT
International
Conference

NAUKOVA
DUMKA

4

HIGH
PRESSURE
SCIENCE
AND
TECHNOLOGY



PROCEEDINGS

XI AIRAPT
International Conference

KIEV 1989

INTERNATIONAL ASSOCIATION FOR THE ADVANCEMENT OF
HIGH PRESSURE SCIENCE AND TECHNOLOGY

HIGH PRESSURE SCIENCE AND TECHNOLOGY

PROCEEDINGS

XIth AIRAPT International Conference

In 4 volumes

Volume 4

Kiev Naukova Dumka 1989

High Pressure Science and Technology: Proc. XIth AIRAPT
Int. Conf.: In 4 vol./International Association for the Advan-
cement of High Pressure Science and Technology. -Kiev: Nauko-
va Dumka, 1989. -Vol.4. - 264 p.

ISBN 5-12-001178-0 (T.4)
ISBN 5-12-001176-4

The Proceedings composed of four volumes contain papers
presented at the XIth AIRAPT International Conference "High
Pressure Science and Technology" (Kiev, USSR, 12-17 July 1987).

Volume 4 of the Proceedings includes the papers on the
following topics: high pressure technique, process control, phy-
sical and mathematical simulations; shock waves and dynamic pres-
sures; liquid crystals and polymers under pressure.

The book is a direct reproduction of the camera-ready manus-
cripts submitted by the authors. No corrections have been made in
the texts.

В сборник, состоящий из четырех томов, включены труды,
представленные на XI Международную конференцию МАРИВД "Высокие
давления в науке и технике" (Киев, СССР, 12-17 июля 1987 г.).

В четвертый том вошли работы по следующим разделам: техника
высоких давлений, процессы контроля, физическое и математическое
моделирование; ударные волны и динамические нагрузки; жидкие крис-
таллы и полимеры под давлением.

Сборник отпечатан методом прямого репродуцирования с рукопи-
сей, представленных авторами. Авторские тексты не редактировались.

N.V. Novikov, Editor-in-chief
Ye.M. Chistyakov, Scientific secretary

H 1604090000-215
M221(04)-89

ISBN 5-12-001178-0 (T.4)

ISBN 5-12-001176-4

(9) Naukova Dumka, 1989

C O N T E N T S

HIGH PRESSURE TECHNIQUE, PROCESS CONTROL, PHYSICAL AND MATHEMATICAL SIMULATIONS

Maksimov L.Yu., Gurjeva L.I., Rozanova N.B. Efficient designs of high-pressure units for laboratory and indust- rial equipment	7
Bachl F., Lüdemann H.-D. An autoclave for high pressure high resolution NMR-studies to 600 MPa between 150 K and 450 K	10
Blank V.D., Aksenonkov V.V., Aleksandrova M.M., Ba- rabanov I.A., Buga S.G., Konjaev Yu.S., Estrin Yu.I. Ap- paratuses for investigation of solid materials under the conditions of shear deformation at pressure up to 86 GPa and principal results of investigation	17
Beresnev B.I., Getmanskii A.P., Efros B.M., Beigel- zimer Yu.E., Loladze L.V. Investigation of pressure dist- ribution in working space between diamond anvils by chan- ge of properties of a deformable spacer	19
Vrbka J., Kněsl Z. Methodology of strength design for the belt chamber	24
Synkov V.G., Glauberman O.E., Astrakhan M.V. Analy- sis of stressed-strained state of deforming tool at high and superhigh pressures	30
Molinar G.F., Legras J.C., Bean V., Borovkov V.M., Jäger J., Keppt A., Lewis S.L., Lewisch R., Möbius K., Rydstrom L., Ulrich J.G., Yamamoto S., Yi-Tang S. Inter- national comparison of pressure measurements in a liquid medium from 20 to 100 MPa	34
Levitas V.I., Idesman A.V., Leshchuk A.A., Polotniyak S.B. Numerical modeling of thermomechanical processes in high pressure apparatus applied for superhard materials synthesis	38
Lukin S.N., Teslya O.P. High pressure chamber for studies of magnetic resonance in millimeter range	41
Scholl W., Lentz H. Apparatus for measurement of C _v at high pressure and high temperature	45
Skoropanov A.S., Valevski B.L., Skums V.F., Vecher A.A. Reference substances for practical high pressure sca- le	49
Neilo G.N. Experimental technique in high-pressure EPR spectroscopy	52
Eremets M.I., Struzhkin V.V., Trojan I.A. High tem- perature diamond anvil cell with the laser heating	55
Prikhna A.I. The high pressure apparatus with sli- ding anvils	59

Blank V.D., Boguslavski Yu.Ya., Buga S.G., Itskevich E.S., Konyaev Yu.S., Shirokov A.M. Pressure self-multiplication effect in a plane-anvil chamber, caused by nonlinear elastic properties of solids	64
Glagovsky B.A., Lysanov V.S., Jashin V.A. Industrial synthesis automatic control of superhard materials with the use of mathematical synthesis models	67
Ruoff A.L., Brister K.E., Weir S.T., Vohra Y.K. Megabar pressures with synthetic diamonds	71
Grosse G., Sellger R., Risse G. Theoretical model for high pressure rapid solidification	77
Malinovsky I.Yu., Shurin Ya.I., Rahn E.N. Analysis of effectiveness and choice of optimal construction of two-stage multianvil unit of split split sphere apparatus	83
Meshcheryakov A.A., Pinakov V.I., Rychkov V.N., Topchian M.E. Obtaining high pressure gas with the help of a free self-wedging piston	86
Bobrovnichy G.S. Concerning press dynamics when instantaneous failure of sealing burr in high pressure unit takes place	91
Skoropanov A.S., Valevski B.L., Skums V.F., Vecher A.A., Maslenko Yu.S. Scientific and technological principles of making "cold" continuous-operating point pressure sensors	96
Borisevitch V.K., Isaenko V.I. Automatic press for sheet-metal explosive stamping.....	99
Siedlaczek J. The DC-200 diaphragm-type gas compressor for 200 MPa	102
Sharma J.K.N., Jain K.K., Bandyopadhyay A.K. Effect of different gas media on the operation of the controlled clearance piston gauge up to 5 MPa	105
SHOCK WAVES AND DYNAMIC PRESSURES	
Dremin A.N. Shock wave chemistry	111
Ree F.H., Calef D.F., Van Thiel M., Hamilton D.C. High-pressure high-temperature phase changes in chemically reactive mixtures	115
Breusov O.N. Substance unloading after shock compression and P,T diagrams	122
Schmidt S.C., Moore D.S., Shaw M.S., Johnson J.D. Vibrational spectroscopy of shock-compressed fluid N ₂ and O ₂	125
Deribas A.A. The explosive working of materials in the USSR	137
Petushkov V.G. Wave formation criterion in explosion welding.....	150

Adamiec M., Bagrowski J., Derentowicz H., Luckner H.J., Swierczyński R. Amplification of liner velocities using multilayer system for generation of high pressure	154
Zvorykin L.O., Fal'chenko V.M., Filatov A.V. The peculiarities of element redistributions in metals during shock wave transmissions	159
Babushkin G.A. United phenomenological theory for transport and elastic properties of materials, obtained by explosive pressure method.....	162
Nesterenko V.F., Pershin S.A. The shear localization at explosive compaction of rapidly solidified metal powders	166
Postnov V.I., Nabatov S.S. Experimental study on electrical conductivity of condensed materials under different dynamic compression regimes	170
Petushkov V.G., Fadeenko Yu.I., Pervoi V.M. Effect of explosion treatment on welded joint performance in structures.....	175
Alexeevsky V.P. Peculiarities of the shock compression of substance in the axial symmetry arrangements of the conservation	178
Voloshin M.N. The peculiarities of structural and phase transformations in cast iron under shock-wave loading...	182
Kaunow A.M., Bukin V.M., Burminskaya L.N. Peculiarities of formation of metallizing layers by shock-wave loading of powder materials and their mixtures onto metallic substrates	186
Chistyakov E.M., Vinnichenko V.N., Belostotskiy A.V., Mukha I.M. Alternating pressure-induced phase transformation in hardmetals	190
Bondarenko A.A., Kashkina L.V., Kirko V.I., Kusovnikov A.A. Shock-wave loading influence on crystallization of metallic glasses	194
Jach K. Numerical modelling of two-dimensional elastic/visco-plastic deformation of materials at dynamic loads	198
LIQUID CRYSTALS AND POLYMERS UNDER PRESSURE	
Shashidhar R. Phase transitions and critical phenomena in liquid crystals at high pressure	201
Buisine J.M. Disc-like mesogens under pressure	213
Chalyi A.V., Boyko V.C., Mögel H.-J. Metastable liquid crystal states near the limit of stability.....	221
Wong P.T.T. Effect of pressure on liquid crystals of aqueous unsaturated phospholipids	224

while assembling, tension law while wrapping, etc.) and also manufacturing methods.

Main parameters of an optimal multi-layer container are determined by the following relations:

$$K = \sqrt{(\sigma_a/\sigma_r - 2P/n\sigma_r)^n}$$

$$K_1 = \sqrt{\sigma_a/\sigma_1 - 2P/n\sigma_1}$$

where K and K_1 are coefficients of wall thickness of the whole container and i -layer counting from inside; σ_1 , σ_a and σ_r - permissible stress for i -layer, arithmetic and geometric mean from permissible stresses for all layers, respectively; P - operating pressure; n - number of layers.

VNIIMETMASH has developed algorithms and programs for computer-aided design of multi-layer containers in reference to mini-computer "Elektronika-60". Structures in which components are joined by winding high-strength tape are considered now to be the most efficient design suitable for high-pressure units of laboratory and industrial equipment. The given structure consists of a relatively thin-walled core, on which a thin tape is spirally wound with variable tension from layer to layer. The tape material is characterised by high mechanical properties (ultimate strength is up to 1900-2200 N/mm²), and the proper selection of an optimal tensioning law while winding provides the most favourable tension distribution in the structure during operation.

The main advantage of the tape-wrapped structures is their high reliability and safety: numerous layers can't be destroyed simultaneously, and their partial fracture is not followed by fragment scattering.

This structure is most preferable for equipment using compressed gases as working medium, which accumulate great potential energy contents at high pressures. In VNIIMETMASH tape-wrapped containers design is carried out on mini-computer "Elektronika-60" by means of algorithms and programs, determining structure dimensions, tensioning law while winding, stresses in structure components at all stages of manufacturing and operation. Method of tape-wrapped containers manufacturing is rather simple. Winding is done either on a special assembly stand or on conventional vertical boring mills or lathes, equipped with tensioning devices.

VNIIMETMASH together with several plants manufactured quite a number of tape-wrapped containers operating at pressures as high

as 200-2500 MPa. The majority of the containers have the diameter of about 2 m and height of 4-5 m.

For equipment operating at pressure exceeding 1500 MPa and units with large-size working chambers VNIIMETMASH has developed a new container design with a slit bush. The structure includes an outer multi-layer and tape-wrapped body and a core consisting of bushes, at least one of them is slit.

The analysis shows that such structure allows not only to increase operating pressures up to 3000-4000 MPa, but also facilitates assembling of the unit and bushes replacement when change-over to new sizes or during maintenance.

Buisine J.M., Zimmermann H., Poupko R., Luz Z., Billard J. Phase behaviour under pressure of pyramidal liquid crystals studied with a scanning numerical metrolemeter	232
Privalko V.P., Pekhteta N.A. Thermal conductivity of polymers under elevated pressures	241
Rymarenko N.L., Privalko V.P. Crystallization of polymers from the melt under elevated pressures	247
Goldman A.Ya. Physical and mechanical properties of polymeric and composite materials at high pressure and temperature	250
Shilov V.V., Lokhonya O.A., Tsukruk V.V., Petrenko K.D., Privalko V.P. Pressure effect on the structural order of liquid-crystalline polymers	254
Slavnov E.V., Timofeev V.M., Ostanin A.I. Hydrostatic extrusion of polycapromide, polytetrafluoroethylene and high-filled polyethylene (technology and properties)	258

EFFICIENT DESIGNS OF HIGH-PRESSURE UNITS FOR LABORATORY AND INDUSTRIAL EQUIPMENT

L.Yu.Maksimov, L.I.Gurjeva, N.B.Rozanova
VNIIMETMASH, Moscow, USSR

While producing laboratory and, particularly, industrial equipment for high-pressure treatment of materials the selection of high-pressure units (containers, block-dies), efficient design is of great importance, because these units determine process parameters and its economy.

For laboratory equipment intended for pressures up to 1000-1200 MPa and industrial units where operating pressure in solid or liquid phase does not exceed 200 MPa, high-pressure unit of simple design in the form of monolithic thick-walled cylindrical shell can be used.

For higher pressures the use of multi-layer, tape-wrapped structures and units with slit inner bushes are preferable.

The reason of such constructions is that for monolithic structures operating with elastic deformation, the permissible pressure does not exceed $P_{don} \leq \sigma_{don} \frac{1-k^2}{2}$ and maximum pressure is $P_{max} \leq \sigma_s \frac{1-k^2}{2}$, where σ_{don} and σ_s are permissible stress and yield strength, k - coefficient of structure wall thickness equal to inner radius (r)/outer radius (R) ratio.

Autofretting allows to increase maximum permissible pressure for monolithic structure up to the value of

$$P_{max}^a = (\sigma_{don} + \sigma_{don}^a) \frac{1-k^2}{2}$$

where σ_{don} - permissible stress in the material after autofretting. When $\sigma_{don}^a = \sigma_{don}$, then $P_{max}^a = 2P_{max}$, i.e. autofretting doubles the permissible pressure. However one should take into consideration that during autofretting the plasticity reserve for high-strength materials is significantly exhausted, whereby structure brittle failure sharply increases. That is why and also for technological reasons when manufacturing industrial high-pressure units autofretting practically is not used. For operation with pressures exceeding 200 MPa the use of multi-layer and high-strength tape-wrapped structures is preferable. VNIIMETMASH has developed a new design scheme of these structures which provides determination of all parameters (number of layers, their dimensions, tension

AN AUTOCLAVE FOR HIGH PRESSURE HIGH RESOLUTION NMR-STUDIES TO
600 MPa BETWEEN 150 K AND 450 K

F. Bachl and H.-D. Lüdemann

Institut für Biophysik und Physikalische Biochemie

Universität Regensburg, D-8400 Regensburg, FRG

ABSTRACT

A new autoclave for multinuclear high resolution NMR is presented that allows the measurement of NMR spectra in the frequency range from 15 to 300 MHz at pressures up to 600 MPa and temperatures between 150 and 450 K. As a first test for the functioning of the autoclave the spin lattice relaxation times T_1 of the protons in $\text{CH}_3\text{CD}_2\text{CD}_2\text{CH}_3$ and $\text{CD}_3\text{CH}_2\text{CH}_2\text{CD}_3$ were measured.

INTRODUCTION

In recent years we attempted to study the molecular dynamics of halogenated methane derivatives and alkanes as function of density and temperature by NMR in order to test the applicability of existing models to the description of the dynamic properties of this class of substances. For the interpolative description of the translational mobility of these methanes the rough hard sphere model introduced by D. Chandler [1] proved most successful. To our surprise it even described the dynamics of the n-alkanes from n-butane to n-decane [2] quantitatively in the temperature range between the melting pressure curve and 450 K at pressures up to 200 MPa.

Measurements in a significantly wider range of pressures and

temperatures on the same substances should provide a more stringent test of the models applied and should yield information about the chances to extrapolate reliably the data obtained in a limited p,T space to higher pressures and temperatures.

INSTRUMENTATION

Fig. 1 shows the autoclaves that were machined from the high strength titanium alloy TiAl6V4. These autoclaves are thermostated by a flow of cold or hot nitrogen in a surrounding brass mantle. The thermally insulated thermostat fits into the 72 mm diameter room temperature bore of the shimunit of the wide bore Bruker superconducting magnets.

The main new feature of this autoclave is the double cone seal machined from phase stabilized zirkoniumdioxide (FRIALIT-PSZ/FZM, Friedrichsfeld, Mannheim/FRG) at the lower end. The form and dimensions of the seal are taken from the literature [3]. This design allows a rather large inner diameter of the autoclave to be sealed with relatively little force.

The sample is contained in a borosilicate glass tube with an inner diameter of 3 mm. The brass bellow, glued to the capillary with aluminumoxide filled epoxy resin, is kept at room temperature in the upper autoclave and compensates volume changes caused by pressure or temperature variation.

The PSZ/FZM cone is used as the electric feedthrough for the RF saddle coil. It provides a very low capacity electrical high pressure feedthrough and permits thus to keep all other parts of the primary electronics of the probehead at ambient pressure and temperature.

Fig. 2 shows the electronics of the probehead. A series of capacitors and, in certain frequency ranges, auxiliary coils

allow the circuit, including the saddle coil, to be tuned at resonance. With a selected assembly of capacities and coils the resonance frequency can be varied within a range of 30 MHz. For larger changes of the frequencies the electronic probehead can be exchanged rapidly without release of pressure. This design has been tested at frequencies between 15 and 300 MHz.

RESULTS

Fig.3 collects isothermes of the proton spin lattice relaxation times of $\text{CH}_3\text{CD}_2\text{CD}_2\text{CH}_3$ and $\text{CD}_3\text{CH}_2\text{CH}_2\text{CD}_3$. Combined with older data obtained at pressures up to 200 MPa for the deuterium- and proton- T_1 of the same compounds, they permit the following conclusions:

The deuterium spin lattice relaxation times of the CD_2 - and CD_3 - groups are determined by the quadrupole interactions [4] and thus monitor single particle rotational motions. Previous experiments [5] showed that at temperatures $T > 400$ K the deuterium- T_1 of the CD_2 - groups possess a stronger pressure dependence than the ^2H - T_1 of CD_3 - groups indicating that the overall rotation of the molecules has a stronger density dependence than the methyl group rotation. The proton experiments given in Fig.3 reveal just the opposite pressure dependence. At 420 K the T_1 of the methyl group shows a larger pressure variation than the methylene protons.

Under the conditions of our experiments the protons relax by dipole-dipole interaction. Their relaxation rate $R^{\text{DD}} = (1/T_1)^{\text{DD}}$ consists of two terms

$$(1/T_1)^{\text{DD}} = (1/T_1)^{\text{DD}} (\text{intra}) + (1/T_1)^{\text{DD}} (\text{inter})$$

The intra rate is determined by single particle rotation, while the inter rate monitors relative translational motions and changes in the local radial distribution function. Obviously the

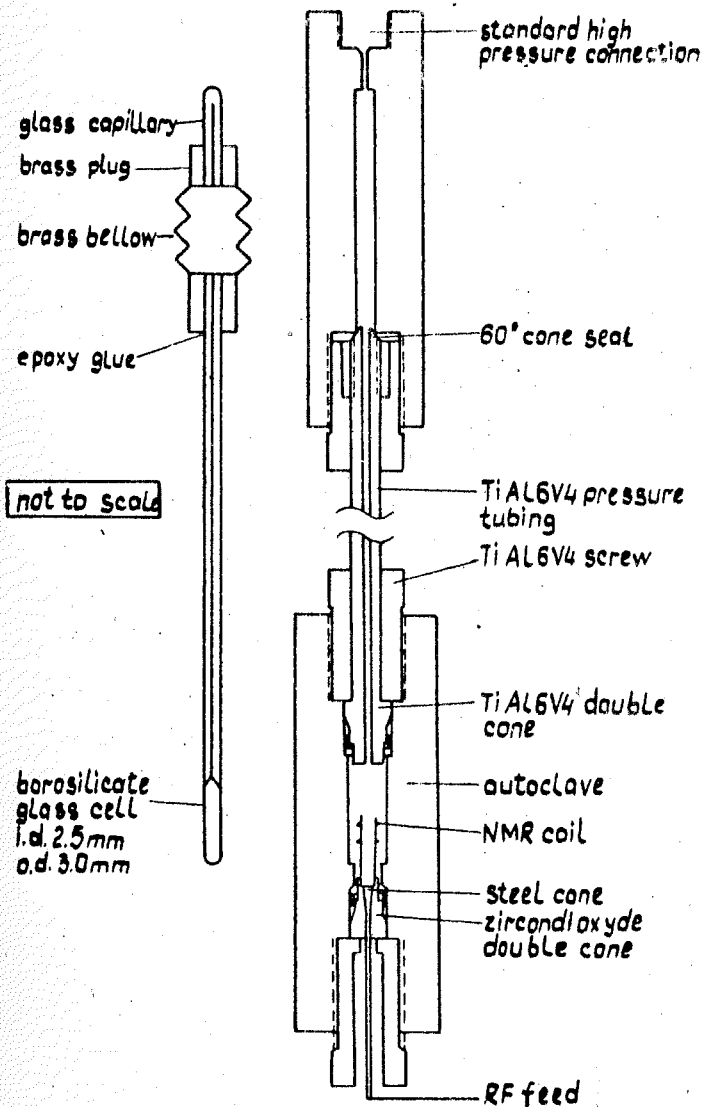


Fig.1. Scheme of the titanium autoclave and the interior glass sample container.

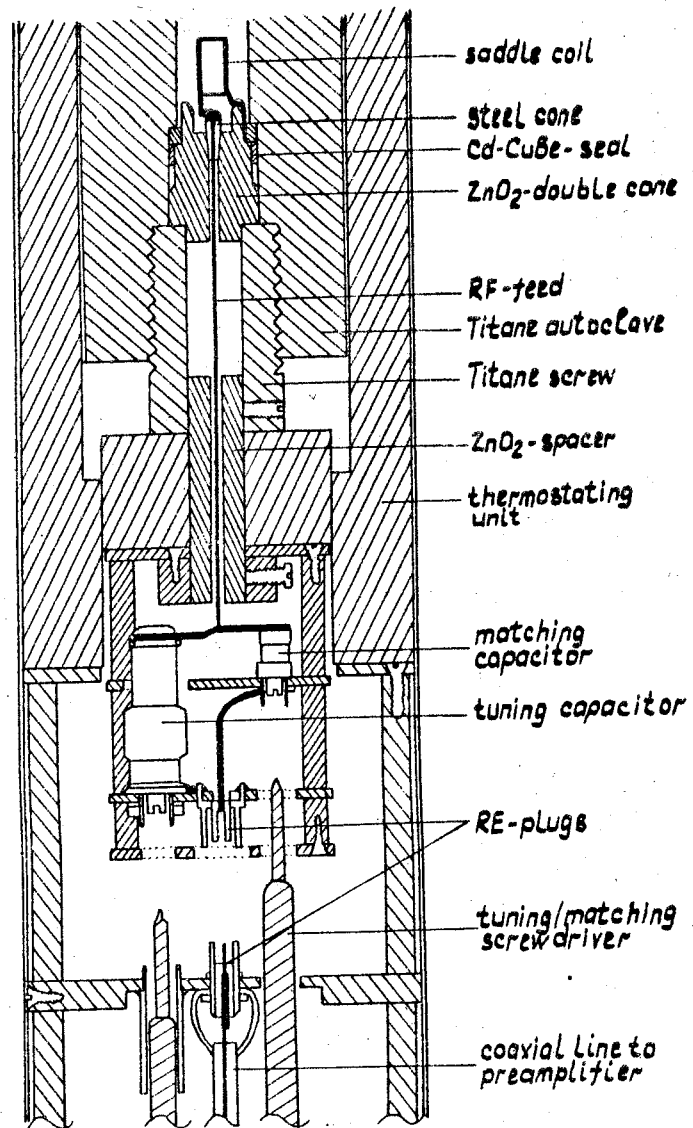


Fig.2. Scheme of the electronic probehead for the high pressure NMR autoclave.

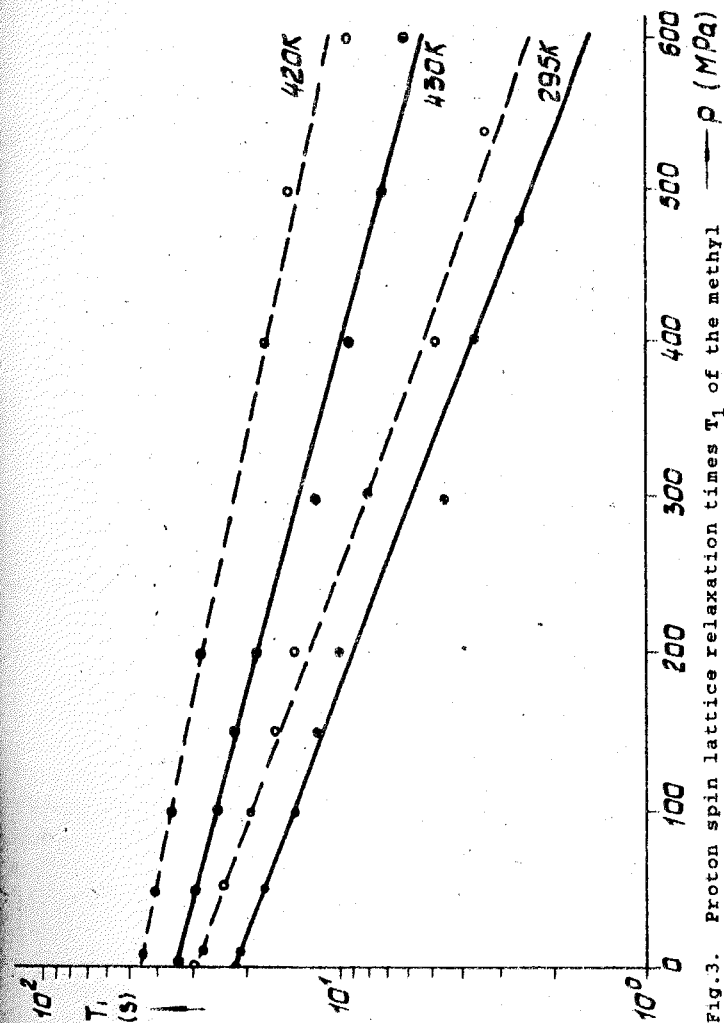


Fig.3. Proton spin lattice relaxation times T_1 of the methyl groups in $\text{CH}_3\text{CD}_2\text{CD}_2\text{CH}_3$ (full circles) and the methylene groups in $\text{CD}_3\text{CH}_2\text{CH}_2\text{CD}_3$ (open circles).

first term must show the same pressure dependence as the deuteron- T_1 of the respective groups. For this term the CH_3 -relaxation must therefore be less pressure dependent than the CH_2 -relaxation.

Thus the inter rate of the methyl groups must reveal an even stronger p-dependence than the total experimental rate $1/T_1$ of that group and the inter rate of the methylene groups. This can only happen if the local environment of the CH_3 -groups is subjected to a larger variation with pressure than the environment of the methylene groups. Quantitative conclusions, however, can only be drawn after the complete sets of proton- and deuteron- T_1 have been obtained.

ACKNOWLEDGEMENTS

Financial support by the DFG and the Fonds der Chemischen Industrie is gratefully acknowledged.

References

1. D.Chandler. J. Chem. Phys. 62, 1358 (1975).
2. F.Bachl, H.-D.Lüdemann. Z. Naturforsch. 41a, 963 (1986).
3. A.Trokiner, N.Dahan, J.L.Miquel, H.Theveneau. Rev. Sci. Instrum. 55, 1616 (1984).
4. A.Abragam. The Principles of Nuclear Magnetism (Oxford, 1961).
5. F.Bachl, H.-D.Lüdemann. Physica, 139 & 140B, 100 (1986).

APPARATUSES FOR INVESTIGATION OF SOLID MATERIALS UNDER THE CONDITIONS OF SHEAR DEFORMATION AT PRESSURE UP TO 86 GPa AND PRINCIPAL RESULTS OF INVESTIGATION

V.D.Blank, V.V.Aksenenkov, M.M.Aleksandrova, I.A.Barabanov, S.G.Buga, Yu.S.Konjaev, Yu.I.Estrin
Institute of High Pressure Physics, Academy of Sciences of the USSR, Troitsk, USSR

The possibility of appearance of new results in physics of high pressure depends considerably on development of apparatuses and methods of investigation. The method of shear deformation, which was offered by Bridgman, is very interesting. But pressures at these investigations were up to 10-12 GPa, because anvils of solid alloys (WC-Co) were used. The necessity of experiments on influence of shear deformation on structure and properties of solid materials at pressure $P \sim 15-20$ GPa permitted to use anvils of the most solid in nature material - diamond.

At the Institute of High Pressure Physics a number of modifications of high pressure cameras for shear deformation were created, including cameras with anvils of natural and synthetic diamonds. At first, a chamber with diamond anvils /2/, which preliminary were mounted plane-parallel by hemisphere was worked up. Shear was created by rotation of one of the anvils through an angle $\pm 5-8^\circ$, violation of plane-parallelism being relatively small. The use of anvils of a natural monocrystal permitted to carry out pressure calibration by luminescence of ruby. Then, a diamond chamber was created, in which both anvils were mounted on the sphere support and motions were provided for lead out centres of anvils to axis of rotation. This ensured plane-parallelism of anvils by unlimited shift angle and permitted to raise pressure up to 86 GPa. Luminescence of ruby was investigated during plastic deformation to 52.5 GPa. It is shown, that $Al_2O_3:Cr^{3+}$ may be used as pressure pickup in these conditions.

However, in all known apparatuses for shear rather thin specimens are used, diameter to thickness ratio being (50 - 100) : 1. That's why apparatuses were created for investigating the influence of shear deformation on properties of solid materials under pressure to 2 GPa using volumetrical specimens with diameter - 5 mm and height up to 5 mm. A chamber of "piston-cylinder"-type, which works in regime of piston's piezometer, was taken as a basis. RbCl was chosen as a model material for investigation using this apparatus. In conditions of shear, pressure of change $B1 = B2$ was

localized, $P_0 = 5.3 \pm 0.1$ GPa at $T = 300$ K and $P_0 = 4.3 \pm 0.2$ GPa at $T = 77$ K. The results obtained don't contradict to data in /3/.

Thus, apparatuses, created at the Institute of High Pressure Physics, expended considerably the range of pressure for investigation, and also for investigation of volumetrical specimens. This permitted to obtain several interesting results, namely - to amorphize antimonide gallium, to realize direct transition at low temperature (77 K) α -BN \rightarrow γ -BN and to discover self-multiplication effect of pressure by phase transition /4/.

References

1. P.B.Bridgman. Investigation of large plastic deformation and rupture. - M., Izdatinlit, 1955, p.422.
2. V.D.Blank, Yu.S.Konjaev, E.I.Estrin, A.I.Kuznetsov. Diamond chamber for investigation of influence of shear deformation on structure and properties of solids under pressure to 43 GPa. PTE, N 5, 1984, p.178-180.
3. E.Yu.Tonkov. Phase diagrams of joints under high pressure. - M., Nauka, 1983, p.280.
4. V.D.Blank, Yu.Ya.Boguslavsky, M.I.Eremets et al. Pressure self-multiplication effect on phase transition under quasi-hydrostatic conditions, Sov. Journ. of IETP, 1984, v. 87, N 3/9, p.922-926.

INVESTIGATION OF PRESSURE DISTRIBUTION IN WORKING SPACE BETWEEN DIAMOND ANVILS BY CHANGE OF PROPERTIES OF A DEFORMABLE SPACER

B.I.Beresnev, A.P.Getmanskii, B.M.Efros, Yu.E.Beigelzimer, L.V.Loladze

Donetsk Physico-Technical Institute, Academy of Sciences of the Ukrainian SSR, Donetsk, USSR

The present paper deals with investigation of phenomena, which form the basis of plastic deformation of spacer materials under superhigh pressures, realized by the diamond-anvil method.

On the diamond-anvil device at superhigh pressure plastic deformation of spacer-containers from stainless steel T-30I and heat-resistant alloy Inconel X-750 was carried out. Loading of the tested device up to pressures ca. 6.5 GPa is accompanied by the appearance of a deformation zone around the compression area. In the range of pressures from 8.5 to 40 GPa one observes the pronounced zone with a ring-like collar around the compression area. Further loading up to pressures ca. 65 GPa doesn't alter shape and dimensions of this zone. In Fig.1* features of the plastic deformed zone for a spacer from steel T-30I are shown. They were studied by electron microscopy using a SEM JSM-35 microscope at the accelerating voltage 50 kV. In Fig.2 the experimental pressure P_0 along the spacer axis vs. deformation level $\varepsilon = (h_0 - h) \cdot 100\% / h_0$, $h_0 = 250$ μ m is given. The obtained data permit to distinguish three main steps of spacer deformation: elastic-plastic, plastic and quasielastic.

Features of plastic deformation by the diamond-anvil method determine the formation of a structure of a spacer polycrystalline material. It is different in comparison from the spacer material structure produced by traditional deformation. The obtained difference is important for properties of deformed material.

Effect of superhigh pressure on residual strength characteristics of spacer material is investigated. Microhardness is chosen as a measure of the latter. It shows the level of material strength.

Let us consider the material deformation in the compressed zone to be uniform and neglect pressure at periphery of this zone in comparison with pressure along the axis. In this case from the difference ΔH_k of microhardness along the axis and the periphery

* The Figure is given at the end of the book.

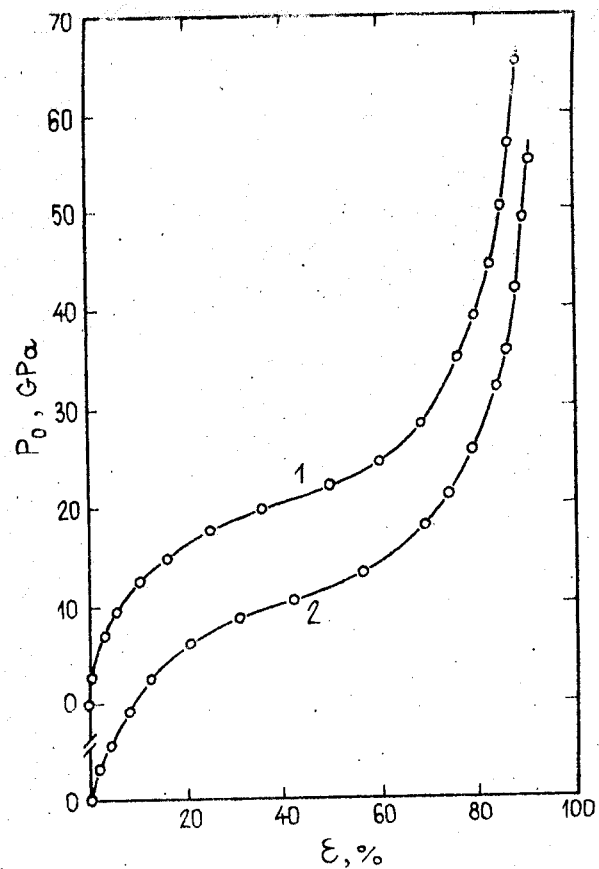


Fig. 2. Pressure P_0 along the spacer axis vs. deformation level for spacers from different materials: 1 - T-301, 2 - Inconel X-750.

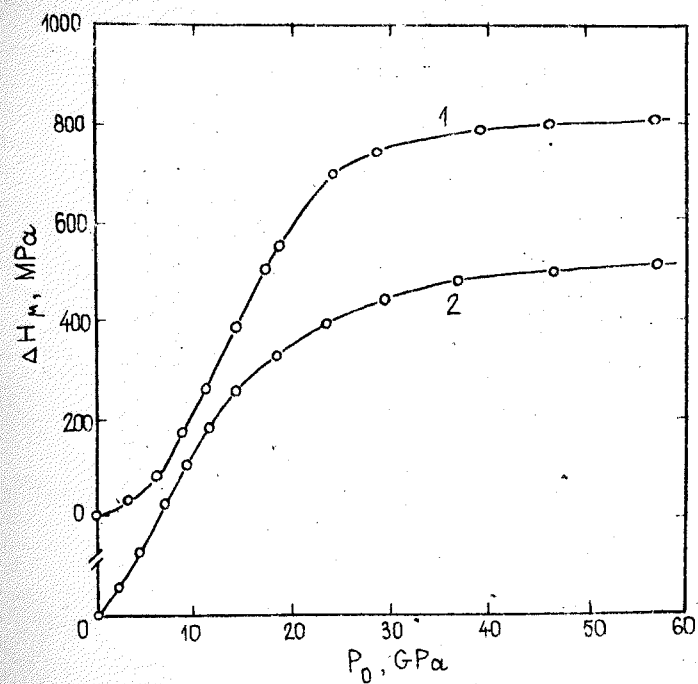


Fig. 3. Level of barohardening ΔH_μ of spacer material vs. pressure P_0 along the spacer axis for different spacer materials: 1 - T-301, 2 - Inconel X-750.

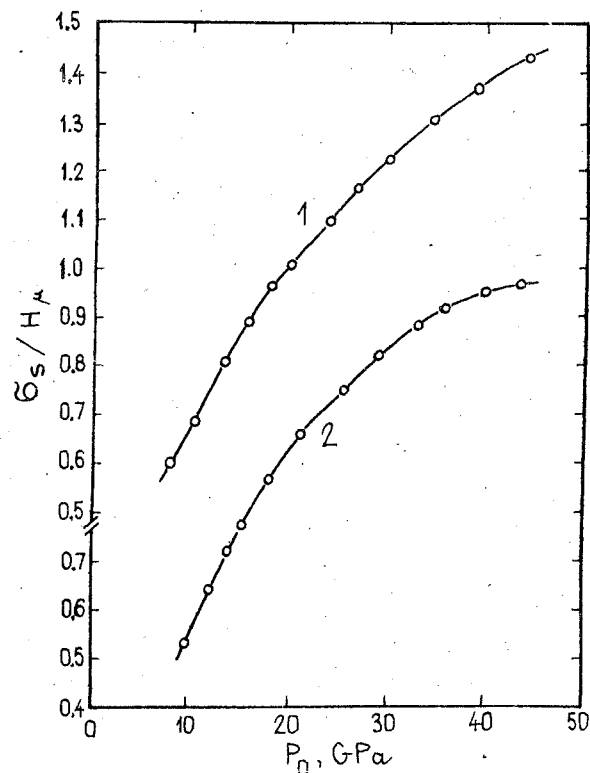


Fig.4. Stress relation σ_s / H_μ vs. pressure P_0 along the space axis for different materials: 1 - T-301, 2 - Inconel X-750.

the compressed zone one can estimate the value of residual hardening. In Fig.3 plots are given for the $P_0 - \Delta H_\mu$ relation. It can be used to recover pressure distribution in the compressed zone using material microhardness distribution values in this zone [1].

In conclusion we compare direct and inherited pressure effects on the level of deformation resistance of spacer materials. Deformation resistance σ_s under pressure we estimate by model identification [1] in experiment. In Fig.4 the relation σ_s / H_μ vs. P_0 is given. Here, H_μ is the mean microhardness over the cross-section. At low pressures the value of σ_s / H_μ is ca. 0.3 ± 0.4 , which corresponds to conclusions of paper [2]. This relation increases with pressure, which indicates the prevailing direct influence of pressure on the deformation resistance value.

References

1. Beresnev B.I., Efros B.M. Pressure generation in a diamond-anvil apparatus // Physica. - 1986. - 139. - P.910-915.
2. Del' G.D. Determination of stresses in a plastic zone by hardness distribution. - Moscow, Mashinostroenije, 1971. - 199 pp (in Russian).

J. Vrbka¹, Z. Kněsl²

¹Technical University of Brno, Brno, Czechoslovakia

²Institute of Physical Metallurgy, Academy of Sciences of Czechoslovakia, Brno, Czechoslovakia

1. Introduction

The Belt chamber is one of the most spread devices for the superhard material synthesis in the pressure range up to 10 GPa. In our contribution we shall restrict ourselves to the high pressure compound vessel (container) (see Fig.1), which is from the point of view of strength a more dangerous part of the Belt chamber than the pistons. In order to reduce the displacements, especially in the sealing conical part, the inner part (matrix) is usually made of sintered WC-Co. Mostly, the outer shape of the compound vessel is given by the production technology and by dimensions of the working space of the used press. The natural aim of the strength design is the optimal construction with respect to the maximum safety and lifetime. In our case, the design parameters are the number n of the vessel components, the cylindrical contact surface radii r_k and the overlaps Δr_k , resp. From an economical point of view (the repeated application of the steel rings) and because of the constant prestrain matrix it is reasonable to load the rings only up to the limiting state of elasticity for more dangerous working state.

The adequate calculation method for the stress and safety analysis of the direct problem for given loading, geometrical and material parameters is a basic assumption for the optimization approach to this problem. At first, we must formulate mathematically the proper computational model, which consists of the physical model (model of the loading, material, geometry etc.), mathematical and numerical model and that of the limiting state for the postprocessing calculations.

2. Formulation of the computational model

Model of the loading. We assume, that the mixture in the reaction cell behaves during the synthesis like an ideal liquid. The pressure here is constant (see Fig.2). Pressure loading in the matrix cone is caused by the compression of the sealing material (graphite or phyllite). The pressure distribution $p(s)$ (1) here was described on the basis of analogy with the relations in Bridgman and

$$p(s) = p_0 e^{\frac{2\mu}{t} s}$$

(1)

where μ is the coefficient of the inner friction and t is the lining thickness.

The curve A in Fig.2 corresponds to the state at the beginning of the synthesis and curve B corresponds to the state during synthesis. Applied pressure distribution $p(s)$ satisfies well the equilibrium equation on the piston in axial direction.

The deformation loading at the cylindrical contact surfaces (Fig.3) must fulfil following deformation conditions (2), (3) for axial displacements u and the conditions (4), (5) for stresses at the doubled points i, j of the contact surface. The shear stress is restricted by the condition (6) based on the Coulomb's law of friction,

$$u_{rk}(j, k+1) = u_{rk}(i, k) + \Delta r_k \quad (2) \quad \left[\frac{\partial u(j, k+1)}{\partial r} \right]_{r_k} = \left[\frac{\partial u(i, k)}{\partial r} \right]_{r_k} \quad (3)$$

$$|\sigma_r(j, k+1)| = |\sigma_r(i, k)| \quad (4) \quad |\tau_{rz}(j, k+1)| = |\tau_{rz}(i, k)| \quad (5)$$

$$|\tau_{rz}(i, k)| \leq f |\sigma_r(i, k)| \quad (6) \quad w(j, k+1) = w(i, k) \quad (7)$$

The condition (3) corresponds to the requirement of the equivalent contact surfaces at the neighbourhood of the points i, j .

Model of the material. We assume the material to be a homogeneous isotropic elastic mechanical continuum with the mechanical properties estimated experimentally on the 1-D stress-strain test.

Mathematical and numerical model. The finite element method (FEM) code PROKOP /1/ is used for the numerical solution of axial symmetrical elastic problem on the computer ICL 2950/10. The program makes use of the triangular elements with a cubic Hermitian interpolation function. Deformation loading in contact surfaces is simulated by means of the double noding technique. Realization possibilities of conditions (2)-(6) were discussed at /2/ in detail. Mostly, the conditions (2) and (3) are sufficient to simulate the relations in the ideal smooth contact surface without friction. The adhesion can be taken into account by addition of condition (7) for axial displacement w . To express the safety of the matrix made of brittle hard metal WC-Co, the combined Mohr's and principal stress limiting theory is used. For ductile steel rings

the hypothesis HMM is applied. The paper /3/ deals with the strength optimization of the compound vessel.

In many cases the compound vessel works with the cracked matrix. With the aim to estimate and to influence the lifetime of the cracked matrix, linear fracture mechanics has been used /4/ /5/. The stress singularity at the crack tip has been modelled by means of the double nodding technique for the displacements, the stress intensity factors K_I , K_{II} were evaluated and the crack growth direction was estimated.

3. Some results of calculations

The results of the stress and safety analysis can be obtained directly from the computer in a graphical form (see Figs. 4, 5). The Figures show the isolines of radial stresses σ_r , MPa and the safety, resp. To demonstrate the influence of the friction in the first contact surface (r_1), we have compared the stress intensity factors K_I , K_{II} for initial crack of 1 mm length in dangerous area of the matrix, Fig. 6. Calculated values for the smooth contact surface without the friction were $K_I = 13.6$, $K_{II} = 1.7$ and for adhesion $K_I = 5.7$, $K_{II} = 0.7 \text{ MPa}\cdot\text{m}^{1/2}$, resp. A great importance of the friction on the crack stability can be seen. Calculated crack path (Fig. 6) corresponds to practical experiences. From the comparison of K_I with the experimentally obtained fracture toughness ($K_{IC} \approx 13 \text{ MPa}\cdot\text{m}^{1/2}$) it follows, that cracks of length already about 1 mm are dangerous. It is in good agreement with the practice. We are able to study the influence of the geometrical shape of the matrix and other factors on the K_I with the aim to minimize its value and thereby to increase the lifetime of the cracked matrix.

The greatest errors (up to the order of 100%) of the computational model exhibit the calculations of the matrix safety. To demonstrate it we present here the calculated safety values k_R for the matrix, which was successful in production. The combined Mohr's and maximal principal stress limiting theory leads to $k_R = 0.26$. The relatively best results were obtained for Balandin's theory - $k_R = 0.52$. Substituting transversal rupture strength of the place of the tensile strength in the limiting theories, the values became greater - $k_R = 0.46$, resp. $k_R = 0.60$. This substitution has a physical reason, because of the great stress gradient at the most loaded part of the matrix. To reduce these discrepancies and to be able to determine the lifetime of the matrix

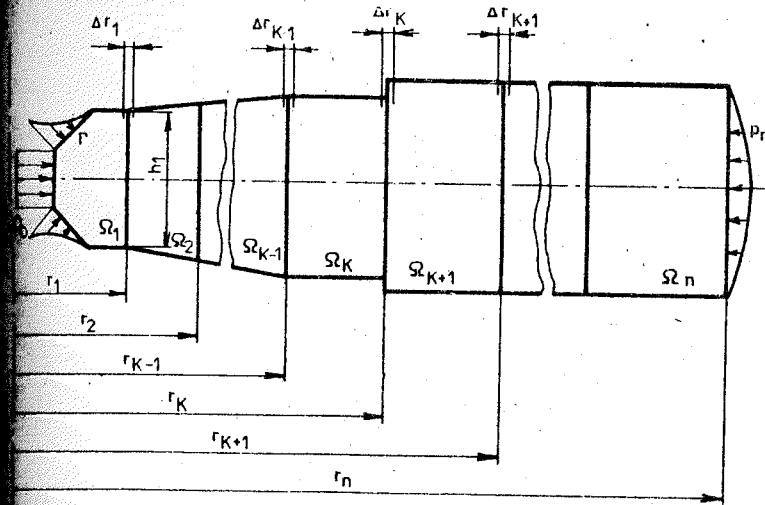


Fig. 1. Scheme of the problem.

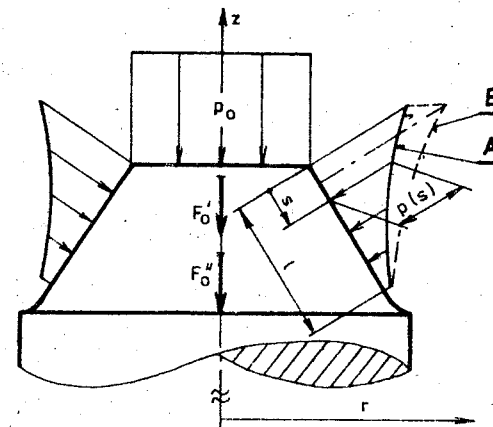


Fig. 2. Pressure loading of the piston.

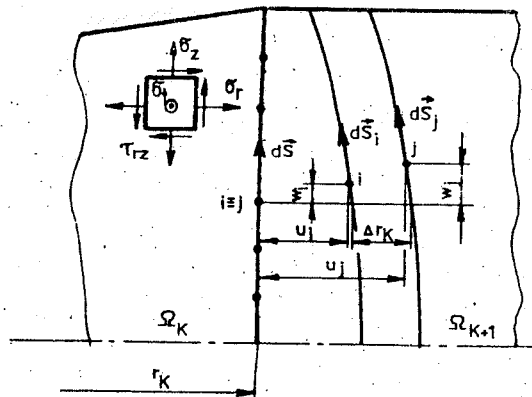


Fig.3. Deformation boundary conditions at the contact surface.

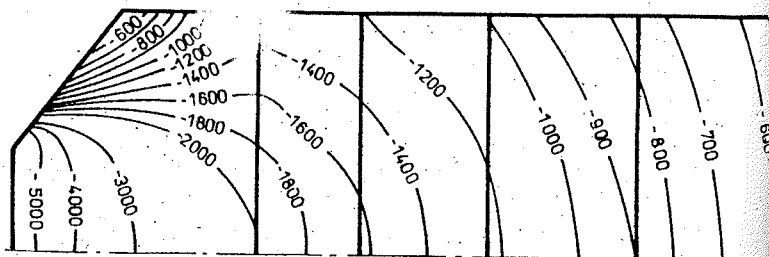


Fig.4. Isolines of radial stresses.

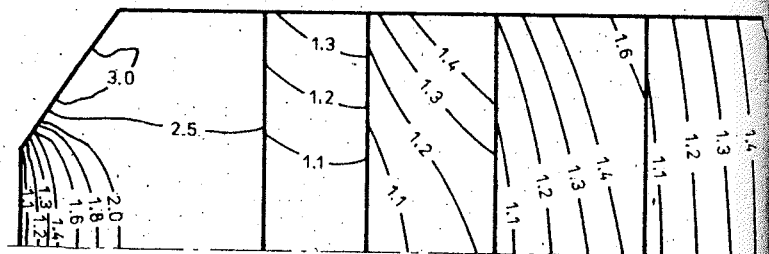


Fig.5. Isolines of safety coefficients.

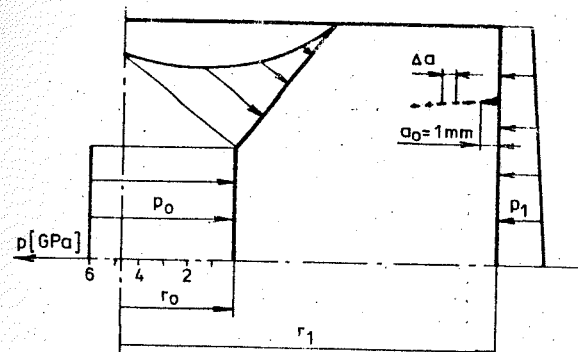


Fig.6. Cracked matrix with simulated crack path.

prepare the low fatigue experiments. Contemporary strength design is based on the stress analysis of the matrix used successfully in practice. The determined maximal effective stress is then taken as a material strength characteristics of the matrix for the safety evaluation (Fig.5).

References

1. Holuša, L. et al., Prokop - version 1 (research report). Regional Computer Center VUT, Brno, Inst. of Physical Metallurgy Czech. Acad. Sciences, Brno, 1983 (in Czech).
2. Vrbka, J., Kněsl, Z., Modelling of constraints in a contact surface - FEM solution. Proc. Conf. Mathematical Methods in Engineering, Czech. Science and Technical Society, Karlovy Vary, 1986, pp.153-158 (in Czech).
3. Vrbka, J., Kněsl, Z., Optimized design of a high pressure compound vessel by FEM. Comp. Struct., 1986, Vol.24, No.5, pp. 809-812.
4. Kněsl, Z., Vrbka, J., Solution of problems of linear fracture mechanics by package PROKOP. Proc. Conf. Mathematical Methods in Engineering, Czech. Science and Technical Society, Karlovy Vary, 1986, pp.647-652 (in Czech).
5. Kněsl, Z., Vrbka, J., Simulation of the fatigue crack growing by FEM. Proc. Conf. Mathematical Methods in Engineering, Czech. Science and Technical Society, Karlovy Vary, 1986, pp.653-659 (in Czech).

ANALYSIS OF STRESSED-STRAINED STATE OF DEFORMING TOOL AT HIGH AND SUPERHIGH PRESSURES

V.G.Synkov, O.E.Glaubergerman, M.V. Astrakhan

Donetsk Physico-Technical Institute, Academy of Sciences of the Ukrainian SSR, Donetsk, USSR

An experimental-design method for determining the boundary conditions in hardly accessible elements of a tool (e.g. in the zones of its contact with a billet, a base, a band, etc.) with the help of the stressed-strained state (SSS) components obtained by a strain measurement of free sections is proposed. If only the case of axisymmetrical problem is regarded, then taking into account that the stress tensor component normal to the surface is equal to zero, at these sections we have:

$$\sigma_{\theta} = \frac{E(\varepsilon_{\theta} + \mu \varepsilon_L)}{1 + \mu^2}, \quad \sigma_L = \frac{E(\varepsilon_L + \mu \varepsilon_{\theta})}{1 + \mu^2}, \quad (1)$$

where E, μ are the elastic constants, $\varepsilon_{\theta}, \varepsilon_L, \sigma_{\theta}, \sigma_L$ are the meridional and tangential strains and stresses.

If m number of the strain gauges is bonded, then n number of the boundary condition components should not exceed $m(n \leq m)$. Using the superposition principle we may write the m set of linear algebraic equations with the n unknowns:

$$\begin{cases} a_{11}P_1 + a_{12}P_2 + \dots + a_{1j}P_j + \dots + a_{1n}P_n = \sigma_1, \\ a_{21}P_1 + a_{22}P_2 + \dots + a_{2j}P_j + \dots + a_{2n}P_n = \sigma_2, \\ a_{m1}P_1 + a_{m2}P_2 + \dots + a_{mj}P_j + \dots + a_{mn}P_n = \sigma_m, \end{cases} \quad (2)$$

where $\sigma_1, \dots, \sigma_2, \dots, \sigma_m$ are the meridional and tangential stresses obtained according to strain measurement and equation (1) and renumbered in a definite order, and $P_1, \dots, P_j, \dots, P_n$ are the components of loading in the hardly accessible parts. Matrix factors (a_{ij}) are determined by the finite element method (FEM) during successive loading of the hardly accessible parts a single load. The desired load components (P_j) are found by solving the set of equations (2) by the least squares method [2].

The interaction between the lower die face ($D = 36$ mm, $d = 12$ mm) and the bed plate has been modelled. The contact zone

divided into three circular sections with 6 strain gauges helping to determine 3 pairs of the contact load components for them. Deviation of the normal load values from the mean stress was -23% , $+16\%$ and $+1\%$ for the external, central and internal sections, respectively. Tangential load of the internal section, directed to the die periphery, makes up 30% of the normal load, the tangential loads along the central and external sections, directed towards the die axis make up 7-9% of the normal loads. In this experiment we note a general error of 12-14% for the boundary condition restorations.

Calculations of the banding die limiting state by the FEM show that the optimum assembly tension depends on geometry, material and loading diagram of the insert and very often it differs from the limiting value according to the assembly conditions.

The optimum tension and influence of its optimum value deviation on the tool carrying capacity are determined by a function contour line of the maximum equivalent stress in all the elements of an insert. This line plotted on the "working pressure (P_1) - tension pressure (P_2)" coordinates is in correspondence with the insert material yield strength. The generalized criterion [3] has been used for a strength criterion.

It has been found that there are several forms of the limiting curves. The most characteristic curves have ($P_{2,0}$) abscissa of the maximum working pressure point ($P_{1,m}$) that either doesn't exceed the maximum possible assembly pressure ($P_{2,m}$) (Fig.1), or exceeds this value (Fig.2). Excess of the optimum tension pressure in the first case is not rational as well as the autosupport utilization. In the second case the autosupport utilization may increase the limiting working pressure substantially.

The first type limiting curve occurs at loading an upper half of a conical funnel of dies made of tungsten carbide with low (4-10%) cobalt content. The maximum tension ($P_{2,m}$) reduces the die carrying capacity to 1/2 - 1/3 in comparison with the optimum tension utilization. The second type limiting curve generally occurs at loading the whole die height or its greatest part.

The finite element method has been used to solve the SSS problem for a brilliant cut diamond anvil with a rectangular girdle ($E = 1141$ GPa, $\mu = 0.07$), regarding diamond as an isotropic body. The main geometrical parameters: working face diameter = 3.5 mm, base diameter = 3.5 mm, girdle width = 0.13 mm, anvil height = 2.2 mm. Four types of the working face boundary condi-

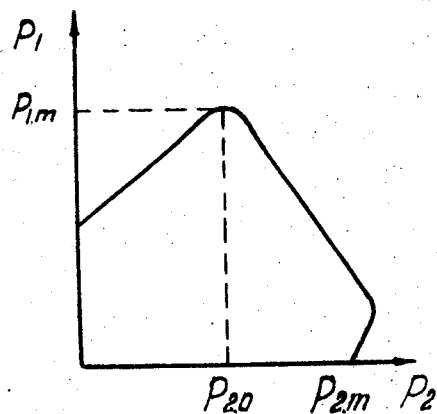


Fig. 1. The form of a limiting curve at loading the upper part of a die made of brittle material.

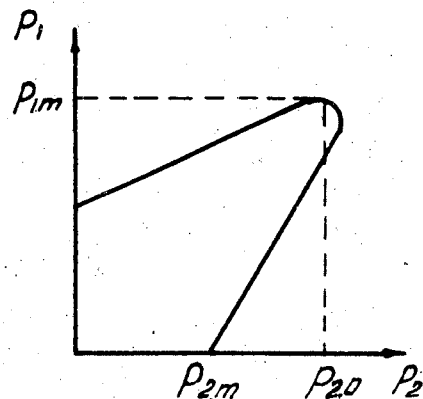


Fig. 2. The form of a limiting curve at loading the whole body of a die.

ns - the uniform pressure distribution, the trapezoidal pressure distribution, the trapezoidal one with a different depth of lateral support have been chosen. For all the types of loading the pressure intensity on the working face centre of an anvil was 50 GPa, on the periphery - 10 GPa. The maximum depth of lateral support was 0.3 mm. The uniformly distributed load was applied to the anvil base.

The analysis revealed existence of two hazard areas, one of them is situated on the anvil axis under the working face, another is close to the lateral face. The generalized criterion [3] has been used for determination of the hazard areas location and limiting state. Calculations were performed for the brittleness coefficient values $\chi = 0.1 - 0.4$. At uniform pressure distribution over the anvil working face the hazard area position does not depend on χ , and the limiting value of allowable pressure variation is in the range 8.7-13.7 GPa. At other loading types the hazard area of the maximum equivalent stress shifts from a lateral face to the axis with the increase of χ . The lateral support depth of 0.2 mm decreases the maximum equivalent stress value by 1.8 times, the limiting pressure increases 1.8 times. The lateral support depth of 0.3 mm increases the allowable pressure range 1.8 times.

References

1. Kov V.G., Glauberman O.E., Verbitskiy E.I. Analysis of the stressed state of the deforming dies surfaces. - *Problemy Prochnosti*, 1986, n.4, p.95-98.
2. Gantmacher I.M. Lectures on linear algebra. - Moscow: Nauka, 1982. - 280 p.
3. Garenko G.S., Lebedev A.A. Deformation and strength of material at stressed state. Kiev: Naukova dumka, 1976. - 166 p.

G.F. Molinar¹, J.C. Legras², V. Bean³, V.M. Borovkov⁴, J. Jäger⁵, A. Kepert⁶, S.L. Lewis⁷,
R. Lewisch⁸, K. Möbius⁹, L. Rydstrom¹⁰, J.G. Ulrich¹¹, S. Yamamoto¹², S. Yi-Tang¹³.

- 1 Istituto di Metrologia "G. Colonnetti" - IMGC - Torino, (I)
- 2 Laboratoire National d'Essais - LNE - Paris, (F)
- 3 National Bureau of Standards - NBS - Gaithersburg, (USA)
- 4 Gosstandart (VNIIFTRI) - Moscow (USSR)
- 5 Physikalisch-Technische Bundesanstalt - PTB - Braunschweig, (FRG)
- 6 Československý Metrologický Ústav - CSMU - Bratislava, (CSSR)
- 7 National Physical Laboratory - NPL - Teddington, (UK)
- 8 Bundesamt für Eich- und Vermessungswesen - BEV - Wien, (A)
- 9 Amt für Standardisierung, Messwesen und Warenprüfung - ASMW - Berlin, (DDR)
- 10 Aeronautical Research Institute - FFA - Bromma, (S)
- 11 Eidgenössisches Amt für Messwesen - EAM - Wabern, (CH)
- 12 National Research Laboratory of Metrology - NRLM - Tbaraki, (J)
- 13 National Institute of Metrology - NIM - Beijing, (The People's Republic of China)

INTRODUCTION

Between 1981 and 1985 an international comparison of pressure measurements in the range from 20 to 100 MPa was organized by the High-Pressure Working Group of the Comité Consultatif pour la Mesure de la Pression. The laboratories of thirteen countries participated in this comparison, which was carried out in three phases.

LNE was the pilot laboratory.

For pressure measurements in the range from atmospheric pressure to 1.4 GPa, the generally accepted primary standard is the pressure balance where pressure is determined from the application of a known gravitational force balanced against an upward force generated by the action of pressure on a known area, which is termed the effective area of the unit. However, the determination of the effective area is made more difficult due to the elastic distortion of the piston and cylinder when subjected to pressure, which is the greatest source of uncertainty in establishing high-pressure standards.

The transfer standard pressure balance was placed at the disposal of the Working Group by the Laboratoire National d'Essais (LNE) and the National Physical Laboratory (NPL). This standard is equipped with a tungsten carbide cylinder and a piston, the nominal effective area of this unit being 5 mm².

Each participating laboratory had to cross-check the transfer standard against its primary

standard over the established 20 to 100 MPa pressure range and send to the pilot laboratory the value of the measured effective area, A_p , of the transfer standard at each pre-established pressure level. Thus the effective area at atmospheric pressure, A_0 , and the pressure distortion coefficient, λ' , of the transfer standard was obtained from the measurements of each laboratory. Details of the procedure and the calculation methods adopted are given in /1, 2, 3, 4/.

LABORATORY STANDARDS AND TRANSFER STANDARD

The standards of all the laboratories are pressure balances, whose differences lie essentially in dissimilar technological design criteria or in a different choice of materials. The procedures adopted by the individual laboratories for the determination of the characteristics of their standards vary as well. Details of such characteristics for each participating laboratory can be found in references /1, 3, and 4/. Essentially, differences appear:

- in the choice of the material of the piston-cylinder unit:

- tungsten carbide (LNE, IMGC, PTB, FFA)
- steel (NPL, NBS, BEV, CSMU, NIM, ASMW, VNIIFTRI)
- steel + tungsten carbide (EAM, NRLM);

- in the type of the piston-cylinder unit used:

- controlled clearance (LNE, NBS, NRLM)
- free-deformation (IMGC, PTB, NPL, CSMU, EAM, NIM, ASMW, VNIIFTRI)
- re-entrant (BEV, FFA).

At the end of each phase by the pilot laboratory on the masses and the calibration of the platinum resistance probe of the transfer standard did not show any significant shift in their values. Measurements of the effective area of the transfer standard were also made by the pilot laboratory at the end of each phase. Reference values of the effective area at atmospheric pressure at the 20°C reference temperature, A_0 , and of the pressure distortion coefficient, λ' , were thus obtained. Shift grew in time; when compared with the first LNE1 determination, the increase amounted to 32 parts per million (ppm) after 15 months (LNE2), 34 ppm after 35 months (LNE3) and 34 ppm after 52 months (LNE4). The opinion advanced at the end of the first phase, that the increase was due to the treatment of the steel piston, which was used immediately after manufacturing, was confirmed by subsequent stabilisation. It is therefore assumed that the increase was continuous. This was also confirmed by similar increase in area with time of a second piston-cylinder unit, which was measured at the same time and kept at LNE. The increases observed on this reserve unit, used in subsequent measurements cycles at LNE, were 32 ppm after 15 months, 50 ppm after 35 months, and 52 ppm after 52 months. An equation to express the LNE reference value of the effective area of the transfer standard as a function of time τ , was obtained by fitting the four series of (A_p, τ) data.

RESULTS

Each laboratory communicated to the pilot laboratory the values of the effective area of the transfer standard, A'_p , calculated at the 20°C reference temperature. Since the results of each laboratory did not show any significant differences between increasing and decreasing pressure, the analysis of results was based on the mean values for each pressure. The effective area at atmospheric pressure, $A'_{0\text{LAS}}$, and the pressure distortion coefficient, λ'_{LAS} , were calculated from these mean values. In order to compare the data, reference values were calculated in the following way. First the difference of the result of each laboratory with respect to the LNE reference value was calculated, with the increase in time being taken into account. Then a mean difference was calculated from the differences of all laboratories which were weighted according to the reciprocal of the square of their stated uncertainty. Participants' results were then tested to see if they agreed with the weighted mean values to within their stated uncertainty. Only those who did so were included in the final reference values.

RESULTS OF A'_0 AND λ' MEASUREMENTS

Differences between the individual laboratory values and the reference value range from few ppm to -167 ppm. Relative differences of effective area determinations of all participating laboratories lie within 204 ppm.

By a similar analysis of the differences of the pressure distortion coefficient values obtained from the transfer standard, a weighted mean value, $\Delta\lambda'$, was calculated and used as a reference. Differences of individual laboratory results from this reference value were subsequently calculated. Results lie within 3.43 ppm/MPa and indicate a marked dispersion; however, if the two extreme values are not taken into account, results lie within 0.72 ppm/MPa.

RESULTS OF A'_{100} MEASUREMENTS

A'_{100} values of the individual laboratories are shown in Fig. 1.

Practically, these values represent the extent to which the various measurements of a pressure can be said to agree, since the uncertainty of the other parameters are much lower, as a rule, than the evaluated uncertainty of the effective area. For eight laboratories, the agreement lies within 78 ppm, for all the laboratories it lies within 414 ppm.

CONCLUSIONS

The comparison organised in the pressure range from 20 to 100 MPa showed large uncertainties and differences. Results showed agreement within about 200 ppm at the lower pressures and within about 100 ppm at the higher pressures. They confirmed the difficulties encountered in the determination of the pressure distortion coefficient, which plays a major role, particularly at pressures higher than 100 MPa. The comparison here described has confirmed that pressure balances are appropriate

standards in this pressure range. Deviations from linearity were within 5 ppm and repeatability, as evaluated from the standard deviation of several measurement series, generally lay within a few ppm.

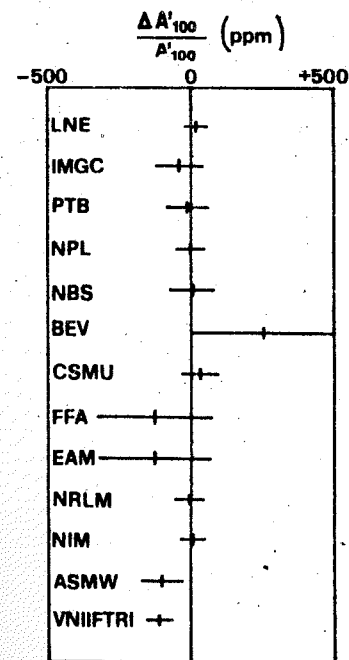


Figure 1: Difference of differences from the mean of effective area A'_{100} of the transfer standard at 100 MPa.

The horizontal bars indicate uncertainty of A'_{100} determinations.

References

1. LIGAS et al. BIPM Internal Report. BIPM-84/2 (First phase) (1984) - available from BIPM.
2. LIGAS et al. J. Phys. E: Sci Instr., 18, pp. 361-363 (1985).
3. LIGAS et al. BIPM Internal Report. BIPM-86/1 (second phase) (1986) - available from BIPM.
4. LIGAS et al. BIPM Internal Report. BIPM-86/3 (third phase) (1986) - available from BIPM.

V.I.Levitas, A.V.Idesman, A.A.Leshchuk, S.B.Polotnyak
Institute for Superhard Materials, UkrSSR Academy of Sciences, Kiev, USSR

The thermostress state of the reaction cell in high pressure apparatus (HPA) is changed during electric heating which results in pressure increase. At the same time phase transformations of reaction zone materials occur starting from some moment of heating corresponding to attaining technological parameters for diamond synthesis. This in turn affects the distribution of electric, temperature and baric fields in HPA. Therefore, the interdependence occurs between the processes of electrical and heat conduction, thermoplasticity and phase transformations, running in HPA during materials synthesis, i.e. there are relations of electric potential field to those of temperature, pressure and diamond concentration; of temperature field to electric potential, pressure and concentration distributions; of stress fields to those of temperature and concentration and of diamond concentration field to pressure and temperature distributions in the reaction zone. Besides, there are physical and geometrical nonlinearities caused by temperature dependence of thermophysical constants, pressure dependence of elastic and plastic constants and by occurrence of large elastic and plastic strains.

A corresponding finite-element model has been developed to describe processes running in HPA during diamond synthesis with allowance for features enumerated. The complete system of determining equations comprises equations of the plastic flow theory with allowance for finite strains [1], equation of electrical conduction, equation of nonstationary heat-conduction, kinetic equation for the rate of the diamond crystals growth, equations for carbon phase equilibrium and metal solvent melting. The reaction zone is considered to be a mechanical mixture of graphite, metal solvent and diamond, the efficient properties of which are determined depending on the components properties and mass concentration. Phase transitions are taken into account through the changes in properties, concentrations and the rapid changes in specific volume. The rate of diamond concentration change, \dot{x} , in the region of its possible synthesis is determined by topochemical Tofeyev equation

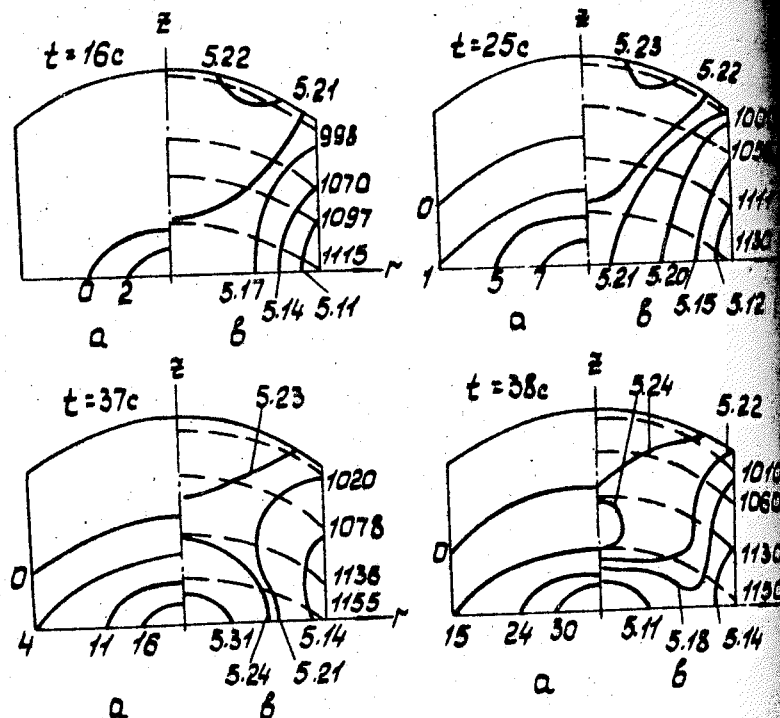
$$\dot{x} = K h \exp(-Kt^h) t^{h-1}, K = A \exp[-Q/(RT)],$$

where h and A are constants, Q is an activation energy, t is the time of diamond crystals growth, T is temperature.

The developed methods have been used to solve the problem of temperature, pressure and concentration fields determination in the reaction zone of HPA under conditions of diamond heating and synthesis. The calculation scheme comprises the whole HPA when solving the problem of electrical and heat conduction; the die and reaction cell when solving the problem of thermoplasticity. The initial state stress field (before heating) is taken from the solution of problem about the reaction cell compression on the anvils of converging block-dies with allowance made for large elastoplastic strains in the reaction mixture and container [2].

The distributions obtained for thermodynamical parameters during diamond synthesis are shown in Figure. The temperature fields are specified by differences of $\sim 150^\circ\text{C}$ along z -axis of the reaction zone and of $\sim 50^\circ\text{C}$ along r -axis. Pressure fields are less heterogeneous, particularly during the initial time of synthesis, when diamond concentration does not exceed 7%. When attaining the concentration value of 30% a sudden drop of pressure occurs in the center of the reaction cell (by about 0.3 GPa) resulted from graphite transition to a more dense modification (diamond) and hence from the reduced specific volume of the reaction mixture. Pressure increase at the initial moments of synthesis can result from increasing temperature and elastic constants of the reaction mixture and from predominance of this process over that of pressure reduction due to phase transitions.

To check the degree of phase transition influence upon the distribution of thermodynamic parameters within the reaction zone the coupled problem of electrical and heat conduction and thermoplasticity is solved without allowance for phase transitions. For instance, temperature at the initial moment of diamond crystals growth is found to be practically independent on phase transformations. With the given concentration, however, the discrepancies reaching 100°C appear in the results obtained with and without allowance for phase transformations. Effect of graphite-diamond phase transitions upon pressure distribution within the reaction volume considered above. Variation in technological parameters of synthesis involves the corresponding variations in geometry for the region of possible synthesis and in the rate of phase transformations occurred therein. Thus for the investigation of processes



Distribution of (a) diamond concentration, %, (b) pressure, GPa, (c) temperature, $^\circ\text{C}$, in the reaction zone of HPA (— pressure, ——— temperature).

running during diamond synthesis allowance for their mutual influence is imperative.

The data obtained are of model character, which depends on insufficient reliability of the used physicommechanical properties of materials and equations for phase transition kinetics. At the present stage, however, one can study in the first approximation the relative influence of a number of parameters (heating power, press capacity, equipment scheme) upon the course of diamond synthesis.

References

1. Левитас В.И. Большие упругоэластические деформации материалов при высоком давлении. — Киев: Наук.думка. 1987 — 232 с.
2. Идесман А.В., Левитас В.И. Напряженно-деформированное состояние элементов АД с учетом больших деформаций. // Получение и применение сверхтвердых материалов: Сб. науч. тр. — Киев: Институт сверхтвердых материалов АН УССР, 1986. — С.80-85.

HIGH PRESSURE CHAMBER FOR STUDIES OF MAGNETIC RESONANCE IN MILLIMETER RANGE

V.V. Lukin, O.P. Teslya

Donetsk Physico-Technical Institute, Ukrainian Academy of Sciences, Donetsk, USSR

Piston-cylinder high pressure chambers (HPC) are convenient for experimental studies [1,2] but for pressures above 10-15 kbar one has to use anvil-type HPC. The latter are adapted for these pressures, however, disadvantages of them are quite numerous: complicated design, low volume of specimens under test, time-consuming production as adaptation of chamber parts must be done with high precision are among them.

Application of EPR radio frequency radiation of millimeter range permits to study paramagnetic centres with great initial settings of ground states, and addition of mechanical treatment provides unique information on structure and properties of such centres.

Below we describe HPC for studies of magnetic resonance in millimeter frequency range (4 and 2 mm) at low temperatures and pressures up to 20 kbar.

In Fig.1 HPC is shown schematically. Chamber parts are of heat-treated beryllium bronze. Chamber body (18 mm in diameter) is of two-shell: removable insert 6 is pressed into the main shell 5. The insert diameter is worked down to the design size (3.5 mm). The shortest chamber channel (due to the effect of support from the loaded chamber shell heavy parts) provides higher pressures in comparison with the long one [3]. To decrease its length down to 10 mm (in liquid chambers down to 20-30 mm) we applied a radio-frequency input to the chamber of special design, a set of working electrodes, solid transmitting pressure medium (indium), an original method of pressure measurement (by the temperature point value of indium transition to superconduction).

A set of working high-pressure cells comprises two modifications. The first is applied if a crystal is hard enough to resist the pressure created by solid medium, then the channel is filled with the metallic indium to an end (Fig.1). A specimen 8, produced as a segment of a sphere adjoins by flat surface to a thrust bush 7. Experiments showed that a degree of modelling hydrostatic pressure in this case is quite adequate.

The second modification is applied in the case of brittle

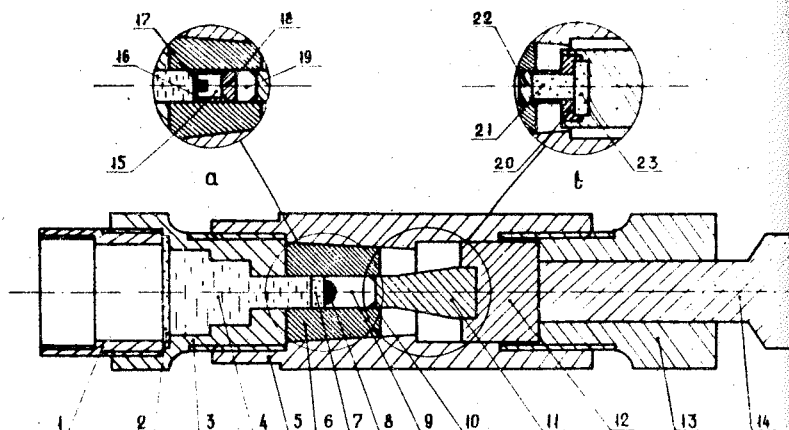


Fig. 1. Schematic view of a high-pressure chamber; 1 - adapter, 2 - fluor plastic disc, 3 - obturator, 4 - waveguide window, 5 - shell, 6 - removable insert, 7 - thrust bushing, 8 - specimen, 9 - indium, 10 - sealing ring, 11 - piston, 13 - stopping nut, 14 - rod, 15 - oil-benzene mixture, 16 - fluor plastic cup, 17 - specimen, 18 - stopper, 19 - indium, 20 - holder, 21 - rod, 22 - spacer, 23 - bearing.

crystals. A specimen is put into a miniature fluor plastic cup 16 filled-up with dehydrated mixture 15 of oil and benzene (Fig. 1, a). The cup is closed with a fluor plastic stopper 18. Pressure to it from the piston is transmitted through an indium tablet 19, serving as a manometer.

It was stated by experiments that a bronze piston 11 can not stand pressures above 15 kbar at low temperatures. A piston of our design (Fig. 1, b) makes possible work at pressures up to 20 kbar at 4.2 K. The piston rod 21 is hexagonal boron nitride (ca. 3 mm in diameter), it is pressed into a bronze holder 20 and is supported by a hexanite bearing 23.

At pressures above 13-15 kbar the chamber channel is irreversibly deformed and after several runs at maximum pressures it must be repaired. An insert 6 is replaced and the channel is worked down to the specification.

An original radio frequency input of radiation to the pressure region /4/ comprises an obturator 3 with drilled along the axis telescope apertures, diameters of which decrease as they approach to the pressure region. Homogeneous mixture 4 of fine powders of Al oxide and NaCl is pressured in the apertures under pressure ca. 10 kbar. The waveguide window thus obtained and a specimen form a part of a superlong resonator of the EPR spectrometer /5/.

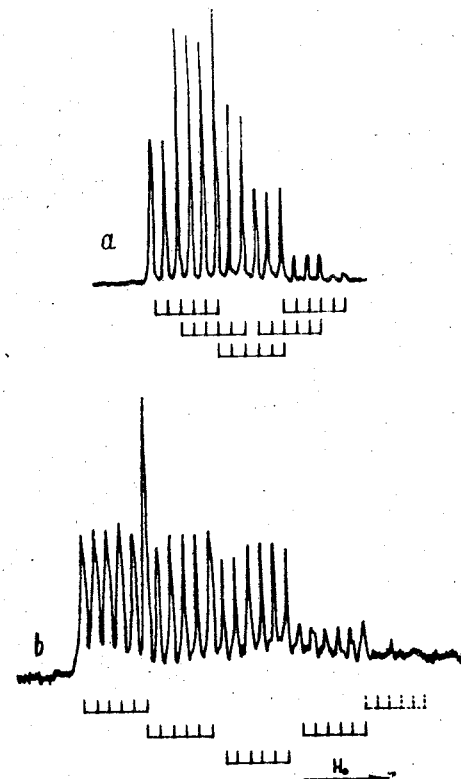


Fig. 2. EPR spectrum of Mn^{2+} ions in $Cs_3Zn_{1-x}Mn_xCl_5$ ($\lambda = 4$ mm, $T = 4.2$ K). Lines of fine and superfine structures of a spectrum are drawn: a - $P = 0$; b - $P = 19$ kbar.

Due to a relatively low quality-factor of a resonator and to a low coefficient of fill-in of it by a specimen the obtained sensitivity of 10^{13} - 10^{14} spin/Oe is not high, but quite adequate in most cases.

An obturator with a waveguide window is screwed into the chamber shell to the rest, then in the insert channel 3-4 mm of the same mixture is stamped and a thrust sapphire bushing 7 is put in place, then a specimen 8, indium rod 9, a sealing ring 10 and a piston 12. This HPC was used by us with success at many runs at 20 kbar, at cooling down to temperature of liquid helium and at heating up to room temperatures.

Application of metallic indium to transmit pressure to a specimen makes possible pressure treatment on it through transition temperature. Statement of transition to superconduction is done by an induction method in a separate cryostat, then the suspension with a cooled high pressure chamber rapidly carried over to the cryostat of the EPR spectrometer. Pressure in the chamber is estimated using the temperature-pressure curve of indium transition to superconduction, recorded during the test /6/.

To illustrate the work of our HPC we present EPR spectra (Fig.2) of Mn^{2+} ions in tetragonal $Cs_3Zn_{1-x}Mn_xCl_5$ under different pressures.

References

1. Itskevich E.S. High-pressure bomb for operation at low temperatures // Priory i Technika Experimenta. - 1963. - N4. - P.148-151.
2. High-pressure chamber up to 18 kbar for operation at helium temperatures // E.S.Itskevich, A.I.Voronovskii, A.F.Gavrilov, V.A.Sukhoparov / Priory i Technika Experimenta. - 1966. - N6. - P.161-164.
3. Tsiklis D.S. A technique of physical-chemical investigations at high and superhigh pressures. - Moscow: Khimia, 1976. - 431p.
4. A.I.C. I280657 AI, Int.cl.⁴ H OI P 5/08. Input of the microwave-frequency energy into high-pressure chamber/ S.N.Lukin, O.P.Teslya. - Publ.30.12.86, Bull. N48.
5. Lukin S.N., Nemchenko E.D., Oranskii L.G. A millimeter range resonator for EPR spectrometer // Priory i Technika Experimenta. - 1977. - N4. - P.116-117.
6. Barman I.V., Brandt N.B., Ginzburg N.I. Study of the influence of pressure up to 30 kbar on critical fields of stanum and indium at 0.1-4 K // Zh.experim.and Theor.Fiz. - 1967. - 53, NI(7). - P.124-131.

APPARATUS FOR MEASUREMENT OF C_V AT HIGH PRESSURE AND HIGH TEMPERATURE

W. Scholl, H.Lentz
Universität-Gesamthochschule Siegen.
Fachbereich 8, Postfach 101240
D-5900 Siegen

The Determination of the specific heat capacity of highly compressed fluids at high temperature suffers mainly from the large heat capacity of the required autoclave.

To overcome this problem, two methods have been developed, both of which exclude any influence of the autoclave's properties on the measured results. To obtain C_V directly according to its definition (1),

$$C_V = \Delta W / (m \cdot \Delta T) \quad (1)$$

a known mass m of the sample fluid must be filled in, a known energy ΔW applied to it and the resulting increase in temperature ΔT has to be measured.

First method, preferably for supercritical fluids:

The sample is heated quickly by a strong electrical heat pulse and measurement of the corresponding mean temperature increase is accomplished by a precision pressure gauge. The supposition is that the measured pressure always represents the mean temperature of the sample. And indeed, the error due to non-ideal properties of the fluid is below 0.1% in most cases when ΔT is as small as 1K.

Immediately after the heat pulse, pressure should maintain its value until the heat front, which is propagating by heat conduction, reaches a wall of the autoclave. At this moment pressure begins to

fall due to cooling of the fluid at the wall. During the time when pressure is at its constant plateau, the fluid can be regarded as thermally isolated and the heat capacity of the autoclave has no influence at all.

However, there are some difficulties. The first arises from compression of the part of the fluid which is not directly heated. The region around the heating coil will be heated by direct heat conduction. Thereby this part of the fluid expands and compresses the directly heated fluid around, which in turn is heated by being compressed. So heat transfer to the walls of the autoclave can start once with the beginning of the heat pulse. The influence of this process on accuracy can be minimized by selecting the best ratios of volumes of directly to indirectly heated fluid and by providing a possibly large heat-transfer-surface of the heating coil.

Another difficulty is convection. With strong heat pulses (heating power above 10 watts) the fluid in and around the coil is accelerated, like smoke in a chimney, that it reaches the top of the autoclave in nearly 1 second. This is an upper limit for the total time of measurement. On the other hand, heating time cannot be shortened arbitrarily. A minimum amount of the average temperature increase is required to perform pressure measurement with sufficient accuracy. Therefore the heat pulse must have a minimum energy. But shortening heating time, heating power must increase. High heating power generates a high over-heating of the heating wire, which cannot transfer enough of its heat to the fluid when the time is too short, even though the wire is very thin and has a great surface area. So a heating time between $\frac{1}{2}$ and 1 second seems to be the best compromise.

A similar idea for experimental determination of C_v has been known around 1920 by Trautz and co-workers [1],[2].

Second method

Inside the autoclave there is an additional inner vessel, which contains a definite part of the sample. The wall of this inner vessel is of special construction. The main kernel consists of austenitic steel with a low, well-defined heat conductivity. This kernel is covered on both the inner and the outer surface with a temperature-sensing foil, whose electrical resistance is a function of the mean temperature all over the concerned surface.

Two modes of operation are possible with this type of wall: The "adiabatic mode" is to use both the sensor foils as well as heating resistors. A certain energy ($\Delta W + \Delta W_{Fl}$) is applied to the inner resistor, and the heating power of the outer resistor is controlled to keep its temperature always equal to that of the inner resistor, during all the heating time. By this "counter-heating" a neutral plane close to the middle of the wall's kernel material is formed, which is not passed by any heat-flow. Either, inner and outer, part of the kernel up to the neutral plane is filled up with heat energy from the corresponding resistor. The temperature reading from the inner foil is used as ΔT to calculate C_v .

When the sample fluid is surrounding the wall inside as well as outside the inner vessel, the heat-transfer conditions are equal on both sides and the position of the neutral plane is nearly independent of the sample substance. Thus it is possible to define a constant effective heat capacity C_{Fl} of the calorimeter. It is contributed exactly by the material of the inner vessel up to the neutral plane and can be easily obtained from a calibration cycle with evacuated autoclave.

The other mode of operation of the described wall is the "heat-flow" mode. The autoclave with all its contents is heated (or

cooled) slowly by an environmental precision thermostat. The heat flowing into the sample, establishes a temperature difference across the kernel material of the inner vessel's wall. This temperature difference is measured with the foil resistors, recorded and integrated. The integral is a direct measure for the heat energy ΔW , which has heated the sample.

Apparatus

The general setup used for both methods consists of a vacuum thermostat with two adiabatic shields. The autoclave itself, also used in either case, is heated with thermocoax wires soldered on its surface. Its temperature is measured with two Pt-100 resistors. Long-time constant regulation of temperature with a resolution of 1 mK at temperatures up to 600°C is done by an AC mains-synchronized 22-bit ratiometric analog-to-digital converter (ADC), a five-channel thermocouple 12-bit ADC with 2 mK resolution and by 6 microcomputer-controlled quasi-linear programmable DC power sources.

The heating power ΔW is delivered by a quick-settling, analog and digitally programmable current source. A microcomputer board performs control of the complete measuring process.

Two additional units, decisive for the first method, are a 1 ppm resolution pressure transducer with digital output and a sampling rate of 1000 per second and a 21-bit ratiometric ADC with the same sampling rate of 1000 per second.

References

1. Trautz, M. and Großkinsky, O.: Die Messung der spezifischen C_p von Gasen mittels der Differentialmethode, Ann. d. Phys. 67, 1922, 462
2. Kh.I. Amirkhanov, G.V. Stepanov, B.G. Alibekov: Isochoric heat capacity of water and steam, Amerind Publ. Co. New Delhi 1978

REFERENCE SUBSTANCES FOR PRACTICAL HIGH PRESSURE SCALE

A.S.Skoroparov, B.I.Valevski, V.F.Skums, A.A.Vecher
Physico-Chemical Problems Research and Development Institute
of the Byelorussian State University, Minsk, USSR

In order to determine solid-phase pressure special calibrants are used in most cases to judge on pressure by the jumping of their electrical properties. Traditional calibrants for a pressure range 2 + 8 GPa (Bi, Ti and Ba), recommended in 1968 by International Conference on Accurate Characterization of the High Pressure Environment, possess some valuable properties, which allow them to be widely used for a long time as pressure calibrants. Those properties are well studied, low cost and possibility of obtaining pure materials. At the same time these calibrants have some shortcomings: they are easily oxidized (appreciably changing their electrophysical properties), some of them (Ti and Bi, in particular) are toxic, they produce insufficiently intensive and distinct electrical signals, neither they embrace the entire range of the pressure scale.

At the same time there is group of materials, characterized by high pressure-induced reversible phase changes, accompanied by sharp variation of their electrical resistance. Those are chalcogenides of the 2nd and 4th group, whose electrical resistance changes, by 4-7 orders due to high pressure influence. In accordance with our data, the conditions of their synthesis, which lead to differences in electrical conductivity and concentration of current carriers as well as to different conductivity type do not practically impact on the phase conversion onset pressure (P_0), though changing the electrical signal intensity and phase conversion rate. In view of this, these substances can be suggested as reference substances for a practical high pressure scale. However, the available P_0 data for these substances are very diverse.

In order to execute the decision of the All-Union Meeting "Advances, Problems and Prospects of High and Superhigh Pressure Estimation" (Minsk, 1986), the group of researchers, headed by All-Union Center on Search, Estimation and Organization of Production of Marked Materials-High Pressure Sensors, carried out investigation of the phase conversion parameters, in particular P_0 , for cadmium, lead and tin tellurides as well as for lead selenide to estimate their possible use as new reference materials for the practical high pressure scale. The researches were carried out by the

present report authors as well as by R.A.Ishbulatov, Yu.A.Litvin, V.A. Kosyakov (IEM, USSR Academy of Sciences), Yu.V. Vorona, Yu.M.Rotner (OGU, Odessa), L.I.Fel'dgun (VNIASH, Leningrad), V.A. Mukhanov, V.A.Laptev, M.I.Samoilovich (VNIISUMS, Alexandrov), A.P. Ryaposoov (IG G SO USSR Acad. Sci.), I.I.Timofeeva, V.M.Volkogon (IPM Uk.SSR Acad. Sci.), Yu.S.Maslenko (ISM Uk.SSR Acad. Sci., Kiev), V.A.Stupnikov, K.P.Burdina, K.N.Semenenko (MGU, Moscow), G.L. Aparnikov, L.M.Okonov (VNIImaz, Moscow). They used the commercial materials, manufactured in the Soviet Union, and those, synthesized by L.V.Prokof'eva (FTI USSR Acad. Sci., Leningrad) and M.R. Allazov and A.A.Movsum-zade (Special Design Bureau on KPMS with O of the Azerb. SSR, Baku).

As it follows from the presented data that not all of the named authors, having the above materials, presented sufficient results. Some findings do not result from direct electrical studies. Also, note, that different authors do not possess a single point of view as to what should be taken as a marked point (or as a phase conversion onset pressure - P_0) for cadmium telluride. Besides, signal in tin telluride is far from being distinct and is rather expanded the pressure scale. So, it seems reasonable to introduce only lead selenide and telluride from examine chalcogenides at the practical high pressure scale, whose data were statistically processed regard the reliability and significance of the findings.

The P_0 are 4.23 ± 0.07 GPa (signal intensity of 3-4 orders) for lead selenide and 5.05 ± 0.09 GPa (3-7 fold change of electrical resistance). Our studies support the suggestion to include cadmium selenide and sulfide, as well as lead sulfide having a distinct electrical signals (at pressures in 1.5 ± 3.74 GPa, 1.5 ± 3.44 GPa and 2.2 ± 2.5 GPa correspondingly, as it is follows from literature sources, see Table) as promising reference substances for the practical high pressure scale. However, it seems impossible as far as to the great scatter of various data (see Table), the more, the information has been obtained, using x-ray analysis, while the researchers and practical workers perform calibration, using electrical resistance equipment, and the x-ray data for the phase conversion onset pressure - P_0 - somewhat differ from electrical resistance data* for one and the same substance. However, we plan ahead to undertake efforts to characterize these substances under pressure with presentation of the recommended data for their P_0 .

* Vereshchagin L.F. and Kabalkina S.S. X-ray Studies at High Pressure. Moscow : Nauka, 1979, 173 p.

Phase transition pressure for cadmium selenide (1) and sulfide (2) and lead sulfide (3).

Compound	Transition pressure, GPa	Method	Authors	Year
1	2.2	x-ray	N.Kh.Abrikosoov et al.	1975
	2.2	x-ray	N.N.Berchenko et al.	1982
	3.4	x-ray	P.I.Baransky et al.	1975
	3.03	R	A.I.Prikhna et al.	1978
	2.9	opt.	I.R.May et al.	1980
	2.5 and 1.5	R	C.Roomans	1969
	2.1	R	A.Onodera	1969
	3.74	R and x-ray	R.T.Johnson et al.	1979
2	2.7	x-ray	P.I.Baransky et al.	1975
	1.5	x-ray	N.Kh.Abrikosoov et al.	1975
	1.5	x-ray	N.N.Berchenko et al.	1982
	3.44	R	R.T.Johnson et al.	1976
	1.6 and 2.0	R and x-ray	C.Roomans	1969
	2.0	x-ray	S.S.Kabalkina et al.	1980
	2.0	x-ray	Z.V.Malyushitskaya et al.	1980
	2.3	R and x-ray	G.A.Samara et al.	1965
3	3.0	x-ray	T.Suzuki et al.	1983
	2.3	R	C.Roomans	1969
	2.2	x-ray	C.W.F.Pistorious	1970
	2.5	ΔV	U.I.Ravich et al.	1968
	2.5	R	A.A.Semerchan et al.	1960
	2.4	x-ray	N.Kh.Abrikosoov et al.	1975
	2.2	x-ray	T.Khattopadkhiya et al.	1983
	2.5	R	N.B.Brandt et al.	1976

R - electrical resistance, ΔV - volume change.

Note, that analysis of the high pressure results on the chalcogenides investigation shows, that other compounds, having phase transition under pressure influence, for the time being can not be recommended this aim (because of their insufficient study first of all), though in literature there are a lot such kind of data (as for binary compounds, as for ternary phase).

G.N. Neillo

Physico-Technical Institute, Ukrainian Academy of Sciences
Donetsk, USSR

The paper gives generalization of studies on development and usage of high-pressure (HP) technique in the EPR spectroscopy for the period of 1957-1985.

This gives possibility to perform: a) analysis of existing designs, b) reveal of most perspective constructions, c) search for the ways of increasing pressure range in the EPR studies.

Analyzing works done during this period it is easy to see that the equipment of the piston-cylinder type and the Bridgman anvils are used as HP generators in the EPR spectroscopy. And the equipment of the piston-cylinder type is as a rule used because of the construction where it is easy to create pressure.

All the constructions are classified according to the type of resonators used and analysed by the same criterion.

It turned out that resonators of four types are used in the EPR spectroscopy at HP. They are: coaxial /1/, hollow with ultrahigh-frequency window /2/, solid-state with dielectric filler /3/ and spiral /4/ ones.

Despite the fact that the creation of a number of devices for the EPR investigation under HP /1-4/ is the essential achievement, their experimental possibilities however are limited. Thus, practically all of them can be used as a rule to investigate spectra of samples having large enough concentration of paramagnetic centres at the room temperature, while observation of spectra of most ions is possible at low temperatures only. Consequently, all of them in the as-constructed form are unacceptable for solving a large variety of problems of the EPR spectroscopy consisting of investigation of the EPR spectra in wide pressure and temperature ranges as well as of the electron spin-lattice relaxation of samples with different concentration of paramagnetic centres.

Creation of "crystal-resonators" completely made of the investigated substance covered with thin metallic layer /5/ and placed in a non-magnetic cylinder high-pressure vessel (HPV) made it possible to study the EPR spectra of samples with heavy paramagnetic dilution in the temperature range of 300-1.5 K.

The crystal-resonators drawbacks consist of the necessity of growing large single crystals and making a new crystal-resonator for each investigation.

The idea of crystal-resonators was further developed and as a result a number of compound resonators made of leucosapphire /6-11/ have been created which were for the first time used in studies on HP effect on the processes of the electron spin-lattice relaxation.

Structurally the resonators are made composite of leucosapphire in the form of cylinders or rectangular parallelepipeds of a corresponding size in which the sample studied is placed either inside the ring washer made of leucosapphire or rubie, or, in case of rectangular resonators, it is placed at one of its steps on the lateral surface. The whole set is closed by a metallic yoke-sleeve. The most universal are the two-frequency resonator /6,7/ and the resonator for the EPR measurement of electric dipole transitions /11/.

It is known that the condition necessary for the EPR observation is the action of the external magnetic field on the sample studied, therefore units of HP equipment are traditionally made of a nonmagnetic material, for example, beryllium bronze having limiting range of attainable pressures of 1.2-1.5 GPa, while in steel vessels of the piston-cylinder type pressures up to 5 GPa can be obtained.

The requirement for the nonmagnetic nature was eliminated which resulted in the creation of the device for the low-temperature EPR investigations at HP /8/.

The essence of the device is as follows. The HPV of the piston-cylinder type is made of high-strength ferromagnetic alloy and for the condition of the EPR experiment to be preserved the source of the external magnetic field, a miniature superconducting solenoid, is placed together with the sapphire frequency resonator and the sample studied in the HPV operating channel. When HPV of nonmagnetic materials and radiospectrometer electromagnet are used /9/, the EPR studies are possible at pressures up to 1 GPa and temperatures of 1.5-4.2 K at arbitrary direction of the magnetic field.

At present, use of the Bridgman anvils seems to be the only way to obtain pressure higher than 5 GPa in the EPR measurements. The superhigh-frequency resonator was constructed /10/ making it possible to carry out the EPR investigations at pressures up to

30 GPa. The set objective was achieved at the expense of the solid-state resonator of H_{011} mode being the composite one, consisting of the leucosapphire cylinder with through axial hole in which movable leucosapphire plungers are placed with a slide fit to whose faces conical diamond anvils are fixed which wring out the metallic spacer with the sample studied.

References

1. Walsh W.M.Jr., Bloembergen N. Paramagnetic resonance of nickel fluosilicate under high hydrostatic pressure//Phys.Rev. 1957. -107, N3.P.904-905.
2. Lawson A.W., Smith G.E. High-pressure microwave window//RSI 1959. -30, N11. -P.989.
3. Kaminov I.P., Jones R.V. Pressure dependence of microwave resonance properties of some spinel and garnet ferrites//Phys. Rev.-1961. -123, N4. -P.1122-1129.
4. Filippov A.I., Yablokov Yu.V. An attachment to EPR-spectrometer for studying substances under high hydrostatic pressure. Theses of works of the All-Union Anniversary Conference on Paramagnetic Resonance, June 24-29, 1969, Kazan, 1969. - P.146.
5. Neilo G.N., Petrenko V.P., Tsintsadze G.A. A videospectrometer with crystal-resonator for investigations in wide pressure and temperature range//Pribory i Technika Eksperimenta. -1972. -N5.-P.210-212.
6. Neilo G.N., Prokhorov A.D., Tsintsadze G.A. Electron spin-lattice relaxation in a paramagnet at high pressures//Zh.Exptl. Teor.Fiz.- 1977. -72, N3. -p.1080-1086.
7. I.C.693232 USSR, Int.cl.² GOI N 27/28. Resonator of the electron paramagnetic resonance spectrometer/G.N.Neilo, A.D.Prokhorov, G.A.Tsintsadze.-Publ.25.10.79. Bull.N39.
8. I.C.966568 USSR, Int.cl.³ GOI N24/10. A device for the low-temperature study of the electron paramagnetic resonance (EPR) at high pressures/ A.D.Prokhorov, G.N.Neilo, V.V.Permyakov, I.G.Gavrish.-Publ. 15.10.82. N38.
9. Prokhorov A.D., Permyakov V.V., Neilo G.N., Gavrish I.G. Obtaining of the magnetic field of arbitrary direction in a high-pressure chamber//Pribory i Technika Eksperimenta.- 1983. -N3. -P.206-208.
10. I.C.1086377 USSR, Int.cl.³ GOI N24/10. Resonator for the EPR measurements at high pressures/G.N.Neilo, A.D.Prokhorov. -Publ. 15.04.84.Bull. N14.
11. I.C. II9I788, Int.cl.⁴ GOI N24/00, 24/12. Resonator of the electron paramagnetic resonance spectrometer/G.N.Neilo, A.D.Prokhorov, -Publ.15.11.85. Bull. N42.

M.I.Eremets, V.V.Struzhkin, I.A.Trojan

Institute of High Pressure Physics, the USSR Academy of Sciences, Troitsk, USSR

A laser radiation focusing in the center of a diamond anvil cell (DAC) allows to provide investigations up to $P \approx 100$ GPa with the pulsed /1/ and sustained heating to 5000 K /2,3/. The use of laser radiation allows to exclude the influence of a heater materials if the sample itself strongly absorbs the radiation. Many materials are transparent for $1.06 \mu\text{m}$ YAG-laser radiation usually used for the heating. Therefore it's necessary to mix absorbing radiation powders, for example, graphite, platinum /2,3/. The use of the powerful CO_2 -laser for the heating considerably extends the scope of the materials under investigation, as the wavelength radiation $\lambda = 10 \mu\text{m}$ is in the range of the strong lattice absorption (absorption coefficient $\sim 10^3 - 10^4 \text{ cm}^{-1}$) of many oxides, nitrides and so on.

Experimental technique. The experimental setup is schematically shown in Fig.1. The radiation from the CO_2 -laser with 100 W (multimode) CW power is focused to the spot of $\varnothing 80 \mu\text{m}$ with NaCl lens ($f=4.3 \text{ cm}$). The incandescent spot can be visually observed. The spectra of a thermal radiation from the both sides of the sample can be recorded. The $\varnothing 10 \mu\text{m}$ part of the spot can be limited with the diaphragm. For the measurements with $\tau \sim 10^{-5} \text{ s}$ the spectrometer was used as a polychromator. In the exit focal plane two stripelike fibers captured light with $\Delta\lambda = 5 \pm 10 \text{ nm}$. After the optical fibers and PEM signals enter the logarithmic divider and then the oscillograph.

DAC parts were made from stainless steel and the diamond supports from tungsten carbide. To avoid the oxidation of diamonds during the heating the DAC was placed in the oven, which was evacuated or filled with inert gas.

The temperature distribution in the diamond anvil. To find out conditions of achieving maximum temperature the estimate of the temperature distribution at the sustained heating was done. The calculations were made on the assumption that the whole radiation power $Q=100 \text{ W}$ was absorbed by the material surface layer and then transferred to the anvil, the other anvil was thermoisolated. The temperature dependence of the thermoconductivity coefficient was taken into consideration. The spot (radius $r=50 \mu\text{m}$)

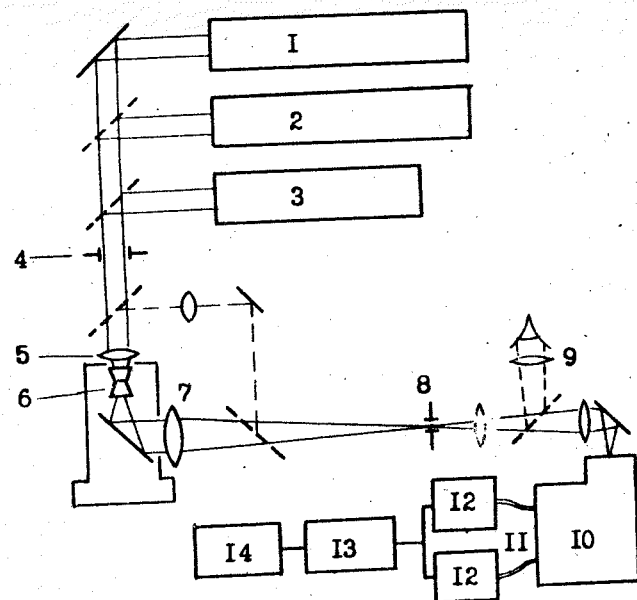


Fig. 1. Block diagram of the optical arrangement:
1 - CO₂-laser (multimode) 100 W; 2 - CO₂-laser (TEM₀₀ mode) 25 W;
3 - YAG-laser, 60 W, 4, 8 - diaphragms, 5 - NaCl lens, 6 - di-
amond anvils, 7 - objective, 9 - eyepiece, 10 - monochromator,
11 - optical fibers, 12 - photomultiplier tube, 13 - divider,
14 - oscillograph.

heated by a focused laser radiation was considered as the point-
-like thermal source with temperature T . Two parts of the anvil
were distinguished for the calculations: a halfsphere, $R=300\text{ }\mu\text{m}$
(radius of the anvil top) and a coneshaped part with base radius
 $R_2=2\text{ mm}$. It proved to be, that with the parameters mentioned above
for 1a type diamond $T=2500\text{ K}$, $T_1=1050\text{ K}$, if $T_2=500\text{ K}$ (T_1 - the
temperature at the boundary of two distinguished above parts of
the anvil, T_2 - the temperature at the base of the anvil). Maxi-
mum T can be achieved by better focusing of the beam ($T>3000\text{ K}$
at $r=25\text{ }\mu\text{m}$). It's possible to heat the sample to a higher temper-
ature by thermoisolating it from the anvils.

Experimental results. The obtained estimates were qualitatively
confirmed by experiments ($P\approx 20\text{ GPa}$). Pressure was determined
by the load applied to anvils after preliminary calibration at
room temperature with the ruby fluorescence method. Ruby, as a
le, was absent in the heating experiments to avoid its interaction

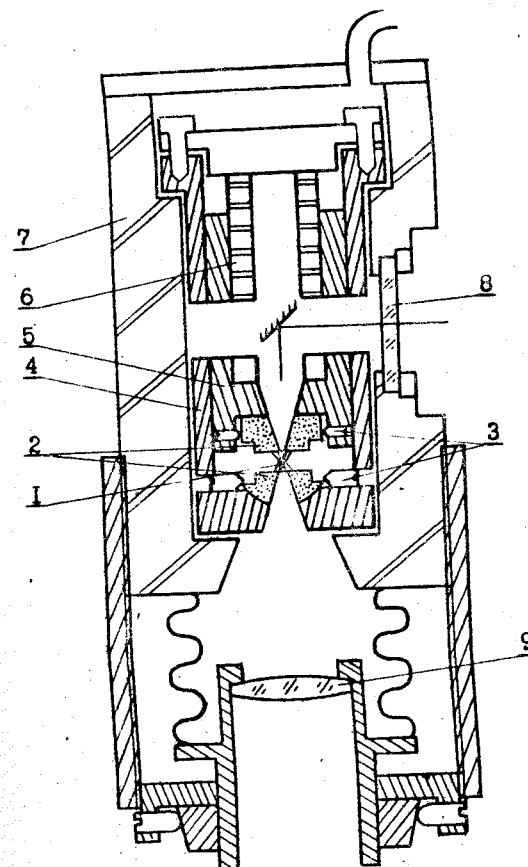


Fig. 2. Diamond anvil cell:
1 - diamond anvils, 2 - rockers, 3 - screws, 4 - cylinder,
5 - piston, 6 - spring, 7 - oven, 8 - window, 9 - NaCl lens
with bellow and focusing system.

tion with the sample. The maximum achieved temperature strongly
depends on the specific conditions of the experiments. A pyrogra-
phite plate isolated from the back anvil by mica was warmed to
 $\approx 1100\text{ K}$. If this plate is placed in mica gasket and isolated from
anvils by MgO powder, then the temperature $T=2000\text{ K}$ is reached.
If a graphite plate is in contact with both anvils, it's impossi-
ble to warm it to the visible glow.

The maximum temperature was achieved during the mica heating. Quartz situated in the hole of $\phi 200 \mu\text{m}$ in mica gasket under a pressure of 15 GPa was warmed to $T=1900 \text{ K}$. The error of the temperature determination (at about 200 K) was caused mainly by the laser power fluctuations.

One pair of anvils can survive a few tens of heating experiments during 10-20 minutes at $T=2000 \text{ K}$ and $P=15-20 \text{ GPa}$. Small cracks often emerged in the heated place and the following repolishing of the anvil tops was required. The air around the anvil being heated, the diamond lateral surfaces near the anvil tops were etched.

So the sustained heating to 2800 K is conducted in the DAS under a pressure of 20 GPa with CO_2 -laser radiation heating. This allows to investigate phase transitions and to produce the laser annealing.

References

1. Bassett W.A., Weathers M.S. Temperature measurement in laser heated diamond anvil cells. - *Physica*, 1986, v.139 & 140B, p.900-902.
2. Ming L.C., Bassett W.A. Laser heating in the diamond anvil press up to 2000 °C sustained and 3000 °C pulsed at pressures up to 260 kilobars. - *Rev. Sci. Instrum.*, 1974, v.45, p.1115-1118.
3. Jeanloz R., Heinz D.L. Experiments at high temperature and pressure: laser heating through the diamond cell. *J. de Physique*, v.C8, p.83-92.

THE HIGH PRESSURE APPARATUS WITH SLIDING ANVILS

A.I.Prikhna

Institute for Superhard Materials, Academy of Sciences of the UkrSSR, Kiev, USSR

The solid-state high pressure apparatuses used in practice, those of recessed-anvil and belt type, are not reliable enough in terms of the pressure retention due to difficulties to ensure the constancy of pressure in their gasket regions. In the design described below the reliability of the HPA is achieved through the incorporation of anvils sliding one over another and arranged in such a manner that the central opening between them can decrease /1,2/.

The HPA shown in Fig.1 was realized according to /2/. It consists of a ring 1 and four sectors 2 and four anvils 3 disposed within the ring. The inner surfaces of the sectors 2 and the surfaces of the anvils 3 conjugated with them are inclined towards the axis of the ring 1 as is shown in Fig.1,b,c. The sectors 2 are fixedly held in the ring 1 by the flange 4. The whole unit is set firmly on the press bed 5 (not shown). The press is equipped with two opposite pistons, the lower one 6 and the upper one 7.

The apparatus operates as follows. The lower piston 6 provided with an isolation gasket 8 is moved up to the anvil 3. The container 9 of electric isolation plastic material having within the sample 10 to be compressed is put into the opening between the anvils. Thereafter, the upper piston 7 is switched on to move downwards when the piston 7 comes into contact with the anvil 3 the in-between opening closes forming a closed cavity and then all the anvils 3 start to move downwards. The sectors 2 surfaces whereon the anvils 3 slide being inclined towards the axis, each anvil 3 moves in the horizontal plane in the directions shown by arrows in Fig.1,a. This results in the decrease of the cavity cross section and, consequently, in the compression of the container 9 and the sample 10.

The force diagrams for various stages of the anvils operating cycle are shown in Fig.2. The force developed by the lower piston 6 equilibrates the pressure exerted on the piston by the container 9 and the sample 10 and in addition it generates in the gaskets 8 the pressure required.

The force developed by the piston 7 counterpoises the force of the piston 6 and all other forces acting on the side faces of

the anvils 3 as well as the frictional forces developing between the gaskets 8 and the anvils 3.

Thus, the surplus of the force developed by the upper piston against that of the lower one is equilibrated by the "non-vertical" forces acting on the anvils 3. The system of forces acting on the anvils in the process of loading is shown in Fig.3. This slide shows the normal force, indicated by the Q-vector, that acts on one of the apparatus cavity walls and the T-vector that represents a friction force generated by the force Q.

The F-vectors are normal forces arising between the adjacent anvils and T are friction forces generated by the forces F. T_3 is the friction force operating on horizontal faces of the anvils. T_2 -vector is the horizontal component of the friction force operating between the anvil base and the adjacent sector surface.

Comparing the diagrams shown in the upper and the lower Figures it is easy to see that the force F and the force R depend on the angle α , all other conditions being equal. Fig.4 depicts the dependence of normal compressive forces at the adjoining anvils and that of a horizontal component force developed in the response of the sector 2 on the angle α all other conditions being the same.

The optimal force F value can be defined by solving a known differential equation that describes the distribution of pressure between the block head and a blank in the process of upsetting which is used in the theory of metals machining by pressure. However, the constant shear strength value should be substituted in the equation with the expression defining its pressure dependence. For a rather wide range of carbonates, magnesia, sodium salt and graphite that are generally used as gaskets between anvils, this dependence is most-fully described by the expression in form:

$$\tau_{sp} = P^n - \frac{m \cdot P}{K^n}$$

The values of n, K and m for various materials and for the values ranging from 10 to 50 kbar may be found using the Bridgman table data. For example, for graphite they are equal to 0.588, 1.130 and 0.636 respectively. Though the equations after the substitution becomes more complex and cannot be integrated by quadratures but its approximate solution does not involve any problems.

A force F that is somewhat larger than analogous one generated in apparatuses incorporating compressible gaskets can be used, e.g. for the apparatus of recessed-anvil type and "belt" type. For these apparatuses: $F/Q \approx 0.6 \div 1$.

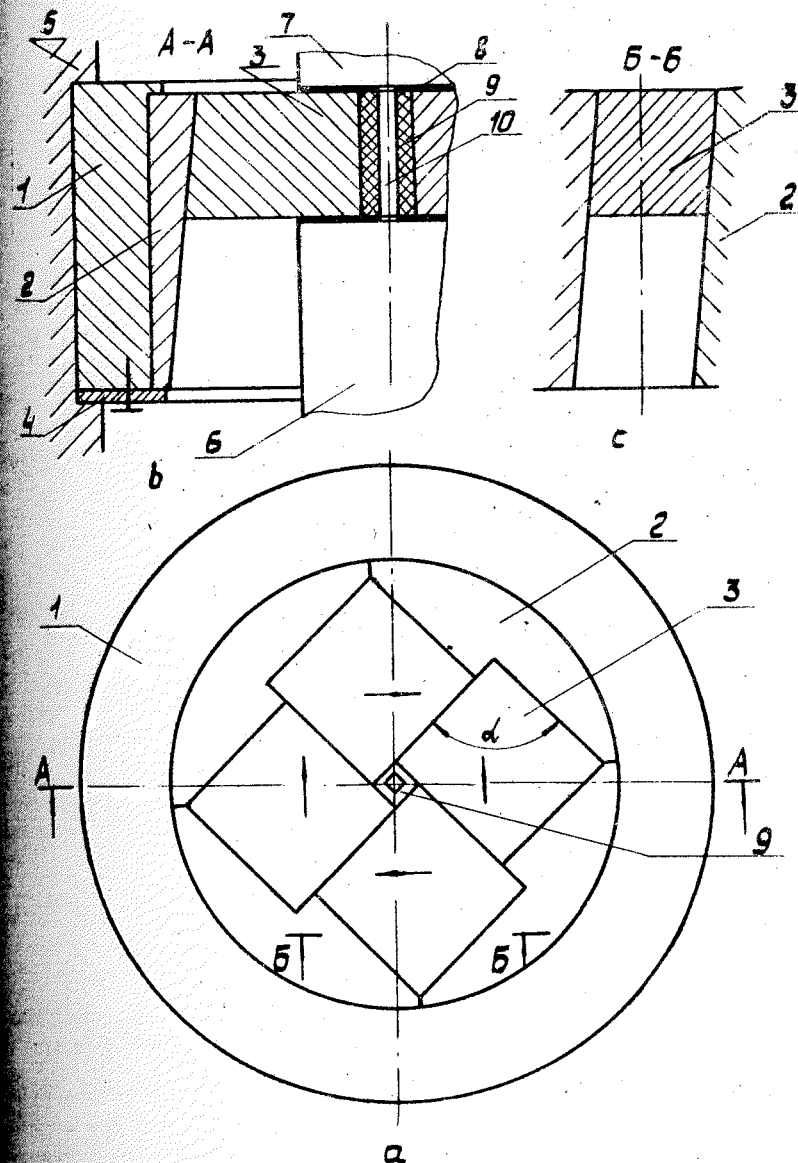


Fig.1. High pressure apparatus with sliding anvils (details in the text).

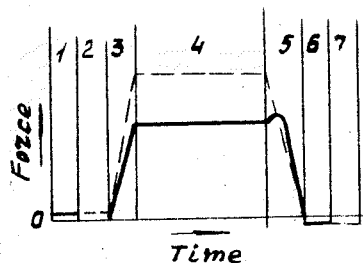


Fig. 2. The force diagram for the pistons:
 — lower one, — upper one at the stages:
 1 - moving the lower piston upwards, 2 - moving the upper piston downwards, 3 - loading, 4 - holding, 5 - lowering the pressure, 6 - moving the lower piston back, 7 - moving the upper piston back

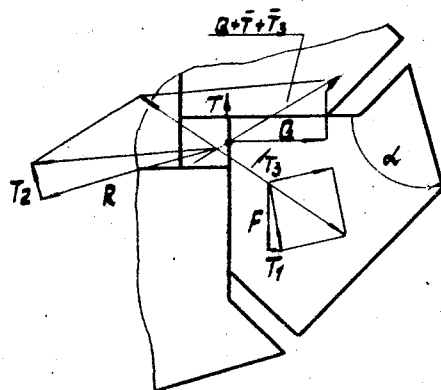


Fig. 3. System of forces acting on the anvil:
 Q, T are acting forces. F, T_1, R, T_2, T_3 are reactions.

As may be well understood from the above, in the HPA described a pressure developed between the press pistons and the bottom faces of anvils can be controlled independently from the pressure within the cavity by varying the lower piston force and the pressure

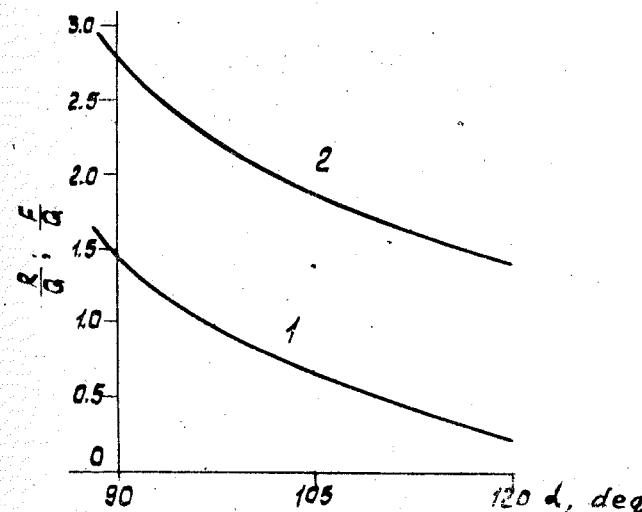
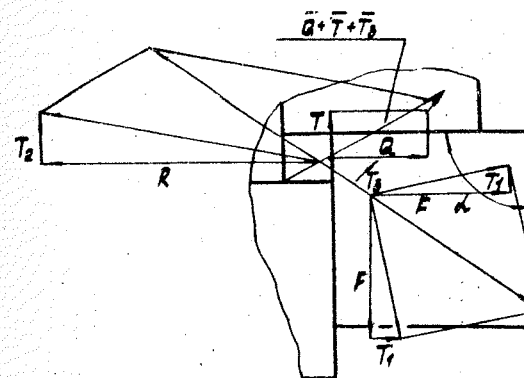


Fig. 4. The dependence of the forces $F(1)$ and $R(2)$ on the values of α (Figs. 1, 3).

sure between the anvils can be controlled by selecting an appropriate angle between the working and the bearing side surfaces of the anvils. This ensures a reliable pressure retention within the cavity.

References

1. Тайна алмаза. Научно-популярный фильм. Киелнаучфильм, 1963 г. Авт. сценария А.И. Прихна, В.А. Кузнецов.
2. А.с. №1258618 СССР, МКИ В22 Г 3/02. В ЗОВ 15/02 Устройство для прессования. /А.И. Прихна Опубликовано 23.09.86. Бюл. №35.

PRESSURE SELF-MULTIPLICATION EFFECT IN A PLANE-ANVIL CHAMBER CAUSED BY NONLINEAR ELASTIC PROPERTIES OF SOLIDS

V.D. Blank, Yu. Ya. Boguslavski, S.G. Buga, E.S. Itskevich, Yu. S. Konyaev, A.M. Shirokov

Institute of High-Pressure Physics, the USSR Academy of Sciences, Troitsk, USSR

The pressure distribution in a solid compressed by hard anvils, depends not only on the anvils shape, but also on mechanical properties of substance being investigated. Namely, increase of elastic moduli caused by pressure, leads to a sharpening of distribution over diameter and to an increase of the maximum pressure in a central part of the sample, as compared with the case of constant moduli. A positive feedback is established: an increase in load increases the pressure and the elastic moduli, and the increase in the moduli automatically ensures a faster rise of the pressure at the centers of the anvils /1/.

The self-multiplication effect should be manifested most efficiently by substances that undergo a phase transition and are in a chamber at two-phase state. Each step of load, rising or falling leads to occur a part of a sample which is in a metastable state in the pressure hysteresis region. Shear deformation or heating initiate the phase transition of this part of substance, so the distribution of pressure at constant load takes place. The effect can be attributed to essentially nonlinear alteration of elastic properties of substance at phase transition.

We have investigated pressure distribution in the samples of KCl before and after shear deformation /1/, and also before and after the heating up to $T = 600$ K in a diamond chamber at the pressure range up to 18 GPa when rising or falling load was applied by steps. The method of creation and registration of pressure is described in /1,2/.

It is shown, that shear strain in KCl sample results in considerable redistribution of the pressure when the polymorphic transition pressure was exceeded. If the load was increased first (BI \rightarrow B2 transition) after applying shear stress, it was found that the pressure increased at the central part of the sample and decreased at the periphery (Fig.1). The changes in the pressure at the center could reach 50-70% of the initial value before shear. The increase of pressure caused by transition BI \rightarrow B2

reaching up to 600 K and initial pressure ~ 6 GPa at the center of sample was $\sim 30\%$ (Fig.2).

The effect is reversible: during the reverse run (B2 \rightarrow BI transition) the pressure decreased at the center and increased at the periphery after shear or heating. The control experiments on the same samples, which have no phase transition in the investigated range of pressures, didn't show described effects.

It should be pointed out that the kinetics of phase transition at conditions of heating is essentially much weaker than in case of shear.

Obviously, the observed effect of the positive feedback can be calculated only in the framework of the nonlinear theory of elasticity.

Let's consider the sample compressed by force F in a plane-anvil chamber that underwent a phase transition and then effected shear or heating. The diameter of the sample, and the diameter of the inner high-pressure phase are D and d , correspondingly. The elastic moduli of the 1st phase do not depend on pressure /1/. The elastic moduli of the 2nd phase are the linear functions of pressure /1/:

$$\mu_2 = \mu_{20} + (\partial \mu_2 / \partial p) |_{p_0} (p - p_0); K_2 = K_{20} + (\partial K_2 / \partial p) |_{p_0} (p - p_0)$$

But in this case the dependence $K_2(p)$ is quite weak and we assume $(\partial K_2 / \partial p) |_{p_0} = 0$. Instead of this parameter we'll use certain effective value \tilde{K}_{20} , determined through the maximum magnitude of pressure and derivative $(\partial K_2 / \partial p) |_{p_0}$. Finally, in the framework of the theory of homogeneous deformations, the pressure in phase 2 can be given by equation:

$$p_2 = -\frac{B}{2A} + \frac{\sqrt{B^2 + \frac{C}{A}}}{\sqrt{4A^2 + \frac{C}{A}}}$$

$$A = \frac{4}{3} \frac{\partial \mu_2}{\partial p} |_{p_0} [3d^2 \tilde{K}_{20} + (D^2 - d^2) \frac{E_{10}}{3}];$$

$$B = \frac{4}{3} \frac{\partial \mu_2}{\partial p} |_{p_0} (K_{20} + 3K_{20}) E_{10} + \frac{3}{4} \pi d^2 K_{20} / M_{20} - 3 \tilde{K}_{20} \frac{\partial \mu_2}{\partial p} |_{p_0} F - \frac{4}{3} \frac{\partial \mu_2}{\partial p} |_{p_0} [3d^2 \tilde{K}_{20} + (D^2 - d^2) \frac{E_{10}}{3}];$$

$$C = 3 \tilde{K}_{20} F (\mu_{20} - (\partial \mu_2 / \partial p) |_{p_0} p_0),$$

where p_0 is the pressure of phase equilibrium; E_{10} - Young modulus of phase 1. We have for KCl /1/: $E_{10} = 24.3$ GPa, $\mu_{20} = 14.5$ GPa, $(\partial \mu_2 / \partial p) |_{p_0} = 1.6$; $(\partial K_2 / \partial p) |_{p_0} \approx 4.6$. Then the value of the self-multiplication, caused by shear (Fig.1) can be calculated. For $F = 1.7$ kN, $D = 0.085$ cm, $d = 0.04$ cm, then $p_2 \approx 5.7$ GPa, $p_2 / p_0 \approx 1.6-1.7$, that is in a good agreement with experimental data ($\bar{p} = 4F / \pi D^2$).

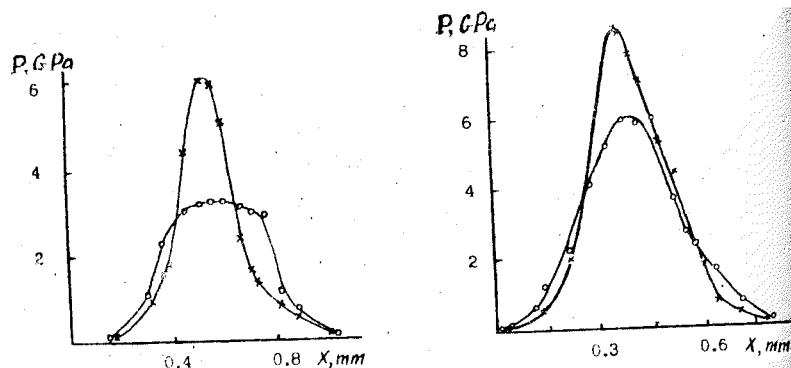


Fig. 1. Distribution of pressure in the chamber before (—o—) and after (—x—) the shear deformation at the load increase.

Fig. 2. Distribution of pressure in the chamber before (—o—) and after (—x—) the heating up to 600 K at the load increase.

The calculated values $p_2 \approx 10$ GPa, $p_2/\bar{p} \approx 1.9$ in a case of heating are certainly higher than the experimental ones. The cause apparently lies in incomplete phase I to phase 2 transition.

It must be noted, that pressure self-multiplication essentially influences the kinetics of the interphase boundaries motion.

The redistribution of pressure takes place with a speed of sound. The speed of the interphase boundary shift is much slower. So, the radical shift of phase boundary takes place at conditions of sharper pressure distribution and the motion quickly slows down. That is why the observed experimentally shift of interphase boundary after shear deformation is much less, than one could expect knowing the place of the points $p_0 \approx 1.9$ GPa at the initial distribution of the pressure.

References

- Blank V.D., Boguslavsky Yu.Ya., Eremets M.I., Itskevich E.S., Konyaev Yu.S., Shirokov A.M., Estrin E.T. Pressure self-multiplication effect on phase transition under quasi-hydrostatic conditions. Sov. Journ. of IETP, 1982, v.87, N 3/9, p. 922-926.
- Eremets M.I., Itskevich E.S., Shirokov A.M., Yakovlev E.N. Optical investigations in the "rounded cone-flat" anvils chamber in megabar range. Letters to the IETP, 1982, v.36, N 1, p. 58-60.

INDUSTRIAL SYNTHESIS AUTOMATIC CONTROL OF SUPERHARD MATERIALS WITH THE USE OF MATHEMATICAL SYNTHESIS MODELS

B.A.Glagovsky, V.S.Lysanov, V.A.Jashin

All-Union Research and Scientific Institute of Abrasives and Grinding - VNIIASH, Leningrad, USSR

The solution of tasks of all-round automation of technological synthesis process of superhard materials (SHM), going over to development of flexible SHM industrial synthesis systems and fully automated (without human beings) manufacturing process are closely connected with working out of means and methods for SHM industrial synthesis automatic control.

As a result of research and engineering developments carried out in VNIIASH in 1967-1987 there appeared some favourable prerequisites for solution of the above-mentioned problems.

Thus there were developed and built:

- information-measuring system for carrying out SHM technological processes investigation both in laboratories and in large-scale industrial production;
- a series of basic electronic automatic regulators for regulation and control SHM synthesis conditions when carrying out the above-mentioned investigations;
- methods of carrying out, processing and analysis of large-scale statistical investigations results of SHM synthesis technological processes under current industrial production conditions.

The results of investigations carried out in 1967-1980 were published in /1,2/ and reported at the International Seminar "Superhard Materials", Kiev, June 1981.

During the same period there was settled the problem of SHM industrial synthesis automatic control being itself a multidimensional random process progressing in extreme (as to control and inspection) conditions on a mass scale.

It should be noted that intermediate results of above-mentioned investigations made it possible to develop the local devices for automatic control of SHM synthesis industrial equipment for concrete technological conditions providing SHM manufacturing of different types and grades (diamond: AC2, AC4, AC6, etc.; Elbor: III and MKB; materials of Elbor-R-, Komposit-05-, Gexanit-R-, Glas-, Karbonado-types, etc. /3/.

The algorithms of SHM synthesis conditions control developed at VNIIASH and taking account of the process dynamics and wear of

in forming output characteristics of the synthesized product, establish principal communications between all the factors of synthesis process and its output indexes. Accurate engineering calculations accepted by developing similar models provide their engineering realization in automatic systems from local devices ACVTH.

The authors investigated two methods of approach to the problem of simulation for SHM synthesis conditions: analytical (determinate) and statistical. It is shown that the most advisable way to develop mathematical models for SHM synthesis is construction of statistical models.

As a result of investigations accomplished in the laboratories of the Institute as well as at some large industrial works manufacturing superhard materials there were developed methods of carrying out statistical investigations and construction of control algorithms for concrete synthesis technological conditions.

It should be observed that similar large-scale investigations were a success only owing to the before-mentioned information-measuring unit and automatic control devices developed at the Institute.

The experiments being carried out answer the principal state-
of regression analysis and are realized with the use of me-
of multifactor mathematical design of experiments.

On the basis of such experiments there was developed a series of mathematical models for concrete synthesis conditions /1/; control algorithms realizing these models are used in automatic control devices developed at VNIISH.

Mathematical models obtained as a result of large-scale statistical investigations of SHM industrial synthesis as a rule look like polynomials of the second power taking into account the effect of the technological process parameters as well as control parameters on the output of the product being synthesized.

The mentioned polynomials are obtained for different combinations of synthesis parameters (voltage, synthesis time, number of reaction periods for technological equipment, power, pressure and of electrical parameters change).

To increase accuracy of developed models formalizing SHM synthesis process there were imposed some engineering limitations on quality of the equipped containers. Thus, to obtain a product with its output variations $\pm 8\%$ it was necessary to select control

ners and their equipment with representability no less than 70% the expectation.

The obtained regression polynomials describing SHM synthesis models are being written in a common form by the following equation:

$$y = b_0 \sum_{i=1}^n (b_{i1}x_1 + b_{i2}x_2^2) + \sum_{i,k=1}^n b_{ik}x_ix_k,$$

where $n = 1, 3, 5$ and 7 - number of the factors of the experiment; x - coding of the factors value, b - coefficient of the regression equation.

The data given in the Table show that when carrying out concrete engineering limitations the models are being concretized considerably simplified.

Variable parameters, %							Variations of the product output, %		
Elastic constants of the container	Characteristics of the container	Rate of voltage change	Power	Material durability	Synthesis time	Voltage	Factor 1 experiment	Factor 5 experiment	Factor experiment
22	80	75	20	100	25	10	0-	0-	
22	80	75	20	-	-	22		0-	
-	-	-	-	100	25	25			+46
-	-	-	24	-	66	5			
-	-	-	-	10	25	25			

The results of the investigations being considered in the present report, and the experience of commercial operation of a series of automatic presses for SHM synthesis with the use of a computer realizing on the base of a mathematical model the information accessing from every synthesis process showed the possibility of principle developing flexible manufacturing systems (FMS) for SHM production.

References

1. VNIISH Transactions. Problems of Abrasive Tools Automatic Control and Testing. L., 1978.
2. VNIISH Transactions. Quality Control and Inspection in Abrasive Materials and Tools Manufacturing. L., 1980.
3. B.A. Glagovsky et al. Automatic Control and Mechanization of Technological Processes for Synthetic Superhard Materials Manufacturing. "Mechanization and Automatic Control", N3, 1980.

MEGABAR PRESSURES WITH SYNTHETIC DIAMONDS

A.L. Ruoff, K.E. Brister, S.T. Weir, Y.K. Vohra

Department of Materials Science, Cornell University, Ithaca, NY 14853 USA

Abstract

One third carat synthetic gray-blue diamonds grown by the General Electric Company were used as anvils in a diamond anvil cell to produce a pressure of 125 GPa in a gasketed sample. Pressure was measured by x-ray diffraction methods by using gold and iron as calibrant and also by optical methods based on the shift of fluorescence peaks of ruby with pressure. The pressure at which the synthetic diamonds failed is nearly as high as the maximum pressure of 170 GPa at which x-ray or optical absorption, reflection or Raman scattering experiments on a gasketed sample which is less stiff and has a lower flow stress than the gasket in a diamond hole have been made with natural diamonds. The future potential of synthetic diamonds for ultra-high pressure research is assessed. The present research shows that very high quality synthetic gemstones can be produced.

Diamonds, either natural or manmade, are ideal for making ultra-high pressure devices; they are the hardest material known and are transparent to photons over a wide energy range [1]. The use of natural diamonds for generating very high pressures and for studying different materials at these pressures is described in detail by Jayaraman [2,3]. Thus far all scientific studies of samples supported by a gasket have used natural diamonds. Onodera et al. [4] recently have used a pair of deep yellow synthetic diamonds (12) with a flat tip to reach a pressure of 68 GPa in a gas-gasketed sample chamber [4].

The diamonds used in this experiment were one third carat type IIa grown by the General Electric Company from an iron solvent. Figure 1 shows a photograph of one of the diamonds. The diamonds are of excellent quality with no flaws visible using an optical microscope with magnification up to 100x. The birefringence of each diamond was found to be below 10^{-4} which indicates that the strains were very low and are comparable to the best natural diamonds. The impurities were mainly boron (4-6 ppm) and iron. Iron impurities were probably in the form of small inclusions.

The Figure is given at the end of the book

sions captured during diamond growth and cause a slight permanent magnetic moment /5.6/.

The diamonds were shaped to have a center flat of 70 μm and a taper of 5 degrees to a total tip diameter of 200 μm . A pre-indent spring steel gasket was used to contain the sample. Initially the sample was 25 μm in diameter and 30 μm thick.

The diamond anvil cell used was similar to the one described by Baublitz et al. /7/. The x-ray set-up is described by Bristow et al. /8/.

We used three methods to determine the pressure of the sample.

1. The pressure induced shift of the ruby R_1 line was measured using a 512 element photo diode array, an optical multichannel analyzer, and an argon ion laser. (Note that the ruby scale is based on the shock equation of state of Cu, Mo, Pd, and Ag /9/).

2. The reduced volume V/V_0 for gold was found from our x-ray data and compared to the equation of state as determined from shock experiments /10/. The shock data was fit to a Birch first order equation of state /11/. The values of the fitting parameters used were $B_0 = 177.3$ GPa and $B'_0 = 4.767$ where B_0 is the zero pressure bulk modulus and B'_0 is its first pressure derivative.

3. We were also able to use the reduced volume for iron in a completely analogous fashion to gold. Here we used the shock data of Brown and McQueen /12/ and found values for fitting parameters of $B_0 = 163$ GPa and $B'_0 = 5.34$. We were able to determine the gold and iron pressures simultaneously by allowing the x-rays to pass through the gasket-sample interface.

The sample was initially loaded to a pressure of 109 GPa using the ruby scale. After this the cell was taken to the Cornell High Energy Synchrotron Source (CHESS) for the x-ray measurements. In Figure 2 we show a diffraction pattern obtained in five minutes at the CHESS wiggler white beam station. Note that there are no diffraction peaks out to at least 62 KeV before the Au and Pb fluorescence lines obscure the data. The experimental Bragg plane spacings are compared to the fitted spacings in Table. The lattice parameter and pressure are $a = 3.687\text{\AA}$ and 112.9 GPa respectively.

Figure 3 shows a diffraction pattern taken when the x-ray beam was directed at the gasket-sample interface. The pressure in this case is 125 GPa based on the gold diffraction peaks and 115 GPa based on the iron peaks. These pressures are the same, within the experimental errors of about 9 GPa.

Comparison of observed and fitted Bragg plane spacings for the five diffraction peaks of gold at 112 GPa. The lattice constant a is the fitting parameter with the least squares value of 3.687 \AA .

(hkl)	observed (\AA)	fitted (\AA)
(111)	2.122	2.129
(200)	1.846	1.843
(220)	1.302	1.303
(311)	1.115	1.112
(222)	1.067	1.064
(331)	0.846	0.846
(420)	0.825	0.824
(422)	0.756	0.753
(511), (333)	0.713	0.710
(440)	0.654	0.652
(531)	0.626	0.623
(600), (422)	0.614	0.614

The ultimate pressures obtainable in both natural and synthetic diamonds may be due to the absence or near absence of dislocations in the highly stressed region about the tip of the diamond /13/. This region extends into the diamond a distance equal to about half the radius of the tip /14/ and has a surface area of πa^2 , where a is the tip radius. If ρ is the density of dislocations (the number of dislocation lines crossing a unit area) then the number of dislocations in this highly stressed region is $\pi a^2 \rho$. For $a = 35 \mu\text{m}$ and $\rho = 10^4 \text{ cm}^{-2}$, typical numbers for high quality gem stones cut for high pressure work, then the probability of finding a dislocation in this region is about 2 out of 5. This means that 3 out of 5 diamonds of this type should act as perfect crystals, assuming no other defects are present. The diamonds used in experiments with gasketed samples have all had extremely low birefringence (4×10^{-5} to 10^{-4}) and hence probably have dislocation densities below 10^{-4} cm^{-2} .

In comparing the maximum pressure attained with these synthetic diamonds to the maximum pressures reported for natural diamonds it is important to note that in this experiment we used a soft sample with a pressure supporting gasket. In the experiments with natural diamonds in the 400-500 GPa pressure range the sample was a material which was very much stiffer and very much harder than the gasket /15/. With a soft sample the maximum pressure reached to date with natural diamonds is 170 GPa /16/.

This experiment has shown it is possible to synthesize diamonds of extremely high quality which are capable of reaching pressures rivaling those which have been reached with natural dia-

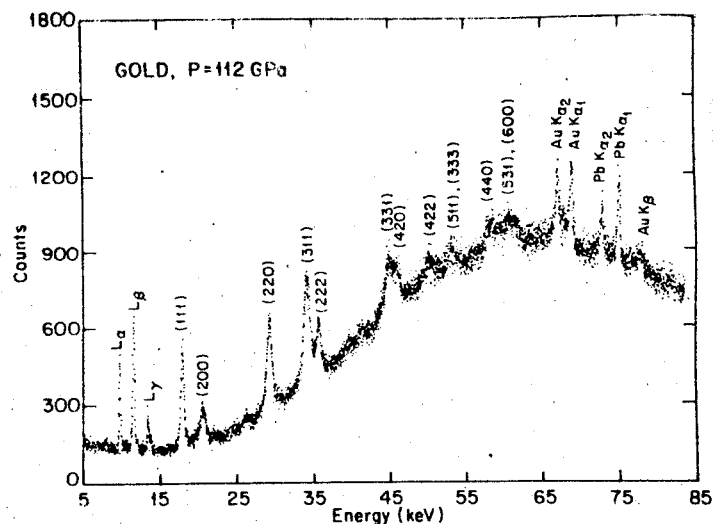


Fig.2. Energy dispersive x-ray diffraction pattern of gold at 112 GPa recorded in 5 minutes with the wiggler white beam line at the Cornell High Energy Synchrotron Source. The angle of diffraction is 9.406 degrees.

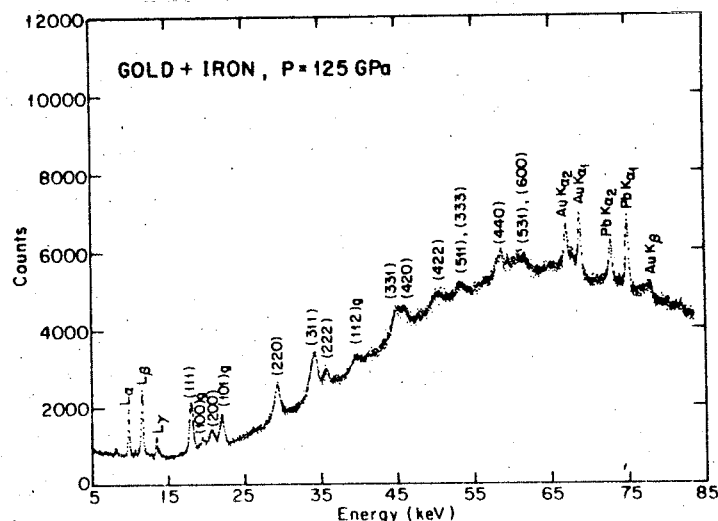


Fig.3. Energy dispersive x-ray diffraction pattern of the highest pressure spot in the cell found by scanning across the sample. The spectrum shown is at 125 GPa and contains gold peaks and iron peaks from the gasket material. The three gasket peaks are marked "g". The diffraction angle is 9.406 degrees.

monds. It should be possible to grow diamonds that exceed natural diamonds in their ability to generate ultra-high pressures. This should make it possible to attain the maximum pressures possible with perfect diamond crystals, estimated to be 780 GPa [17].

This work was supported by National Science Foundation (NSF) grant DMR 8612289. One of us (K.E.B.) thanks the NSF for support through the Cornell Materials Science Center. S.T.W. thanks the Eastman Kodak Company for a fellowship. We are indebted to the General Electric Company for supplying the synthetic Type IIB diamond crystals used in this work and Robert C. deVries of the General Electric Research Laboratory for making the arrangements. We greatly appreciate the helpful discussions with Robert C. deVries, Herbert M. Strong, Steven J. Duclos, and Serge Desgreniers. We also thank the entire CHESS staff for their help.

References

1. Field JE, ed. The Properties of Diamond, Academic Press, New York (1979), 674 pages.
2. Jayaraman A, "Diamond Anvil Cell and High-Pressure Physical Investigations", Rev. Mod. Phys. **55**, 65-108 (1983).
3. Jayaraman A, "Ultrahigh Pressure", Rev. Sci. Instrum. **57**, 1013-31 (1986).
4. Onodera A, Furuno K, Yazu S, "Synthetic Diamond as a Pressure Generator", Science **232**, 1419-20 (1986).
5. Koivula JI and Fryar CW, Gems and Gemology, **20**, 146 (1984).
6. Rossman GR and Kirschvink JL, Gems and Gemology, **20**, 163 (1984).
7. Baublitz MA, Arnold V, and Ruoff AL, "Energy Dispersive X-Ray Diffraction From High Pressure Polycrystalline Specimens Using Synchrotron Radiation", Rev. Sci. Instrum. **52**, 1616-24 (1981).
8. Brister KE, Vohra YK, and Ruoff AL, "Microcollimated Energy-Dispersive X-Ray Diffraction Apparatus for Studies at Megabar Pressures with a Synchrotron Source", Rev. Sci. Instrum. **57**, 2560-3 (1986).
9. Mao HK, Bell PM, Shaner JW, and Steinberg DJ, "Specific Volume Measurements of Cu, Mo, Pb, Ag and Calibration of the Ruby R. Fluorescence Gauge from 0.06 to 1 Mbar", J. Appl. Phys. **49**, 3276-83 (1978).
10. Jamieson JC, Fritz J, and Manghani MH, "Pressure Measurement at High Temperature in X-Ray Diffraction Studies: Gold as a Primary Standard", Adv. Earth Planet. Sci. **12**, 27-48 (1980).
11. Birch F, "Finite Strain Isotherm and Velocities for Single-Crystal and Polycrystalline NaCl at High Pressures and 300 K", J. Geophysical Research, **82**, 1257-68 (1978).

12. Brown JM and McQueen RG, High Pressure Research in Geophysics, S. Akimoto and M.H. Manghnani (Reidel, Dordrecht, Holland 1982), p. 611-25.
13. Ruoff AL, High Pressure in Research and Industry, C.-M. Backman, T. Johansson and L. Tegner, Arkitektkopia, Uppsala, Sweden (1982) Vol. I, p. 108-21, 854 pages.
14. Chan KS, An Analysis of the Maximum Pressure Attainable with Indentors which are Bodies of Revolution, Master's Thesis, Cornell University, Ithaca NY (1977).
15. Xu JA, Mao HK, Bell PM, "High-Pressure Ruby Fluorescence: Observations at 0.21 to 0.55 Terapascal", Science, 232, 1404-6 (1986).
16. Reichlin R, Ross M, Martin S, and Goettel KA, "Metallization of CsI", Phys. Rev. Lett., 56, 2858-60 (1986).
17. Whitlock J and Ruoff AL, "The Failure Strengths of Perfect Diamond Crystals", Scripta Metallurgica, 15, 526-9 (1981).

THEORETICAL MODEL FOR HIGH PRESSURE RAPID SOLIDIFICATION

G. Grosse, R. Sellger, G. Risse

Central Institute for Solid State Physics and Material Research, Academy of Sciences of the GDR, Dresden, GDR

1. Introduction

It is well accepted that glass formation requires cooling of a melt with a rate higher than a critical one to avoid detectable nucleation and crystallization [1]. Nucleation frequency and crystallization rate and thus glass forming ability can be influenced by changing the melt composition c_s . E.g. the critical cooling rate R_c necessary for glass formation is enhanced with increasing deviation of c_s from the eutectic composition. Pressure application affects nucleation frequency and crystallization rate, too. The aim of this paper is to investigate the dependence of R_c on pressure p and to compare theoretical calculations with experimental results.

2. Model

2.1. Basis equations

The crystalline part X forming on undercooling a melt for an instant t depends on the nucleation frequency I and the crystallization rate v . For non-impeding spherical crystallites X is given by [2]:

$$X = \frac{4\pi}{3} \int_0^t I(t') dt' \left[\int_{t'}^t v(t'') dt'' \right]^3 \quad (1)$$

And v are functions of time via their temperature dependence $v(t)$. The time constant for establishing a steady state nucleation frequency for metals is of order of 10^{-6} s. During this time in high pressure rapid solidification devices the temperature decrease is smaller than 1K. Therefore we may use in (1) the steady state nucleation frequency. Neglecting heterogeneous nucleation I is given by [2]:

$$I = \frac{I_0}{\eta} \exp\left(-\frac{\Delta G^*}{kT}\right) \quad (2)$$

with η being the viscosity. ΔG_c is given by

$$\Delta G_c = \frac{80\pi}{3} \frac{r^3}{v_s \Delta g^2} \quad (3)$$

$$\Delta g = (\Delta h + p \Delta v) \left(1 - \frac{T}{T_s}\right) \quad (4)$$

with the molar volume of the nucleus (solid phase) v_s , the specific surface energy between nucleus and melt γ , the solidus temperature T_s , the differences of enthalpy Δh and molar volume Δv between nucleus and melt, respectively. At atmospheric pressure $\Delta G_c = 60 \text{ kT}_s$ at an undercooling of $T_s - T = 0.2 T_s$ is a common approach for metallic systems. The crystallization rate is given

$$v = \frac{v_0}{\eta} \left[1 - \exp\left(-\frac{\Delta h(T_1 - T)}{kT T_1}\right) \right] \quad (5)$$

I_0 and v_0 are constants with typical values of $10^{35} \text{ Pa m}^{-3}$ and 0.1 Pa m for metallic melts. For the viscosity an Arrhenian-like behavior has been assumed

$$\eta = K \exp(E/kT) \quad (6)$$

Equation (1) determines the critical cooling rate R_c which corresponds to a given crystalline part X_c . For constant cooling rates the equation (1) can be transformed to

$$X = \frac{C}{R_c^4} F(E_1, E_2, E_3) \quad (7)$$

$$\text{with } C = \frac{4\pi}{3} \frac{v_0^3 I_0}{K^4} \quad (8)$$

and

$$F = \int_0^1 \exp\left(-\frac{E_1}{T_r'} - \frac{E_3}{T_r'(1-T_r')^2}\right) \left\{ T_r' \exp\left(-\frac{E_1}{T_r'}\right) + E_1 \text{Ei}\left(-\frac{E_1}{T_r'}\right) - \exp(E_2) \left[T_r' \exp\left(-\frac{E_1 + E_2}{T_r'}\right) + (E_1 + E_2) \text{Ei}\left(-\frac{E_1 + E_2}{T_r'}\right) \right] \right\} dT_r'$$

with the exponential integral $\text{Ei}(x)$. The index r denotes dimensionless (reduced) temperature $T_r = T/T_s$. The crystalline part transformed is governed by three different activation parameters E_1

$$E_1 = E/kT_s$$

$$E_2 = \Delta h/kT_s$$

$$E_3 = \frac{80\pi\gamma^3}{3 v_s (\Delta h + p \Delta v)^2 kT_s}$$

For a convenient discussion (7) is re-formulated

$$\theta_c = \frac{R_c(p)}{R_c(p_0)} = \left[\frac{F(p)}{F(p_0)} \right]^{1/4} \quad (11)$$

describing the change of the normalized critical cooling rate with pressure.

2 Pressure dependence of the E_1

The pressure dependence of the activation parameters E_1 is determined by the activation volume v_a

$$E = E_0 + p v_a \quad (12)$$

According to [3] v_a is connected with the molar volume of the melt v_l

$$v_a = \xi v_l \quad (13)$$

with ξ typical 0.1 for metals. Neglecting the much smaller pressure dependence of γ , Δh , Δv , v_s compared with that of ΔG obtain

$$\frac{\partial \Delta G_c}{\partial p} = - \frac{2 \Delta G_c \Delta v}{\Delta h + p \Delta v} \quad (14)$$

From (12) and (13) we obtain

$$E_1(p) = \frac{E_0 + \xi v_l p}{kT_s(p)}$$

$$E_2(p) = \Delta h/kT_s(p) \quad (15)$$

$$E_3(p) = \frac{80\pi\gamma^3}{3 v_s (\Delta h + p \Delta v)^2 kT_s(p)}$$

increases with pressure the activation parameters E_2 and E_3 are decreasing functions of pressure. Depending on the established functional relation of $E(p)$ and $T_s(p)$ E_1 may be an increasing or a decreasing function of pressure. Assuming the Simon-equation [4] for the pressure dependence of T_s

$$\frac{\Delta p + a}{a} = \left[\frac{T_s(p)}{T_s(p_0)} \right]^c \quad (16)$$

critical pressure p_c may be calculated

$$p^c = \frac{E_0 / \varepsilon v_1 - a c}{c - 1} \quad (17)$$

If $p > p_c$ than E_1 is a monotonously increasing function of pressure.

3. Results

The function F has been calculated numerically for different values of E_1 (Fig.1). In the considered parameter range $1 \leq E_1 \leq 15$, $1 \leq E_2 \leq 5$ and $0.5 \leq E_3 \leq 1.2$ the function F only slightly depends on E_2 and may be approximated by the relation

$$F = F_0 \exp(-az) \quad (18)$$

with $z = E_1 + b E_3$, $a=6.56$, $b=4.47$ and $F_0=2.65 \cdot 10^{-5}$. With this expression we obtain for the normalized critical cooling rate θ_c

$$\theta_c = \exp(-a [z(p) - z(p_0)]) \quad (19)$$

The pressure dependence of z affects the behaviour of the critical cooling rate R_c . For two real systems the pressure dependence of θ_c is calculated (Fig.2) using material parameters listed in Table. It can be seen that in the Fe-B system the critical cooling rate for glass formation is shifted to higher values under pressure. This result is corresponding with the experimental fact that at high pressure rapid solidification a metastable Fe_3B phase has been detected instead of the expected amorphous Fe-B phase [5]. In the copper-tin system the critical cooling rate decreases with increasing pressure making glass formation easier under high pressure conditions.

	Unit	Fe-B	Cu-Sn
a	Pa	$3.5 \cdot 10^8$	$4.46 \cdot 10^5$ *
c		1.75	1 *
E	kJ mol^{-1}	210	30
h	kJ mol^{-1}	13.76	12.5
T_B	K	1448	1013
v_1	$\text{m}^3 \text{mol}^{-1}$	$7 \cdot 10^{-6}$	$8 \cdot 10^{-6}$
v	$\text{m}^3 \text{mol}^{-1}$	$3.5 \cdot 10^{-7}$	$2.8 \cdot 10^{-7}$

* Parameter was determined from the Clausius-Clapeyron equation

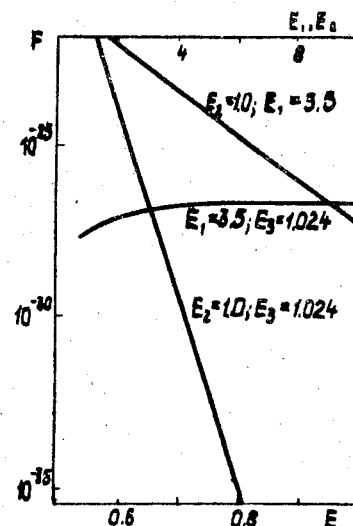


Fig. 1. F as a function of one activation parameter E_1 . The other parameters were kept constant.

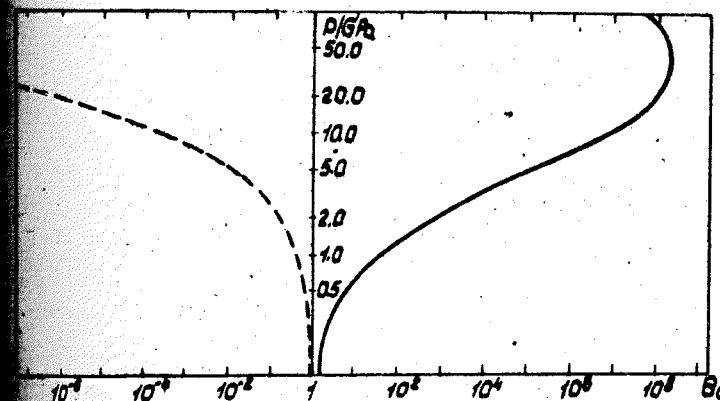


Fig. 2. Normalized critical cooling rate as a function of pressure for Fe-B (bold line) and Cu-Sn (dashed line).

The amorphous state of Cu-Sn could be obtained by melting and rapidly solidifying samples of powder under a pressure between 2.5 - 5 GPa and applying a cooling rate of $10^3 - 10^4$ K/s /6/. Under atmospheric pressure a cooling rate of approximately 10^8 K/s is necessary to obtain an amorphous phase giving a normalized cooling rate at that pressure in the order of 10^{-4} .

4. Conclusions

The change of the critical cooling rate for glass formation under pressure has been calculated using the theoretical concepts of nucleation and crystal growth. Depending on the variation of the material parameters with pressure the critical cooling rate R_c is increased (e.g. in Fe-B) or decreased (e.g. in Cu-Sn). In the latter case a higher glass forming ability under high pressure conditions is obtained. Despite of the uncertainties in the experimental parameters especially the pressure dependence of the expansion volume v_a and the solidus temperature T_s the correspondence of theoretical and experimental results is quite well.

References

1. D.R.Uhlmann, J.Non-crystalline Solids, 1972, 7, 337.
2. J.W.Christian. The Theory of Transformation in Metals, Pergamon Press, Oxford, 1975
3. C.A. Swenson, Solid state physics, 1960, 11, 41.
4. R.S.Bradley, High Pressure Physics and Chemistry, pt.I, Academic Press, 1963.
5. J.A.Sekhar, G.S.Reddy and P.Venkateswararao, in Rapidly Solidified Materials, ed P.S. Lee and R.S.Carbonara, American Society of Metals, 1985, pp.83-90.
6. V.V.Brazhkin, S.V.Popova, Metallofizika, 1985, 7. 103.

ANALYSIS OF EFFECTIVENESS AND CHOICE OF OPTIMAL CONSTRUCTION OF TWO-STAGE MULTIANVIL UNIT OF SPLIT SPHERE APPARATUS

I.Yu.Malinovsky¹, Ya.I.Shurin², E.N.Rshn²

¹Institute of Geology and Geophysics, Novosibirsk, USSR

²Special Design Technological Bureau of Single Crystals, Novosibirsk, USSR

Construction of two-stage multianvil unit is the main type practically used in "split sphere" apparatus /1,2/, due to their capacity to centre anvils of the whole unit automatically. The optimal construction is that of maximum useful volume under other equal conditions and of minimum liquid pressure under equal useful volume. The minimum volume (mass) of the inner stage anvils usually made of tungsten carbide can serve as an additional criterion. We analysed the construction in which the working chamber is of regular polyhedron form, a number of the inner stage anvils (n) is equal to a number of polyhedron faces, and a number of the outer stage anvils (i) is equal to a number of the regular polyhedron faces formed by the inner stage anvils.

The force produced by every outer anvil is determined by the area of its basis (S_1) projected on to the plate normal to the anvil axis /3/:

$$S_1 = \frac{jx}{2\pi} \operatorname{tg} \frac{x}{2} \operatorname{ctg} \frac{2}{j} \cdot \pi R^2 = q\pi R^2,$$

$$\gamma = \arccos \frac{2 \cos \frac{2\pi}{j} + 1 + \cos(1 - \frac{2}{j} + \frac{4}{ij})\pi}{1 - \cos(1 - \frac{2}{j} + \frac{4}{ij})\pi},$$

number of anvil lateral faces, γ - the central angle of anvil face sector.

The full effective area (S_1) and force (F_1) of the outer

are: $S_1 = iq\pi R^2 = K_1 S$, $F_1 = K_1 PS$,

where P is the full sphere surface, $K_1 = iq/4$ is the coefficient of the outer stage effectiveness.

As the basis faces of the inner stage anvil are tilted at an angle β towards the anvil axis, a partial loss of force being exerted from the outer anvils face occurs on the stage boundary

$$F_n = F_1 \sin \beta = K_n F_1 = K_n K_1 PS = K_{ni} PS,$$

where K_{ni} is the coefficient of the inner stage effectiveness,

K_{ni} is the coefficient of two-stage construction effectiveness on force.

The useful volume (v) includes the volume of the reaction chamber, heater and heat-isolated enclosure.

The useful volume is considered to be restricted by the cylinder, inscribed into the working chamber polyhedron as the cylindrical heater is the most technological one. The extent of use of working chamber V_0 is characterized by the coefficient $t_v = v/V_0$ at optimal orientation of the inscribed cylinder on the axis L_2 in tetrahedron, on L_4 in cube, on L_3 in octahedron and dodecahedron, on L_5 in icosahedron.

The force F_n is applied to the surface of the working body (S_0) and lateral faces of the inner anvils. The force of anvil lateral support is in complex dependence on contact pressure distribution over the area of the lateral faces, on the property of compressible gasket material and so on. However, for comparative analysis it is sufficient to admit the same force produced by the inner anvils to be used for the lateral support. Thus, the equilibrium condition of the multianvil unit under load may be expressed as follows:

$$F_n = K_{ni} P S = \lambda P_0 S_0 = \lambda P_0 \tau_n \left(\frac{v}{t_v t_n} \right)^{2/3},$$

where $\lambda = 2+3$ is in the pressure range $P_0 = 50-80$ kbar, τ_n and t_n are proportionality coefficients surface-to-edge squared and volume-to-edge cubed, respectively, of a regular polyhedron. Therefore

$$v = t_v t_n \left(\frac{4\pi K_{ni}}{\tau_n} \right)^{3/2} R^3 \left(\frac{P}{\lambda P_0} \right)^{3/2} = K_v R^3 \left(\frac{P}{\lambda P_0} \right)^{3/2},$$

where K_v is the useful volume efficiency at the constant value of liquid pressure P , working volume pressure P_0 , contact pressure on the step boundary P_1 and sphere radius R .

At the constant useful volume and with other conditions being equal, the liquid pressure efficiency coefficients K_P are defined:

$$P = \frac{\tau_n}{4\pi K_{ni} (t_v t_n)^{2/3}} \lambda P_0 \frac{v^{2/3}}{R^2} = K_P \lambda P_0 \frac{v^{2/3}}{R^2}$$

Under the same conditions, the inner stage anvil volume efficiency K_v is:

$$v = \frac{t_n}{t_v t_0} \left(\frac{\tau_0}{\tau_n K_n} \right)^{3/2} v \left(\frac{\lambda P_0}{P_1} \right)^{3/2} = K_v v \left(\frac{\lambda P_0}{P_1} \right)^{3/2}$$

When comparing the efficiency of two-stage constructions (see Table), the construction 20/12 with icosahedral working volume is to be preferred.

Efficiency coefficients of two-stage constructions of multi-anvil unit

Anvil unit type	Working volume		Inner stage			
	shape	t_v	shape	n	K_n	K_v
4/4	tetrahedron	0.34	tetrahedron	4	0.33	15.11
6/8	cube	0.79	octahedron	6	0.58	3.10
8/6	octahedron	0.46	cube	8	0.58	4.62
12/20	dodecahedron	0.48	icosahedron	12	0.79	3.08
20/12	icosahedron	0.57	dodecahedron	20	0.79	2.36

Anvil unit type	Outer stage		Unit efficiency		
	1	K_1	K_{ni}	K_v	K_P
4/4	4	0.75	0.25	0.10	4.68
6/8	8	0.87	0.50	0.85	1.12
8/6	6	0.83	0.48	0.50	1.60
12/20	20	0.94	0.74	1.13	0.92
20/12	12	0.92	0.73	1.35	0.82

However, the conclusive choice of the optimal design is specified, with a relatively small difference in the efficiency of the systems 20/12 and 6/8 taken into account, by the labour expenditure on the apparatus fabrication and exploitation, which increases sharply with the anvil number. Thus, the construction 6/8 with cubic working volume, which at the same useful volume requires liquid pressure and anvil mass 1.4 and 1.5 times, respectively, less than the common design 8/6 with octahedral working chamber, is to be considered as the optimal alternative.

References

- Patent No. 1200934, Japan, B 01j3/00. High pressure generating method and apparatus. N.Kawai, 5.08.1970.
- Kawai N., Endo S. The generation of ultrahigh hydrostatic pressures by a split sphere apparatus. Rev.Sci.Instr., 1970, 41, N8, 1178-1181.
- Malinovsky I.Yu., Rahn E.N. Dependence of "split sphere" outer stage effort on anvil number. In: Experimental investigations on mineralogy, Novosibirsk, 1975, 139-143 (in Russian).

OBTAINING HIGH PRESSURE GAS WITH THE HELP OF A FREE SELF-WEDGING PISTON

A.A. Meshcheryakov, V.I. Pinakov, V.N. Rychkov, M.E. Topchian
Lavrentyev Institute of Hydrodynamics
Siberian Division of the USSR Academy of Sciences,
Novosibirsk, USSR

Devices of adiabatic compression with a free piston are widely used when obtaining high gas pressures. In this case the problem of gas pressure retention at the end of a compression cycle is difficult to be solved [1]. An insertion of the system of wedges furnished with an antifriction cover in the piston construction allows us to obtain and to retain the pressure more than 200 MPa [2,4]. Schematic drawing of the piston is presented in Fig.1. It consists of a plunger 1, rings 2 and wedges with elastic elements 4. The piston in tube 5 is accelerated by gas from a receiver (balloon) 6 after cutting a washer 7. The middle part of the piston consists of truncated cones 9 having an apical half-angle α . The wedges 3 are bushes sectioned to four parts, the inner surface of which is furnished with antifriction cover 8. In the acceleration stage the inertion forces shift the wedges back, and the elastic elements press them to the plunger providing thereby the clearance between wedges and the tube walls.

In the deceleration stage the wedges shift forward and lose the contact with the tube. The friction force acting on the wedges on the part of the tube prevents the forming of high contact pressures which could result in damage of the wedge and the surface at their mutual motion.

After the piston has stopped, this force changes the direction, and due to a considerable difference in friction coefficients it appears to be more than the friction force between the plunger and the wedges. Therefore at the backward movement of the piston the wedges remain immovable. The piston becomes wedged.

After the pressure has decreased, the plunger is pressed forward. The piston becomes free, and it is possible to return it back in the start position.

The main advantage of such a construction is a possibility of excluding the reverse valves which work under extremely high conditions and require the change in each 2-3 cycles of operation.

For the piston operating really at a gas compression up to 200 MPa the contact pressure does not exceed 3.2 MPa in the

of deceleration. For wedging it is necessary to fulfill inequality

$$\tan \alpha \leq \frac{\eta_1 - \eta_2}{1 + \eta_1 \eta_2}$$

under which the friction force of the wedges against the tube wall exceeds the sum of axial components of forces produced by the piston. If we designate $\eta_1 = \tan \alpha_1$, $\eta_2 = \tan \alpha_2$ (where α_1 and α_2 are the friction angles), the wedging piston will operate under the following condition:

$$\alpha_2 < \alpha < \alpha_1 - \alpha_2$$

The average radial stresses in the contact zone of the wedges with the tube have the form

$$\bar{\sigma}_z \approx \frac{R}{2h \tan \alpha} P$$

It is seen that with an increase in the wedging zone length it is possible to reduce the value of $\bar{\sigma}_z$ down to the values less than those of gas pressure.

The dependences obtained in [2] were used at creation of the experimental equipment. The first unit was tested under the spike pressures up to 800 MPa. In the experiments air was compressed at initial pressure of 0.4 MPa. The temperature of gas reached 2.100 K. A back shift of the piston relatively wedges the pressure decreased down to 400 MPa. The stationary average pressure of the piston on the tube was also equal approximately to 400 MPa.

In one of the experiments the spike pressure was more than 800 MPa, and on the inner tube surface the wedges left their marks, the identity of which was indicative of the uniform stress distribution. This unit was used to test the material erosion endurance which is due to heated gas outflowing through the profiled jets. Air and nitrogen compressed by the initial pressure ranged from 0.8 to 1.2 MPa were used in the second unit having the piston diameter of 10 mm and the initial tube volume of 3.390 cm³. In the head part the tube had a chamber from which compressed gas flowed out through a nozzle. The pressures up to 210 MPa were measured. In Fig.2 presented are the oscillograms of pressures P_1 and P_2 as temperature T in this chamber. The maximum value of $P = 210$ MPa and $T = 1.070$ K. The sweeping time is 1 ms per division. This unit was also used to investigate the properties of gas flowing out under the initial pressure up to 200 MPa. The measure-

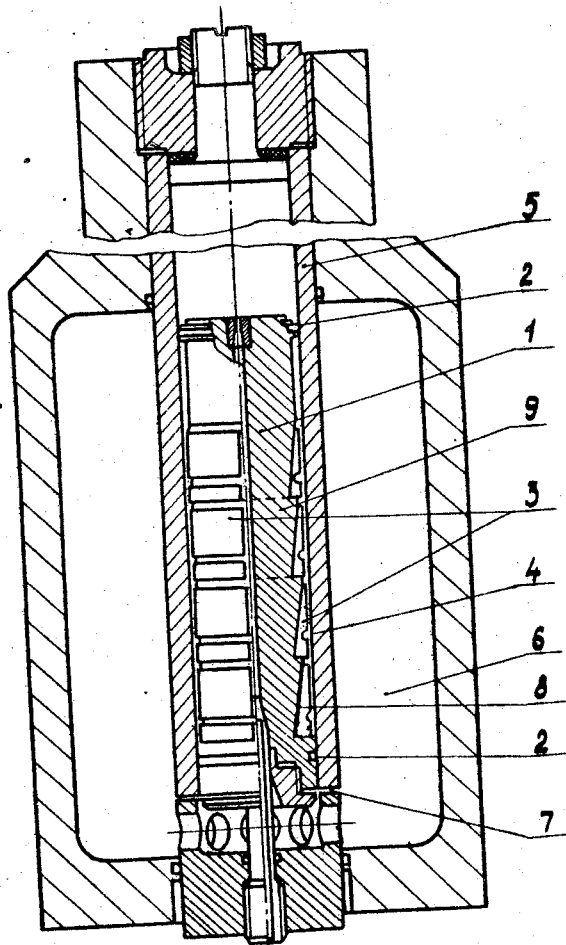


Fig. 1. Schematic drawing of the piston.

ments of total enthalpy and heat losses were fulfilled for gas outflow through a conical nozzle. With this aim a direct measurement of the flow velocity was realized. The method of the velocity measurement and the calculation of heat losses are presented in /3/. The data on heat losses are shown in Fig. 3. The character of disposition of curves showing the heat losses is determined by duration of gas outflow from the chamber to the moment of the velocity measurements. This duration was 4.6 μ s for curve 1, 16 ms and 108 ms for curves 2 and 3, respectively. A long-term (more than 10 years) performance of the units with a self-wedging piston had demonstrated its good reliability and high exploitation qualities.

References

- Von Karman Institute for Fluid Dynamics. Education and Research 1956-1976. 1976.
- A.A. Meshcheryakov, V.I. Pinakov, M.E. Topchian. PMTF, 1980, No. 2.
- V.N. Rychkov, M.E. Topchian. Direct measurements of flow velocity at numbers $M \approx 10$ and estimation of enthalpy losses in the tube of gas-dynamic unit under high pressure in the chamber. In: Sbornik IV Vsesoyuznoi shkoly po metodam aerodinamicheskikh issledovani. Novosibirsk, 1986.
- A.A. Meshcheryakov, V.I. Pinakov. Author's certificate No. 390315. - Bulletin, discovery, invention, industrial samples, trade marks. 1973, No. 30.

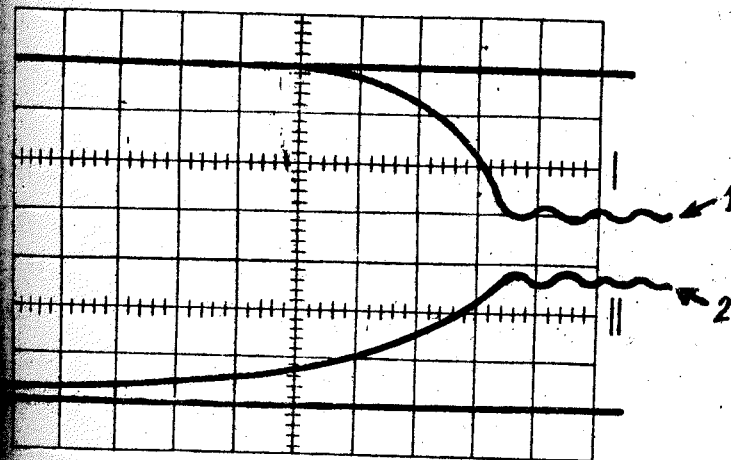


Fig. 2. Oscillograms of pressures (1) and gas temperature (2) in the chamber.

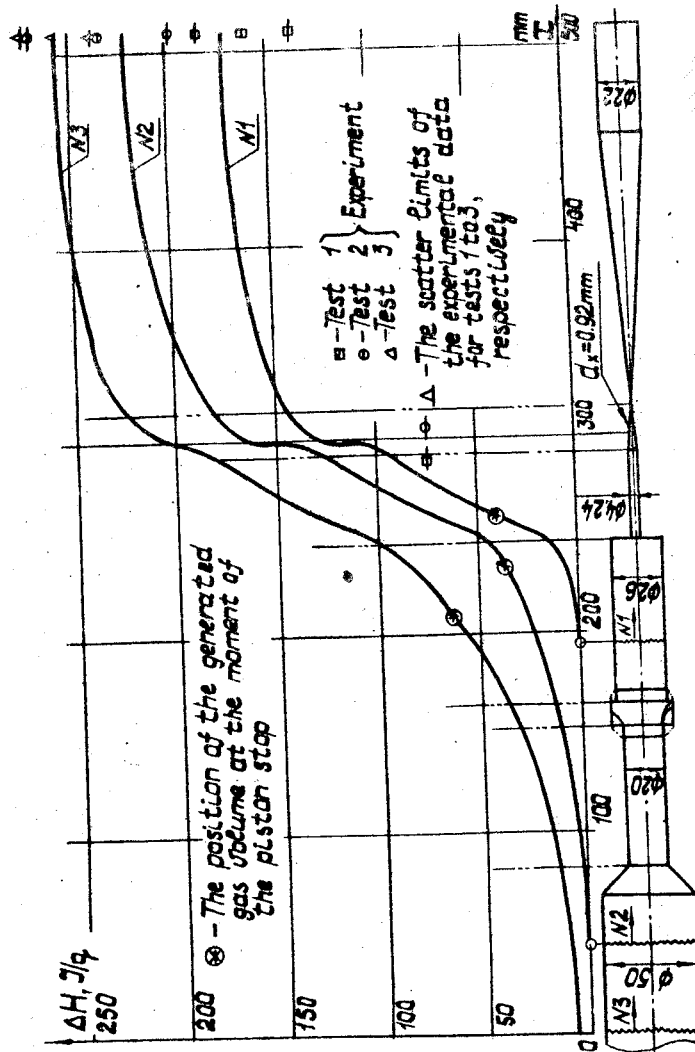


Fig. 3. The increase in enthalpy losses during the movement of the gas generated volume along the path of the device.

CONCERNING PRESS DYNAMICS WHEN INSTANTANEOUS FAILURE OF SEALING BURR IN HIGH PRESSURE UNIT TAKES PLACE

G.S. Bobrovnichy

All-Union Scientific-Research and Planning-Design Institute of Metallurgical Machine Building, Moscow, USSR

When designing presses with a composed frame, prestressed by a high-tensile strip, for high-pressure material processing it is necessary to create such a preliminary tightening that no-opening of frame joints could be ensured not only when loading, but also during the processes connected with the instantaneous failure of partial sealing burr in the high-pressure unit.

To determine the required tightening, i.e. preliminary compressive strain of frame pillars in the conditions of instantaneous partial unloading, two steps of movement in the press should be taken into consideration: first, the motion of movable masses from the moment of unloading before collision, and second, further joint motion of masses after collision.

In this case the following assumptions should be made: the press is considered to be a two-mass deformed system, consisting of two concentrated absolutely rigid masses connected to one another by springs of corresponding rigidity; the low part of the press is firmly connected with a foundation; modulus of elasticity for liquids over a period a partial decreasing of pressure is considered to be a constant; masses come into collision on a thin elastic packing, a thickness change of which in the course of collision is not important. A partial mass of pillars and a prestressed high-tensile strip are regarded to a motionless mass.

Motion of masses before collision

Design scheme of the first step of motion is shown in Fig. 1. Motion of masses before collision is indicated in design scheme. The downward motion of mass m_1 is considered to be a positive motion, and the upward motion of mass m_2 is considered to be a negative one.

The equations for mass motions before collision according to the indicated design scheme will be:

$$m_1 \ddot{x}_1 = P_n - C_p \cdot x_1 \quad (1)$$

$$m_2 \ddot{x}_2 = P_n - C_f x_2 \quad (2)$$

where m_1 - mass of the upper assembly of the press; cross-bar

plates, a half of a high-pressure unit, one third of the mass of two pillars and a prestressed high-tensile strip; m_2 - mass of movable assembly: plunger, cross-piece, plates, a half of a high-pressure unit; P_h - nominal force of a press; C_p - transformed rigidity of pillars and a prestressed high-tensile strip;

$$C_p = C_s + C_m = 1 - \frac{E_s \cdot F_s \cdot L_m}{E_m \cdot F_m \cdot L_s}$$

where E_m , E_s - moduli of elasticity of pillar's materials and a prestressed high-tensile strip; F_m , F_s - cross-sections of pillar and a prestressed high-tensile strip; L_m , L_s - length of pillar and a prestressed high-tensile strip;

$$C_f = \frac{E_f \cdot F_p}{h_f};$$

where E_f - modulus of elasticity of liquid depending on the amount of pressure; F_p - area of plunger; h_f - liquid column height in hydraulic cylinder transformed to the atmospheric pressure;

Solution of equations (1) and (2), considering initial conditions $t=0$; $X_1=X_2=0$; $\dot{X}_1=\dot{X}_2=0$, has a form:

$$X_1 = -\frac{P_h}{C_p} (1 - \cos \omega_1 t) \quad (3)$$

$$\dot{X}_1 = \frac{P_h}{C_p} \omega_1 \cdot \sin \omega_1 t \quad (4)$$

$$X_2 = \frac{P_h}{C_f} (1 - \cos \omega_2 t) \quad (5)$$

$$\dot{X}_2 = \frac{P_h}{C_f} \cdot \omega_2 \cdot \sin \omega_2 t \quad (6)$$

Circular frequencies of mass oscillations

$$\omega_1 = \sqrt{\frac{C_p}{m_1}}; \quad \omega_2 = \sqrt{\frac{C_f}{m_2}}$$

Motion of masses after collision

Design scheme of joint motion of masses after collision is shown in Fig.2. The downward motion of masses is considered to a positive motion.

Initial speed of joint motion of masses after collision will

determined from the equation of quantity of motion.

$$m_1 \dot{X}_{1y} - m_2 \dot{X}_{2y} = (m_1 + m_2) \dot{X}_\Sigma \quad (7)$$

$$\dot{X}_\Sigma = \frac{m_1 \cdot \dot{X}_{1y} - m_2 \cdot \dot{X}_{2y}}{m_1 + m_2} \quad (8)$$

Motion of joint masses m_1+m_2 after collision is determined by equation:

$$(m_1+m_2) \ddot{X}_\Sigma = -(C_p+C_f)X_\Sigma - C_p \cdot X_{1y} + C_f X_{2y} \quad (9)$$

Solution of this equation under initial conditions $t=0$; $X_\Sigma=0$; $\dot{X}_\Sigma=v_N$ (8) has a form:

$$X_\Sigma = A \cos \omega_\Sigma \cdot t + B \sin \omega_\Sigma t - A \quad (10)$$

$$\dot{X}_\Sigma = -A \omega_\Sigma \cdot \sin \omega_\Sigma t + B \omega_\Sigma \cos \omega_\Sigma t \quad (11)$$

where

$$A = \frac{C_p \cdot X_{1y} - C_f \cdot X_{2y}}{C_p - C_f}; \quad B = \frac{v_N}{\omega_\Sigma}; \quad \omega_\Sigma = \sqrt{\frac{C_p + C_f}{m_1 + m_2}}$$

Information and loads in pillars

Residual deformation of the pillar under loading of the press by a working force is:

$$X_1^P = \frac{G_s^P \cdot L_s}{E_s}$$

where G_s^P - compressive strain in pillars under a working loading.

Compressive deformation of pillars at the moment of collision $X_1^B = X_1^P + X_{1y}$.

Joint does not open, if $X_1^B > X_\Sigma^{\max}$.

Deformation in a low position of masses after collision

$$X_1^H = X_1^P + X_{1y} + X_\Sigma^{\min}$$

Then, the compressive strain in pillars in a low position of masses after collision will be:

$$G_s^H = G_s^0 \frac{X_1^H}{X_1^0}$$

where G_s^0 - compressive strain in a pillar with a selected coefficient

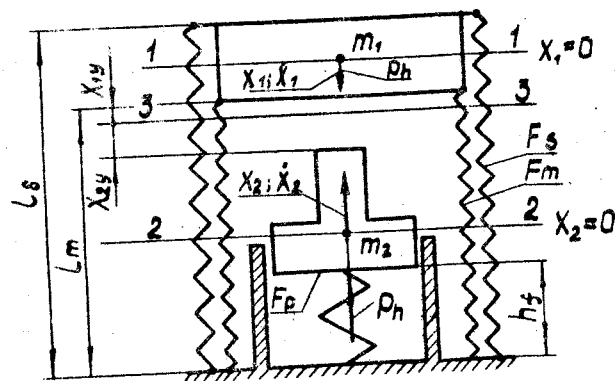


Fig. 1. Design scheme of the press in the course of motion of movable masses from the moment of the beginning of unloading to collision:
1-1 and 2-2 - position of the centre of gravity of m_1 and m_2 masses, respectively, in the case of working loading of the press, reference point; 3-3 - line of the mass collision; X_{1y} and X_{2y} - path, covered by m_1 and m_2 masses, respectively, before the moment of collision.

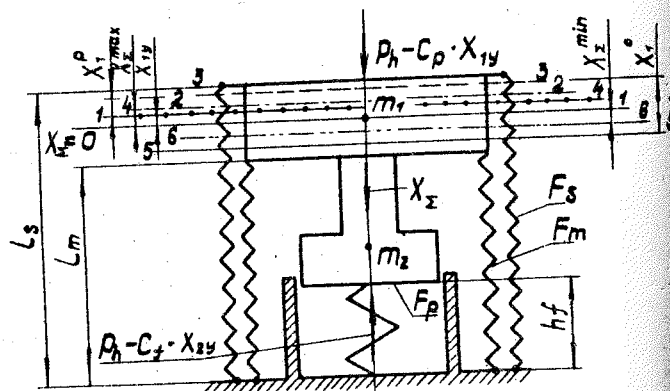


Fig. 2. Design scheme of the press in the course of joining of movable masses after collision:
1-1...6-6 - position of the centre of gravity of the m_1 and m_2 masses, respectively, at the moment of collision ($X_z = 0$), after collision, in the case of unloading pillars, under working load of the press (compressive strain of pillars X_z^p); in the case of tightening of the frame (compressive strain of pillars X_z^t) after collision.

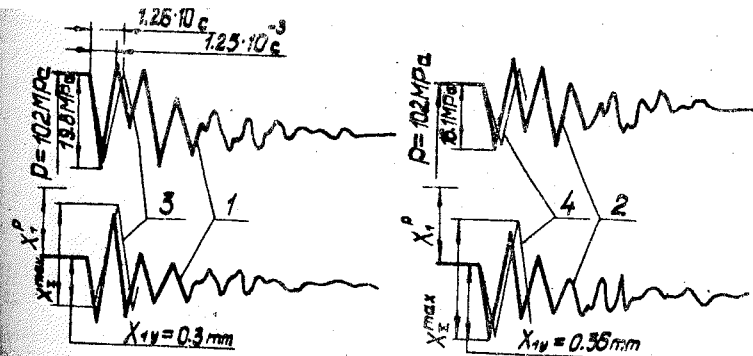


Fig. 3. Pillar deformation and the pressure in the main cylinder of the press with a force of 20000 kN:
1 and 2 - recording in the course of stroke equal to 42 mm and 23 mm, respectively; 3 and 4 - calculated values in the course of stroke equal to 42 mm and 23 mm, respectively.

ment of tightening; $X_1^p = \sigma_s^0 \frac{L_s}{E_s}$ - pillar deformation in the case of tightening.

Experimental check of the proposed technique was carried out on the presses with a force of 20000 kN.

Fig. 3 shows recordings of pillar deformations and the pressure in a hydraulic cylinder with various strokes of plunger. Data of calculations for deformations of first amplitudes are laid upon recordings. Calculated deformations are somewhat higher than experimental ones.

SCIENTIFIC AND TECHNOLOGICAL PRINCIPLES OF MAKING
"COLD" CONTINUOUS-OPERATING POINT PRESSURE SENSORS

A.S. Skoropany¹, B.L. Valevski¹, V.F. Skums¹, A.A. Vecher¹,
Yu.S. Maslenko²

¹Physico-Chemical Problems Research and Development Institute
of the Byelorussian State University, Minsk, USSR

²Institute for Superhard Materials of the UkrSSR Academy of
Sciences, Kiev, USSR

The increase of the reaction volumes of high-pressure chambers and automatization of manufacturing suggests setting of pressure sensors for each sinter in high pressure technological processes. The industry puts forward the following requirements to pressure sensors: small size, production and application effectiveness, multipurpose design, unnecessary additional electric lead-ins for the high-pressure chamber, ease access and low cost. One of the sensor should embrace rather a wide range of steady test pressures. "Cold" continuous-operating pressure sensors, based on chalcogenides, meet all these requirements /1/. A chalcogenide sensor substance (CSS) is the central element of a pressure indicator (PI).

When designing pressure indicators, the problems, concerning synthesis (connected with development of the optimal methods of making chalcogenides powders), material science (modification of materials for changing of electrobaric signal to required form and high intensity in the phase conversion region), mathematics (to choose the required composition of material with necessary form of signal, intensity and phase conversion rate), design (solving the same problems, as mathematics, but by efficient arrangement of one or several pressure indicators in a reaction volume) and metrology (connected with introduction of making materials and high pressure practical scale as reference substances), were solved. From /1,2/ it is followed, that compounds of $A^{II}B^{VI}$ and $A^{IV}B^{VI}$ - type as well as solid solutions on their basis are most promising for CSS-PI making.

Developing the optimal CSS-PI making methods we have examined the potentialities of the following ones: traditional ("melt"), through the gas phase transfer, by sintering components powder mixtures and using superhigh pressure technique. It is peculiar of CSS-PI, melting at rather high temperatures they are formed of fusible components, some of which possess vapour pressure.

The traditional synthesis through "melt" turned to be only useful for some CSS-PI and it has essential lacks. The reaction with gas transfer in some cases provides materials with improved, as compared to previous technique, electrobaric characteristics. However, it is time-consuming, complicated and extremely seldom used in production.

We have developed CSS-PI production method by linear heating of pressed powder component mixtures /3/. It implies that upon achieving certain temperature, the most fusible element in the system is melting first, thus appearance of liquid impells the onset of chemical interaction of components. With temperature rise by 90-250 K the process is completed. The holding of alloys at achieved temperatures for 5 to 15 h results in complete alloy homogenization.

We have tried-out the high pressure technique to enhance sintering. The application of the pressure above 1.4-5 GPa is found to promote of CSS-PI production without deteriorating their electrobaric properties /4/.

Analysis of literature sources allows to make conclusion on possible manufacturing of CSS-PI by synthesis of chalcogenides by applying dynamic superhigh pressure or static pressure up with shift deformation, etc.

Modification of CSS-PI electrobaric properties is based on doping, production on a base of binary CSS-PI, forming between themselves solid solutions, three-component CSS-PI /5,6/. Note depend on the $R = f(P)$ curve may be allowed for as it is the case for ZnTe at 3 GPa due to the sharp changes in the electronic structure of the material under high pressure influence /7/.

A variation of electrical resistance also owes to the compression of the chalcogenides compounds with defective structure /8/. Note, that in producing the mixture of two CSS-PI by their mixing /9/ electrobaric properties were found to change.

So, we have dwelt upon main methods in producing and modification of CSS-PI with one electrical resistance jump. However, it is important to know a point pressure throughout the entire loading cycle, i.e. to continuously measure a point pressure. In this case, the marked (sensors) material should have at least two steps on $R = f(P)$ curve or possess the same pressure change of electrical resistance as bismuth does (step, then linear section, and step again). The CSS-PI with an electrobaric two-type signal may be implemented by producing mixture of

individual CSS-PI, having $\sqrt{\quad}$ - and \angle - shaped signals. The idea of "bismuth indicator" may be realized by choosing a mixture of components, characterized by similar character changes of electrical signal. The composition of a particular mixture is mathematically chosen upon analytical description of basic CSS-PI.

Metrological aspects of the problem are presented in separate report.

Nowadays, a base has been arranged at Special Technical and Design Bureau On Working Up of Mineral Raw Materials With Experimental Production of the Azerb.SSR Academy of Sciences (Baku) to produce experimental CSS-PI batches.

References

1. Skoropanov A.S., Laptev V.A. Prospects and problems in designing point pressure indicators with control properties for continuous pressure recording. In: High Pressure Application to Design New Materials and Enhanced Chemical Processes, Coll. Abs., M.: MGU, ch.2, p.117, 1986.
2. Prikhna A.I., Maslenko Yu.S., Belousov I.S., and Miasnikov E.P. Peculiarities of methods for estimation of pressure and temperatures in high pressure chambers. In: Experience and Technique of High Gaseous and Solid Pressures, M.: Nauka, 1978, p.189-192.
3. Valevski B.L., Vecher A.A., Skoropanov A.S. Quantitative differential thermal analysis of ternary intermetallic compounds $\text{GeTe-Bi}_2\text{Te}_3$. Sov.Zh.Fiz.Khim., 1983, v.57, N3, p.733-734.
4. Valevski B.L., Skoropanov A.S. High pressure technique to produce multicomponent chalcogenides. In: High Pressure Application to Design New Materials and Enhanced Chemical Processes, Coll. Abs., M.: MGU, ch.1, p.101-102, 1986.
5. Skums V.F., Valevski B.L., Skoropanov A.S. et al. Effect of some admixtures on electrical resistance in solid-phase pressure induced PbSe phase conversion. Sov.Zh.Fiz.Tekhn. Vys. Davl., 1986, vyp.23, p.18-22.
6. Ohno Y., Endo S., Kobayashi M., Narita S. Pressure dependence of the absorption edge in ZnTe. Phys. Letters, 1983, v.97, N7, p.407-408.
7. Hailing H., Saunders G.A., Penfold J.W. Pressure-induced phase transition in the vacancy compounds $\text{Hg}_5\text{Ga}_2\text{Te}_8$, $\text{Hg}_3\text{Ga}_2\text{Te}_6$ and HgIn_2Te_4 . High Temp.- High Pres., 1983, v.15, p.533-538.
8. Johnson R.T., Morison Ir.B. High-pressure effects on the electrical resistivity and structure of single-crystal cadmium sulphide. High Temp.- High Pres., 1976, v.8, p.31-44.
9. Valevski B.L. Influence of mechano-chemical development of chalcogenides on their electrobaric properties. In: High Pressure Application to Design New Materials and Enhanced Chemical Processes, Coll. Abs., M.: MGU, ch.2, p.101.

AUTOMATIC PRESS FOR SHEET-METAL EXPLOSIVE STAMPING

V.K.Borisevitch, V.I.Isaenko

Kharkov Aviation Institute, Kharkov, USSR

At present sheet-metal explosive stamping is performed mainly in basins. The creation of such equipment requires the minimum capital expenses and its application in experimental and small-scale production gives high economic effect. However with parts output growing the low basin cost does not compensate high labourious operations because of low mechanization degree and high time expenses. At basin stamping it is difficult to design the universal device for die assembling-disassembling and blank sealing as it will be subjected to shock waves direct action as its diving into the basin. The blank motion is very durable during technological cycle that makes complicate to mechanize the operations.

Last time therefore the stamps for sheet-metal explosive forming in closed volume have been designed and developed in many countries /1, 2, 3/. Such stamps combine explosive stamping advantages with high productivity.

In order to realize sheet-metal explosive stamping into large-scale production the universal stamp has been designed (Fig.1*) that makes possible to perform the following technological operations: delivery, forming and calibration of the parts from the tubular blanks; extrusion - drawing of the parts from the flat blanks simultaneously with forming and calibration of the bottom and side reliefs, tappings; holes group perforation.

The main elements of the stamp are an explosive chamber and frame, connecting the chamber with a die. The frame consists of plates fastened by four columns. The explosive chamber has inertia-power locking. Contrary to the rigid locking when all the energy of high explosive is used to elastic deformation of the stamp frame, at inertia-power locking of the chamber after the blasting the latter begins to move, compressing the shock absorber which brakes its motion and after that returns it smoothly to reference position.

Carried researches /3/ show that as explosive chamber mass three orders higher than blank mass, the blank is stamped out at the displacement of the chamber and its motion does not influence largely the process of high explosive charge transmission.

Figure is given at the end of the book

The loading on the stamp frame decreases significantly as the pressure generated by the gas cavity in the chamber decreases. It is due to the fact that because of the chamber displacement and fluid draining from it the chamber volume increases and the fluid content decreases. Since the loading from the explosive chamber transfers to the stamp frame through the shock absorber, the loading amplitude decreases at the same pulse value and its duration increases.

The internal surface of the stamp chamber has the form of a parabola /4,5/.

The stamp is equipped with a movable table, where mechanism die is arranged. The stamp is surrounded by a protective device preventing detonation products getting into the shop place and providing for permissible noise level.

Stamp technical data

Overall dimensions, m	- 2.2x5.9x4.7
Maximum charge weight, kg	- 0.15
Operation table dimensions, m	- 1.4x1.9
Maximum die dimensions, m	- 1.4x1.9x0.8
Maximum clamping force of the blank flange, kN	- 3000
Fluid pressure in explosive chamber, MPa	- 200
Stamp electric drive power, kW	- 15
Technological cycle duration, min	- 1
Maintenance personnel, pers	- 1
Stamp occupied area, m ²	- 72
Stamp weight, t	- 25

Standard parts are given in Figs.2, 3*

Such labourious operations as die assembly/disassembly, explosive charge positioning, die filling with transmitting medium and its removal, die travelling into and from the operation have been made automatic. The stamp is supplied with automatic block devices, providing for the safety of operations.

References

1. Kortenski C., Wodenitscharov S. Sprengverformungsmaschine NTS VDI 1986 Donnerstag, 10. April 12.00 h, Halle Nr.24

* These figures are given at the end of the book

Zhang Shi-biao. Explosive metalworking towards machinery, automation and indoor process. The Vth International Symposium "Use of explosive energy in manufacturing metallic materials of new properties". Gottwaldov. October 1985. p.495-503.

О ПРИМЕНЕНИИ взрывных прессов с инерционным замыканием камеры В.К.Борисевич, В.И.Исаенко, В.П.Сабелькин, С.Н.Солодянкин// Кузнечно-штамповочное производство. -1976. -№8. -С.31-32.

Исаенко В.И., Борисевич В.К., Каныгин С.Л. К вопросу выбора параметров камер для взрывных прессов//Импульсная обработка металлов давлением: Сб. научн. ст. Харьков. 1979. Вып.8.С.130-133.

Волновые взаимодействия при подрыве заряда БВВ в камере с параболической внутренней поверхностью/В.И.Исаенко, В.К.Борисевич, С.Л.Каныгин, Н.С.Воронов//Импульсная обработка металлов давлением: Сб.научн.ст. Харьков. 1982. Вып. 10.С.142-150.

THE DC-200 DIAPHRAGM-TYPE GAS COMPRESSOR FOR 200 MPa

Jan Siedlaczek

High Pressure Research Center, Polish Academy of Science,
"UNIPRESS", Sokolowska 29/37, PL-01142 Warsaw, Poland

Introduction

The high purity gases can be compressed without any contamination by the DC-200 diaphragm-type gas compressor. This is a basic feature distinguishing diaphragm-type compressor from the piston-type one, where the contamination of the compressed gas with lubricants takes place. There is a great demand for the compressed high purity gases in the physical and chemical labs, as well as in the industry, e.g.: wherever the high purity gases are manufactured.

Application

Helium up to 200 MPa may be compressed with the DC-200 diaphragm gas compressor using supply pressure within the range 1-15 MPa. Below 10 MPa the output pressure is proportional to the supply pressure. Other neutral gases as nitrogen, argon etc. can also be processed. In this case the compressed efficiency can nearly be doubled in comparison to helium. The special design of the diaphragm-type gas compressor allows for the hydrogen and the aggressive gases to be worked.

Action

Diaphragm moved by the pressurized oil causes the gas volume to decrease within the lens-shaped working chamber (see Fig.1). The oil pressure is generated by the piston-type pump controlling the gas suction and compression cycles. The contact between the compressed gas and the oil, the non-metallic and the lubricated parts are completely eliminated. During compression the gas does not change its chemical and mechanical purity.

Test data

Gas : Nitrogen
Temperature : 20 °C (68 °F)
Pump speed : 150 strokes per minute
Oil : Hydrol 10

Technical data

Maximum output pressure
(for input pressure 10-15 MPa)

200 MPa

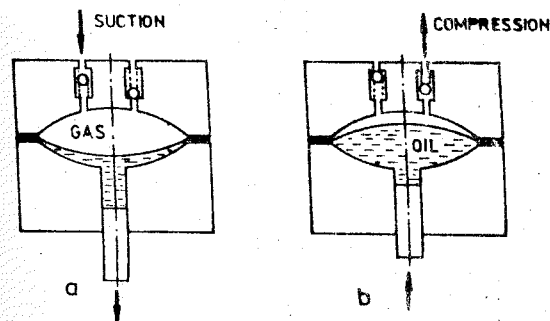


Fig.1. Working chamber:
a) gas suction, b) gas compression.

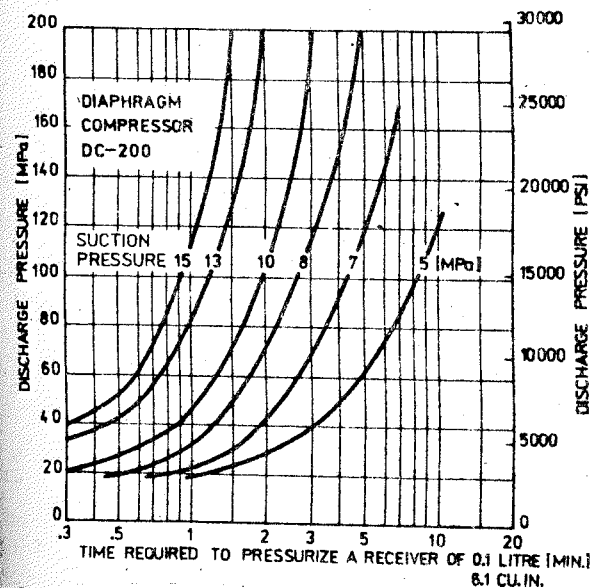


Fig.2. Performance curves.

Capacity (for input pressure 15 MPa)	3 Nm ³ /h
Strokes per minute	150
Power supply (3x380 V, 50 Hz)	1.5 kW
Weight	175 kg
Dimensions (l x w x h)	850x400x700 mm

Additional informations

When the diaphragm-type gas compressor to the 2nd compression stage of special design is attached, the neutral gases such as helium, nitrogen, argon, etc. up to 1.5 GPa can be compressed, eliminating the necessity of the standard GCA piston-type compressor (made by Unipress, as well) to be used.

Our experience enables us to offer our help in various measurement and investigation problems. The technical data of our instruments can -on request- be adapted to your particular requirements.

EFFECT OF DIFFERENT GAS MEDIA ON THE OPERATION OF THE CONTROLLED CLEARANCE PISTON GAUGE UP TO 5 MPa

J.K.N.Sharma, K.K.Jain, A.K.Bandyopadhyay
National Physical Laboratory, New Delhi-110012, India

Introduction

In a controlled clearance piston gauge, as long as the piston is floating, the pressure at the reference level of the gauge is constant and can be expressed as /1/

$$P = \frac{M_g (I - P_{air}/P_M) + \sqrt{C} + T_w}{A_0(I + bp) [I + (\alpha_p + \alpha_c)(T - T_R)] [I + d(P_Z - P_j)]} \quad (1)$$

The symbols used here are the same as mentioned in reference /1/.

P_Z and P_j are obtained from the measurement of the fall rate (ds/dt) which are related by /1/

$$(ds/dt)^{1/3} = K'(P_Z - P_j) \quad (2)$$

where K' is a constant which is slightly different from K as mentioned in Eq.(4) of reference /2/ here K' is associated with kinetic viscosity of the working fluid used in the pneumatic pressure region.

In the pneumatic pressure region as there is no surface tension effect, the contribution of the term \sqrt{C} in Eq.(1) is neglected in computing the pressure. Apart from the different parameters such as $(I - P_{air}/P_M)$, $[I + (\alpha_p + \alpha_c)]$ and $(I + b.P)$ which contribute some finite value of uncertainty in the pressure generated by the piston gauge, the contributions in the overall uncertainty are mainly from the area of the piston (A_0), the elastic distortion of the cylinder (d) and the stall jacket pressure (P_Z). Uncertainty in the measurement of A_0 and d , can be improved by taking a series of diametrical measurements supplemented by the measurement of the roundness and straightness of both the components. Similarly, the uncertainty in P_Z value can be improved to a great extent by studying the fall-rate during its characterisation, which has already been established by Sharma et al./2/.

In the past, nitrogen was used as the working fluid in the pneumatic pressure region. But very little work has been reported on how the use of different fluids with different molecular weights and viscosities would affect the overall uncertainty in the pressure generated by the piston gauge. The authors in this paper have made a systematic study of the fall rates up to 5 MPa

in a controlled clearance piston gauge using different working fluids such as argon, nitrogen, helium and hydrogen in order to see their effect on the overall uncertainty in the pressure generated by the gauge and the effect of ambient temperature from 291 - 302 K has also been studied.

A controlled clearance piston gauge manufactured by M/S Harwood Engineering Inc., USA (Model DWT 1000 N), was used during these measurements. For these studies, an arrangement to rotate the piston at a prefixed uniform speed was made and also an additional Bourdon gauge (16" dial size) to measure P_j within an accuracy of ± 0.05 MPa was provided. Further, in order to minimize the volume of the fluid, beneath the piston a fine needle valve had been used in the measured pressure line. Fall-rates were measured using a linear voltage displacement transducer (LVDT) with digital read out (Model: Schaevitz DTC-45I) having a resolution ± 0.01 mm and a sensitivity better than 1 mV/V. The temperature of the piston and cylinder was measured through a PRT with an accuracy better than ± 0.01 K. The purity of the gases as per the manufacturer is better than 99.999%.

Results and discussion

The fall rate curves for all the working fluids such as N_2 , He and H_2 were taken at 296 K and 58 rpm by increasing the pressure in steps, which are arbitrarily fixed at 1.10, 3.09 and 5.09 MPa and similarly by decreasing the pressure in steps which were fixed at 4.09 and 2.09 MPa. At least three measurements were made at each pressure value in order to determine the reproducibility. An improvement in the reproducibility of the fall rate is observed by using helium and hydrogen as compared to that of argon and nitrogen.

The typical fall rate curves for He are shown in Fig. 1. They are the typical representation of the average of the three measurements at each pressure value. The fall rate curves of H_2 are not shown here but are consistent with the results for He as represented in Fig. 1. The value of P_z for all the media increases linearly with the applied pressure as shown in Fig. 2. At a particular pressure (P_M), a large variation in the values of P_z of Ar is obtained when compared to the P_z values of He, however, not much difference is found when compared to the value of N_2 .

At the full scale pressure of 5.09 MPa, uncertainty in the measured

to be 25, 26, 27 and 28 ppm whereas at the lowest pressure of 1.1 MPa, the uncertainty increases to 31, 33, 35 and 37 ppm for Ar, N_2 , He and H_2 respectively. As stated above, an improvement in the overall uncertainty in P_M can be achieved if the value of d is obtained with better accuracy. The value of d is indirectly dependent on the engagement length, therefore, it would be appropriate to study the slope of the fall rate curve which is defined as

$$m = C (\sqrt{L/P_M})^{1/3} \quad (3)$$

and in the present case this is reduced to

$$C' = CL^{1/3} = m (P_M/\sqrt{L})^{1/3} \quad (4)$$

where \sqrt{L} is kinematic viscosity and defined as viscosity/molecular weight and L is the engagement length. In the deduction of Eq. (3) and (4) it was assumed that the engagement length (L) and C are constant, and hence C' in Eq. (4) may also be a constant quantity and is independent of the measured pressure or gas media used. It is clear from Fig. 3 that C' changes with pressure and is entirely different for gases which indicates that the assumption of the constancy of the engagement length in deriving Eq. (3) may not be correct. Therefore, there is a high probability that d , the coefficient describing the distortion of the cylinder, is also varying with pressure, which has again been observed earlier in the hydrostatic pressure medium [2].

A better reproducibility of the fall rate is obtained in helium and hydrogen as compared to that of argon and nitrogen. This indicates that the working fluid having a higher kinematic viscosity is preferred over the others having comparatively low kinematic viscosity. But the use of hydrogen as a working fluid is restricted for two counts: first, one has to use all the time comparatively high value of P_j to obtain a reasonable fall rate for any pressure, second, from the safety point of view, whereas in helium the overall uncertainty of the measured pressure is less than that of hydrogen. It is inert and now easily available, therefore, the use of helium as a working fluid in the pneumatic pressure operation of the piston gauges is suggested. The use of materials with widely different linear thermal expansion coefficients for the materials of the piston and cylinder, the change of temperature may cause a change in the clearance between the piston and cylinder and thereby increase or decrease the P_z values. This is supported by the fact that the computed

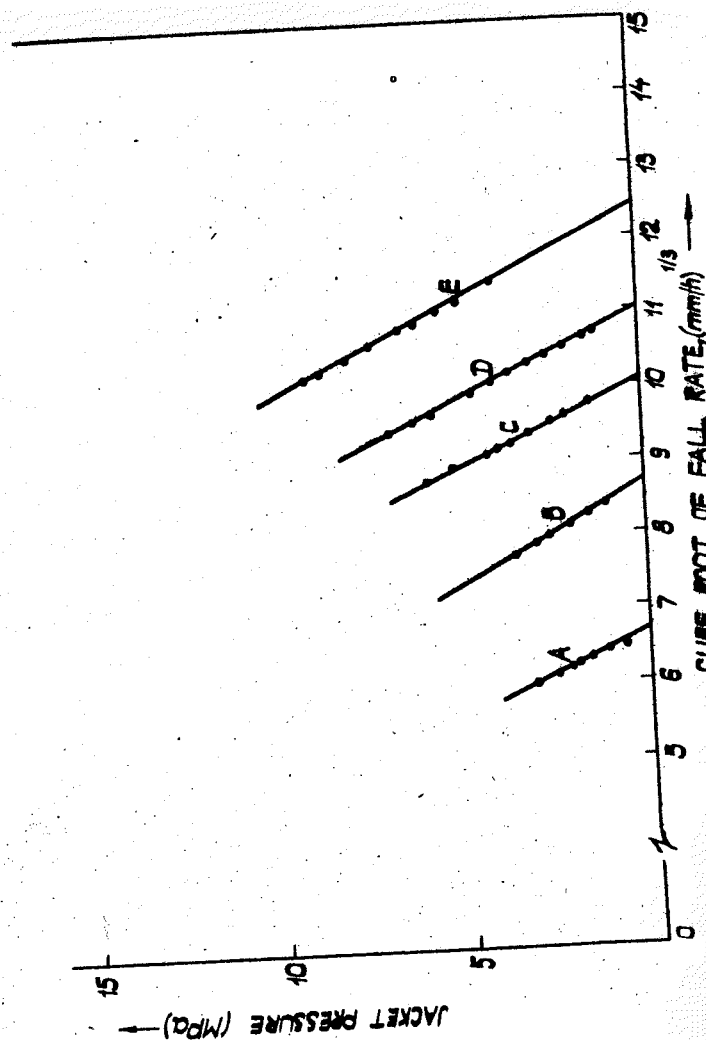


Fig. 1. Jacket pressure as a function of the cube root of the fall rate for helium (He) at 58 rpm and 296 K. Curves A, B, C, D and E are for pressures of 1.09, 2.09, 3.09, 4.09 and 5.09 MPa respectively. The values of P_0 for these pressures.

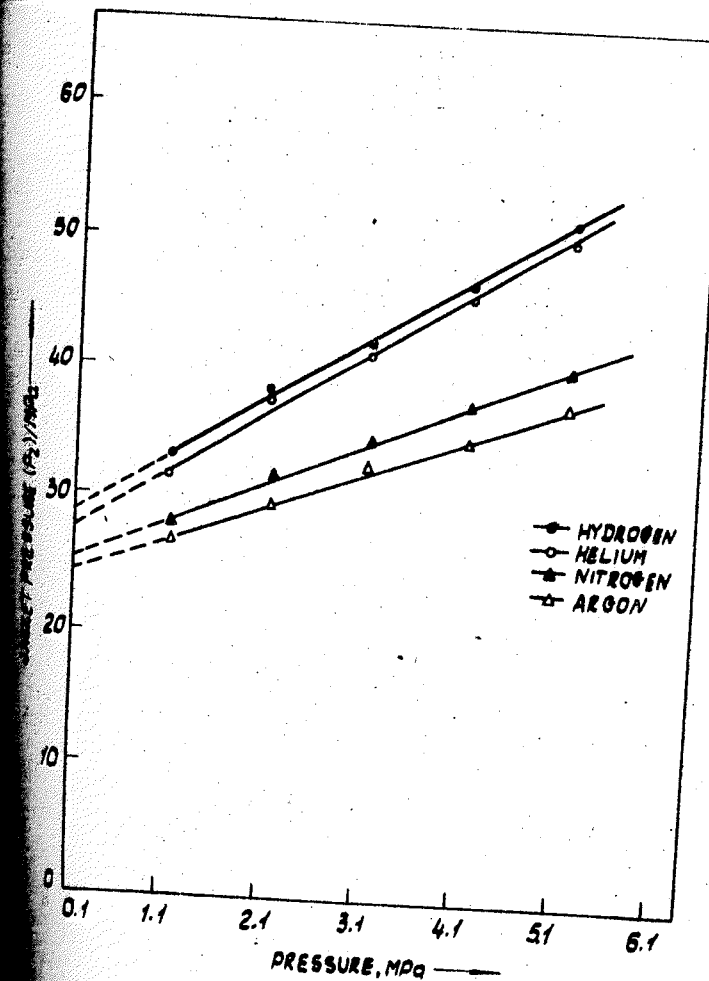


Fig. 2. Jacket pressure as a function of pressure for four working fluids, argon, nitrogen, helium and hydrogen at 58 rpm and 296 K.

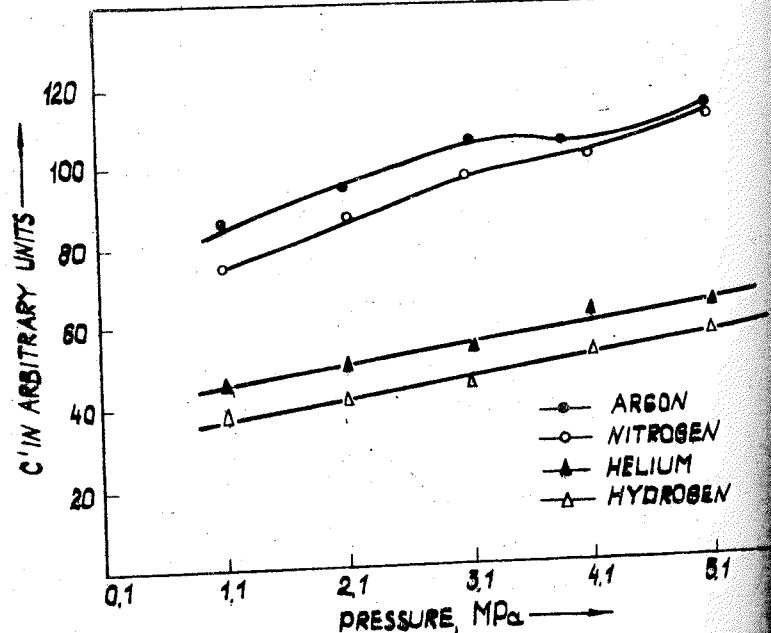


Fig. 3. C' as a function of pressure for argon, nitrogen, helium, and hydrogen.

uncertainty value at different temperatures from 291-302 K, ways within 1 ppm even at full scale pressure value /4/.

References

1. Heydemann, P.L.M., and Welch, B.E. Experimental Thermodynamics, Vol. II edited by B. Le Neindre and B. Vodar, Butterworths, London, 1975, 147-202.
2. Sharma, J.K.N., Jain, Kamlesh K., Bean, V.E., Welch, and Lazos, R.J., Effects of viscosity, temperature, and of rotation on pressure generated by a controlled clearance piston gauge, Rev. Sci. Instrum. 1984, 55, 563-569.
3. Molinar, J.F., and Maghenzani, R., A General use of the gauge apparatus for gas pressure measurements up to 10 kbar, High Pressure in Research and Industry, ed. C.M. Bucci, et al., Uppsala, 1982, 768-771.
4. Sharma, J.K.N., Jain, K.K., and Bandyopadhyay, A.K., pressure measurements by a controlled clearance piston gauge using different working fluids (under publication).

SHOCK WAVE CHEMISTRY

A.N. Dremin

Institute of Chemical Physics, the USSR Academy of Sciences
USSR

Shock wave chemistry, a new scientific trend, deals with chemical aspects investigations of substance state under the new type of affect. Indeed, shock wave affect is not a more imposition of pressure and temperature actions. Characteristic features of the affect are the tremendous rates of substance loading and subsequent unloading. The affects result in substance strongly non-equilibrium state. The state life time is governed by relaxation processes of those phenomena which are provoked by shock waves in substance. For instance, in the case of a substance consisting of complex molecules with a large number of internal degrees of freedom, varying strongly in excitation times, all kinetic part of the energy is at first absorbed by the translational degrees of freedom inside shock wave front. Then, the energy is redistributed into the vibrational degrees of freedom. Obviously, the non-equilibrium state time is not longer than the excitation time of the most excited vibrational degrees of freedom ($10^{-10} - 10^{-9}$ s). The same order of magnitude is the relaxation time of liquid substances polarization caused by dipolar molecules mechanical turn in the shock discontinuity zone affect. In polymers the zone affects some separate groups of polymer molecule atoms. In such a case the relaxation period, on the contrary, may last as long as milliseconds. As far as "hot spots" are concerned, their life time is determined by thermal relaxation regularities and it depends on the material. The hot spots in solids appear during shock compression at the sites of an imperfect substance structure. In liquids the hot spots can originate when a shock wave front passes through negative density fluctuations. It transforms the fluctuations of very small size and of high probability into some positive temperature regions of big size and extremely low probability in equilibrium state behind the wave front. The hot spots in polymers (possibly in liquids too) appear due to the affect of stresses in shock front. Point and lengthy defects of solid materials occur under the affect. The lengthy defects appear in the wave front due to the transition from one-dimensional to three-dimensional compression. The transition takes place if the wave intensity is larger than the dynamic elastic limit of solid under investigation. In brittle materials the transition results in their

grinding into fragments and in the fragments relative displacement. Some liquid melted layers of substance appear between the fragments in the process of displacement. Their lifetime is also determined by the thermal relaxation regularities and probably is small. Nevertheless, the layers obviously govern the spall strength of brittle solids and promote solid-phase shock reactions. The defects created in solid by shock affect can exist for a long time if solid substance residual temperature is lower than its recrystallization temperature. Therefore, solid substance treatment by shocks of proper intensity can increase their chemical reactivity.

Shock wave chemistry as the new scientific trend is still in its infant stage although it began more than 40 years ago. Shock wave aftereffect investigations have shown that the affect results in various chemical reactions (or chemical and physical properties change) in liquid and solid substances, polymorphic transformations, production of alloys of strongly-differing components, and so on. A large number of substances have been investigated and results have been obtained (see early reviews /1-3/ and later /4-8/ which contain new data). The synthesis of diamond and diamond-like boron nitride modifications, strengthening and welding of metals, pressing of powders or their activation in order to improve subsequent sintering at static conditions have now become practical use.

The realization of the fact that the shock wave affect is really a new type of action is the general conclusion of the investigation efforts. However, the detailed mechanism of action is unknown. It has only been realized that a highly non-equilibrium state (chemical, physical, electromagnetic) appears, unlike conditions in static compression at the very beginning of shock wave action. The state, obviously, governs unusual fast chemical reaction rates as well as polymorphic and phase transformations during shock waves. Of course, a principal possibility of these chemical reactions and transformations at the shock-compressed state is governed by thermodynamics. But as far as their rates are concerned, they are governed by the action specific features. First of all, the action specificity manifests itself by the fact that the shock wave affect of extremely narrow in time shock front (in various cases from 10^{-12} s to $\sim 10^{-9}$ s) at non-equilibrium state activation of particles or new modification (phase) nuclei originates. A considerable relative displacement of the shock-compressed substance particles in relief waves also represents shock wave affect

specific feature. The displacement promotes peculiar diffusion of atoms and molecules and thereby increases substance change. It also results in the new modification nuclei sticking together and origins of particles of larger size than that of the critical one at residual temperatures. A tremendous rate of material cooling ($>10^9$ degrees/s) in relief waves is the other shock wave affect feature. The feature promotes freezing of the products originated in the shock-compressed state. So, if substances suffer chemical or polymorphic transformations in the shock-compressed state, it is possible to obtain transformation products which are metastable at ambient conditions.

At present it is known that not all chemical reactions occur during the shock wave action. Moreover, it should be mentioned that a majority of investigations on the shock wave chemistry were made on samples not during shock wave passing through the samples but on samples recovered after the shock wave affect. In this case it is even unknown when the discovered transformations of substances occurred: whether it took place in the shock wave front or in the relief wave or during some later time. Only recently, visible progress has been achieved in the problem. We have developed a technique of continuous (in time interval of 10^{-7} - 10^{-2} s) observation of substance state at the shock wave action of some microseconds duration /9/. For example, this technique showed that a reaction for synthesizing Sn monosulfide from elements starts after the shock wave affect of 16 GPa in $\sim 10^{-3}$ s and is completed after about 10^{-1} s.

Thus, the foregoing considerations lead to the conclusion: to reveal the real intrinsic nature of the shock wave affect on condensed media, first of all it is necessary to study the shock wave front structure and substance non-equilibrium state in it practically at the very beginning of the front action. Some efforts have already been made in this respect. The front structure is studied theoretically by molecular dynamic methods. It is known that some attempts have been made to use quantum-chemical calculations to reveal possible ways of complex organic molecules destruction reactions at the shock wave affect (see /10/ and references in it). There are also experimental works devoted to the problem. Different Raman spectroscopy techniques have just begun to be used for studying the material state in detonation and shock waves /10,11/. At present, measurements of shock and detonation fronts with time resolution of $\sim 10^{-9}$ s are possible by means of laser interferometry. However, the resolution power of experimental methods is still far from

necessary level. In fact, one needs time resolution $\sim 10^{-12}$ s to observe non-equilibrium process in substance just from the very beginning of the shock compression. In spite of scarcity of information on the detailed front structure and non-equilibrium processes in it, one may suggest, taking into account only current available data, the following. As far as the chemical reactions and polymorphic transformations during the shock wave affect are concerned, their rates obviously are governed not by temperature, but mainly by pressure. It follows from the fact the occurrence of active molecular particles or new modification nuclei of proper concentration takes main share of the total time of the processes under statics. At the compression in dynamic situation, on the contrary, it occurs inside of the shock front. Obviously, the shock front parameters - its intensity and gradient of stresses inside of the shock discontinuity zone - govern the mentioned concentration.

References

1. Batzanov S.S. Physico-chemistry of impulse pressures. - *Izvestiya Akad. Nauk SSSR, Tekhnicheskaya Fizika*, 1967, v.12, 104-119.
2. Dremine A.N., Breusov O.N. Processes in solid materials under strong shock wave effect. - *Uspekhi Khimii*, 1968, v.37, 898-916.
3. Duval G., Graham R. Phase transitions under shock wave loading. - *Rev. Modern Phys.*, 1977, v.49, N3, 523-579.
4. Dremine A.N., Babare L.V. The shock wave chemistry of organic substances. - *SWCM Conf.* 1981, N.Y., *Amer. Inst. Phys.*, 1981, 27-41.
5. Graham R.A., Morosin B., Horie Y. et al. Chemical synthesis under high pressure shock loading. *SWCM Conference 1985*, London, Plenum Press, 1986, 693-711.
6. Adadurov G.A. Chemical processes experimental study at dynamic compression conditions. - *Uspekhi Khimii*, 1986, v.1, 578.
7. Batzanov S.S. High dynamic pressure inorganic chemistry. *Uspekhi Khimii*, 1986, v.1V, N4, 579-607.
8. Dremine A.N. Dynamic high pressure work. *Proc. 9th AIRAP* 1983, Elsevier Sci. Publ. Co., 1984, pt III, 151-158.
9. Nabatov S.S., Dremine A.N., Shubitidze S.O., Yakushev V. Use of electroconductivity measurement method for physical substance change inside recovery device. - *Fiz. i Vzryva*, 1986, v.22, 130-134.
10. Dufort S., Delpuech A. A molecular mechanism for the initiation of secondary explosives. Influence of a shock-loading. *Proc. 8th Symp. (Int) on Det.*, Albuquerque, N.M., 221-229.
11. Schmidt S.C., Moore D.S., Shaner J.W. Raman spectroscopy of shock-compressed materials. *SWCM Conference 1985*, New York, Academic Press, 1986, 293-302.

HIGH-PRESSURE HIGH-TEMPERATURE PHASE CHANGES IN CHEMICALLY REACTIVE MIXTURES

F. H. Ree, D. F. Calef, M. van Thiel, and D. C. Hamilton

University of California, Lawrence Livermore National Laboratory
Livermore, California 94550 USA

Abstract

Using a multiphase, multicomponent statistical mechanical code, we have examined experimental data on shock dissociation of condensed nitrogen, carbon solidification, supercritical fluid phase separation, and their implications to the detonation behavior of high explosives. We present results of the calculations. Discussions are given on the rates and scales required to achieve thermodynamic equilibrium in these systems.

Introduction

Some interesting changes that occur in nature involve mixtures at high pressures and temperatures. These mixtures may exist in a single phase or in several phases. One example for the former is a shock-wave induced transition of condensed nitrogen from molecular to atomic state [1]. Examples for the latter are a supercritical fluid phase transition [2] and condensation of carbon in detonation products [3,4]. This paper reports statistical analyses of these systems.

We will study phase changes and chemical reactions using a multiphase, multicomponent statistical mechanical model. Since our calculations assume chemical equilibrium, the computer code employed in our study is called "CHEQ". Details of the CHEQ code are described earlier [2,5]. The CHEQ code evaluates thermodynamic properties by minimizing the Gibbs free energy, G , with respect to composition at fixed temperature, T , and pressure, P . Computation of the fluid-phase portion of G employs statistical theory together with an improved one-fluid van der Waals' mixture model. Pair (exp-6) potentials with parameters from [2] are used to represent the intermolecular attractions.

Dynamic and kinetic behavior of shocked molecular nitrogen

Experimental data [1] on liquid nitrogen show a significant softening of the shock pressure during the transition. The observed physical changes have been attributed to dissociation of molecular nitrogen into monatomic species [6,7]. The N_2 - N exp-6 parameters [2] used to fit the shock data in the undissociated regime below 30 GPa. We use the N_2 parameters from a combination rule [8] and adjust the N - N parameters to fit the data above 30 GPa (Fig. 1). One characteristic of the resulting (preliminary)

N-N exp-6 parameters ($r^* = 0.35 \text{ nm}$, $\epsilon/k = 20 \text{ K}$, $\alpha = 20$) is a shorter repulsive range than that ($r^* = 0.41 \text{ nm}$) of the $\text{N}_2 - \text{N}_2$ interaction. Namely, the shock compression and shock heating make the N_2 molecules energetically favor dissociation. Calculated shock temperatures in Fig. 1 agree closely with the experimental data [1]. A calculated reflection shock path also agrees reasonably. Efforts to "fine-tune" the N-N parameters [9] are in progress.

To estimate the barrier to dissociation [10], we construct two free energy curves for N-N, based on quantum mechanical calculations, and another using the aforementioned $\text{N}_2 - \text{N}_2$ potential. The contribution to the free energies due to the surrounding detonation medium is computed in the hard-sphere approximation. The relative height of the two free energy minima is adjusted to yield equilibrium concentrations predicted by CHEQ. A three-dimensional plot (Fig. 2) of the free energy vs. the N-N reaction coordinate and shock pressure shows the decrease of the barrier height with increasing pressure along the principal Hugoniot. The dimensionless barrier height, $\Delta F^\ddagger/k_B T$, is 9.3 at 20 GPa ($T = 0.12 \text{ eV}$ and $\text{N}_2 = 99.98 \text{ mole } \%$) and 1.4 at 85 GPa ($T = 1.24 \text{ eV}$ and $\text{N}_2 = 56 \text{ mole } \%$). To estimate the time scale for dissociation from the rate constant, $k = A e^{-\Delta F^\ddagger/k_B T}$, with A from Holian's work [11]. Values of k^{-1} are 5000 ns at 20 GPa and 1.23 ns at 85 GPa. The former value is long compared to the time scale (order of 100 ns) of the shock experiment. But, since dissociated atoms are few in number, thermodynamic properties are essentially the same as those of the undissociated system. However, both time scales will cross each other at some shock pressures above 20 GPa. An apparent "shoulder" in the experimental Hugoniot in Fig. 1 may be a manifestation of this rate effect.

B. Fluid phase separation and its effect on detonation properties

The phase behavior of N_2 , CO_2 , and H_2O mixtures, which are major detonation products of high explosives, is sensitive to the exp-6 parameter r^* for $\text{N}_2 - \text{H}_2\text{O}$ and CO_2 interactions [2]. If we increase r^* ($\text{N}_2 - \text{H}_2\text{O}$) and reduce r^* ($\text{H}_2\text{O} - \text{CO}_2$) by about 10% from the Lorentz-Berthelot values [8], the mixed phase region is shifted to lower P and the theoretical Chapman-Jouguet point of PBX-9404 may be shifted from the single-phase region to the mixed phases containing N_2 -rich and N_2 -poor fluids. Hugoniot calculations [2] which include this modification also give an excellent agreement with experiment. That such small changes in r^* lie well within the combined uncertainty in the intermolecular potentials of the detonation products.

In Fig. 3 we use TNT as an example to illustrate how chemical reactions and phase changes influence detonation properties of TNT [12]. The fluid-phase change separates a two-phase (D+F) region and a three-phase (D+F₁+N₂) region, where D, F, N₂, and F₁ are the diamond, single-phase fluid, nitrogen-rich and nitrogen-poor fluid phases, respectively. A still lower-pressure (G+F) region is due to the transformation of the single-phase fluid to the graphite (G) phase. The C-J point, the principal expansion isentropic overdriven Hugoniot, and a porous Hugoniot with its initial density $\rho_0 = 1 \text{ Mg/m}^3$ are shown in Fig. 3.

In Fig. 4 we compare the detonation velocity vs. ρ_0 between theory and experiment [4]. We note that the experimental data [4] changes the slope above $\rho_0 > 1.55 \text{ Mg/m}^3$. The equilibrium graphite to diamond transformation predicts a similar break, but at $\rho_0 = 0.95 \text{ Mg/m}^3$, this suggests that the equilibrium conditions are not exactly obeyed. To simulate this nonequilibrium effect, we modify the standard heat of formation (1.90 kJ/mole) of diamond by changing it to a spread over 6.49 to 9.96 kJ/mole. We argue this is reasonable, since the short time scale of a detonation experiment can only produce small diamond clusters whose (size-dependent) heat of formation should be larger than that of bulk diamond. In Fig. 4 our equilibrium results at $\rho_0 < 0.95 \text{ Mg/m}^3$ give slightly higher detonation velocities. The nonequilibrium results in Fig. 4 are based on the use of $\rho_0 = 1.48 \text{ Mg/m}^3$, instead of ρ_0 of graphite, corresponding to the density of some carbyne structures [13]. The resulting calculation in Fig. 4 improves agreement with experiment.

Stability and transformation rate of graphite and diamond clusters

The above analysis of detonation velocity indicated that carbon microclusters in detonation products will occur in the graphitic phase within the (P,T) range where the diamond phase is thermodynamically stable. To qualitatively explain this, consider a carbon cluster with the shape of a cube having n atoms along each side. If the cube is a diamond cluster, interior atoms have tetrahedral coordination, while the surface atoms have three, or one dangling bonds, depending on whether the atoms lie on the corner, edge, or face. In the case of a graphite cluster, we neglect the weak van der Waals interplanar interactions but consider the single and double bonded carbon atoms. Using standard values for C-C and C=C bond strengths, one can calculate the energy difference between the diamond and graphite clusters. The calculations show that a graphite cluster with n less than about 10 (or, 10^3 carbon atoms) is stable with respect to a diamond cluster, even if the diamond phase is favorable in the limit of $n \rightarrow \infty$.

The above conclusion is consistent with a static experiment of Hirano et al. [14] at 9 GPa. They showed that diamond formation from glassy carbon requires an intermediate temperature to enter the graphitic phase. We have estimated the rate constants by fitting their data to simple rate equations. This has allowed us to infer the time for the formation of diamond and graphite clusters at different temperatures. The time t_1 for 95 mole % conversion of amorphous carbon and the time t_2 for 95 mole % conversion to diamond are shown in Table. The time scale required to grow a significant amount of diamond under detonation condition (3500 K to 4000 K) is much longer than the time scale of shock experiments. Note that the above result is applicable strictly at 9 GPa, since the pressure dependence of the activation free energy is neglected. Similar experiments at different pressures may provide a more reasonable estimate of the equilibration times relevant to detonation with a high carbon content.

Conclusion

The application of the CHEQ code for analyses of experimental data provides us with a new insight into the interaction of complex molecules under high pressure and

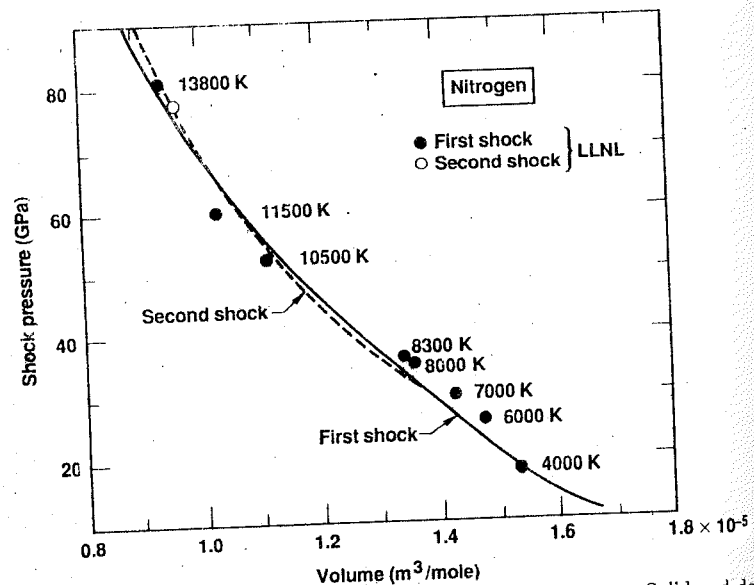


Fig. 1. Theoretical and experimental Hugoniots of liquid nitrogen. Solid and dotted lines indicate theoretical principal and reflected Hugoniots. The corresponding experimental data [1] are indicated by solid and open circles, respectively. Calculated shock temperatures are also indicated.

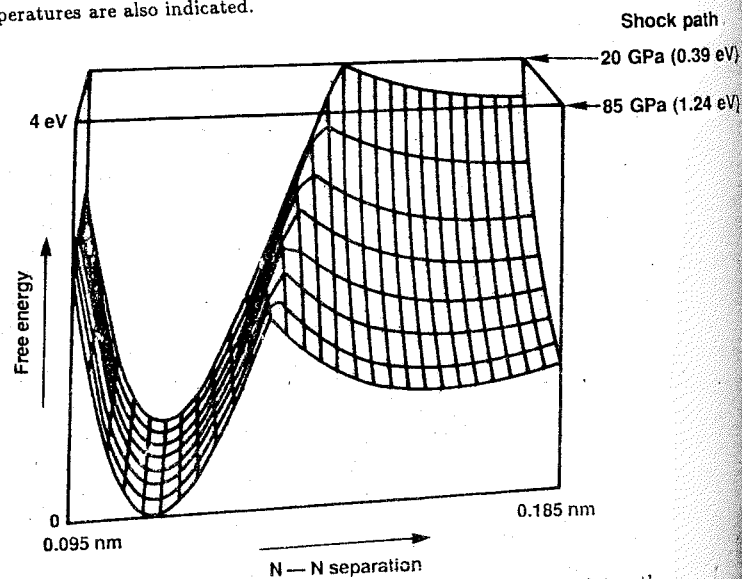


Fig. 2. Kinetic barrier for $\text{N}_2 \rightarrow 2\text{N}$ reaction along the Hugoniot path.

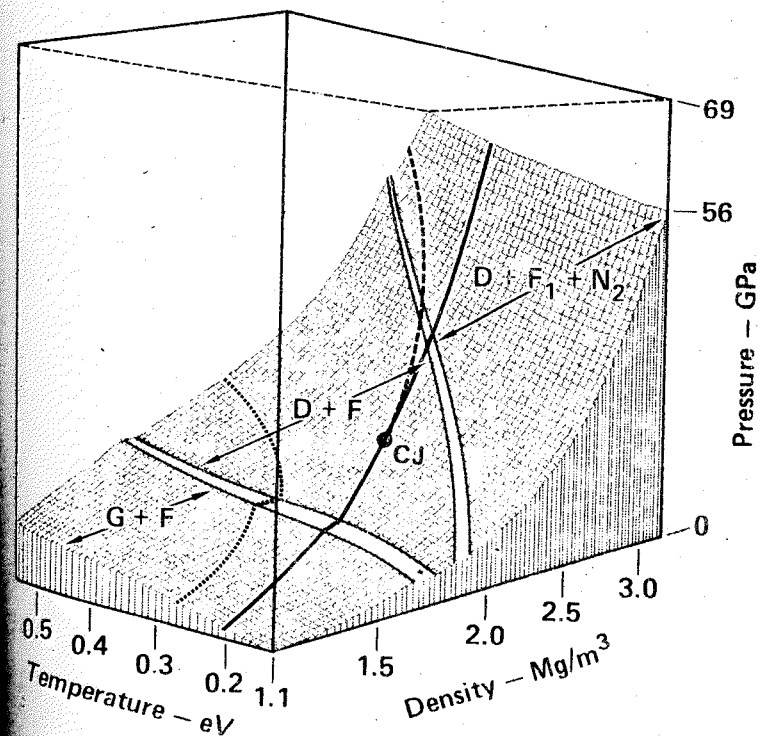


Fig. 3. Thermodynamic surface of detonation products of TNT. See the text for phase changes and thermodynamic paths indicated here.

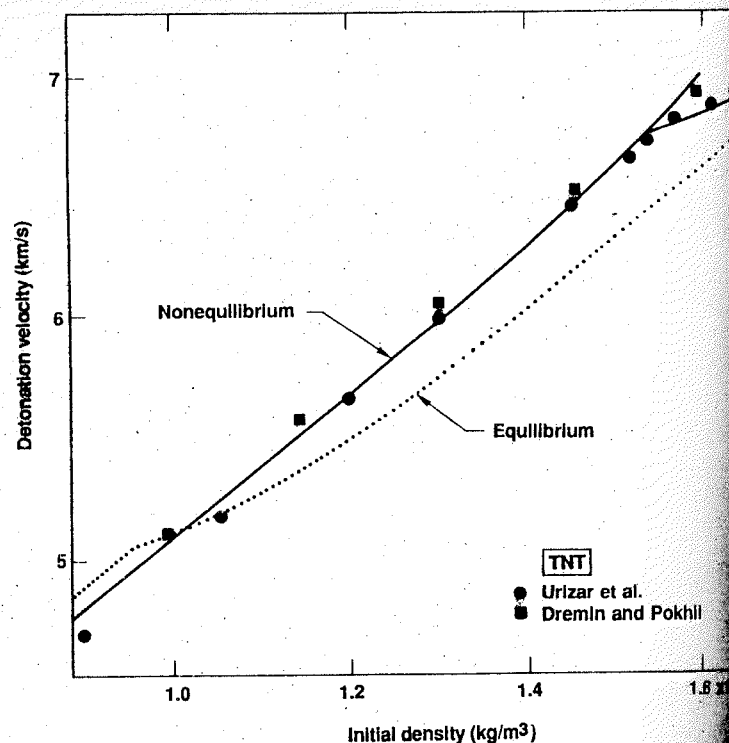


Fig. 4. Theoretical and experimental [3,4] detonation velocity vs. initial density of TNT.

The time (t_1) for 95 mole% destruction of amorphous carbon and the time (t_2) to convert it to 95 mole% diamond at 9GPa at different temperatures. These times are inferred from [14]. See the text.

Temperature (K°)	t_1 (sec)	t_2 (sec)
1000	7×10^{-2}	1.9×10^6
2000	2×10^{-1}	3.7×10^5
3000	2×10^{-3}	6.9×10^2
3500	5×10^{-3}	1.9×10^2
4000	4×10^{-6}	1.9×10^2

temperature. Application of our model shows that molecular nitrogen dissociates under the combined effects of high shock temperature and pressure. A simple model to estimate the energy barrier and the dissociation rate is used to interpret the experimental data. The model also predicts that detonation products can phase separate and that carbon microclusters in detonation products occur in a graphitic phase rather than in the thermodynamically more stable diamond phase.

Work performed under the auspices of the U. S. Department of Energy by the Lawrence Livermore National Laboratory under contract NO. W-7405-ENG-48.

References

1. Radousky, H. B., Nellis, W. J., Ross, M., Hamilton, D. C., and Mitchell, A. C., "Molecular dissociation and shock-induced cooling in fluid nitrogen at high densities and temperatures," *Phys. Rev. Lett.* (1986) **57**(19), 2419-2422; see references quoted therein.
2. F. H., "Supercritical fluid phase separations: implications for detonation properties of condensed explosives," *J. Chem. Phys.* (1986) **84**(10), 5845-5856.
3. Star, M. J., James, E. Jr., and Smith, L. C., "Detonation velocity of pressed TNT," *Fluids* (1961) **4**(2), 262-274.
4. Minin, A. N. and Pokhil, P. F., "The detonation wave parameters of trotyl, hexogen, glycerin and nitromethane," *Proc. Acad. Sci. USSR, Phys. Chem. Sec.* (1959) **4**, 839-841.
5. F. H., "Statistical mechanical theory of chemically reacting multiphase mixtures: application to the detonation properties of PETN," *J. Chem. Phys.* (1984) **81**(3), 1251-1261.
6. M., "Dissociation of dense liquid nitrogen," *J. Chem. Phys.*, to appear.
7. G. I. and Switendick, A. C., "Theory of molecular dissociation in shocked carbon and oxygen," in *Shock Waves in Condensed Matter*, ed. Y. M. Gupta (Plenum Press, New York, 1968), p. 95.
8. T. M. and Gubbins, K. E., *Applied Statistical Mechanics* (McGraw-Hill, New York, 1973), p. 32.
9. H. and Hamilton, D. C., to be published.
10. D. F. and Ree, F. H., "An estimate of the barrier to and rate of dissociation of nitrogen under shock conditions," to be published.
11. B. L., "Simulation of vibrational relaxation in dense molecular fluids. I," *J. Chem. Phys.* (1986) **84**(6), 3138-3146.
12. Thiel, M. and Ree, F. H., "Properties of carbon clusters in TNT detonation products: the graphite diamond transition," *J. Appl. Phys.* (1987), to appear.
13. Shukin, V. L., Korshak, V. V., Kudriavtsev, Yu P., Sladkov, A. M., and Stern, O., "On crystalline structure of carbyne," *Carbon* (1973) **11**(1) 70-72.
14. S.-I. Shimono, K., and Naka, S., "Diamond formation from glassy carbon under high pressure and temperature conditions," *J. Mat. Sci.* (1982) **17**(7), 1856-1862.

SUBSTANCE UNLOADING AFTER SHOCK COMPRESSION AND P,T DIAGRAMS

O.N. Breusov
Institute of Chemical Physics, the USSR Academy of Sciences, USSR

It is well known that many phase transformations have been accompanied by the hysteresis. Location of the hysteresis lines of direct and reverse /1,2/ transformations depends on chemical and phase purity, crystal structure perfection and experimental conditions, i.e. the rate of P,T parameters change and macro- and microplastic flow intensity under shock compression. Parameter change quickness is conducive to hysteresis zone broadening and plastic flow - to its narrowing. In fact, one deals with the extreme cases. Changes in the shapes of the shock adiabats, caused by the phase transformations, are often different under the same pressures, when the direct transformations of the static experiments are the same /3/. Many substances, especially those with dynamic yield strength, exhibit hysteresis zone broadening /4,5/.

This paper discusses the behaviour of a substance which is transformed into a high pressure phase under shock compression to the equal pressures but different temperatures (for example by shock compression with the different initial temperatures). The transformation cannot begin until the figurative point of substance finds the field outside the hysteresis zone independently on the transformation type - martensite or diffusional. When the shock adiabat will intersect the hysteresis line, which corresponds to the direct transformation, the transformation will occur and run the faster the higher the shock compression temperature. If the metastable part of the melting curve of the initial phase is in the field of high pressure stability, the curve determines the upper bound of possible low pressure phase existence. The condition for the occurrence of the metastable melting will depend on its viscosity, that is on the mobility of the positive atoms and groups. In favorable cases a material can be completely crystallized into the high pressure phase still during the high dynamic pressure action. However, the kinks on the shock adiabats can be conditioned not only by the fast crystallization, but also by the melting condensation owing to the change of only next coordination of atoms /4/.

The phase composition of recovered samples, after shock compression, depends on their phase composition under maximum

conditions during shock loading and also on unloading path. If the shock compression completely melts the substance and if the unloading path lies within the dynamic hysteresis zone and the initial state after unloading is within the static zone, the substance will remain amorphous. By a correct choice of experimental parameters, one can realize such a result for any substance, when the equilibrium phase line has a positive slope.

Even if the metastable melting of the initial phase and its complete or partial transformation into the high pressure phase is available, the unloading path within the hysteresis zone gives the generating part of this phase a chance for a complete recovery. However, this will not occur if residual temperatures are too high.

Thus, if the samples are unloaded at the same pressure and different temperatures, their transformation should be absent for initial temperatures and its yield should increase with temperature to a maximum value and then should decrease. The experimental results obtained in /6/ confirm this conclusion.

However, it is not the only way to produce a high pressure phase in recovered samples. If the melting unloading path passes inside the high pressure phase stability field but intersects the metastable melting line in the field of ordinary phase stability, the Ostwald's rule predicts that the metastable phase can be crystallized from the supercooled melting. This has been observed by detonation of an mixture of an explosive substance and a material with variable compositions and by quenching detonation products through adiabatic expansion /7/.

The pattern under consideration becomes fundamentally complicated by the fact that the shock compression is accompanied not only by the shock heating but by the occurrence of essential temperature inhomogeneities, both because of shock wave pattern combination of the recovery experiments and by the origination of layers between crystal blocks, which result from the initial phase fracture. However the last reason disappears at the moment of the stable or metastable melting of total volume of substance.

The experimental situation on the hysteresis in dynamical phase has been discussed in /8/. The information of the thermodynamic stability of the high pressure phase allows one to estimate positions of the reverse transformation lines.

References

1. Estrin E.I. Kinetics of the phase transformations under shock compression and high pressure phase synthesis. Problemy Metallovedeniya i Fizika Metallov. Metallurgiya, 1973, N2, p.6-13.
2. Estrin E.I. Some problems of the phase transformations under high pressure. Problemy Metallovedeniya i Fizika Metallov. Metallurgiya, 1975, p.28-29.
3. Altshuler L.V. Transformations mechanisms behind the shock wave front. Detonazija. Kriticheskiye javleniya. Fiziko-khimicheskiye prevrashcheniya v udarnykh volnakh, 1978, p.119-122.
4. Ananjin A.V., Breusov O.N., Dremin O.N., Pershin S.V., Tatev V.F. Shock wave influence on silicon dioxide. Kvarz. Fizika gorenija i vzryva. 1974, N3, p.426-436.
5. Kutsar A.R., German V.N. Phase composition and titanium structure after shock-wave compression. Fizika impul'snikh davleniy. VNIIFTRY, 1979, vypusk 44 (74), p.166-170.
6. Adadurov G.A., Bavina T.V., Breusov O.N. Thermal activation of the phase transformation of graphite-like boron nitride into dense modifications by quasiisentropic dynamic compression. Fizika gorenija i vzryva, 1981, N2, p.159-161.
7. Breusov O.N., Drobyshhev V.N. For problem of metastable phase formation of the variable composition under shock compression. J. Neorganicheskoi khimii, 1979, N11, p.3128-3133.
8. Pjaternev S.V., Pershin S.V., Dremin A.N. Dependence of graphite-diamond transformation by shock pressure initiation on initial graphite dense and hysteresis line of this transformation. Fizika gorenija i vzryva, 1986, N6, p.125-130.

VIBRATIONAL SPECTROSCOPY OF SHOCK-COMPRESSED FLUID N_2 AND O_2 *

C. Schmidt, D. S. Moore, M. S. Shaw, and J. D. Johnson
 Los Alamos National Laboratory
 Los Alamos, NM, 87545, USA

Single-pulse multiplex coherent anti-Stokes Raman scattering (CARS) was used to observe the vibrational spectra of liquid N_2 shock-compressed to several pressures and temperatures up to 41 GPa and 5200 K and liquid O_2 shock-compressed to several pressures and temperatures up to 10 GPa and 1000 K. For N_2 , the experimental spectra were compared to synthetic spectra calculated using a semi-empirical model for CARS intensities and estimated vibrational frequencies, peak susceptibilities, and Raman line widths. The question of excited state populations in the shock-compressed state is addressed.

Recently the high-pressure, high-temperature behavior of N_2 and O_2 has received considerable attention. Several dynamic [1-7] and static [8-16] experiments have produced equation of state and thermodynamic data for N_2 at pressures up to 130 GPa and at elevated temperatures to beyond 10,000 K and for O_2 at pressures up to 140 GPa and to temperatures beyond 10,000 K. These measurements have been complemented by calculations which describe the thermodynamic state of the solid [17,18] or the fluid [19-23]. An increase in compressibility along the Hugoniot at pressures above 30 GPa has been attributed [18,19,23] to dissociation. The intramolecular stretching frequencies for solid N_2 [12,24,25] and for liquid N_2 [13,26-28] have been measured and calculated [29,30] using a perturbation analysis in conjunction with appropriately chosen intra- and intermolecular potential functions [22,23]. Vibrational frequencies have also been measured for fundamental and some excited-state transitions of fluid N_2 at pressures and temperatures up to 34 GPa and 4400 K [11,31]. Recently Monte Carlo techniques using a model based on a sphericalized potential [33], have been used to calculate the N_2 vibrational frequency at pressures and temperatures up to 34 GPa and 4400 K respectively. There have, however, been no measurements or calculations of the vibrational frequencies of N_2 under the auspices of the Department of Energy.

tions of O_2 vibrational frequencies in the dense-fluid state. Such results at higher pressure/temperature data for N_2 would be of value both to characterize the intramolecular potential functions of these molecules and possibly to verify directly the existence of dissociation. Measurements of ground- and excited-state vibrational-transition intensities could also provide an upper limit estimate for dense-phase fluid-vibrational relaxation times [34,35].

Reported here are coherent anti-Stokes Raman scattering (CARS) measurements for N_2 and O_2 shock-compressed to 41 GPa and 10 GPa, respectively. The pressure and temperature states were achieved by dynamic compression techniques using an experimental apparatus described previously [36,37]. Briefly, a projectile launched by a two-stage light-gas gun dynamically compressed a liquid N_2 or O_2 sample that had been condensed in a cryogenic target assembly. The target was designed to reflect the CARS signal from a highly polished 304 stainless steel target plate at the front through a 6.3-mm-diam quartz or lithium fluoride window at the rear. Impactor and target plate thicknesses were chosen, and the assemblies were installed in the ~1.5-mm-long liquid sample, so as to insure that rarefaction waves would not compromise the one-dimensional character of the compression in the region observed optically. Single shock velocities were conservatively measured to ± 0.2 km/s and the initial pressure and temperature of the liquid sample were determined to ± 0.1 GPa and ± 1 K respectively. Initial sample densities of N_2 and O_2 were taken from Jacobsen, et al. [38] and Weber [39], respectively. The samples were condensed from gaseous N_2 (purity greater than 99.9%) and gaseous O_2 (purity greater than 99.6%).

A Nd:YAG laser was used to pump the two dye lasers used to generate the CARS signal. The laser dye DCM was used in the broadband dye laser to produce Stokes frequencies from 630 nm to 650 nm. The pump frequency in the CARS process was obtained by using approximately 40% of the Nd:YAG laser output to pump a narrow-band dye laser (Quanta-Ray PDL-1) at near 557 nm for N_2 experiments and at 582 nm for O_2 experiments. Multi-channel detection of the CARS signals was achieved using an intensified photodiode array (Tracor Northern Model 6132) and analyzed with a spectrum analyzer (Tracor Northern Model 6500). In addition, the broadband dye laser spectral profile was measured in each experiment using another one-meter spectrometer.

either a photodiode array (Reticon Model RL512S) and a transient digitizer (Data Translation Model 805) or a Princeton Instruments OSMASystem.

Pressures and temperatures, as given in Figs. 1 and 2 for the singly and doubly shocked regions, were calculated using an effective spherical potential [14,23] that has been shown to reproduce accurately both nonspherical molecular dynamics simulations and experimental Hugoniot and brightness temperature data for N_2 . Taking into account the accuracy of the method for N_2 , and the similarity of potentials for N_2 and O_2 an effective spherical potential for O_2 was fit directly [7] to Hugoniot data [6] and was checked by its good fit to reflected shock data [6]. In this work, doubly-shocked states are inferred from impedance matching of the initial shock, at the measured shock velocity, reflecting off the known window material assuming the theoretical equation of state for N_2 or O_2 . The equation of state parameters for quartz and lithium fluoride are from published data [40]. Based on the previously stated experimental errors, estimated uncertainties in pressure are about ± 1 GPa for principal Hugoniot measurements and ± 2 GPa for reflected shocks. These uncertainties are dominated by the experimental uncertainty in the shock velocity. Temperature uncertainties are dominated by a systematic shift of up to 10 percent depending on the theoretical model chosen [17,20].

CARS [41-46] occurs as a four-wave parametric process in which three waves, at a pump frequency, ω_p , and one at a Stokes frequency, ω_s , are mixed in a sample to produce a coherent beam at the anti-Stokes frequency, $\omega_{as} = 2\omega_p - \omega_s$. The efficiency of this mixing is greatly enhanced if the frequency difference, $2\omega_p - \omega_s$, coincides with the frequency of a Raman active mode of the sample. The intensity of the beam at ω_{as} is given by

$$I_{as} \propto \sum_j \frac{\omega_{as}^2 I_p^2 I_s (N_1 L_1)^2}{n_p^2 n_s n_{as}} \left(\frac{n_{as}^2 + 2}{3} \right)^2 \left(\frac{n_s^2 + 2}{3} \right)^2 \left(\frac{n_p^2 + 2}{3} \right)^4$$

$$\left[\left(\sum_j \frac{\Gamma_j \chi_j^{pk} (\omega_j - \omega_p + \omega_s)}{(\omega_j - \omega_p + \omega_s)^2 + \Gamma_j^2} + \chi^{NR} \right)^2 + \left(\sum_j \frac{\Gamma_j^2 \chi_j^{pk}}{(\omega_j - \omega_p + \omega_s)^2 + \Gamma_j^2} \right)^2 \right] \quad (1)$$

and

$$\Gamma_j \chi_j^{pk} \frac{h}{2\pi c} \omega_p \omega_s^3 = \left(\frac{d\sigma}{d\Omega} \right)_j (\rho_j - \rho_k)$$

where h is Planck's constant, c is the speed of light, and n_{as} , n_s , and n_p are the refractive indices at ω_{as} , ω_s , and ω_p , respectively. I_p and I_s are the incident intensities of the pump and Stokes beams respectively. $N_i L_i$ corresponds to the Lagrangian density of the i th layer, and the sum is over non-interfering layers. χ^{NR} is the non-resonant susceptibility, χ_j^{pk} is the peak third order susceptibility, Γ_j is the half width at half maximum (HWHM) linewidth, and $(d\sigma/d\Omega)_j$ is the spontaneous Raman cross-section of the j -to- k vibrational transition. ρ_j is the number density in vibrational level j . The sum on j is over transitions. Equations (1) and (2) hold only in the case of no electronic resonance enhancement [42].

Phase-matching is assumed to be experimentally optimized in the sample for the focusing conditions used. The dispersion in the N_2 sample is assumed to scale linearly with the increase in refractive index due to compression according to the empirical relation $n = 1.22 + 0.52(1-V/V_0)$. V/V_0 is the relative volume due to compression and 1.22 is the approximate index of refraction of ambient liquid N_2 [48,49]. Linear scaling of the dispersion results in the same phase-matching angle at all compressions. These refractive indices are also used in the local-field-correction terms of Eq. (1).

Wavelength calibrations ($\pm 2 \text{ cm}^{-1}$) were all done using vacuum wavelength atomic emission lines [50]. For the N_2 experiments, the narrowband dye laser was placed near or in coincidence with the 17947.4 cm^{-1} transition of the intensified-diode array that detects CARS signals was calibrated using the 19931.9 cm^{-1} and 20311.6 cm^{-1} transitions of He and the 19844.6 cm^{-1} transition of Ne, or the 19882.0 cm^{-1} and 20641.3 cm^{-1} transitions of Xe. For the O₂ experiments, the narrowband dye laser was placed in coincidence with the 17111.4 cm^{-1} transition of Ne, and the intensified-diode array was calibrated using the 18753.8 cm^{-1} and 18511.4 cm^{-1} transitions of Ne. For both sets of experiments

a broadband-dye-laser spectral profile was calibrated against either the 1515.2 cm^{-1} and 15662.3 cm^{-1} or 15782.4 cm^{-1} and 15364.9 cm^{-1} transitions of Ne. A spectral slit function of the spectrometer/intensified-diode-array combination was measured using the 19931.9 cm^{-1} line of He and an $100\text{-}\mu\text{m}$ -wide entrance slit. A good representation of this slit function was obtained by use of a 10 cm^{-1} FWHM triangle. The spectral profile of the narrowband laser was accurately measured and was fit best by a Gaussian with 1.3 cm^{-1} width at $1/e$ -amplitude.

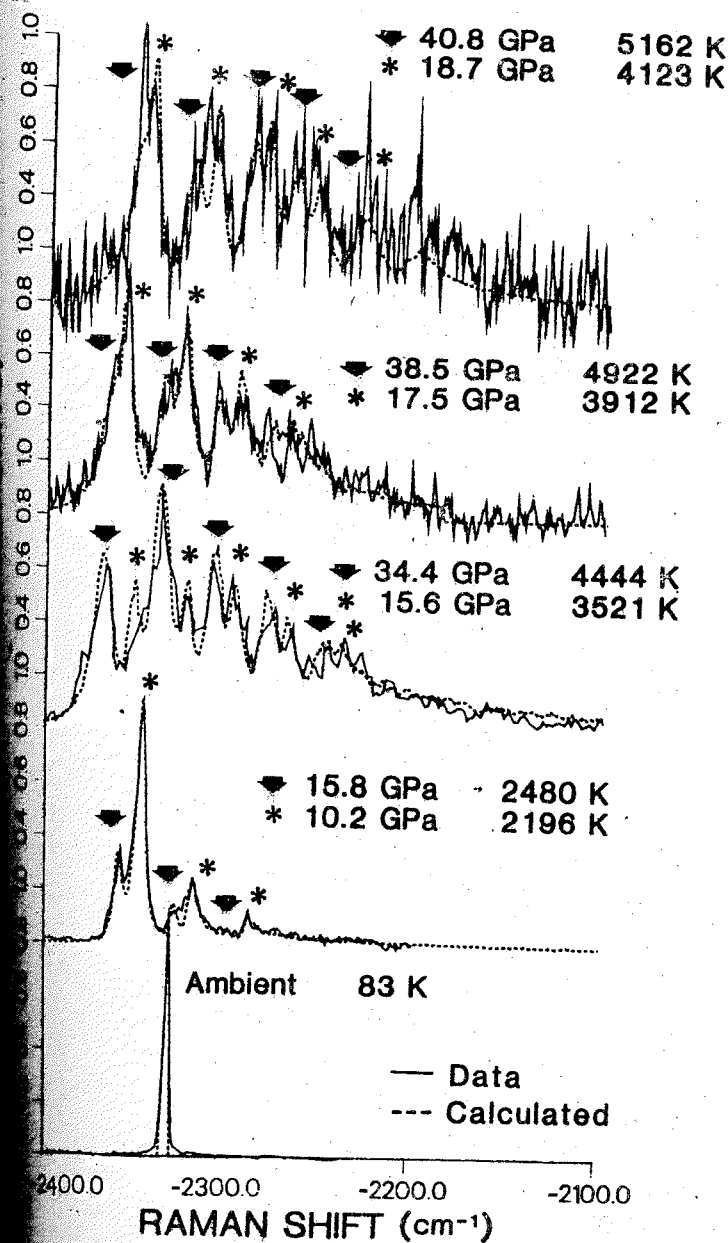
The observed single-pulse CARS spectra of ambient pressure and eight (four experiments) dynamically-compressed states of liquid nitrogen are shown in Fig. 1. Also shown are preliminary calculations of synthetic spectra made using Eq. (1). Because of timing constraints and the desire to have no unshocked sample at the time the laser pulses arrived, the shockwave in the experiments has been let off of the rear window back into the once-shock-compressed sample, leaving a doubly-shocked region. Because the ambient liquid N_2 Raman linewidth is sufficiently narrow [51-53] and because the line broadening with pressure is not here to be sufficiently slow, spectral features from both the singly- (marked in Fig. 1 by asterisks) and doubly- (arrows) shocked regions are clearly visible.

Previous observations by Reichlin, et al. [12] for solid N_2 show that the Raman frequencies tend to first increase and then decrease with increasing pressure. Visual inspection of the data in Fig. 1 suggests this same phenomenon occurs at Hugoniot conditions, only with the reversal occurring at much higher pressures. This behavior has been suggested by the calculations of Etters, et al. [32] and LeSar [33]. The data are presently being analyzed using techniques discussed previously [31] to obtain more accurate values for transition frequencies, peak Raman susceptibilities, and Raman line widths.

Experimental results [34,35,54,55] show that the dense-fluid- N_2 vibrational relaxation time decreases from greater than 7 ns at atmospheric pressure to approximately 0.2 ns at 0.3 GPa. Because these times are long it is unclear whether the shock pressures and temperatures shown in Fig. 1, the relaxation

time will decrease sufficiently rapidly (to ≈ 50 ns) to enable equilibration of the vibrational levels in the shock-compressed region interrogated by CARS. It is also unclear what effect impurities will have on the density dependence of the relaxation time [34,35]. Ratios of Eq. (2) for excited-state to fundamental transitions for the lower pressure data [31] were used to explore the possibility of a non-Boltzmann population distribution for the excited states. The right-hand-side ratios were calculated using the harmonic oscillator approximation of the variation of the Raman cross section with vibrational level, $(d\sigma/d\Omega)_{j \rightarrow j+1}$, and assuming a Boltzmann distribution for ρ_j . For these transitions, ratios of the left side determined using previous experimental values [31] agree with the values calculated for the right-hand side. This suggests that, subject to the stated approximations, vibrational equilibration occurs faster than expected at these pressures and temperatures. However, because of the large uncertainties in the experimental quantities [31], particularly the peak third-order susceptibilities and the Raman half-widths, this conclusion does not yet merit a definitive statement. We are presently doing similar calculations for the higher-pressure data.

The observed single-pulse CARS spectra of ambient pressure and five experiments) dynamically-compressed states of liquid oxygen are shown in Fig. 1. For the higher-pressure data in these experiments, the shock wave had not reached the rear window of the target assembly. Hence only the singly-compressed (asterisks) and ambient-pressure (unlabeled) states are observed spectrally. We are presently analyzing these data using the semiclassical model, Eq. (1), for CARS intensities. Because a possible absorption [26,27,56], due to either the van der Waals interaction-induced or a collisionally-induced transition at the frequencies of the CARS lasers, could dramatically influence the third-order susceptibility in Eq. (1) [45], it is first necessary to perform an absorption experiment at the pressures and temperatures of interest. Such measurements are in progress. A visual inspection of the data, however, suggests that, for the N_2 results given in Fig. 1, a nonlinear increase with pressure is evident for the O_2 0-1 transition frequency.



Experimental and computed spectra for high pressure and temperature N_2 .

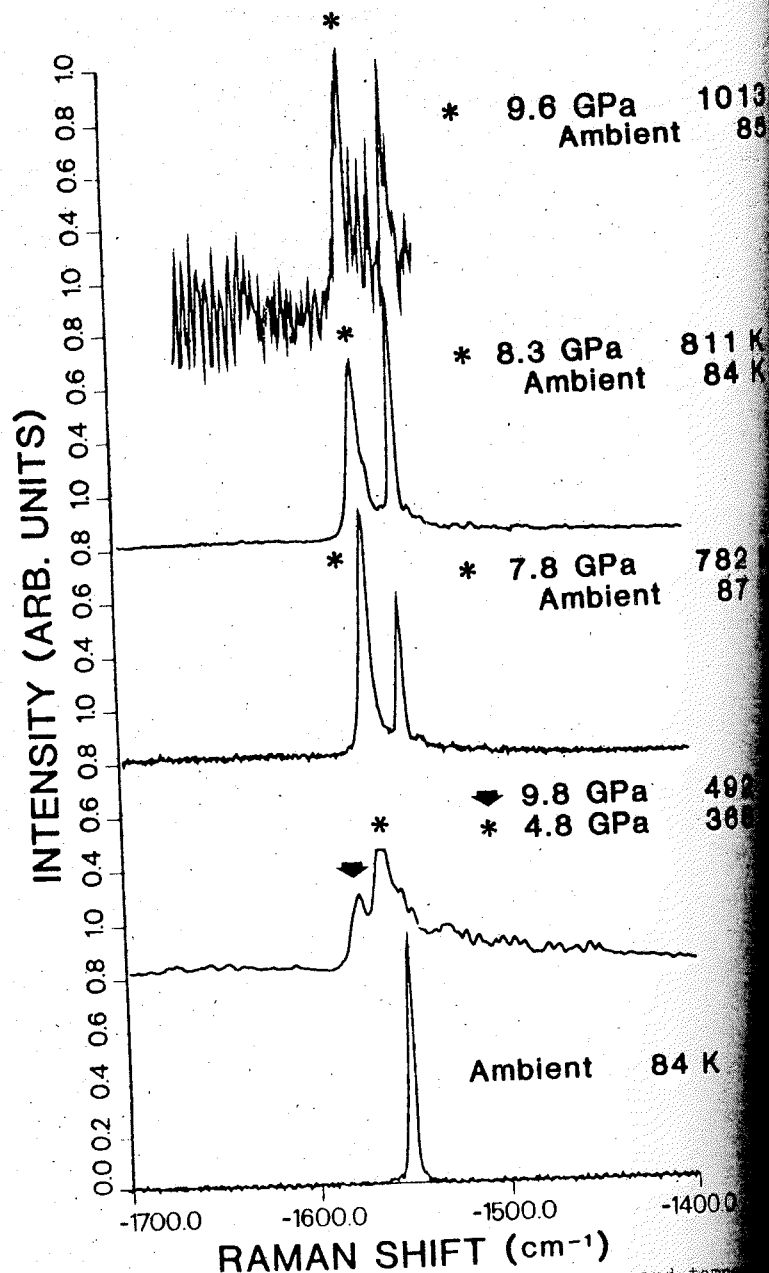


Fig.2. Experimental spectra for high pressure and temperature.

In summary, the observation of vibrational transitions of the N_2 and O_2 , at pressures up to 41 GPa (5200 K) and 17 GPa (1000 K) respectively, suggests that under these conditions, N_2 and O_2 still exist as molecular fluids. Visual inspection of the N_2 and O_2 spectral data suggests that for both molecules the vibrational frequencies initially increase with increasing pressure along the adiabat, but at higher pressures this trend is reversed. This would indicate a narrowing and then a broadening of the intramolecular potential function. At higher vibrational states in N_2 are excited in <50 ns. Within the limits of the approximations used and the experimental error, thermal equilibration of the levels is suggested.

ACKNOWLEDGMENTS

The authors wish to thank John Chavez, John Chacon, Rick Eavenson, James F. Joseph, Joseph Fritz, Concepcion Gomez, Vivian Gurule, Robert Livingston, Janet David O'Dell, George Pittel, Dennis Price, Terry Rust, and Dennis Shampine for their invaluable work in obtaining the results presented in this paper. The authors are especially grateful to J. W. Shaper for his encouragement and support of this work.

REFERENCES

1. Zubarev and G. S. Telegin, *Sov. Phys. Dokl.* **7**, 34 (1962).
2. Dick, *J. Chem. Phys.* **52**, 6021 (1970).
3. Nellis and A. C. Mitchell, *J. Chem. Phys.* **73**, 6137 (1980).
4. Nellis, N. C. Holmes, A. C. Mitchell, and M. van Thiel, *Rev. Lett.* **53**, 1661 (1984).
5. Radousky, W. J. Nellis, M. Ross, D. C. Hamilton, and A. C. Mitchell, *Rev. Lett.* **57**, 2419 (1986).
6. Barle, W. L. Seitz, and J. C. Jamieson, in "Behavior of Dense Media at High Dynamic Pressure," (Gordon and Breach, New York, 1968), p. 85.
7. Schott, M. S. Shaw, and J. D. Johnson, *J. Chem. Phys.* **82**, 4264 (1985).
8. Schuch and R. L. Mills, *J. Chem. Phys.* **52**, 6000 (1970).
9. Mills, D. H. Liebenberg, and J. C. Bronson, *J. Chem. Phys.* **63**, 4026 (1975).

10. D. Schiferl, D. T. Cromer, and R. L. Mills, *High Temp. High Pressures* **10**, 493 (1978).
11. A. S. Zinn, masters thesis "Raman Spectroscopy and Melting of Nitrogen at 4.5 GPa and 290 K and the Growth of a Single Crystal of ϵ Oxygen," University of California at Los Angeles, 1986.
12. R. Reichlin, D. Schiferl, S. Martin, C. Vanderborgh, and R. L. Mills, *Phys. Rev. Lett.* **55**, 1464 (1985).
13. M. Nicol, K. R. Hirsch, and W. B. Holzapfel, *Chem. Phys. Lett.* **68**, 49 (1979).
14. H. S. Armstrong, W. B. Holzapfel, and M. Nicol, *J. Phys. Chem.* **85**, 13 (1981).
15. D. Schiferl, D. T. Cromer, and R. L. Mills, *Acta Cryst.* **B37**, 1329 (1981).
16. D. Schiferl, D. T. Cromer, L. A. Schwalbe, and R. L. Mills, *Acta Cryst.* **B39**, 153 (1983).
17. R. LeSar, *J. Chem. Phys.* **81**, 5104 (1984).
18. A. K. McMahan and R. LeSar, *Phys. Rev. Lett.* **54**, 1929 (1985).
19. F. H. Ree and N. W. Winter, *J. Chem. Phys.* **73**, 322 (1980).
20. M. Ross and F. H. Ree, *J. Chem. Phys.* **73**, 6146 (1980).
21. R. Grover and F. H. Ree, in *High Pressure in Research and Industry*, edited by C.-M. Backman, T. Johansson, and L. Tegner (Artkitektkopia, Uppsala, Sweden, 1982), p. 217.
22. M. S. Shaw, J. D. Johnson, and B. L. Holian, *Phys. Rev. Lett.* **50**, 1141 (1983).
23. J. D. Johnson, M. S. Shaw, and B. L. Holian, *J. Chem. Phys.* **80**, 1279 (1984).
24. F. D. Medina and W. B. Daniels, *J. Chem. Phys.* **64**, 150 (1976).
25. R. LeSar, S. A. Ekberg, L. H. Jones, R. L. Mills, L. A. Schwalbe, and D. Schiferl, *Solid State Comm.* **32**, 131 (1979).
26. K. Syassen and M. Nicol, in *Physics of Solids Under High Pressure*, edited by J. S. Schilling and R. N. Shelton (North-Holland Publishing Co., Amsterdam, 1987), p. 33.
27. M. Nicol and K. Syassen, *Phys. Rev. B* **28**, 1201 (1983).
28. B. I. Swanson, S. F. Agnew, L. H. Jones, R. L. Mills, and D. Schiferl, *J. Phys. Chem.* **87**, 2463 (1983).
29. R. D. Etters and A. A. Helmy, in *Physics of Solids Under High Pressure*, edited by J. S. Schilling and R. N. Shelton (North Holland, Amsterdam, 1981), p. 39.
30. R. D. Etters and A. Helmy, *Phys. Rev. B* **27**, 6439 (1983).
31. S. C. Schmidt, D. S. Moore, and M. S. Shaw, *Phys. Rev. B* **35**, 493 (1987).
32. R. D. Etters, J. F. Belak, and R. LeSar, to be published, *Phys. Rev. B*.
33. R. LeSar, *J. Chem. Phys.* **86**, 4138 (1987).
34. M. Châtelet, J. Kieffer, and B. Oksengorn, *Chem. Phys.* **79**, 413 (1983).
35. M. Châtelet and J. Chesnoy, *Chem. Phys. Lett.* **122**, 550 (1985).
36. D. S. Moore, S. C. Schmidt, and J. W. Shaner, *Phys. Rev. Lett.* **50**, 1819 (1983).
37. S. C. Schmidt, D. S. Moore, D. Schiferl, M. Châtelet, T. P. Turner, J. W. Shaner, D. L. Shampine, and W. T. Holt, in *Advances in Chemical Reaction Dynamics*, edited by P. M. Rentzepis and C. Capellas (D. Reidel Publishing Co., Dordrecht, Holland, 1986), p. 425.
38. R. T. Jacobsen, R. B. Stewart, R. D. McCarty, and H. J. M. Hanley, *National Bureau of Standards Technical Note* 648 (1973).
39. L. A. Weber, *J. Res. Nat. Bur. Stand. (U.S.)* **74A**, 93 (1970).
40. S. P. Marsh, *LASL Shock Hugoniot Data* (University of California Press, Berkeley, California, 1980); W. J. Carter, *High Temp. High Pressures* **5**, 313 (1973).
41. J. W. Nibler and G. V. Knighten, in *Raman Spectroscopy of Gases and Liquids*, edited by A. Weber (Springer-Verlag, Berlin, 1979), p. 253.
42. P. D. Maker and R. W. Terhune, *Phys. Rev.* **137**, A801 (1965).
43. M. Bloembergen, H. Lotem, and R. T. Lynch Jr., *Indian J. Pure Appl. Phys.* **16**, 151 (1978).
44. M. Bloembergen, *Nonlinear Optics* (W. A. Benjamin, Reading, MA, 1965).
45. A. J. Druet and J. P. E. Taran, *Prog. Quant. Electr.* **7**, 1 (1981).
46. B. Roh, P. W. Schreiber and J. P. E. Taran, *Appl. Phys. Lett.* **29**, 174 (1976).
47. L. Vedam, in *Critical Reviews in Solid State and Materials Sciences*, edited

- by D. E. Schuele and R. W. Hoffman (CRC Press, Boca Raton, FL, 1983).
48. J. F. Ely and G. C. Straty, J. Chem. Phys. 61, 1480 (1974).
 49. Handbook of Chemistry and Physics, edited by R. C. Weast (Chemical Rubber Company, Cleveland, OH, 1965).
 50. M.I.T. Wavelength Tables, (The MIT Press, Cambridge, MA, 1982) Volume 1.
 51. W. R. L. Clements and B. P. Stoicheff, Appl. Phys. Lett. 12, 246 (1968).
 52. M. J. Clouter and H. Kieft, J. Chem. Phys. 66, 1736 (1977).
 53. S. A. Akhmanov, F. N. Gadzhiev, N. I. Koroteev, R. Yu. Orlov, and I. L. Shumai, JETP Lett. 27, 243 (1978).
 54. C. Manzanares and G. E. Ewing, J. Chem. Phys. 69, 1418 (1978).
 55. D. W. Chandler and G. E. Ewing, J. Chem. Phys. 73, 4904 (1980).
 56. C. A. Long and G. E. Ewing, J. Chem. Phys. 58, 4824 (1973).

THE EXPLOSIVE WORKING OF MATERIALS IN THE USSR

A.A. Deribas

Special Design Office of High Rate Hydrodynamics,
Siberian Division of the USSR Academy of Sciences,
Novosibirsk, USSR

I. INTRODUCTION

The studies of the processes related to working the materials with explosive energy were initiated in the Soviet Union during the Second World War II. The process of armour piercing by shaped charges developed at the beginning of the XX-th century in the United States and in Germany was investigated. The investigations were carried out by a research team of Academician M.A. Lavrentiev in Kiev in 1946 and several modifications of the explosive welding phenomenon were detected /1/. In the mid-fifties, investigation of explosive powder compaction were begun in Moscow by Professor Yu.N. Izrael /2/. In the early sixties, M.A. Lavrentiev undertook a large-scale research program on explosive hardening and welding in Novosibirsk /1/. Later, explosive powder compaction was also included into the research program /3/. The first attempts to investigate the strength of the explosive chambers relate to the same period /4/.

The main research trends in the field of explosive hardening, explosive welding and powder compaction will be reviewed below and their main applications will be discussed.

2. HARDENING

The idea of explosive hardening was first suggested in the late 1950s /5/. Contact charges of plastic explosives, providing the detonation front pressure of the order of 20 GPa, are used for metal hardening. If the detonation front moves along the surface to be hardened, the pressure in the shock wave propagating in the metal is also of the order of 20 GPa; if the flat detonation front is normal to the surface to be hardened, pressure in the refracted shock wave will be about twice as great as with the contact one. The action of the actual charges of up to 10 mm thickness proceeds during several microseconds, the layer thickness wherein mechanical properties are appreciably modified varies from 10 to 50 mm. Fig. 1 presents different arrangements for explosive hardening of materials. Shock wave action on metals and

alloys results in their hardening, i.e. their hardness, yield strength and ultimate strength increase, while their plasticity and impact strength decrease. The Table contains values of different parameters characterizing hardening of different steels by different explosive treatments. Note, that the geometry of the charge should be chosen in practice in such a way as to minimize the residual deformation and to avoid destruction of the part by release waves. It is recommended that the surface of the part contacting the explosive charge be under the conditions wherein it will be compressed from all directions simultaneously.

2.I. High-manganese steel

The explosive hardening method was first tested on austenitic high-manganese steel 113J (Hadfield steel) [5]. At present, industrial hardening of railway frogs using different modifications of the arrangement presented in Fig.2 is carried out in the USA and Canada. The service life augmentation is highly dependent upon the steel grade and castings quality and varies within 1400%; lower quality parts are sorted out.

Other parts, namely, dipper teeth, linings of the crushing mills and some others made from high-manganese steel are also explosively worked in the USSR along with the railway frogs. Their wear resistance increase is approximately the same.

All over the world the tendency is to use more and more ores which results in increased amount of rock masses worked making urgent the problem of increase in wear resistance of working parts of mining machines. These are made from high-manganese steel now and the situation will hardly change in the near future. Hence, there are favorable prospects for wider application of explosively hardened articles from high-manganese steel. In fact, there are no alternatives as concerns hardening parts of this kind.

2.I.I. Explosive and thermal treatment (ETP)

By seventies, an important improvement was introduced in the method of explosive hardening of high-manganese steel. The shock wave action results in increase in strength and decrease in plasticity of the material. The changes in these mechanical properties are caused by lattice defects saturation in the bulk of the material under treatment. To avoid the plasticity decrease, a special thermal treatment was suggested providing for the final

structure: the defects could nucleate new grains and to provide plasticity and impact viscosity increase under low temperature. The Table presents mechanical properties of high-manganese steel following the explosive and thermal treatment and in Fig.2 impact viscosity is plotted against temperature. The optimization of mechanical properties is evident which provides for considerable service advantages.

Material	State	$\sigma_{0.2}$, MPa	σ_b , MPa	δ , %	ψ , %	Impact viscosity, MJ/m ²
Hadfield steel	Initial	435	875	36	33	2.7
	20 GPa	730	1025	31	28	1.9
	ETP*	475	975	46	31	2.7
Low-carbon steel	Initial	325	540	21	-	I2
	5 GPa+TE ³⁰⁰	390	610	19.6	-	I5
	10 GPa+TE ³⁰⁰	365	565	24	-	I0
	Fine-grained ⁰ 10 GPa	473	600	15	-	I9
Stainless steel	Initial	350-450	600-700	30-40	39	-
	9 GPa	610	720	35	31	-
	12 GPa ³⁰⁰	790	880	20	25	-
	13 GPa ³⁰⁰	790	880	20	30	-
	20 GPa	1120	1200	10	10	-
	40 GPa	1440	1540	6	-	-
	5 GPa ³⁰⁰	830	860	4	-	-

* - explosive and thermal treatment (20 GPa + water quenching at 1050 °C)

TE³⁰⁰ - thermal treatment at 700 °C for 30 min.

TE³⁰⁰ - triaxial shock waves

TE³⁰⁰ - afterflow

TE³⁰⁰ - water quenching at 900 °C, tempering at 700 °C for 30 min.

TE³⁰⁰ - hardening of other materials

The effects of shock waves on mechanical properties of different materials and alloys are intensely studied at the research institute of the Siberian Branch of the USSR Academy of Sciences. Results of hardening studies of different steels are presented in Table 1. Some results on low-carbon and stainless steels are given in Table 2. The creep of a number of Ni-based superalloys was studied, the curves prior and following the hardening process.

ture are given in Fig.3. At operating temperatures, an increase in service life of the loaded specimen by a factor of 7-8 is stated which is explained by elimination of zones free from precipitates and ceramic particles providing for hardening of the alloy lattice and to their uniform deposition on defects generated by the shock.

In /7/ an attempt was undertaken to integrate the results relating to hardening metals and alloys by shock waves and to formulate universal correlations characteristic of the hardening process: an increase in hardness and yield point as determined by the ratio of pressure at the shock wave front to the shear modulus of the material to be hardened. It can be seen from the curves that in principle there is a possibility to significantly increase the yield point and hardness of many metals and alloys in wide use.

3. EXPLOSIVE WELDING

As mentioned above, the studies of the explosive welding in the USSR were initiated by the team of Academician M.A.Lavrenko in 1944-1946. By now, a great number of papers and monographs and /9/ appeared in different countries wherein physical and mechanical regularities of the process are analyzed whose numerous applications are used industrially in many countries.

3.1. Basic physical and mechanical characteristics of the process

Fig.4 presents the most common explosive welding arrangement. Along with the initial parameters (explosive charge weight, magnitude determining the acceleration path of the elements, etc.) here are indicated the main dynamical parameters determining the collision regime: contact point velocity v_k and collision angle γ . At present all these parameters are measured accurately enough in experiments and there are design formulas relating them with the initial parameters of the welding.

Numerous studies have shown the knowledge of v_k and γ as a first approximation to be sufficient for determining the welding area of a definite pair of metals to be welded. In the v_k - γ plane the welding area can be represented in the following way (Fig.5 /1/). According to the present day knowledge there is a lower welding boundary and the most sound welds containing a maximum quantity of melts occur near this boundary. The weld surface can be both wavy and waveless; in both cases, however, the weld strength is in excess of the weaker of the metals because welding in the vicinity of the lower boundary is carried out by the minimum quantity of the explosive, so that the heat

is obtained in an economical way, it is quite natural that considerable efforts of scientists are directed to theoretical and experimental determination of the lower boundary. Studies /10/ and /11/ have much contributed in this as concerns some important metal combinations. In /10/ a hypothesis was suggested according to which the lower welding boundary is due to the substance flow preceding the contact point providing for self-cleaning of the surfaces to be bonded. Lately, the lower boundary position was determined theoretically and the theoretical results obtained have shown a good agreement with experimental data for a number of metal combinations. In future, main physical parameters determining the actual bonding process in the vicinity of the contact point, such as pressure, temperature and others should be determined more precisely. Of special interest are those parameters which are somehow related to parameters γ and v_k .

3.2. Metallographic examinations

The 25-year period of explosive welding research resulted in several hundreds of different metal combinations obtained. Metallographic examinations of the bonding zone carried out by different authors shows the bonds obtained to fall into two great groups. Examinations of the intermediate layer adjoining the interface serve to identify a particular metal combination. This layer is formed during the welding process of several microseconds duration and its thickness varies from several hundreds of microns to fractions of a micron. The layer is difficult to investigate due to its small thickness; it is studied mainly by means of microprobes. If the materials bonded do not form chemical compounds, there are different concentrations of one material contained into another independently on their mutual solubility under usual conditions. Bonding occurs both in case of extremely low mutual solubility of the materials and in case of their actual insolubility. If the materials bonded can form chemical compounds, the intermediate layer contains them in different proportions covered by all possible compounds. As a rule, these metals are not able to join by usual methods due to appearance of intermediate intermetallics which are brittle and deteriorate mechanical properties of the welds. Explosive welding results in extremely thin, non-uniform intermetallic layers which are not so harmful as in conventional welding. In a number of practically important cases, as, for instance, in case of "steel + titanium"

and "steel + aluminium" combinations, the bond strength may be in excess of the weaker of the two metals.

The crystalline structure of the intermediate layer remains unclear. There were suggestions that the metal contained in the layer is in amorphous state /12/; however, the technique used in the study could not give sufficient support to the idea.

At present much discussed is the problem whether explosive welding occurs in solid or in liquid state. To our opinion, no one has positively proved that metal in the vicinity of the contact point is in plastic state during the several microseconds of the welding process; in this state metal can flow like a liquid because the stresses are significantly in excess of its strength. Probably, the lattice is not destroyed by the process though it is somewhat mis-shapen as it is the case with the lattice in the cumulative jet /13/. So, explosive welding is situated somewhere in between the welding processes taking place in solid and liquid states.

It should be noted that excessive collision energy can result in a partial or full melting of surface layers of metals, so that the final bond structure would be indistinguishable from that obtained by welding in the liquid state. However, this melting is probably, a secondary factor not determining the essential properties of the process. Especially difficult to study are the cases when no intermediate layer is detected even with maximum magnification. To our opinion, such a layer still exists and it should be studied using progressively improved methods of analysis permitting to see details whose order of magnitude is near that of the lattice dimension. These studies should answer many questions relating to the nature of explosive welding.

3.3. Practical applications

The flat multilayer metal plates are produced in the Soviet Union using explosive welding technology beginning from the sixties. Of utmost practical interest is production of three-layer plates wherein a 08K11 low-carbon steel plate is cladded on both sides with IX18H9T stainless steel plates. In manufacture of this trimetal low-carbon steel plate is cladded in two shots: the both sides by stainless steel plates. The three-layer steel obtained is rolled using a conventional arrangement so that a sheet which is 2-4 mm thick is obtained while the stainless steel layer varies within 0.15-0.18 mm. This material is used in agricultural machinery industry for manufacturing some parts of machines

for applying liquid ammonia fertilizers. The corrosion resistance of the stainless steel cladding provides for necessary operational characteristics of the working units.

Two-layer blanks of plain bearings wherein a steel base is clad with an antifriction layer explosively applied to it are also produced in the USSR. A brass layer of 0.5 to 1.5 mm thickness is used as an anti-friction layer. Use of explosive welding instead of conventional anode surfacing results in significantly increased efficiency while consumption of expensive and scarce copper alloys is decreased by several times. Use of the steel base allows to increase the bearing strength while the uniform thickness of the brass layer applied permits to almost to do away with machining in bearing production. The process is realized in a special shop at the plant with the use of an explosive chamber. The bearing blanks of different diameters are now produced on a commercial scale.

The explosive welding process is used also in producing plain bearing blanks made from bimetal "steel + AO20 aluminium tin alloy" which can be used in strong diesel engines. A combined technology can also be used wherein metal obtained by rolling is explosively welded to the steel base of necessary thickness.

The explosive welding process is widely used now for manufacturing parts to be used in metallurgical equipment; the steel + copper blanks obtained by explosive welding are employed in manufacturing different parts of electric metallurgical units. The use of the steel + copper bimetal provides for necessary strength due to the steel base, and for necessary heat conduction due to the copper layer of a corresponding thickness. Among the parts produced on a commercial scale one could mention two-layer water jackets for re-smelting furnaces as well as two-layer crystallizers of different designs (Fig.6).

The explosive welding method permits to obtain strong welds in those cases when conventional welding methods are difficult or impossible to realize (steel + aluminium and aluminium alloys, steel + titanium and its alloys and some other combinations). Such corrosion-resistant metal as titanium can be used for cladding internal surfaces of different vessels, containing chemically active liquids; to this end large-scale production of steel + titanium bimetal is organized in different countries of the world. Different steel + aluminium transition joints are largely produced to be used for connecting aluminium rods to steel nipples in manufac-

turing current-carrying parts of electrolyzers used in aluminium production.

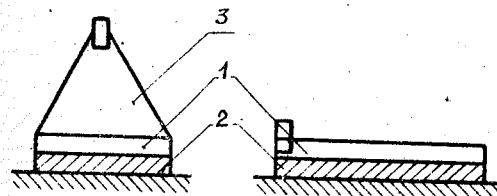
4. POWDER COMPACTION

The powder compaction arrangement using cylinder contained shown in Fig.7 was studied most thoroughly. The shock wave configurations arising due to variations in weights of the explosive charge and container were described in detail in /14/. Fig.8 presents some of the possible configurations. It should be noted that the similar configurations can be observed also in the case of powder compaction using flat geometries, though in this case they arise the release waves tending to rupture the container which is difficult to neutralize. It is evident that in order to uniformly compact the powder, a shock wave configuration should be generated which contains conical shock wave in it. Large computers are used in order to realize calculation of different shock wave regimes; an example of sufficiently complete theoretical calculation is presented in /15/.

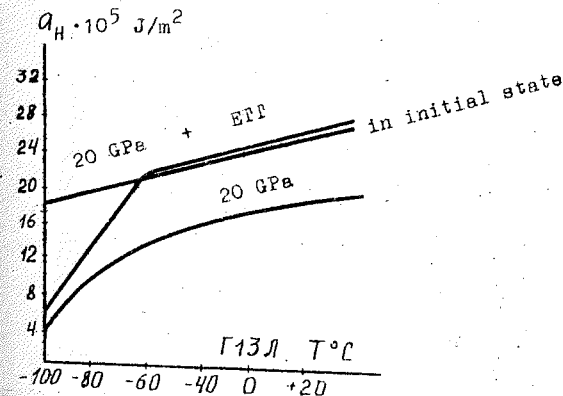
The bonding mechanism of powder particles in the explosive compaction process is described in /16/ and in a number of other publications. The main process which results in formation of metallic compacts is the plastic deformation determining the heat release on the boundaries of the powder particles. Of great importance is the characteristic relation of the powder particle size to the shock wave front. If the powder particles are too small, the heat release beyond the shock wave front is nearly uniform and specific phenomena resulting in explosive powder compaction do not occur.

4.1. Practical applications: some examples

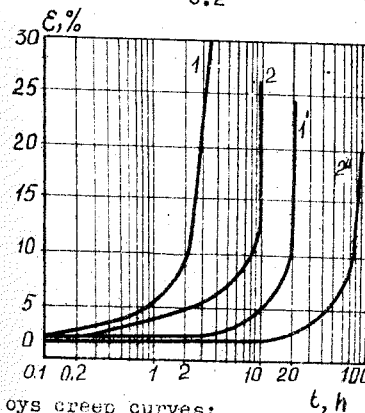
Several causes conditioned rise of interest to explosive powder compaction. First, there was a desire to transcend some limitations and to bond some materials which could not be welded by conventional explosive welding method, for instance, to attach brittle non-metal materials, ceramics, for example, to metals. At present metal + ceramics + metal compositions have been obtained and are successfully used in industry. Of interest are also prospects of improving properties of some materials which could be obtained by explosive compaction. A number of tests have been undertaken to study BK hard alloy (tungsten carbide + cobalt) under compaction /17/. The tests have shown hardening of the



Hardening arrangement: 1 - explosive charge; 2 - material to be hardened; 3 - generator of shock wave.



High-manganese steel hardening (temperature dependence of viscosity after explosion and ETT):
 $\sigma_b = 850-900$ MPa, $\sigma_{0.2} = 460-470$ MPa, $\delta = 32-40\%$;
 ETT - $\sigma_b = 950-1000$ MPa, $\sigma_{0.2} = 450-500$ MPa, $\delta = 45-48\%$;
 $\sigma_b = 950-1100$ MPa, $\sigma_{0.2} = 640-820$ MPa, $\delta = 27-36\%$.



Superalloys creep curves: 1 - before hardening; 2 - after hardening.
 $\sigma = 210$ MPa, $T = 800$ °C; 2 and 2' - $\sigma = 210$ MPa, $T =$

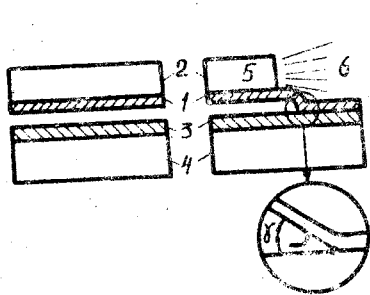


Fig. 4. Explosive welding arrangement:
1 - thrown plate; 2 - explosive charge; 3 - stationary plate;
base; 5 - detonation front; 6 - detonation products.

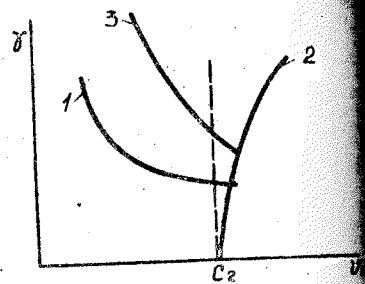


Fig. 5. Diagram of $V-V_k$ plane welding process:
1, 3 - lower and upper welding boundaries, respectively; 2 -
personic region limit.

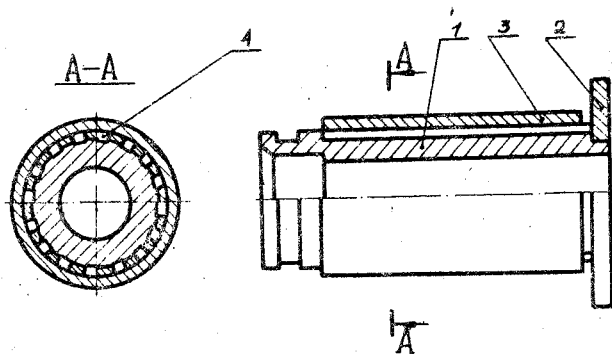


Fig. 6. Bimetal cylindrical crystallizer:
1 - copper tube; 2 - steel ring; 3 - steel shell; 4 - rigid

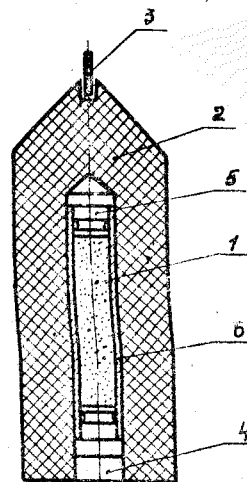


Fig. 7. Cylindrical arrangement for explosive compaction:
powder; 2 - explosive (6XB ammonite); 3 - electric detonator;
5 - lower and upper plugs, respectively; 6 - outer shell.

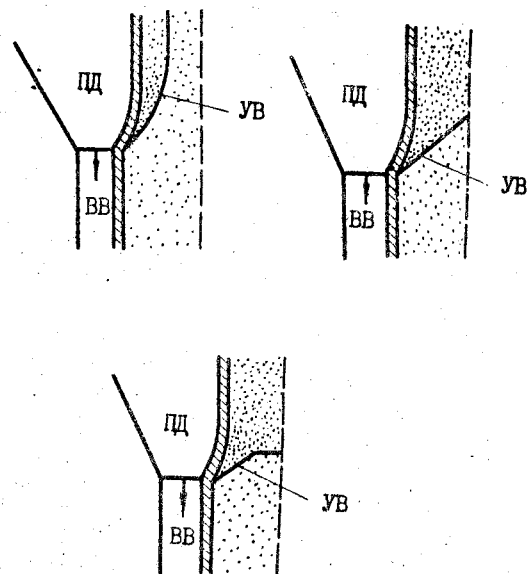


Fig. 8. Shock wave configurations arising in explosive compacting
porous materials using cylindrical geometries:
detonation products; YB - shock wave; BB - explosive.

binder to take place as well as deformation of the tungsten cathode particles. The effects observed suggest better working properties of tools made from the hard alloy treated using the explosive compaction method. The synthesis of several superconductors was carried out [18] and their characteristics were studied. In the synthesis of barium titanate from a powder mixture using a cylinder container is presented; polarization of the crystals obtained was also stated in this case. In [20] increase of catalytic activity of several oxides following the explosive treatment is analyzed.

Lately, a keen interest to the problem of explosive treatment of amorphous materials, the so called "metallic glasses" is characteristic of our scientific community. These alloys having different chemical compositions are obtained under laboratory and industrial conditions due to super-rapid melt cooling, so that no ice is formed during the solidification process. The materials have unique corrosion resistance, strength and magnetic properties. However, now only thin foils and fine-grained powders can be obtained by these methods which greatly limit the possibilities of using the advantages of these materials. Obtaining the solid specimens by conventional welding or sintering methods is impossible, because the over-heatings result in lattice formation. The tests wherein "metal glasses" were treated by shock waves were undertaken in the USSR and some other countries have shown that explosive treatment permits to retain the amorphous state of the monolithic specimens obtained. This opens good prospects for various applications of these materials and methods in future.

References

1. Deribas A.A. Fizika uprochneniya i svarki vzryvom.- 2. Novosibirsk: Nauka, 1980.- 220 P.
2. Riabinin Yu.N. Sublimatsiya kristallicheskoj reshetki pri istviiem silnoi udarnoi volny// DAN SSSR.- 1956.- Vol. N2.- P.289-291.
3. Deribas A.A., Dobretsov H.L., Kudinov V.M. Udarnoe uprochnenie poroshkov SiO_2 // DAN SSSR.- 1966.- Vol. 168, N3.- P.66-68.
4. Demchuk A.F. Odin metod rascheta vzryvnykh kamer// DAN SSSR.- 1968.- N5.- P.47-48.
5. Patent No. 2 703 297 USA/ McLeod, March 1955.
6. Vzryvnoe uprochnenie nekotorykh klassov stalei/A.A. I.N. Gavriliev, E.E. Zubkov, A.N. Kiselev, T.M. Sobolev, T.S. Teslenko// Trudy II soveshch. po obrabotke metallov.- Novosibirsk, 1982.- P.78-85.
7. Deribas A.A., Nesterenko V.F., Teslenko T.S. Univers

zavisimost' uprochneniya metallov ot intensivnosti udarnovo-volnovogo vozdeistviya// Fizika goreniya i vzryva.- 1982.- Vol. 18, N6.- P.68-74.

Crossland B. Explosive welding of metals and its applications Oxford: Clarendon Press, 1982.

Blazinski T.Z. Explosive welding, forming and compaction.- London-New York: Applied Science Publ., 1983.

Zakharenko I.D. Calculation of the lower boundary of the explosive weld area// Proc. 8-th Int. Conf. HERR, San Antonio, USA, June 1984.

Deribas A.A., Pai V.V., Simonov V.A. Osobennosti soudarenia krupnogabaritnykh plastin i nekotorye dopolnitelnye ograniicheniya oblasti svarki// Obrab. metallov vzryvom.- Marian ske Lazne, 1976, Vol. I.- P.117-130.

Hammerschmidt M., Kreye H. The role of adiabatic shearing in explosive welding// Trudy II soveshch. po obrabotke metallov vzryvom.- Novosibirsk, 1982.- P.117-126.

Green R.E. First X-ray diffraction photography of a shaped charge jet: Fin. Rep. on Tsk Order 72-574 for Batell Columbus Lab., Durham Oper., Jan. 1974// Res. Sci. Instrum.- 1975.- N46.- P.4173.

Deribas A.A., Staver A.M. Udarnoe szhatie poristyykh tsilindricheskikh tel// Fizika goreniya i vzryva.- 1974.- Vol. 10, N4.- P.568-578.

Wilkins M., Kusubov A., Cline C. Dynamic compaction of aluminum nitride powder// Proc. Int. Conf. "Explomet-85".- Portland, 1985.

Nesterenko V.F. Vozmozhnosti udarno-volnovykh metodov polucheniya i kompaktirovaniya bystrozakalennykh materialov// Fizika goreniya i vzryva.- 1985.- Vol. 21, N6.- P.85-98.

Khagshvili E.Sh. Vzryvnoe uprochnenie metallokeramicheskogo tverdogo splava// Fizika goreniya i vzryva.- 1971.- Vol. 7, N2.- P.275-280.

Barski I.M., Dikovskii V.Ya., Matytsin A.I. Udarnyi sintez superkhprovodiashchikh intermetallicheskikh soedinenii// Fizika goreniya i vzryva.- 1972.- Vol. 8, N4.- P.578-586.

Deribas A.A., Staver A.M. Udarnoe szhatie smesi poroshkov $\text{Al}_2\text{O}_3 + \text{BaCO}_3$ // Fizika goreniya i vzryva.- 1970.- Vol. 6, N1.- P.122-123.

Preskov G., Sazonova I., Maly V. The influence of shock compression on the catalytic properties of oxide semi-conductor catalysts, behaviour of dense media under high dynamic pressures. Symp. HDR, Sept. 1967, Paris.- Paris: Dunod, 1968, P. 39-396.

WAVE FORMATION CRITERION IN EXPLOSION WELDING

V.G. Petushkov

E.O. Paton Electric Welding Institute of the UkrSSR Academy of Sciences, Kiev, USSR

The region of explosion welding existence in γ , V_c coordinates is delineated by the A, B and C curves (Fig. 1). On the left it is limited by the D curve, corresponding to conditions under which such pressures are achieved at the collision point which are comparable to the theoretical strength of the metal crystal lattice.

The most interesting is the lower boundary (LB) of explosion welding (A curve) where certain limit (critical) conditions of the colliding bodies occur, at which surface effects are assumed to be still possible.

At small γ angles of collision LB is given by the equation

$$\gamma \cdot V_c = k \sqrt{HV/9},$$

where V_c is the contact point velocity, k is empirical coefficient ($k = 0.6 \dots 1.2$), which is determined by the conditions of the critical pressure achievement in the welded metal collision point. The magnitude of this pressure depends on certain metal strength characteristics. It is usually the easy-to-determine Vickers hardness HV, although besides HV the above expression often include Hügöniet's limit of elasticity, static yield strength and ultimate strength.

In explosion welding similar metals the above expression does not contain any formal contradictions and satisfactorily describes the experimental data. However, when attempting to plot for explosion welding dissimilar metals, with markedly different static strength (hardnesses), there arise basic difficulties in substantiating the selection of hardness (as well as density) of one of the two metals being welded. Proceeding from the hypothesis on the necessity of the mass backflow as explosion welding criterion, attempts were made to introduce into the equation the hardnesses of both the stronger and the softer metal or the semi-sum of their hardnesses. However, if LB is determined from the condition of the formation of mass backflow from the softer metal surface, it remains unclear how at the pressure critical for the soft metal the harder metal shape is changed so as to

150

waves in it. Just as invalid is the introduction into the equation of the stronger metal hardness, since at an appropriate pressure the softer metal of the pair is certainly overloaded, and this must lead to its melting or anomalous mass losses, not detectable experimentally near LB, and the use of the semi-sum of hardnesses is none other than a compromise.

The process of explosion welding of similar and dissimilar metals of both close and markedly different nominal (static) strength is accompanied by more or less pronounced wave formation at the joint boundary when certain collision conditions are realized. There exist several wave formation theories, including that based on the concept of appearance and interaction of plastic deformation "humps" in front of the contact point. Thus, the wave formation is a process of interpenetration of metals, which, at least for the explosion welding LB, preserve their crystalline structure, and, hence, obey the laws of deformable solid mechanics. Therefore, the colliding metals under the conditions realized in the contact point vicinity (stress tensor, temperature, strain rate) should have identical resistance to local contact interaction - irreversible shape changes, yielding. The universal physical characteristics, displaying the mentioned metal properties, can be the dynamic yield point σ_d , characterizing metal resistance to plastic deformation, the value of which is quite sensitive to the deformation rate. It follows naturally that in explosion welding wave-like joint formation is only possible when the force interaction of the colliding metals, given by the values γ and V_c , corresponds to their joint plastic flow with such different deformation rates in the general case, to which exactly the same dynamic yield point corresponds under these conditions.

Explosion welding leads to rather high deformation rates in the metal layer adjacent to the contact surface, reaching up to 10^7 s^{-1} . At so high deformation rates the dynamic yield point σ_d exceeds the static value of σ_0 which is usually determined at a deformation rate of 10^{-3} s^{-1} . Despite the fact, that the actual experimental material is, mainly, concerned with deformation rates $< 10^5 \text{ s}^{-1}$, the relative increment of the dynamic yield point is found to greatly depend on its static value. Such dependence as well as σ_d values for the deformation rate range of $10^{-3} \dots 10^5 \text{ s}^{-1}$, taken from literature* are given in Fig. 2 for essentially differing in strength.

* V.G. On strength characteristics of colliding bodies in explosion welding. - Automat. svarka, 1986, N10, p. 35-38.

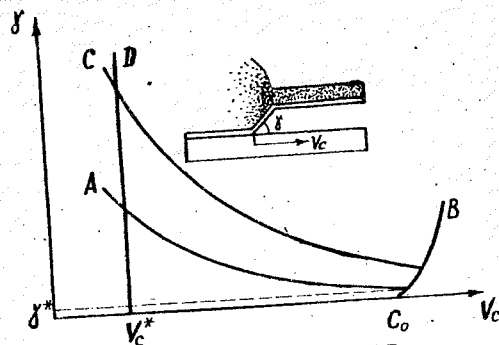


Fig. 1. Region of explosion welding existence.

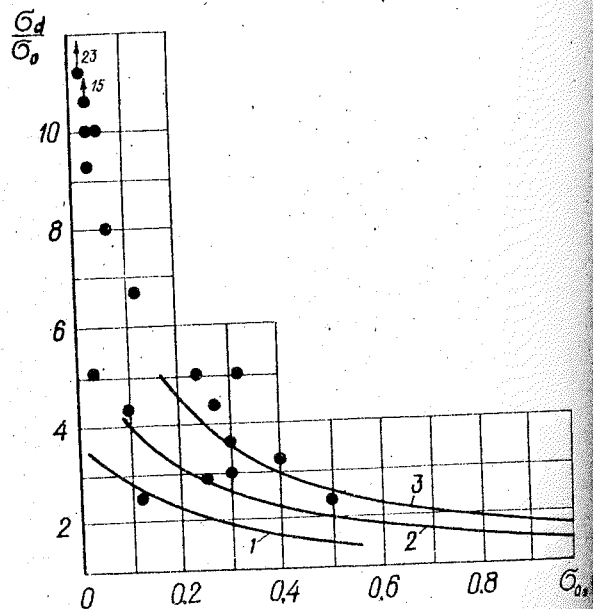


Fig. 2. Dependence of relative value of the dynamic point on its static value.

It follows from these data that metal resistance to plastic deformation increases drastically at high rate of the latter, its increase being the quicker and the higher, the lower the σ_0 . At a certain high enough deformation rate the absolute σ_d values of metals with different σ_0 can become identical, reaching the values, needed for a satisfactory description (including that in terms of the existing hydrodynamic concepts) of experimentally found LB for explosion welding of various metal combinations by the above formula with the formal substitution of σ_d for HV into them. This can be easily seen, since already at the rate of uniaxial tension of $5 \cdot 10^4 \text{ s}^{-1}$ the dynamic points of say armco iron ($\sigma_0 = 0.18 \text{ GPa}$), CT3 steel ($\sigma_0 = 0.5 \text{ GPa}$) and CT45 steel ($\sigma_0 = 0.5 \text{ GPa}$) become the same ($\sigma_d = 0.5 \text{ GPa}$) and approach HV of CT45 steel.

Thus, the condition $\sigma_{d1} = \sigma_{d2}$ where indices 1 and 2 denote softer and harder metal, correspondingly, can be postulated as the wave formation criterion in explosion welding of metals, taking those of different initial strength. Hence, at the boundaries of transition from the wave-free to wave-like joint line the criterion condition is that of the soft metal yield point (dynamic strengthening) increasing to the harder metal level taking into account its dynamic strengthening at the deformation rates of the layers adjacent to the contact surface, which are realized in both metals being welded at given γ and V_c . A possible form of the LB equation, following from the given concepts and determining the set of parameters controlling the wave formation process together with a review of the appropriate publications are given in the above review.

AMPLIFICATION OF LINER VELOCITIES USING MULTILAYER SYSTEM FOR GENERATION OF HIGH PRESSURE

M. Adamiec, J. Bagrowski, H. Derentowicz, H. J. Luckner, R. Świerczyński

S. Kaliski Institute of Plasma Physics and Laser Microfusion
P.O. Box 49, 00-908 Warsaw, Poland

Abstract

The paper presents the results of the numerical analysis of metal liners driving using multilayer systems in plane and cylindrical symmetry. In calculations there were adopted the data corresponding to the experimental system investigated in /6/. The result analysis confirms the experimental results. It was stated that the velocity of the accelerated liner was 3.5 as much in comparison to the velocity of the striking liner, in the cylindrical system consisting of six pairs of layers plexiglass-Cu.

Introduction

Achieving high velocities of metal liners, exceeding considerably the detonation velocity in the explosive is not possible in a simple system of explosive acceleration. In the paper /1/ there was proposed a method of increasing of the liner velocity by using the following driving system: striking liner accelerated by the detonation products to the velocity v_0 - light intermediate layer (buffer) - driven liner.

In the papers /2-4/ there were presented numerical analyses based on the idea suggested in /1/. The authors of /2/ worked on the numerical optimization of one-stage, multilayer system of acceleration in plane symmetry. The aim of the optimization was to determine the thickness of the buffer layer for which the velocity of the driven liner attains its maximum value. The papers /3,4/ present the results of the numerical analysis of the analogous multilayer concentric system. It was shown that - in comparison to the plane system - one can achieve almost 100% increase of the liner velocity.

Some experimental works were also carried out /5,6/. The paper /6/ presents the results of experimental investigations upon copper liner acceleration in the multilayer cylindrical system consisting of six pairs of plexiglass-Cu layers. It was stated that the velocity of the last liner was 3.5 as much in comparison to the velocity of the striking liner directly accelerated by detonation products.

This paper is a continuation of investigations of the authors /4,6/. The results of a numerical analysis of cylindrical multilayer system investigated experimentally in /6/ were presented.

Results of a numerical analysis

Numerical calculations were carried out on the basis of the algorithm described in /2,3/ and also used in /4/. It means the problem was reduced to that of the numerical solution of a one-dimensional set of hydrodynamic equations for a multilayer medium (liner (Cu) striking with the v_0 velocity - six pairs of layers plexiglass-Cu in cylindrical symmetry, in Lagrangian coordinates). The constitutive equations, describing cuprum behaviour, were accepted in a form proposed by Tillotson /7/, for plexiglass in a form of Mie-Grüneisen equations /8/. Such a formulated problem was being solved by means of the Richtmyer-von Neumann scheme /9/.

According to /6/ the following data was adopted in the calculations. Striking liner (Cu): internal radius - $R_0 = 1.6 \cdot 10^{-2}$ m, $3.8 \cdot 10^{-3}$ m, $v_0 = 3.85$ km/s; relative thickness of heavy liners $\rho_1/\rho_n = 0.543$; relative thickness plexiglass layer - $\rho_1/\rho_n = 0.543$; thickness of the driven liner of copper $\rho_6 = 1.0 \cdot 10^{-4}$ m. Figs. 1-3 show the calculation result. First two show the dependence of the velocity of free surface of cylindrically accelerated liner - v_{FS} and the velocity of its external surface - v_{ES} on time. For the comparison's sake there were also presented the results for the multilayer plane system and for the cylindrical system with plexiglass concentrator. It results from the figures: acceleration velocity in the multilayer cylindrical system is of 60% higher than in the plane symmetry. Acceleration of the liner in the investigated multilayer system occurs on a very short time, of the order of two liner thicknesses. In the multilayer cylindrical system one achieves high, in comparison to the striking liner, velocity of liner acceleration (of the order of 12.7 times) what stays in good agreement with the result of experimental investigations /6/. Maximum pressure which can be achieved in the case of cylindrical symmetry (Fig.3) reaches the value of 600 GPa. This is a confirmation of the thesis saying that in the proposed system ensures the generation of high pressure.

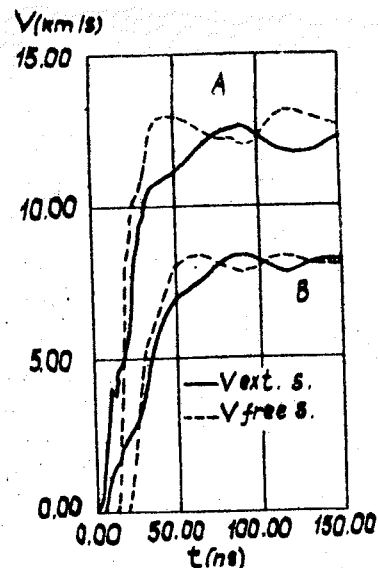


Fig. 1. The velocity of the driven liner as function of time (A-cylindrical symmetry, B-plane symmetry; thicknesses of layers are the same as in the case A).

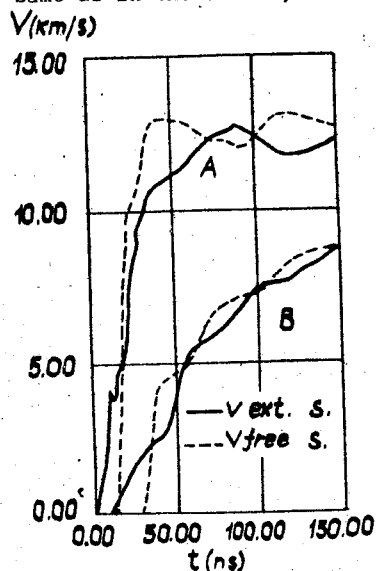
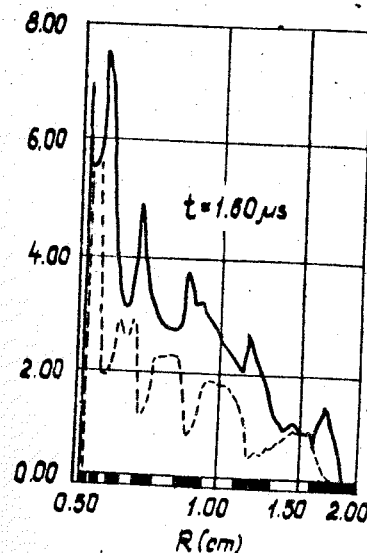
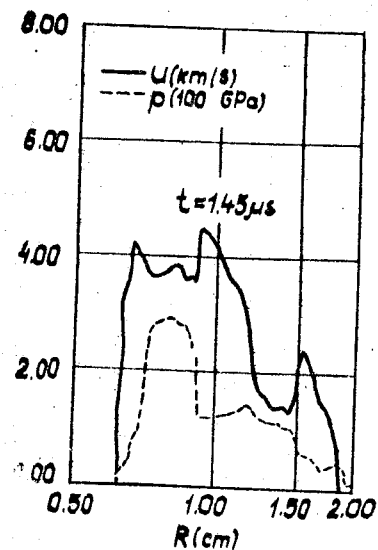


Fig. 2. Influence of the multilayer system on the movement of the accelerated liner (A-cylindrical system of six plexiglass-Cu layers, B-cylindrical system with the plexiglass-Cu concentrator; data of the striking driving liner are the same as in the case A).



Pressure and velocity of the multilayer medium particles of the cylindrical system as a function of the initial radius of the particles. The below diagram shows the situation at the time when maximum value of pressure is being achieved. The diagram also presents the geometry of the analysed system.

References

1. A.S.Balchan, G.R.Cowan, Method for accelerating flat plates to high velocity. Rev.Sci.Instrum. 1964, 35, 8, 937.
2. R.Świerczyński, J.Tyl, E.Włodarczyk, Layered single stage driving system for plane liners. J.Techn. Phys, 1985, 26, 2, 207-224.
3. R.Świerczyński, J.Tyl, E.Włodarczyk, Analysis of layered concentric liner-driving systems, J.Techn.Phys. 1986, 27, 1-2, 109-124.
4. R.Świerczyński, J.Tyl, E.Włodarczyk, Acceleration of liners in layered systems. Physica B, 1986, 139 and 140, 603-606.
5. M.Adamiec, J.Bagrowski, H.Derentowicz, J.Luckner, Badania trzy i szesciostopniowych ukladow cylindrycznych dla system "strumien". IPPLM 7/IV/1986.
6. J.Bagrowski, H.Derentowicz, J.Luckner, Experimental investigations of an explosive cylindrical multilayer system of metal liners accelerated to high velocities. Physica B, 1986, 139 and 140, 575-581.
7. J.H.Tillotson, Report GA-3216 (1962).
8. R.S.Hawke, D.E.Duerre, J.G.Huebel, H.Klapper, D.J.Steinberg, R.N.Keeler, Method of isentropically compressing materials to several megabars. J.Appl.Phys, 1972, 43, 6, 2734.
9. J. von Neumann, Collected works. Vol.6. New York, 1963.

THE PECULIARITIES OF ELEMENT REDISTRIBUTIONS IN METALS DURING SHOCK WAVE TRANSMISSIONS

L.O.Zvorykin, V.M.Fal'chenko, A.V.Filatov

Institute of Metal Physics, Academy of Sciences of the UkrSSR, Kiev, USSR

In many works the investigators observed a considerable increase in the rates of such processes as crystal growth, chemical reactions and phase transformations under shock compression. All these processes, characteristically, are limited under quasi-equilibrium conditions by atomic mobility, which is determined by intensity of element redistributions. The use of the radioisotope methods allowed to determine, that penetrating of the elements from thin coating layer (0.3 μ m) into metallic matrix is observed under the transmission conditions of shock waves, at the same time the most considerable depth of penetration is observed in metals with lower binding energy. The loading was carried out by generating plane shock waves having various characteristics. The following parameters of the plane shock waves (amplitude, compression-pulse length, a configuration of increasing pressure front) were varied.

With changing of the plane-shock wave amplitude from 10 to 100 GPa the penetration depth of coating elements into the metallic matrix increases direct-proportionally.

Taking into account a possible effect of the temperature factor, which is due to heating-up of a shock-compressed crystal, it should be noted, that a thermal diffusion can provide a penetration of labelled atoms into a depth, which does not exceed 2-3% of the mass-transfer one, achieved during experiments with dynamic deformation. In this connection the heating-up temperature may not be a factor, determining a dependence of the penetration depth of the penetrating atoms on shock-wave amplitude. More essential for the mass-transfer process in shock-compressed crystals is an increase of pressure gradient in the loading front with increase of the compression wave amplitude. A change in the compression pulse length does not affect the penetration depth of surface isotopes. It may be stated, that processes, occurring under high quasi-hydrostatic pressure behind the increasing shock-wave pressure front, affect mainly the mass transfer. A formation of multiwave fronts of increasing shock-wave pressure resulted in findings being analogous to those, obtained at multiple pulse treatment. Under these conditions

tions the penetration depth did not alter in practice, but the penetrating-element concentration increased for shallow depths. For the regularity obtained, the maximal wave amplitude (of the loading-front components) affects decisively a size of coating element penetration zone.

For the mass transfer zone, formed in the result of shock-wave transmission, a volume character of element distribution penetrating into the metallic matrix from a surface, is typical. The analysis of ^{57}Fe mass transfer zone in Ti using the TEM spectroscopy shows that these elements formed solid solutions in the range under investigation. It may be possible only, if the element-redistribution processes occur on an atom level under high-dynamic pressure.

With changing deformation conditions of Cu samples with coating during shock compression a degree of the residual deformation was altered over a range from 20 to 48%. The redistribution zone of Ni and Cu did not alter considerably due to this fact, with the exception of decreasing its sizes proportionally, with the residual-deformation degree from 100 to 25 μm . The relation obtained may be explained on the basis of the assumption, that the unloading processes, determining the residual deformation degree during the experimental conditions, proceed after the mass-transfer zone formation and decrease its size. Changes in roughness of contacting Fe-Cu surfaces over a range of $R_{\text{max}} = 0.6$ resulted in an increase of the penetration depth of Fe from 9 to 25 μm . This seems to be connected with increasing temperature of the contact zone for two metals when the shock wave transmits through less dense contacting medium of the rough surfaces.

It is established, that changes in stacking-fault energy in Co alloys with changes in Ni content result in a proportionate increase of the penetration depth of Ni atomic coating which is connected with changes in front configuration of increasing pressure in Co alloys due to the dependence of the critical pressure of the phase transition on Ni-content. With transmitting shock-waves, changes in dislocation density in Cu do not affect considerably the penetration of Fe-atoms of coating.

Under conditions of the shock waves transmitted through metal-metal contact boundary (copper-tin, copper-zinc) the mass-transfer zone, unlike the analogous phase one, obtained under equilibrium thermal annealing conditions, formed. By determining

that of the elements, being formed in the phase interlayers, by using the micro-X-ray analysis, their identification by the equilibrium phase state diagrams is not succeeded. It should be noted, that when the shock wave transmits through the powder Zn-Sn boundary, contacting with Cu, the formed phases are closer to the equilibrium state diagram. This seems to be connected with an effect of residual heating-up being more considerable under shock compression of a porous medium. The plastic deformation traces and structural defects being analogous to ones, which are observed in main material out of the mass-transfer zone after transmitting of the shock wave, are the typical structural properties of the mass-transfer zone caused by shock compression. In the case of generation of large-amplitude shock-waves, initiating the recrystallization processes, the formation of grain boundaries is observed for both the main material and mass-transfer zone is observed. These testify a high rate of the mass-transfer zone formation and a preferential effect of an increasing shock-wave pressure front on this process. The analysis of the observed regularities allows to propose a model for atomic redistribution over the increasing-pressure front of the shock wave in proportion to its propagation over the crystal. Such a hypothesis allows to explain regularities revealed. It should be noted, that in the case of mass-transfer zone, formed beyond the shock wave, the deformation traces and available recrystallization is not succeeded to explain. Within the framework of a proposition concerning to atomic agitation over the increasing shock-wave pressure front theoretical estimations and experimental results are in agree-

G.A. Babushkin

Institute of Metallurgy, Ural Science Center of the USSR Academy of Sciences, Sverdlovsk, USSR

For shaping hardly pressurable and amorphous powders dynamic compaction methods are suitable, including explosive pressure method (EPM)/1,2/.

1. EPM-compaction of powders gives rise to some peculiar characteristics of the finished materials: 1) initial properties of materials of powder remain in the volume of each powder particle; 2) surface properties of powder particles material change; 3) it determines the formation of amorphous and high-imperfection interparticle contacts; 4) formation of such kind of contacts affects the quantity and concentration of phases of composites.

2. The influence of EPM on the effective properties of powder materials is studied. The classification of possible structures of materials which are determined by the peculiarities of EPM is given (see Figure). Method of calculation of these properties of materials obtained by EPM reduces to the consideration of the structure determined by the peculiarities of EPM, to quantitative distribution of concentrations between the phases and, to the determination of thickness of amorphous phase. This problem is connected with the procedure to determine characteristics of materials and contact interaction of phases. The actuality of the last item is underlined in /3,4/.

In this paper the restrictions in /3-5/ are put down and a unified phenomenological theory for transport and elastic properties (EEP) of composites is developed on the basis of /6,7/. The universality of the method is determined by equivalent forms of expressions for GC and EEP for the case of MM and for the case of systems of infinite clusters (SIC)/6/ (components are metallic)

$$\mathcal{X}_{ef} = \mathcal{X}_I \left\{ I + A + (I/2)A^2 \left[I - (3-B)\mathcal{X}_I\mathcal{X}_2 / [(\mathcal{X}_2 - \mathcal{X}_I)(\mathcal{X}_2 + (2-B)\mathcal{X}_I)] \right] \right\}$$

$$A = (3-B)v_2(\mathcal{X}_2 - \mathcal{X}_I) / [\mathcal{X}_2^2 + (2-B)\mathcal{X}_I];$$

$\mathcal{X}_{ef} = \mathcal{X}_V - (\mathcal{X}_V - \mathcal{X}_R) / (2a)$, $\mathcal{X}_V = \sum_{\alpha} \mathcal{X}_{\alpha} v_{\alpha}$, $I/\mathcal{X}_R = \sum_{\alpha} v_{\alpha} / \mathcal{X}_{\alpha}$; $\alpha = 1, 2$; where \mathcal{X} - GC or EEP, v - bulk fraction of phase, suffixes denote die and inclusions, $B = 0$ for GC, $B = (9-15\nu_I)/(\nu_I + 10)$ for EEP.

shear moduli, $B = 6\nu_I / (1 + \nu_I)$ for bulk moduli (ν - Poisson's ratio).

3. Materials, produced from amorphous powders, have structure which is shown in Figure, a; and according to the equation (1) can be given by $\mathcal{X}_{ef} = \mathcal{X}_I(I + A_0 + A_0^2/2)$, $A_0 = -(3-B)v_2/(2-B)$.

Materials produced of two-phase amorphous powders, have inclusions of all in ball"-type (Figure, b) with GC and EEP (in linear approximation)

$$\mathcal{X}_0 \{ I + (3-B_C) (I-H/2)^3 v_2 (\mathcal{X}_2 - \mathcal{X}_C) / [\mathcal{X}_2 + (2-B_C)\mathcal{X}_C] \}, \quad (3)$$

where $v_1 > v_2$

where C denotes contact layer with thickness h , R - radius of particles. Effective GC and EEP of the composite is determined by equation (1), where GC and EEP of inclusions are given now by expressions (3) and instead of v_2 it is assumed that $v_2' = (I-H/2)^3 v_2$. Amorphous SIC have structure which adequately is shown in Figure, c, and effective properties have

$$\mathcal{X}_V - A_I = [I / (2a)] (\mathcal{X}_V - A_I - \mathcal{X}_3)^2 [\mathcal{X}_V - A_I - \mathcal{X}_3 + \mathcal{X}_3(I - v_3)/v_3]^{-1};$$

$$v_1 v_2 (\mathcal{X}_I - \mathcal{X}_2)^2 / [2a(\mathcal{X}_I v_2 + \mathcal{X}_2 v_1)], \quad (4)$$

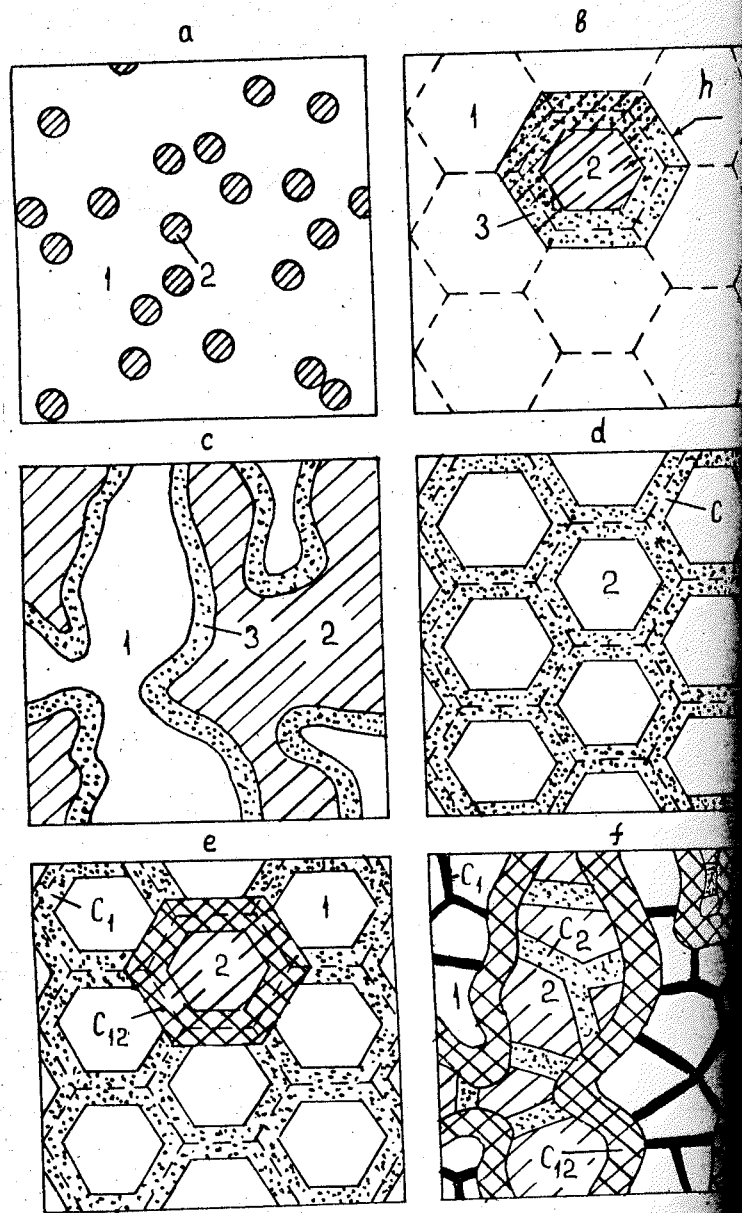
$$\mathcal{X}_V = \sum_{\alpha=1}^3 v_{\alpha} \mathcal{X}_{\alpha}, \quad v_I \approx v_{I0} - v_3/2; \quad v_2 \approx v_{20} - v_3/2, \quad v_3 = 3kv_{I0}v_{20}H,$$

where suffix 0 and 3 are related to initial and contact phases, respectively.

Materials, obtained by EPM from polycrystalline powders a structure with interparticle amorphous layers /1,2/ is realized. The structure of monophase materials obtained by EPM, adequately is shown in Figure, d. When thickness of a layer considered as a matrix is small, then a method /4/ with regard for field distortion of inclusions $\mathcal{X}_{ef} = \mathcal{X}_C + v_2(\mathcal{X}_2 - \mathcal{X}_C) [I + \mathcal{X}_C / (\mathcal{X}_2 v_C + \mathcal{X}_C v_2)] / 2$ is developed. However the thickness of contact layer may be taken into account. When GC and EEP are given by (1), where now concentration of inclusions (volume of particles, which remain their initial properties) is connected with H by $v_2' = (I-H/2)^3 v_2$. By consolidation of a polycrystalline mixture, which corresponds to matrix in Figure, e), we find properties of MM, where the matrix is polycrystalline, which have largest concentration.

In the case of SIC (Figure, f) one may find properties each of the clusters, formed of the particles of single sort.

Highly imperfectioned contacts are caused by plastic deformation under high pressure of impact (detonation) waves, which leads to emission of energy and high concentration of unbalanced



anced vacancies. The thickness of contact layer may be estimated by (1) and (2). The amorphous contacts affect essentially the effective GC and EEP due to large difference in properties of polycrystalline and amorphous media /8/ and strong interrelation between these properties, for example, between strength of particles cohesion and concentration of the unbalanced vacancies /9/.

References

1. Роман О.В., Горобцов В.Г. Теоретические основы импульсного прессования порошковых материалов // Исследование и разработка теоретических проблем в области порошковой металлургии и защитных покрытий: Материалы Всесоюзной конф., ч.2. Минск, 1984. - С.3-12.
2. Митин Б.С., Васильев В.А. Порошковая металлургия аморфных металлических сплавов // Аморфные металлические материалы. - М.: Наука, 1984. - С.127-130.
3. Райченко А.И., Федорченко И.М. О вычислении электропроводности двухкомпонентных металлокерамических тел // Физика металлов и металловедение. - 1960. - 2, вып. 6. - С. 815-822.
4. Skorochođ V.V. Metody výpočtu fyzikálních vlastností dvoufázových slitin se zřetelem na jejich strukturu // III. Int. Konference über Pulvermetallurgie, CSSR, Karlovy Vary, 1970, S.29-41.
5. Заричняк Ю.П. Влияние диффузионного взаимодействия компонентов с неограниченной взаимной растворимостью на проводимость порошковых композиций // Порошковая металлургия. - 1980. - № 7. - С. 16-20.
6. Бабушкин Г.А. Эффективные кинетические коэффициенты и упругие модули многокомпонентных материалов // Grundlagen, Herstellung und Eigenschaften pulvermetallurgischer Werkstoffe, Bd. 2: VIII. Internat. Pulvermet. Tagung, DDR, Dresden, 1985. - S. 149-167.
7. Бабушкин Г.А. Упругие модули многофазных материалов // Физика металлов и металловедение. - 1986. - 61, вып.6. - С.1103-1113.
8. Сверхбыстрая закалка жидких сплавов /Под ред. Г.Германа. - М.: Металлургия, 1986. - 376 с.
9. Бабушкин Г.А. Диффузионно-кинетический механизм сцепления порошкового покрытия с основой // Журн. прикл. механики и техн. физики. - 1986. - № 1. - С. 130-133.

types of powder materials structures obtained by EPM from amorphous (a-c) and polycrystalline (d-f) powders: a - under pressure of mono-phases powders, 2 - pores; b - under pressure of two-phases powders by concentrations, correspond to MM, 3-amorphous high-imperfectioned polycrystalline) layer; c - under pressure of two-phases powders, correspond to SIC; d - under pressure of two-phases powders, 2-polycrystalline phase, C - contact amorphous phase; e - under pressure of two-phases powders by concentrations, correspond to MM, 1 and 2 - polycrystalline phases, C₁ and C₂ - amorphous phases of atoms of type 1 and of type 2, C₁₂-amorphous phase of atoms of types 1 and 2; f - under pressure of powders by concentrations, correspond to SIC, the designations are the same as the Figure, e. For more simple form the pores are not considered.

THE SHEAR LOCALIZATION AT EXPLOSIVE COMPACTION OF RAPIDLY SOLIDIFIED METAL POWDERS

V.F.Nesterenko, S.A.Pershin
Special Design Office of High Rate Hydrodynamics
Siberian Division of the USSR Academy of Sciences
Novosibirsk, USSR

The dynamic compaction of high-strength metal alloy powders has attracted recently a considerable deal of attention [1].

The shear localization (SL) phenomenon arising at explosive compaction of rapidly quenched powders in cylindrical containers is studied. The SL is to be avoided in most cases of practical applications, because it results in formation of "stagnation" zones relative to the particle shear deformation, decreases the possible densities obtained and worsens the inter-particle bonding quality. Besides, rupture along the SL lines is possible [1, 2].

The localization process develops in two scales. The inter-particle shear (Fig.1*) arises in a particle on the intense powder compaction stage due to a peculiar local loading characteristics and can spread over adjoining areas. This shear originates in the stress concentrators on the particle surface and inside the latter. Another SL type is the trans-particle shear (Fig.2*) noted earlier for ceramic powders [3,4]. It develops in the layer adjacent to the container wall and proceeds through the whole of the specimen. The following parameters serve to describe this kind of shear: N - number of shears and $\bar{\epsilon} = \sum_{i=1}^N \epsilon_i / N$ - mean shear amplitude, which are determined from the microstructural analysis data of transverse microsection metallographic specimen.

In all experiments the internal radius of the container was 0.9 cm. The pressure of the shock wave entering the powder was

varied by variations of the explosive layer thickness h (6 *B ammonite, $\rho = 1 \text{ g/cm}^3$) and the container wall thickness ℓ , which was characterized additionally by the width of a gap filled with powder t . Experiments have shown the different materials of the metallic container not to essentially affect the SL character and parameters and it is unrelated to the instability of the wall formation.

The strength of the materials compacted is the main factor affecting the SL emergence in this case as well as in the case of metallic materials. The SL appears only in the hardening process of particles of the fine-grained "Alnicko" alloy in the compaction process from 550 HV to 900 HV measured near the container wall ($h = 2.5 \text{ cm}$; $\ell = 0.3 \text{ cm}$; $t = 0.5 \text{ cm}$). It should be noted that in case of annealed particles (down to 400 HV), the localized shear appears under more severe loading parameters ($h = 3 \text{ cm}$).

The dependence of the shear amplitude from the compaction rate in case of 71KHCP amorphous alloy is shown in Fig.3. As h increases resulting in ϵ augmentation due to the increased pressure and deformation rate it is followed by the increase of SL sites. A correlation occurs also at $h > 4 \text{ cm}$, when the amplitude decreases resulting in the lowered number of SL sites (Fig.3). This can be explained by a considerable heat liberation on the particle boundaries and formation of plastic material on their periphery promoting uniform deformation. A series of experiments were performed on powder mixtures composed from 2HCP amorphous alloy powder as well as nickel and copper powders ($\sim 5 \mu\text{m}$ fraction), which serves to plastic layer located on the amorphous particle boundaries (Fig.4). It is evident that pre-heating the powder can promote the elimination.

As the heating degree of the surface layers of the powder particles depends (other conditions being the same) on their size,

* The Figure is given at the end of the book

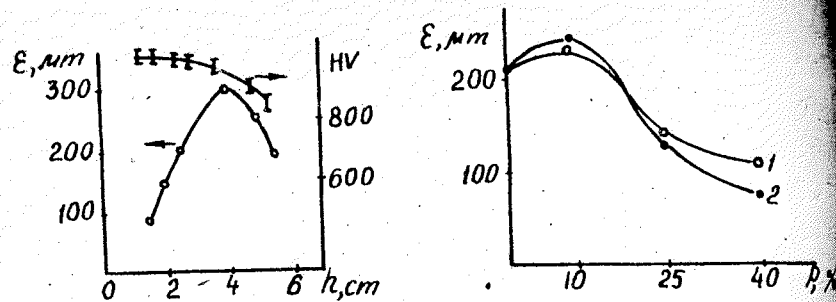


Fig.3. Dependence of microhardness and ϵ on h for 7IKHCP ($l = 0.1$ cm, $t = 0.5$ cm, $\rho_0 = 4$ g/cm³).

Fig.4. Dependence of ϵ on weight content of Ni(I) and Cu(2) in mixture with 2HCP ($l = 0.1$ cm, $t = 0.9$ cm, $\rho_0 = 3.4$ g/cm³, $h = 1.8$ cm).

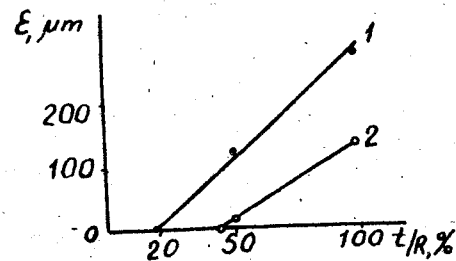


Fig.5. Dependence $\epsilon(t)$ for 7IKHCP ($l_1 = 0.1$ cm, $l_2 = 0.2$ cm, $h = 2.5$ cm, $R = 0.9$ cm).

the latter determines the powder deformation characteristics, it follows that this parameter affects SL as well. The following values of $\epsilon_1 = 150$ μ m, $\epsilon_2 = 225$ μ m and $\epsilon_3 = 220$ μ m were obtained for the 2HCP alloy powder ($\rho_0 = 3.4$ g/cm³; $l = 0.1$ cm, $t = 0.9$ cm, $R = 1.8$ cm) for the following three fractions $a_1 < 40$ μ m; $40 < a_2 < 90$ μ m; $90 < a_3 < 110$ μ m, respectively. It has been stated that orientation of the plate-like particles (obtained by grinding amorphous foils) also affects the SL characteristics.

However, besides the factors mentioned there are needed additional requirements whose satisfaction is needed in order that the SL takes place, i.e. "pliant" boundary whereto it might be directed. In case of compaction using a centrally disposed mandrel, the conditions for SL occurrence are limited, so that is thin enough layer of powder is compacted, there is no SL altogether (Fig.5).

The phenomenon described occurs at compacting flat specimens as well.

References

- Nesterenko V.F., Potential of shock-wave methods for preparing and compacting rapidly quenched materials // Combustion, explosion and shock waves.-1985.- Vol.21, No.6.-F.85-98.
- Nesterenko V.F. Heterogeneous heating of porous materials at shock-wave deformation and criteria for obtaining solid compacts // Proc. of the 9-th Int.Conf., August 18-22.- 1986.- Novosibirsk.- P.157-163.
- Prümmer R. Explosive Compaction of Powders. State of art // HERF: Proc. of the 9-th Int.Conf., August 18-22.-1986.- Novosibirsk.-1986.-P.169-178.
- Leonard R.W. et al. Advances in Explosive Powder Compaction/ Proc. 2nd Int.Conf.HERF, Estes Park Co., USA.- P.8.3.I.- 8.3.23.
- Olson G.B. et al. Adiabatic Deformation and Strain Localization// Shock Waves and High-Strain-Rate Phenomena in Metals: Concepts and applications.-New York-London:Plenum Press, 1984.- p.221 - 247.

V.I. Postnov, S.S. Nabatov

Institute of Chemical Physics, the USSR Academy of Sciences, USSR

The present work discusses the experimental results on the electrical conductivity measurements in condensed materials, both the traditional shock-wave compression (for sulphur and quartz) and the quasiisentropic loading. In the second method loading was performed in two ways:

a) placing the easily compressed material (sulphur, iodine, sodium chloride) between rigid plates in which the shock wave generated by metal strikers accelerated by the explosion wave

b) by using the property of materials with anomalous shock compression (glass) to "spread" the shock; the run substance bismuth.

The pressure profile was recorded with manganin detectors calibrated to 100 GPa [1].

Sulphur, iodine [2-4]. The plots of specific resistance as a function of the compression pressure (Fig. 1) show an initial decrease in ρ , which subsequently reaches a nearly constant level of $\sim 10^{-2}-10^{-3}$ ohm-cm. The change in the dependence occurs at about 17-18 GPa for sulphur and at about 15 GPa for iodine. It is supposed that sulphur and iodine reach the metallic state.

Bismuth. The test sample of about 50 μ m thick was placed between the glass plates. At pressures up to 15 GPa glass was used to produce shock waves owing to the anomalous shock compression below the elasticity limit and the kinetic behavior during transition into the plastic state. As a result, loading will proceed along the isentrope. This experimental set-up makes it possible to derive, based on a single run, the dependence of resistance R on pressure, by analogy with one-cycle pressure increase and release, achieved on static apparatus. The p dependence of R/R_0 under static compression, shown in Fig. 2, b, reveals distinct phase transitions. Comparing this relationship with data (Fig. 2, a), one can also see the transitions, although not so distinctly expressed. This is probably due to the kinetic nature of the Bi phase transformations in dynamic experiments. In the present experiments reversed transitions have also been

are even less distinct and confined to lower pressures, as compared with the straight lines.

Fused quartz [5]. Experimental results for fused quartz are shown in Fig. 3. For pressures below 29 GPa the cell resistance (quasi-type) under compression varies with time. The minimum R_{min} is registered at the moment the shock wave reaches the second electrode. The resistance then goes on to increase smoothly and in ~ 0.5 μ sec reaches the constant level R_c . With increasing pressure, the difference between R_{min} and R_c levels out to appear completely at $p = 29$ GPa. At about 29 GPa the value of R increases abruptly by a factor of 2. Analysis of the processes involved in the shock compression of SiO_2 has shown that the temperature dependence of the resistance stems from the cooling of hot interlayers which develop in quartz disintegrated into microblocks. The abrupt change in the $\rho - p$ relationship is brought about by the microblock transition into a high-density phase and, as a consequence, a sharp decrease in the amount of the low-conductivity material relative to the conductors in liquid interlayers.

Sodium chloride. As in single shock-wave experiments, the electrical conductance of the monocrystalline NaCl under multiple compression is also unbalanced. At the same time the isentropic compression was found to result in a considerable decrease in the electrical conductivity in contrast to the values obtained in single runs (Fig. 4). We believe that the appearance of the unbalanced character of ρ is related (as in fused quartz runs) with the local build-up during solid shock compression.

Conclusion. In the SiO_2 and NaCl-type materials the front of the shock wave is followed by the unbalanced relaxation component of the electrical conductivity which develops mainly with the appearance of defects and heat release at the block boundaries. This effect masks nearly the specific nature of dynamic experiments on solids, which are by far insufficient to produce a transformation into the metallic state, and thus precludes any static interpretation. At the same time, in metals and other substances transition to metals (Bi, S, I), unbalanced phenomena, typical of dynamic compression, do not materially affect the nature and magnitude of the electrical conductivity.

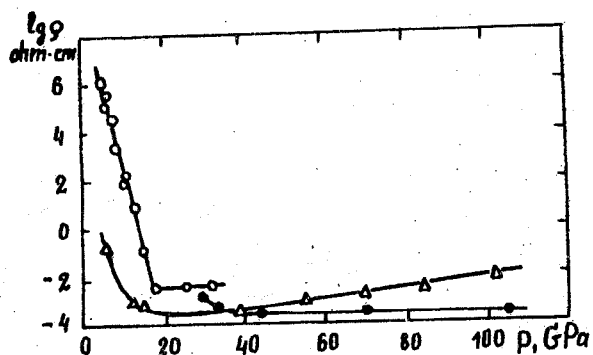


Fig. 1. Dependence of sulphur and iodine specific resistance on dynamic pressure:
 ○ - sulphur, single loading; ● - sulphur, multiple loading; Δ - iodine, multiple loading.

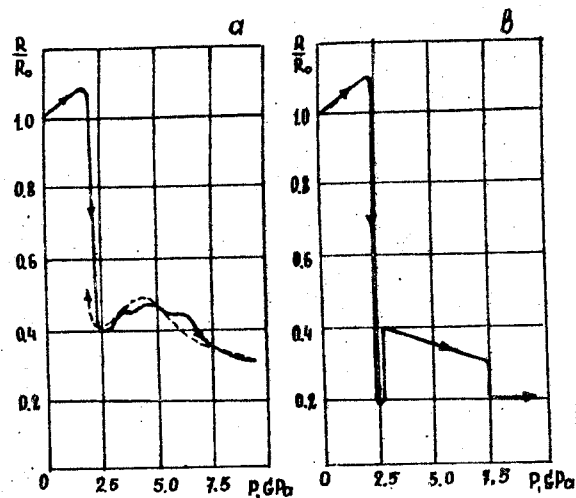


Fig. 2. Dependence of bismuth relative electrical conductivity on pressure:
 R_0 - initial resistance of the sample, a - isentropic compression and release (authors' data); b - static experiment.

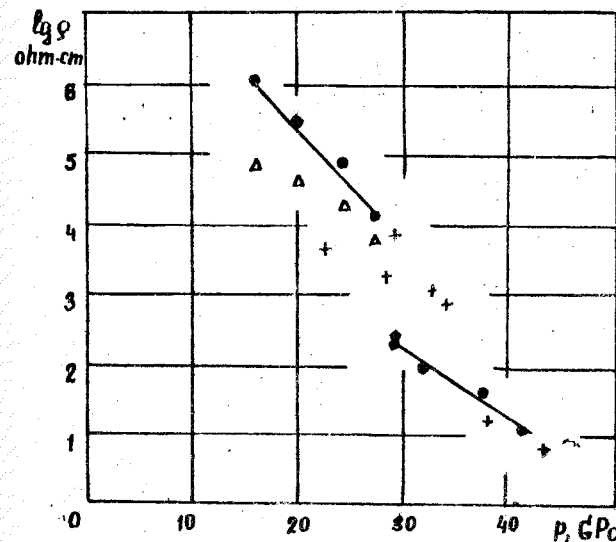


Fig. 3. $Q - p$ dependence for fused quartz:
 Δ - the data for R_{min} ; ● - the data for R_0 ; + - [Sawada A., J. Appl. Phys., 1981].

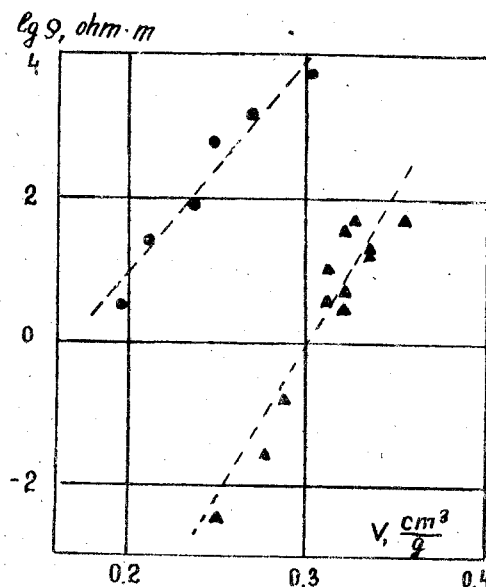


Fig. 4. $Q - V$ (specific volume) dependence for NaCl:
 - single shock compression [Al'tshuler and others, JETPh, 1960];
 - multiple loading (authors' data).

References

1. Postnov V.I. - The use of manganine detectors in pressure measurements to 1 Mbar - In: Non-standard problems of hydrodynamics, Novosibirsk, 1980, v. 48, p.II6 - II9.
2. Nabatov S.S., Dremine A.N., Postnov V.I., Yakushev V.V. - Sulphur electroconductivity measurements at superhigh dynamic pressures - Letters to JETPh, 1979, v.29, N7, p.407-409.
3. Nabatov S.S., Dremine A.N., Postnov V.I., Yakushev V.V. - Measurement of the electroconductivity of the condensed matter compressed up to 1 Mbar by multiple shock waves - In: Chemical physics of processes of combustion and explosion. Detonation. 1980, p.II7-II9.
4. Postnov V.I., Ananjeva L.A., Dremine A.N., Nabatov S.S., Yakushev V.V. Sulphur electroconductivity and compressibility under shock compression - FGV, 1986, v.22, 4, p.I06-I09.
5. Postnov V.I., Nabatov S.S., Yakushev V.V. - Behaviour of fused quartz behind the shock front by measuring electroconductivity - Proceedings of the 9th International Conference on High Energy Rate Fabrication, Novosibirsk, 1986, p.I06-I09.

EFFECT OF EXPLOSION TREATMENT ON WELDED JOINT PERFORMANCE IN STRUCTURES

V.G.Petushkov, Yu.I.Fadeenko, V.M.Pervoi
E.O.Paton Electric Welding Institute of the Ukr.SSR Academy of Sciences, Kiev, USSR

A new trend has recently formed in the industrial application of explosion energy, namely welded joints treatment in order to improve their performance and increase the metal structure reliability and life. Here, the decisive factor appears to be the lowering or rational redistribution of residual stresses (RS), inevitably developing in welding, as well as the formation, if necessary, of compressive RS local zones going down to a considerable depth from the loading surface.

The welded joint explosion treatment has several features which distinguish it from other known metal treatment processes. These are the locality of strong pulse application, whose intensity and spatial distribution can be easily controlled. The working pressure range is unusually limited to 1...10 GPa. The minute cord strip charges with very small specific masses of explosives can be used. The explosive charge is placed directly in the welded joint zones most susceptible to fracture initiation, in which high tensile welding stresses are generated and numerous small geometric stress raisers (undercuts, craters, rolls, etc.) are found. By placing inert gaskets of various thickness between the charge and metal, the plastic deformation zone depth can be varied from several tenths of μm to tens of mm, which greatly exceeds the possibilities of other methods of surface plastic deformation. The latter, as a rule, are characterized by one of the factors, namely, of lowering of initial RS, development of favourable compressive stress fields, surface hardening. Here, the improvement of one parameter can be accompanied by deterioration of the other. For instance, the welded joint thermal treatment to lower the welding RS is accompanied by a noticeable lowering of fatigue strength [1]. The explosion treatment has a combined effect.

The practical experience has shown that the explosion treatment allows to increase considerably the welded joint resistance to corrosion, fatigue and brittle fractures, their hardness and impact-abrasive wear resistance, product size stability, etc. The information about explosion treatment effect on welded metal structures service properties and examples of its practical application

in industry are given in /2,3,4/. In particular, explosion treatment results in qualitative changes in the failure mode of welded structures which are in contact with corroding media. For instance, after explosion treatment, the pipes carrying hydrogen sulphide containing gas, fail in pipe base metal at a distance from the weld, this corresponds to magnitude and distribution peculiarities of RS and electrochemical potential (Fig.1).

When the local explosion treatment is used to improve the welded joint fatigue strength a considerable positive effect is achieved by inducing the favourable biaxial compressive RS in the stress concentration zones, as well as by lowering the level of acting in the direction of the working loads. Here, the explosion treatment positive effect manifests itself not only at the fatigue crack initiation stage, but at its propagation stage as well. Fig. 2 shows the fatigue curves for alloyed steel welded joints.

The explosion welding positive effect on brittle fracture resistance is accounted for by the following factors: the magnitude of tensile RS is drastically lowered, the plastic deformation growth near the stress raisers is slowed down under load, the stress intensity factors are decreased, the brittle transition temperature is lowered. The local zones of compressive residual stresses can form, which become barriers in the brittle propagation path.

The explosion treatment leads to changes in steel structure especially in the near zone of explosion, where the pressures exceed those of $\alpha - \gamma$ -transition in iron (> 13 GPa). The low-alloy steels are characterized by such positive factors as strain hardening, improved hardness and wear resistance and by negative factors, i.e. increase of the brittle transition temperature, sometimes lowering of impact toughness. Subsequent thermo treatment is used in those cases when recrystallization and grain refinement are required. In alloyed steels of a complex composition the explosion and explosion-thermal treatments result in several insufficiently studied structural and phase transformations. For instance, formation of martensite in austenitic stainless steel.

References

1. Trufiakov V.I. Welded joint fatigue, Naukova Dumka, 1973, 215 p.
2. Petushkov V.G., Kudinov V.M. Welded joint explosion treatment, Avtomaticheskaya svarka, 1985, N 7, p.1-7.

Petushkov V.G., Soskov A.A., Kudinov V.M. The effect of RS distribution through the thickness of explosion-treated welded joints on their corrosion resistance. Avtomaticheskaya svarka, 1980, N 6, p.II-13.

Kudinov V.M., Trufiakov V.I., Petushkov V.G., et al. Parameters of explosive charges for RS relieving in welded joints. Avtomaticheskaya svarka, 1976, N 1, p.46-49, 61.

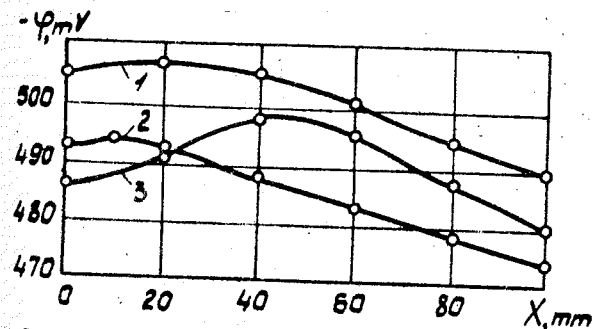


Fig. 1. The electrochemical potential distribution in the HAZ of welded steel 20 pipe in as-welded condition (1), and after thermal (2) and explosion (3) treatment.

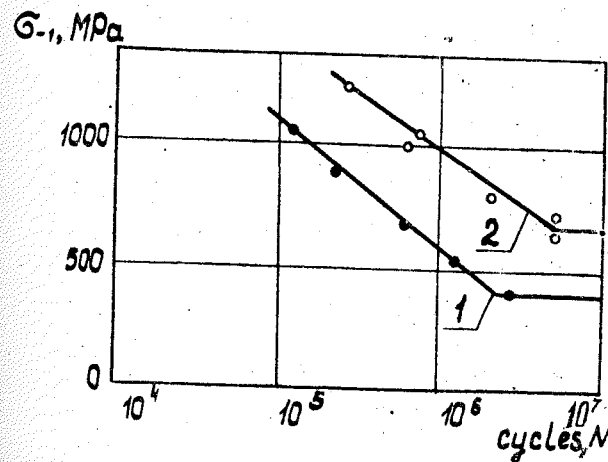


Fig. 2. The dependence of fatigue stress on cycle number ($R_G = 0$) for welded 15XCH steel specimens in the initial condition and after explosion treatment (2) /2/.

PECULIARITIES OF THE SHOCK COMPRESSION OF SUBSTANCE IN THE AXIAL SYMMETRY ARRANGEMENTS OF THE CONSERVATION

V.P. Alexeevsky

Institute for Materials Sciences, Academy of Sciences of
the UkrSSR, Kiev, USSR

Pressure, temperature and time of their action under the
shock compression /SC/ of a substance determine processes occurring
in it. Peculiarities of changing these values under SC in the
symmetry arrangements of the conservation are discussed.

In the cylindrical arrangement of the conservation with the
compact substance when using the charge with diameter 1.5-2 times
as high as the diameter of the arrangement made of an explosive
substance /ES/ with high decompose parameters, the shock wave
mechanism of the substance compression is predominant. Under the
formation of the three-wave configuration of shock waves SC-parameters
are determined by the technique using shock adiabatic lines /
and pressure is estimated by the equation:

$$p = \int \rho Du$$

where p - pressure; ρ - initial substance density, D - the
decomposition rate of ES; u - the mass rate of the substance behind
shock wave.

In the ring-shaped arrangement of the conservation /2/
the fine dispersed sample and the charge with diameter 3-4 times
the diameter of the arrangement SC of the substance occurs
the plastic flow of a metal of the cylindrical wall of the
arrangement of the conservation. Such "tube collapsing" even with
ES which have low decompose parameters is accompanied by the
arrangement and the concentration of energy on its inner surface
the rate of energy being increased with collapsing. As a result
pressure in the sample could exceed significantly that in the
decomposition front of ES used.

Under SC current flows of the substance appear in pores
cavities, local areas of heating and the action of superheating
pressure form which affect homogeneity of sample properties of
its decomposition and even the destruction of the arrangement
the conservation as a whole.

To estimate pressure values in axial symmetry arrangements
the conservation under SC of the substance by the set of equations
and to determine conditions of the sample conservation

using equations and expressions given in /3/, sums of col-
lapsing by suddenly applied constant pressure have been solved; of
the metallic tube, filled with the substance the state of which
described by the Tet's formula, and of the empty tube.

The highest p_0 in the substance at the stop moment of the
is:

$$p_0 = A [(1 - \omega_0)^{-n} - 1] \quad (2)$$

the tube radius at this moment a_0 is:

$$a_0 = a \sqrt{1 - \omega_0}$$

$$\omega_0 = \frac{I_0^2}{a^2 \gamma [p_b - k(1 - \frac{a^2}{b^2})] \ln \frac{b}{a}} \ll 1; \quad A = \frac{\gamma_0 c_0}{n}$$

γ, k - the initial inner and external radii of the tube,
density and coefficient of plasticity of a metal, from which it
is made, respectively; I, p_b - the impulse occurring at the moment
of applying pressure to the external tube surface and its con-
stant value, respectively; γ_0, c_0, n - density, the sound rate
index of polytrope of the substance compressed, respectively
approximation of ω_0 to unity corresponds to pressures under
the next conservation of the substance compressed is impos-

sible to determine conservation conditions of the substance under
it is necessary to consider local processes occurring in it.
The complexity of the pores and cavities configurations in
substances, variety of flows accompanying the collapsing make
the precise description difficult.

The simplest approximation of these processes by collapse
of the cylindrical axial symmetry tube is used /3/ for which
the parameter ratio of the process ("dynamic coefficient") is:

$$\omega = \left| \frac{I^2}{a_0^2 \gamma [p_0 - 2k_0 \ln \frac{b_0}{a_0}] \ln \frac{b_0}{a_0}} \right| \leq 1 \quad (3)$$

b_0, γ_0, k_0 - the initial inner and external radii of
the substance, density and coefficient of plasticity of the substance
respectively. The radii are expressed through the char-
acteristic size of the particle δ and porosity of the sample

by the equations:

$$\frac{\delta}{1 - \sqrt{1 - \epsilon}}; \quad b_0 = \frac{\delta}{1 - \sqrt{1 - \epsilon}} \quad (4)$$

where I , p_0 - the impulse, which occurs under the loading of sample with pressure p_0 (2). From (3) one can see the importance of pressure increase for SC results. When weak ES is used and the charge has a higher value $p_0 \neq 0$; $I = 0$ the pores would not close. When using powerful ES with thin charge the impulse loading only occurs $I \neq 0$; $p_0 = 0$ the pore collapsing takes place resulting in the destruction of the sample and the arrangement $\omega \gg 1$.

The analysis of the resolution obtained and experimental results show: 1) at $\omega < 1$ the pores do not collapse completely, SC-process is accompanied by the plastic flow of the substance irrespective of its nature, e.g. refractory carbides [2,5]; 2) at $\omega \approx 1$ the pores in the substance are closed completely, the temperature in any substance near a pore at the collapsing moment reaches the melting temperature irrespective of its thermophysical characteristics [3]. When there are many pores, the whole sample reaches the melting temperature. For example, the model tube has been made of the crushed titanium shavings in the ring-shaped arrangement of the conservation using SC-method, the tensile strength of the tube being 0.491 GPa, which agrees with the strength of cast titanium.

At $\omega > 1$ in the location of pore collapsing the substance comes overheated and starts to transform into plasma. If the destruction of the sample and the arrangement of the conservation could be prevented the active substance-transfer in the sample is observed (which is accompanied by synthesis of chemical compounds) from the sample to the wall of the arrangement of the conservation [7] and vice versa [6]. Such increase in sample temperature promotes synthesis of the phases of high pressure, e.g. cubic tungsten carbide [8].

Thus, the substance flow in the sample near pores and cavities affects greatly the final result of its SC.

References

1. Ададунов Г.А., Дремин А.Н., Конель Г.Н. и др. Определение параметров ударных волн в веществе при его сохранении в гидродинамических ампулах // Физика горения и взрыва. - 1967. - № 3. - С. 281-285.
2. Самсонов Г.В., Алексеевский В.П., Божко С.А. и др. Влияние ударных волн на структуру тугоплавких карбидов // Проблемы металлургии. - 1972. - № 1. - С. 93-99.
3. Алексеевский В.П. Действие ударных нагрузок на твердое тело. (Теория одного класса течений) // Тезисы докладов II Всесоюзной конференции "Лаврентьевские чтения по математике, механике, физике" (Киев, 9-11 сентября 1986).

гидродинамики им. М.А.Лаврентьева СО АН СССР, 1985. - С. 11-13.

Зельдович Я.Б., Райзер Ю.П. Физика ударных волн и высокотемпературных гидродинамических явлений. - М.: Наука, 1966. - 696 с.

Самсонов Г.В., Алексеевский В.П., Божко С.А. и др. Действие взрыва на тугоплавкие карбиды // Физика и химия обработки материалов. - 1973. - № 5. - С. 108-112.

Алексеевский В.П., Дубок В.А., Зайцева В.А., Михеев В.А. Некоторые особенности ударного сжатия чистого и легированного кремнезема в осесимметричных устройствах сохранения // Тезисы докладов XI научного семинара "Влияние высоких давлений на вещество" (Одесса, 16-19 сентября 1986). - Одесса, 1986. - С. 18.

Алексеевский В.П., Мазанко В.Ф., Печенковская Л.Е. и др. Исследование процесса миграции углерода в кристаллической решетке при ударном сжатии стеклотуглерода в стальном контейнере // ЖТФ. - 1979. - 49, № 4. - С. 824-827.

Самсонов Г.В., Алексеевский В.П., Билецкий Ю.И. и др. Кубический нитрид тантала, полученный методом ударного сжатия. - Киев, 1975. - С. 219-223. - (Препринт АН УССР. Ин-т проблем материаловедения; Исследование нитридов).

THE PECULIARITIES OF STRUCTURAL AND PHASE TRANSFORMATIONS IN CAST IRON UNDER SHOCK-WAVE LOADING

M.N.Voloshin

Institute for Superhard Materials of the Ukr.SSR Academy of Sciences, Kiev, USSR

At present much attention is paid to the problems of materials behaviour affected by high impulsive pressures. It is connected with the possibility of recording the material metastable states, improving their diffusibility, obtaining new physico-mechanical properties.

A number of works known /1-4/ have been done with the purpose of studying structural and phase transitions of Armco iron and steels subjected to dynamic loading.

The peculiarities of shock-wave loading of grey cast iron based on ferrite and pearlite at pressures higher than 6.0 GPa are discussed in the present paper.

The specimens were loaded by the plain shock wave generated by a liner accelerated up to high velocities in the result of explosion.

The metallographic study shows that the effect of impulsive pressure as high as 6.0 GPa on cast iron with the initial structure of ferrite and plate-like graphite results in the material strengthening through the ferrite twinning (Fig. 1a,b*). The grain microhardness has grown by 25 to 30% as compared with initial ($H_V = 1.5$ GPa).

The pressure amplitude increase provides for twinning and for traces of ferrite multiple distortion. The different degree of grain etching is observed in pressure range 20 to 30.0 GPa. The light grains usually have traces of distortions, while the dark ones are smooth (see Fig. 1c*). The hardness measurement does not show any essential difference between the grain strengthening and that means that all the grain transformation states are the same. The absence of the visible boundaries is apparently connected with their disordered dislocation structure.

The pressure amplitude further increasing up to 50.0 GPa causes the ferrite structure multiple distortion (Fig. 1d*). At the real metal strengthening can be observed at pressures above 50.0 GPa (Fig. 2). Applying of the higher loadings results in microhardness decrease.

* The figure is given at the end of the book

Such an effect is reported by /4/ when compared the results of Armco iron hardness measurements, subjected to loading with pressures of 45.0 to 100.0 GPa with the data obtained by G.E. Dieter at lower pressures. The metal hardness increase was observed with increasing the pressure amplitude to approximately 40.0 GPa only.

The hardness decrease should apparently be attributed to the effect of the loading heat component. According to R.H. McQueen and S.P. Marsh /5/ the temperature of iron in the shock wave reaches approximately 1000K under 50.0 GPa and after the unloading the residual temperature is about 500K. That creates the conditions for annealing.

Cast iron is a heterogeneous medium, its components having different wave and thermophysical characteristics. This accounts for the fact that the different components have essentially different temperature, the loading intensity being the same. Due to short-term loading (1 to 10 microsec) and inertia of the heat exchange processes the inhomogeneous temperature field in cast iron with higher temperature localities in the graphite impurities persists for some time after unloading too (For more details see /6/).

The temperature field inhomogeneity at dynamic loading of cast iron is the reason of both structural and phase transformations of the components. Thus when loading specimens with pressure 55.0 to 65.0 GPa the grinding of ferrite grains with the reduction of their average size from ~60 μm (initial) to about 6 μm is observed. The distortion traces are absent. The microhardness is raised down to 2.0 to 2.2 GPa.

The observed recrystallization was also reported by /1, 4/ with Armco iron loading. But in our case regions of the partial recrystallization around the graphitic impurities (Fig. 1d) and the regions wherein the process did not take place are mixed together with the regions of the full ferrite grains recrystallization.

Similar results have been obtained when pearlite cast iron structural transformations were investigated. But due to low plasticity of cementite much higher strains are needed for plastic deformation to transmit in pearlite.

Intensive deformation as a rule leads to a strong pearlite distortion and makes it difficult to determine the boundaries. Pearlite as well as ferrite undergoes the recrystallization.

The figure is given at the end of the book

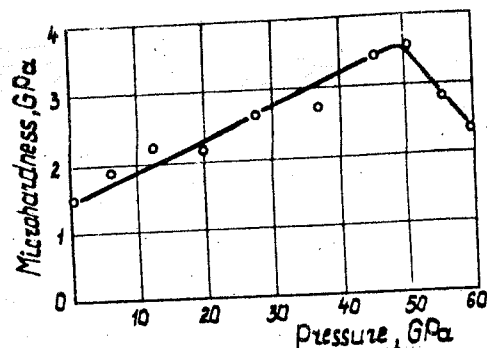


Fig. 2. The microhardness of ferrite grains in cast iron specimens vs. the applied loadings.

stallization but it occurs at higher pressures when the graphite-diamond phase transition takes place. The pearlite recrystallization is usually observed in the intensive diamond formation and is accompanied by decarbonization.

The graphite-diamond phase transition in the studied specimens was recorded under the pressures above 65.0 GPa. The inhomogeneity is also characteristic of it. Together with the diamond aggregates (consisting of a diamond skin and a graphite core) diamond and graphite impurities are present (Fig. 3*). Including metal regions are observed in the impurity-metal interface.

The analysis of iron and graphite Hugoniot as well as mathematical simulation of the diamond to graphite transformation process after unloading [7] show that the graphite inclusion affects significantly the phase transformations in cast iron.

References

1. Zukas E.G., Fowler C.M. The behavior of iron and steel impulsive loading // Response of metal to high velocity impact. - New York: Interscience Publishers, - 1961. - p. 369.
2. Атрошенко Э.С., Пашков П.О., Рядинская И.М. Исследование процесса взрыва армо-железа // ФММ. - 1966. - Т. 21. - С. 92-96.
3. Соболенко Т.М. Ударное сжатие малоуглеродистых сталей // ФММ. - 1966. - № 4. - С. 124-129.
4. Бражнев В.Б., Гелунова З.М., Пашков П.О. Некоторые особенности ударного нагружения железа // Металловедение и прочность материалов. Тр. Волгогр. политехнич. института. - С. 150-158.

* The figure is given at the end of the book.

Мак-Квин Р.Г., Мэри С.П. Уравнение состояния девятнадцати металлических элементов по ударноволновым измерениям до 2 Мбар // Динамические исследования твердых тел при высоких давлениях. - М.: Мир, 1965. - С. 93-143.

Андреев В.Д., Волошин М.Н., Малик В.Р. Исследование динамики установления равновесных температур в гетерогенной среде Me-C при ударном нагружении // Сверхтвердые материалы. - 1983. - № 6. - С. 5-9.

Андреев В.Д., Волошин М.Н., Малик В.Р. Исследование динамики графитизации алмаза в чугунах при ударном нагружении // Сверхтвердые материалы. - 1985. - № 3. - С. 9-14.

PECULIARITIES OF FORMATION OF METALLIZING LAYERS BY SHOCK-WAVE LOADING OF POWDER MATERIALS AND THEIR MIXTURES ONTO METALLIC SUBSTRATES

A.M.Kaunow, V.M.Bukin, L.N.Burminskaya
Volgograd Polytechnical Institute, Volgograd, USSR

The present work is a continuation of examining peculiarities of formation of metallizing layers under high pressures which are being developed during the shock-wave loading process of powder materials onto metallic substrates [1,2]. The main aim of this work is to examine the effect of shock-wave loading parameters on the character of formation, structure and strength of metallic powder and powder mixture coatings. The scheme of loading of the powder material with a metallic striker was applied in experiments. It permitted to vary widely the principal parameters of loading: collision rate of powder material with the substrate (V_c) and the rate of load movement along the surface to be coated (V_k). Both one-component powders Ti, 12X18H9, Cr, Ni, PGXH808 and powder mixtures Ni+Al, Cr+C, which were loaded onto the steel substrates were used as coating materials. The structure and phase composition of coatings were examined by metallographic, X-ray diffraction analyses as well as by X-ray spectroscopic analysis.

Sharing was carried out to determine adhesion strength of coating to the base materials in accordance with the method [3].

It was found out the existence of critical conditions for one-component metallic powders under the investigation. They determine the solid-liquid transition mechanism of forming the coating. These conditions are uniquely characterized by the V_c and V_k values. Thus, if V_k is less than the sound velocity in the substrate material then the powder material melts when V_c is forming a thin layer of several dozens of micron on the substrate material. If V_k is higher than the sound velocity in the substrate material then the melting of powder material occurs when the collision rate is $V_c > V_{c2}^*$, the value of which is 2 and more than the V_{c1}^* . An estimate of this critical collision rate V_{c2}^* can be obtained from the melting condition of powder material taking into account the melting temperature changes with pressure according to the following dependence:

$$V_{c2}^* = \sqrt{\frac{2(H + C_v(T_m - T_0))}{1 - C_v \frac{\rho_m \rho_0}{\rho_m \rho_0} \cdot T_m \frac{V_{liq} - V_{sol}}{H}}}$$

where H - latent heat of fusion; C_v - specific heat capacity; T_m and T_0 - melting and starting temperatures of powder material, respectively; ρ_0 and ρ_m - bulk density and the density of the powder grains, respectively; V_{sol} and V_{liq} - specific volume of solid and liquid phases of powder grains, respectively.

The results obtained allow to build up the structural diagram for every coating powder material by means of calculations and tests (Fig.1). The diagram enables to predict the conditions of coating formation, composition and properties. Some other coating formation peculiarities should be taken into account in this case.

It has been established that the structure and strength properties of coatings just as in the case of explosive compacting [4,5] are determined by the character of the plastic grain deformation in the process of expanding the shock wave along them. During this process the coarse grains with more developed surface are subjected to maximum deformation. It is the result of greater amount of concentration of shock wave energy on their contact boundaries. The intense plastic flows of the surface layers grains lead to the decrease in the critical collision rate (Fig.2). The upper and lower curves in Fig.2 limit the corresponding V_c values, above which coatings are formed by the liquid phase mechanism, below which value they are formed by the solid phase mechanism.

Adhesion strength tests of coatings formed by the solid phase mechanism have shown that the plastic deformation of grains definitely influences the strength properties of coatings as well. The adhesion strength increases with grain sizes (Fig.3).

The adhesion strength of the solid phase coatings depends on the method of preparation of the substrate surface. It is found that the surface roughness may influence greatly the adhesion strength of the coating. Thus, the adhesion strength of nickel coating deposited on the ground surface is higher than that of coating on a cutter-machined surface (Fig.4). It can be proved by the results of the present in the shock-wave loading process of the powder material that the air present in inter grain pores is partially expelled towards the surface and is compressed. In the case of rougher surface the air expelling beyond the base material to be coated in the process of the slicing shock wave expansion is rather difficult because of relatively high microirregularities and it propagates partially closed among these microirregularities. The air having travelled and unloading done, the closed and compressed air expands and may cause the rupture of bonds between the coating and the base, which results in discontinuity

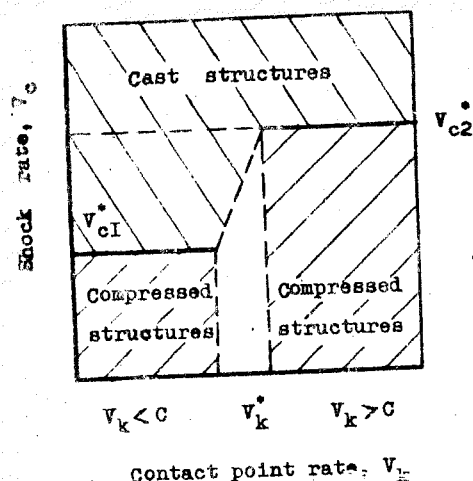


Fig. 1. Structure-phase diagram for predicting the rational conditions of creation and the types of the structures of the powder coatings.

Fig. 2. The influence of the powder dispersion on the critical shock rate of the powder material and the metallic base material: 1 - 12X18H9-spongy; 2 - 12X18H9-spherical; 3 - Ti-spongy.

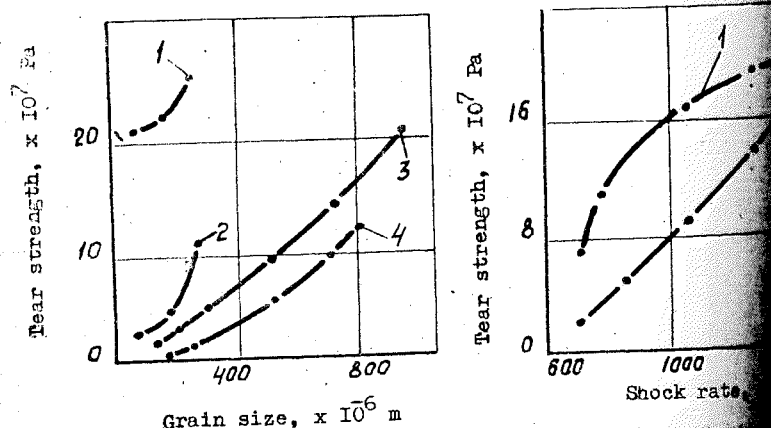


Fig. 3. Influence of the dispersion of the powder material on the adhesion strength of coatings formed by solid phase mechanism: 1 - 12X18H9-spongy; 2 - Ti-spongy; 3 - 12X18H9-spherical; 4 - PGXH80SR-3-spherical.

Fig. 4. Dependence of adhesion strength of nickel coatings on the collision rate and the surface roughness of the base material:

1 - base material was ground; 2 - base material was cut

along the bond boundaries. In the case of higher surface finish the air being expelled towards the metallic base material has apparently time to escape it. As a result the adhesion between the base material and cladding is of much higher quality.

The studies of the peculiarities of the formation of coatings from metallic and non-metallic powder mixtures Ni+Al, Cr+C showed that no essential indication of reaction throughout the coating has been observed during the solid-phase formation. However, intense heating during the process of plastic deformation of the surface layers results in creating the conditions for formation of the chemical interreaction zones along the contact boundaries. Thus the solid phase coating formations from nickel and aluminium powder mixtures in the supersonic contact regions leads to the formation of the layer of 15-30 μ m thickness along the boundaries which is the solid solution on NiAl base. The most favourable conditions for physico-chemical reactions between the initial components of powder mixtures emerge in the case of complete melting of at least one the components in reaction. The phase composition of coatings formed by the liquid phase mechanism both in supersonic and in undersound regime ranges is the same and doesn't correspond to the equilibrium one. It depends on the percentage of the initial powder mixture components. The system Ni+Al was found to produce intermetallide Ni₃Al in the whole of concentration range. Formation of Cr₃C₂, Cr₇C₃, Cr₂₃C₆ carbides was observed in the system.

Thus, the results obtained allow to predict both the formation, composition, structure of powder coatings as well as their properties that should be taken into account in practice.

References

1. M. Kaunov. On some peculiarities of coating formation by explosion powder spray on solid supports. Proc. of the 11th Congress on Explosion Treatment of Materials. Novosibirsk. 1982, p.272-274.
2. M. Kaunov. Explosion welding of powders with metals. Proc. of the International Symposium on Explosion Treatment of Metals. Novosibirsk, 1982, p.236-246.
3. I. Glaskov, A.M. Kaunov, V.S. Sedich, A.P. Sonnov. Investigation of the cohesion strength of claddings applied to steel base by explosion. Problems of Strength, 1976, N7, p.120-122.
4. V. Roman, V.F. Nesterenko, I.M. Pikus. Effect of powder grains on explosive compacting process. Burning and Explosion Physics, 1979, N5, p.102-107.
5. I. Staver, G.E. Kuzmin, V.F. Nesterenko. Experimental study of shock waves in porous media. Proc. of the 11th Congress on Explosion Treatment of Materials. Novosibirsk. 1982, p.150-156.

ALTERNATING PRESSURE-INDUCED PHASE TRANSFORMATION IN HARDMETALS

E.M.Chistyakov¹, V.N.Vinnichenko², A.V.Belostotskiy³,
I.M.Mukha⁴

¹Institute for Superhard Materials,

²Advanced Training Institute, ³Kiev Polytechnic Institute,

⁴S.P.Korolev Plant

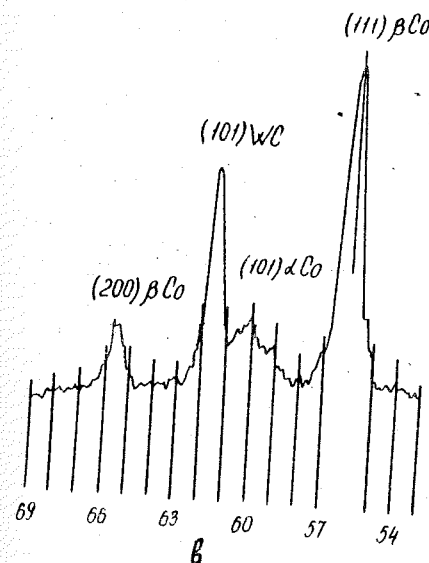
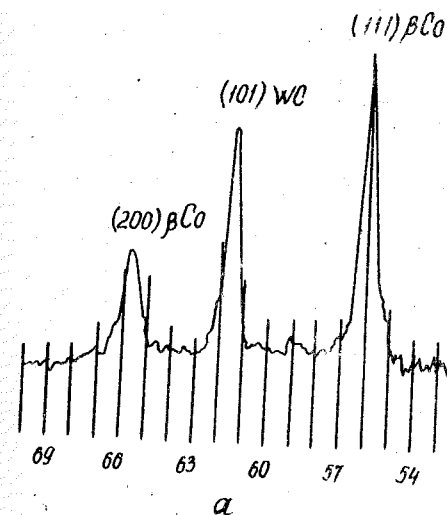
The effect of ultrasonic vibrations on physico-mechanical properties of a variety of hardmetals is investigated. A hard-metal grade, an intensity of ultrasonic waves, as well as an exposure time are found to effect greatly on the phase composition of hardmetals causing changes in their physico-mechanical properties.

Investigations were done with specimens of BK2, BK3, BK8, BK20 and BK50 hardmetals. Intensity of ultrasonic waves introduced into the specimens ranged from $100 \cdot 10^4$ to $120 \cdot 10^4$ J/m².c.

The results were analyzed using a combination of various testing procedures including X-ray diffraction analysis, electron microscopy, metallographic tests, dilatometric, thermomagnetic, sistometric and durometric test techniques as well as a high rate X-ray analysis and impact and strength tests. Mathematical processing of the data obtained was done on model M6000 electronic computer.

The analysis of diffraction patterns from BK20 hardmetal -received shows that a hexagonal modification of Co is not present at all or is present in quantities which can not be detected by a diffractometer (Fig.1).

Ultrasonic treatment causes changes in the phase composition of hardmetals: diffraction patterns from hardmetals exposed to ultrasonic waves for 120 s exhibit α -Co lines indicating the presence in a hexagonal Co content in binder phases of hardmetals. The intensity of β -Co lines being somewhat attenuated while, in its turn, the decrease in cubic Co content.



A fragment of the diffractogram of BK20 hardmetal before and (b) after ultrasonic treatment.

A high-cobalt BK50 hardmetal was taken as an example to measure α -Co content in binder phases in hardmetals as a function of the exposure time. It is found from the dilatograms that α -Co content in a binder phase in a nontreated hardmetal is about 18% to 18%.

Ultrasonic treatment causes increase in α -Co content which is the function of the exposure time. Thus, 60 s exposure doubles α -Co content, after 300 s exposure it rises 2.5-fold and after 7200 s it triples (see Table), the interval of the phase transformation being increased by 100 °C, 120 °C and 130 °C, respectively. The beginning and the completion of the phase transformation at an exposure time approaches 7200 s shift to higher temperatures by 60 °C and 180 °C, respectively (as compared with that for nontreated hardmetals).

Because of the phase transformation in a binder phase induced by ultrasonic waves a relief specific for martensite transformation appears in sites of the phase occurrence (Fig.2*).

Thus, ultrasonic treatment causes the phase transformation of Co in a binder phase in a hardmetal, extends an interval of phase transformation shifting it to higher temperatures.

It is shown that the hexagonal modification of Co influences to a great extent the crack propagation in these materials under subsequent static or dynamic loading. Thus, slip bands in grains resulted from ultrasonic treatment of the hardmetals in the propagation direction of cracks which cross these bands in a binder phase of ultrasonically treated hardmetals the crack propagation is restrained with clusters of stacking faults and α -Co crystals. Co-interlayers in ultrasonically treated hardmetals may arrest the crack propagation at all due to the

* This Figure is given at the end of the book.

Effect of exposure time on the phase transformation of Co-binder in BK50 hardmetal

Exposure time, s	Interval of the phase transformation, °C		α -phase content, %
	$t_{\text{begin.}} - t_{\text{compl.}}$	Δt	
0	460-580	120	I7-I8
30	480-680	200	28-30
60	480-700	220	33-34
300	480-720	240	43-44
3600	520-760	240	47-48
7200	520-760	240	47-48
After annealing	460-580	120	I7-I8

internal forces, which suffice for crack propagation in specimens exposed to ultrasonic waves.

The durometric test results show that ultrasonically treated hardmetals tend to the increase of their hardness.

Ultrasonic treatment improves the strength properties of hardmetals. Bending strength of a variety of hardmetals may be increased by up to 110-115%.

The results obtained were used for the improvement of the wear resistance of hardmetal tools. Thus, for example, ultrasonic treatment doubles or triples the wear resistance of solid hardmetal tools used for drilling holes in printed-circuit boards.

SHOCK-WAVE LOADING INFLUENCE ON CRYSTALLIZATION OF METALLIC GLASSES

A.A. Bondarenko, L.V. Kashkina, V.I. Kirko, A.A. Kusovnikov
Institute of Physics of Siberian Branch of the USSR Academy of Sciences, Krasnoyarsk, USSR

We discuss here the advantages of powder dynamic compacting approach for preparation massive components from metallic glasses. In this context the studying the structural changes in metallic glasses caused by shock-wave loading is of particular interest. It is established that such a treatment influences the structure of the alloys and may manifest itself in crystallization processes changes [1-3].

The aim of our research was to study influence of shock-wave loading on crystallization of Fe-B metallic glasses, to compare results with those, received in static pressure experiments [4].

We investigated $Fe_{1-X}B_X$ -type metallic glasses ($X = 16-25$ at%) which have been produced in the shape of films 25-30 μm thick and 10-20 mm in width by quenching from melt. Diagram of shock-wave loading experiments with pressure ~ 50 GPa and duration $1 \mu s$, is shown in Fig. 1. The pressure was created with a metal striker which was thrown by explosive matter against a pocket of plates with samples between them. Pressure and residual deformation had been checked.

Film samples were studied with X-ray analysis, (Cu K α - radiation) and differential analysis (isochronous heating, speed $deg./min$ to $900^\circ C$). Changes in surface were studied with EMMA-scanning electron microscope. The film samples were glued on the surface of X-ray cuvette, waveness of film surface was not checked.

The film samples were reduced to small fragments for differential thermal analysis. We investigated the influence of sample shape on DTA curve shape and found, that film samples cannot be tolerated for these measurements due to visible shift of temperature peak and changes in DTA-curves.

It was found, that surface of samples changed essentially after shock-wave loading. We may see some narrowing of the X-ray diffraction curve peak after the influence of pressure. Shock-wave loading does not change the shape of DTA-curve, but some changes in position of crystallization peak are seen.

Surface phenomena due to flowing sample matter in roundness of the surface produce difficulties during the analysis of

surface changes. To limit the deformation of the surface its irregularities were filled with liquid. In this case shock-wave loading formed circular structure on the surface of the samples similar to that observed for 71 KNSR alloy [5].

Characteristic DTA curve for initial alloys is shown in Fig. 2a. Eroding relaxation maximum at $\sim 200^\circ C$ and four exothermic peaks at temperature between $460-900^\circ C$ are observed. The first of them corresponds to temperature of crystallization, the others define the different stages of crystallization. The samples were heated in vacuum to temperatures, defined by DTA and were quenched for the purpose to define the structure of the precipitated phases. Phase composition of $Fe_{83}B_{17}$ alloy is given in Table. It was shown by X-ray diffraction analysis, that the samples kept amorphous state after shock-wave loading up to 50 GPa. The temperature of crystallization T_x rose up to $\sim 10^\circ C$ for the alloys investigated. The temperature of subsequent crystallization stages did not shift according X-ray differential analysis, composition of the phases did not change after shock-wave loading (for $Fe_{83}B_{17}$ alloy).

It was found, that crystallization heat defined from area under the first peak for $Fe_{84}B_{16}$, $Fe_{83}B_{17}$, $Fe_{82}B_{18}$ compositions practically did not change after shock-wave loading. However, for $Fe_{75}B_{25}$ alloy we saw crystallization heat increase by a factor of 1.5. Ratio of the total area under the II and III peaks to area under the I peak of DTA-curve is shown in Fig. 2b. A slight reduction of this value after shock-wave loading due to decrease of total area is observed, which is essential for $Fe_{75}B_{25}$ alloy.

Discussion

The temperature of crystallization of Fe-B amorphous alloys changes by 15 K/GPa with static pressure [4]. Some increase in temperature after shock-wave loading may be caused by difficulties in diffusion processes due to condensation of matter. At the same time under static conditions changes were observed in the structure of precipitated phases, due to lowering of Fe-fraction and change in correlation between orthorhombic α - Fe_3B and tetragonal γ - Fe_3B . So far as γ - Fe_3B -phase is denser than α - Fe_3B , we suppose, that this phenomena is influenced by shock-wave loading. But X-ray analysis becomes complicated due to close proximity of α - Fe_3B and γ - Fe_3B lines. The reduction of total area under the II and the III peaks in Fig. 2a,b which corresponds to de-

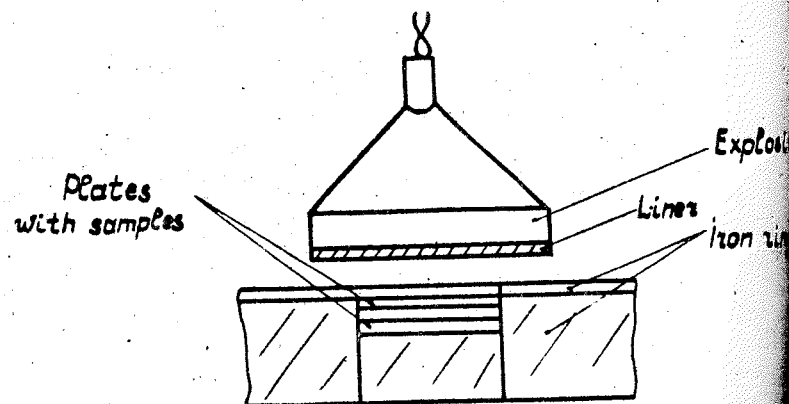


Fig.1. Diagram of shock-wave loading for $\text{Fe}_{83}\text{B}_{17}$ amorphous alloy.

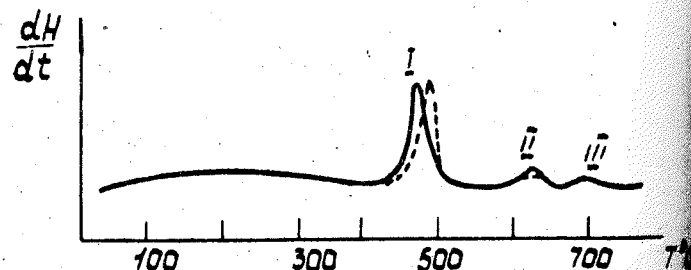


Fig.2a. DTA curve for $\text{Fe}_{83}\text{B}_{17}$ alloy: (—) in initial state; (---) as treated with shock-wave loading.

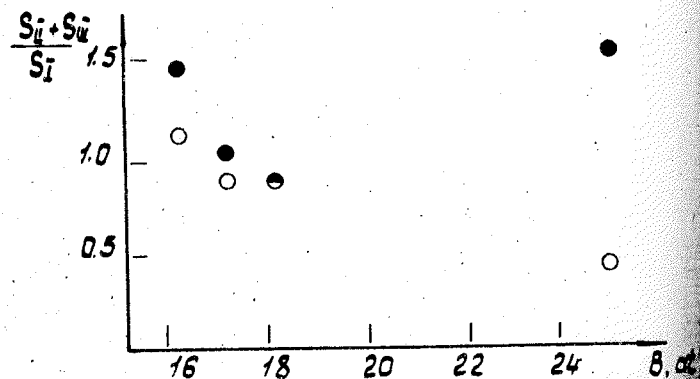


Fig.2b. Relation between areas under II and III peaks ($S_{II} + S_{III}$) and area under Ist peak (S_I) as a function of B concentration in initial (●) and treated (○) alloys.

composition of Fe_3B into Fe and Fe_2B verifies changes in $\alpha\text{-Fe}_3\text{B}/\gamma\text{-Fe}_3\text{B}$ ratio.

Composition of $\text{Fe}_{83}\text{B}_{17}$ alloy after crystallization

Alloy	Point of crystallization T_x , TOC	Number of a peak	Phase composition
$\text{Fe}_{83}\text{B}_{17}$	480	I	$\alpha\text{-Fe} + \alpha\text{-Fe}_3\text{B} + 2\text{Fe}_2\text{B} + \text{FeB}$
	640	II	$\alpha\text{-Fe} + \gamma\text{-Fe}_3\text{B} + \text{Fe}_2\text{B}(\text{traces}) + \text{FeB}$
	690	III	$\alpha\text{-Fe} + \gamma\text{-Fe}_3\text{B} + \text{Fe}_2\text{B} + \text{FeB}$
	900	IV	$\alpha\text{-Fe} + \text{Fe}_2\text{B} + \text{FeB}(\text{traces})$

Conclusions

It was found, that Fe-B amorphous alloys preserved their structure after shock-wave loading under pressure of 50 GPa. We suppose, that heat of crystallization changes after treating due to redistribution between $\alpha\text{-Fe}_3\text{B}$ and $\gamma\text{-Fe}_3\text{B}$, $\gamma\text{-Fe}_3\text{B}$ being predominant.

References

- R.S. Iskhakov, V.I. Kirko, A.A. Kusovnikov et al. Shock-wave loading effect on the structure and magnetic characteristic of amorphous alloys. The 3d Symposium on amorphous magnetism, Samarkand, 1983. Abstracts, p.41.
- Wang Wen-Kni, He Shou-An, H. Iwosaki, Y. Syono, T. Goto. Phases stability of an amorphous $\text{Co}_{80}\text{B}_{20}$ alloy under high pressures and high temperatures. Mat. Res. Soc. Symp. Prog. Vol. 22 (1984) Els. Sci. Publ. Co.
- A.M. Durachenko, E.Y. Malinovichka, N.D. Markelov. Influence of shock-wave loading on structure and properties of $\text{Fe}_{60}\text{Si}_{90}\text{B}_{20}$ amorphous alloy. Isv. Acad. Soc. USSR, Metals, 1986, N 2, p. 170-172.
- I. Ogawa, S. Endo, M. Kiritani, F.E. Enjita, A. Fukisava. Effect of pressure on the crystallization of amorphous Fe-B alloys. Jap. J. Appl. Ph. Vol. 23, N2, 1984, p.142-145.
- R.S. Iskhakov, V.I. Kirko, A.A. Kusovnikov et al. Investigation of changes in microstructure of amorphous alloys under shock-wave loading. The IXth Int. Conf. on High Energy Effect Rate on Materials, Novosibirsk, 1986, p.70-74.

K. Jach

S. Kaliski Institute of Plasma Physics and Laser Microfusion
P.O. Box 49, 00-908, Warsaw, Poland

1. Introduction

The paper presents exemplary results of numerical calculations dealing with deformation and acceleration of metal layers by the explosive material (phenomena of the so called classical and reverse cumulation). Those results were achieved by means of a numerical code which was based on the so called "method of free particles" /1,2/. This code enables to solve non-stationary, two-dimensional problems of explosive materials detonation, reaction between detonation waves and solid bodies and deformation and acceleration of these bodies /3,4,5,6/.

2. Mathematical-physical formulation of the problem

The detonating explosive material was described by classic equations of gas dynamics and by semi-empirical equations of state.

The body loaded by the pressure of detonation products is shown in the examples, a copper cumulative liner with the obtuse angle of 150° (Fig. 1* - the so called reverse cumulation) and 60° (Fig. 2 - classical cumulation).

Previous experiences /1,2/ indicated that, in order to achieve qualitative and quantitative compatibility between the theory and experiment, the description should include as follows:

- general equations of the theory of elastic/visco-plasticity
- phenomenological model of cracks forming in solid bodies

Constitutive relations are as follows:

$$\dot{S}_{ik} = 2\mu \left(\dot{\epsilon}_{ik} - \frac{1}{3} \dot{\epsilon}_{11} \delta_{ik} \right) - \frac{\mu}{\eta} \Phi S_{ik}$$

$$\Phi = 1 - \frac{\sqrt{\frac{2}{3}} Y}{\sqrt{S_{ik} S_{ik}}}; \quad \Phi \geq 0$$

The dependence of Y and μ on plastic deformation, pressure and temperature was adopted according to the Steinberg model. The model of forming and growth of cracks was adopted like in /7/:

* The Figure is given at the end of the book

$$\dot{V}_c = K \operatorname{sign}(\delta) \left[|\delta| - \delta_0 \frac{V_{cI}}{V_c + V_{cI}} \right] (V_c + V_{c0})$$

$$\dot{V}_c = 0 \quad \text{for } |\delta| < \delta_0 \frac{V_{cI}}{V_c + V_{cI}}$$

$$V_c = \frac{I}{\rho} - \frac{I}{\rho_s}$$

where: V_c is the specific volume of cracks, ρ_s is the density of the solid body phase, K , V_{cI} , δ_0 , V_{c0} - constants.

Computer experiments showed that the dependences of the viscosity on temperature $\eta = \eta(T)$ and limitation of Y , μ and η caused by the growth of cracks volume are very important for achieving compatibility between the theory and experiment. The best results achieved so far were the ones in which, like in /8/, the dependence $\eta(T)$ was adopted as follows:

$$\eta = 5 \cdot 10^{-3} e^{\frac{4380}{T}} \quad [\text{Pa} \cdot \text{s}]$$

is temperature in Kelvin scale.

However, the limitation of Y , μ and η caused by the growth of cracks volume was accepted in the following form /7,9/:

$$Y^T = Y \cdot F; \quad \mu^T = \mu \cdot F; \quad \eta^T = \eta \cdot F; \quad F = \exp(-7\rho V_c)$$

Conclusions

The presented model and numerical code enable to achieve effective solutions of cumulation theory problems (including phases of very big deformations and fragmentations).

The dependences: $\eta = \eta(T)$ and Y , μ , $\eta = f(V_c)$ have a great influence for achieving quantitative compatibility of the theoretical and experimental results. The dependences mentioned above have not been investigated. They should be treated, at present, as one of the possible solutions of the problem. In the conditions of computer experiments carried out by the author they showed good compatibility between the theory and experiment. (Fig. 1* - theory, Fig. 2 - experiment).

References

1. Jach, E. Włodarczyk, J. Techn. Phys., 1986, 27, 1-2.
2. Jach, PMTF, 1987, 2.
3. De Rouvray, et al., Structural Impact and Crashworthiness, Wiley Lectures, 1994, 1.
4. Merziesky, et al., DAN USSR, 1986, 290, 6.

5. N.Légrand, J.Ovadia, Symposium H.D.P. Paris, 1978.
6. P.C.Chou, et al., J.Appl.Phys., 1976, 47, 7.
7. S.G.Sugak, et al., FGV, 1983, 19, 2.
8. M.M.Carrol, et al., J.Appl.Phys., 1986, 59, 6.
9. L.Seaman, et al., J.Appl.Phys., 1976, 47, II.

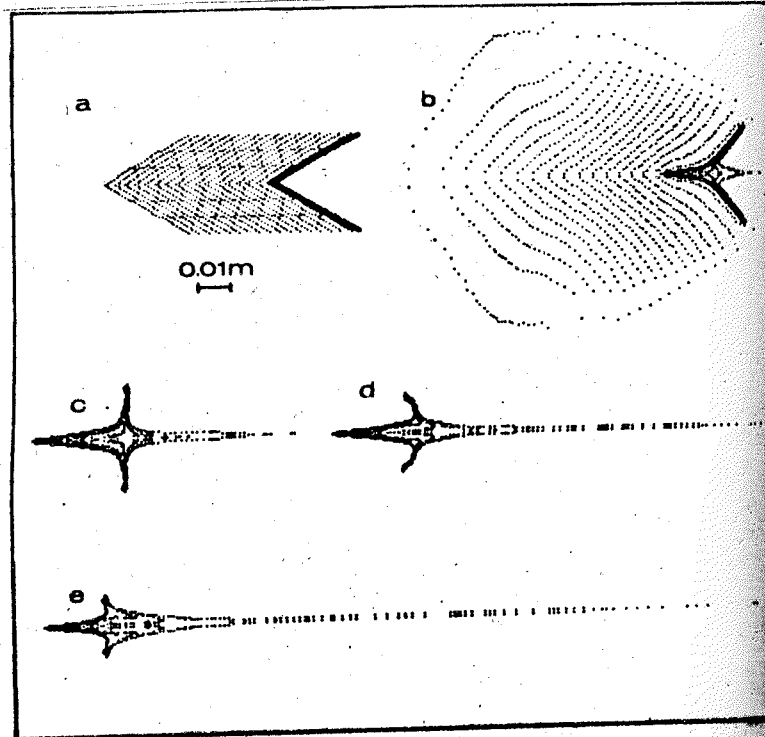


Fig.2. Classical cumulation $\alpha = 60^\circ$, cylindrical symmetry;
a) $t = 0$; b) $t = 13 \mu s$; c) $t = 20 \mu s$; d) $t = 33 \mu s$; e) $t = 40 \mu s$

PHASE TRANSITIONS AND CRITICAL PHENOMENA IN LIQUID CRYSTALS AT HIGH PRESSURE

R. SHASHIDHAR
Raman Research Institute
Bangalore 560080, India

Abstract. Liquid crystals are amongst the most interesting condensed states of matter. Some important advances in high pressure research on phase transitions and critical phenomena in liquid crystals are reviewed. Analogies with similar phenomena observed in other areas of condensed matter physics like magnetic systems and superconductors are discussed.

Introduction

Liquid crystals belong to a state of matter which is intermediate between a fully ordered crystalline solid and completely disordered isotropic liquid [1]. Liquid crystals are amongst the most interesting condensed states of matter. It is now realised that insights gained into their properties can help us to understand other condensed phases that exist in nature. In all condensed phases there are thermally excited fluctuations. Depending on the spatial dimensions, symmetry and nature of inter particle interactions, these fluctuations play a major role in determining the properties of condensed matter. In some materials, the fluctuations do not play an important role and the properties can be understood by means of mean field theory. In some other materials the fluctuations alter the properties profoundly in the vicinity of phase transitions. This is the class of phase changes which are known as critical phenomena. Thanks to the recent outstanding theoretical developments due to Kadanoff, Fisher and Wilson, there has been a considerable improvement in the understanding of the phase transitions and critical phenomena. It is for this reason that an understanding of the phase transitions in liquid crystals is considered an important advancement in condensed matter physics. The purpose of this article is to give an overview of the important discoveries and developments which have been achieved in phase transitions in liquid crystals using high pressure as a probe.

We shall be concerned here only with the three simplest types of liquid crystals, viz., the nematic, smectic A and smectic C liquid crystals. The molecular arrangement in these phases is schematically represented in Fig. 1. The nematic liquid crystal (Fig.1a) has long range orientational order, but no long range positional order. The smectic A and C liquid crystals are layered in one-dimension, i.e., the

have nematic order combined with a one-dimensional density wave along the director. The molecules are orthogonal in the case of the former and tilted in the case of the latter (Figs. 1b & c).

The nematic-isotropic transition is generally weakly first order while the smectic A-nematic (A-N) transition can be either first order or second order [2]. The smectic A-smectic C transition which is always second order is supposed to belong to the same universality class as the superfluid transition in Helium [4]. The nematic-smectic C transition is a fluctuation driven first order transition [4]. It is therefore clear that the potentialities for multicritical phenomena in liquid crystals is very rich. The field is relatively new and it is exactly here that high pressure comes in very useful. A number of important discoveries have been made by studying liquid crystalline transitions at high pressure [5]. I shall enumerate here only three of these, viz., the smectic A-nematic tricritical behavior, the reentrant nematic phenomenon and the nematic-smectic A-smectic C multicritical point.

A. The Smectic A-Nematic Tricritical Point

The close analogy between the smectic A and the charged superfluid was first pointed out by de Gennes. The vector potential of the superfluid corresponds to the director (mean molecular direction) of the smectic A while the superconducting order parameter corresponds to the translational order parameter of smectic A. The tricritical point is defined as that at which the order of a phase transition changes from first to second order under the influence of a field which is not directly coupled to the order [6]. The possibility of observing the smectic A-nematic (A-N) tricritical point was pointed out theoretically by McMillan [7] who predicted that the A-N transition should become second order when the ratio of the smectic and nematic-isotropic (N-I) transition temperatures is less than 0.88. The observation of a tricritical point in a liquid crystal using high pressure technique was by Keyes, Weston and Daniels [8] who on the basis of their measurements on the intensity of transmitted light identified a tricritical point for the smectic A-cholesteric transition in cholesteryl oleyl carbonate. (The cholesteric phase is looked upon as a nematic with a helical structure superposed on the uniaxial nematic.) This result was confirmed by DTA studies of Shashidhar and Chandrasekhar [9] and by the volumetric studies of Shichijyo, Okamoto and Takemura [10]. The former studies showed that the heat associated with the transition diminishes as one approaches the tricritical point (Fig. 2) while the results of Shichijyo *et al.*

show that the volume change at the transition goes to zero at $T_{AN}/T_{NI} \approx 0.89$ (Fig. 3) which is in good agreement with theory. There have also been reports on the observation of a tricritical point for the smectic A-nematic transition [11,12].

Thus the A-N tricritical point in a single component liquid crystal is quite well established. This tricritical behavior arises due to the coupling between the smectic and nematic orders. As the range of the nematic phase decreases (i.e., with decreasing T_{AN}/T_{NI}) this coupling gets weaker and the A-N transition becomes first order. Experiments to determine the exponents associated with the A-N transition near the tricritical point are underway. These data should throw more light on the expected helium-like critical-tricritical crossover. Indeed such a crossover has been seen very recently in binary liquid crystal mixtures at atmospheric pressure [13].

The Reentrant Nematic Phenomenon

Cladis *et al.* [14] observed an unusual universal pressure-temperature (P-T) diagram for 4-n-octyloxy-4'-cyanobiphenyl, a material with a strongly polar cyano group. This diagram which is reproduced in Fig. 4 showed that the A-N phase boundary curved back towards the temperature axis. As a consequence, they observed that in the pressure range of 1.6-1.8 kbar, the sequence of transitions on cooling was smectic A - nematic - smectic A. This second or lower temperature nematic phase has been designated as the "Reentrant Nematic Phase". The appearance of a more symmetric or less ordered nematic phase at a lower temperature raises basic questions for the understanding of liquid crystals. It is interesting that this reentrant phenomenon has been predicted theoretically [15] and found experimentally in superconductors.

Since this important discovery of Cladis, a large number of materials have been synthesized which exhibit the reentrant nematic phase at atmospheric pressure. Exhaustive pressure studies [17,18] have been conducted on such materials and these have led to two important observations. (i) The A-N phase boundary is generally curved. (A typical P-T diagram is shown in Fig. 5) and (ii) the maximum pressure (P_m) up to which the smectic A exists at high pressure is related to the atmospheric pressure (P_0) and the range (R) at atmospheric pressure by the expression, $P_m = P_0 \exp(-mR)$, where P_0 and m are empirical constants which depend on the molecular structure. The validity of this relation has been confirmed for over 30 substances. This remarkable universal-like relation which indicates a coupling between smectic and nematic orders is not explained by any of the existing theories so far.

Another dramatic manifestation of the coupling between the nematic and smectic ordering in reentrant nematic systems is seen in Fig.5. It is seen that the major axis of the elliptic shaped A-N phase boundary is parallel to the nematic-isotropic (N-I) phase line. Studies on different systems showed that the tilt of the major axis is in fact exactly the same as that of the N-I line although the slope varies widely from system to system. [19]. This is perhaps the most striking proof of the existence of a strong coupling between smectic and nematic ordering. The effect of such a coupling on the phase diagram has not been predicted theoretically. However fresh phenomenological approaches are being made to account for the experimental observations.

Recently doubly reentrant and even triply reentrant polymorphism has been reported [20]. However, we shall not discuss them here. There have been theoretical attempts to explain the origin of the reentrant nematic behavior at a molecular level. However these have been successful only qualitatively and a complete quantitative understanding of the various aspects of the reentrant nematic phenomenon still eludes us.

C. The Nematic-Smectic A-Smectic C Multicritical Point

The nematic-smectic A-smectic C multicritical point or the NAC point for short, is by definition a point in temperature-concentration (T-X) or pressure-temperature (P-T) plane at which the AN, NC and AC phase boundaries intersect, all the three being second order transitions at this point. The three phases are therefore indistinguishable at the NAC multicritical point. (In contrast at a triple point the three phases would merely coexist.) Such a point was predicted theoretically [21] and soon observed experimentally [22] in the T-X diagram of a liquid crystal system. This was followed by detailed high resolution experiments which permitted explicit comparisons with the theory which predicted the point to be a type of Lifshitz point. Johnson and his coworkers at Kent State University then made a significant observation. From their high resolution T-X diagrams of four binary systems they found that despite gross differences in global features the topology of the phase diagram near the NAC point is universal, i.e., universal rules near the NAC point [23]. This universal plot of Johnson is shown in Fig. 6. This is indeed a remarkable result because no such universal behavior has been seen in phase transitions in liquid crystals before. However all these studies are on binary mixtures which could conceivably have problems due to concentration fluctuations. It therefore became important to observe the NAC point in a

single component system at high pressure (wherein such fluctuations are absent) and to test the concept of universality near such a point. This was in fact achieved soon.

Fig.7 shows the complete P-T diagram of a single component liquid crystal. The NA and AC phase boundaries are initially straight, but they curl up dramatically and join at the NAC point. Fig.8 shows the high resolution data collected in the immediate vicinity of the NAC point [24]. The striking similarity between Figs.6 and 8 is evident. Quantitative similarity between the two phase diagrams was examined by fitting the P-T data for the NA, NC and AC phase boundaries individually by the following expressions (which are similar to those used by Johnson's group except that X is replaced by P):

$$T_{NA} - T_{NAC} = A_{NA}(P_{NAC} - P_{NA})^{\eta_{NA}} + B(P_{NAC} - P_{NA}), \quad (1a)$$

$$T_{NC} - T_{NAC} = A_{NC}(P_{NC} - P_{NAC})^{\eta_{NC}} + B(P_{NC} - P_{NAC}), \quad (1b)$$

$$T_{AC} - T_{NAC} = A_{AC}(P_{NAC} - P_{AC})^{\eta_{AC}} + B(P_{NAC} - P_{AC}). \quad (1c)$$

The computations carried out in this manner gave exponents $\eta_{NA} = \eta_{NC} = 0.575 \pm 0.02$ and $\eta_{AC} = 1.523 \pm 0.02$. These are, within the statistical uncertainties, the same as those evaluated by Johnson's group ($\eta_{NA} = \eta_{NC} = 0.573 \pm 0.02$, $\eta_{AC} = 1.52 \pm 0.02$). A remarkable fact that the η values obtained from the P-T diagram of a single component system agree so closely with those evaluated from the T-X diagrams of four binary mixtures shows that the NAC point exhibits universal behavior. A noteworthy feature about the universality behavior is its simplicity - the scaling laws are the same as the experimental axes (P and T or X and T) and not a linear combination of these variables. Recently it has been demonstrated that this universal behavior holds even when the sequence of transitions are changed [25].

On the theoretical side, the Lifshitz point model [21] appears to be quite successful - the fluctuation crossover predicted by the theory has indeed been observed experimentally. Nevertheless, important discrepancies remain with the predictions of the model in the immediate vicinity of the NAC point. There has also been a renormalization group approach to the NAC problem which predicts the existence of a biaxial nematic (N') phase near the NAC point [26]. However none of the experiments so far have shown the existence of the N' phase. Further insights in the understanding of the NAC multicritical point would be invaluable for understanding critical phenomena in other areas of condensed matter physics.

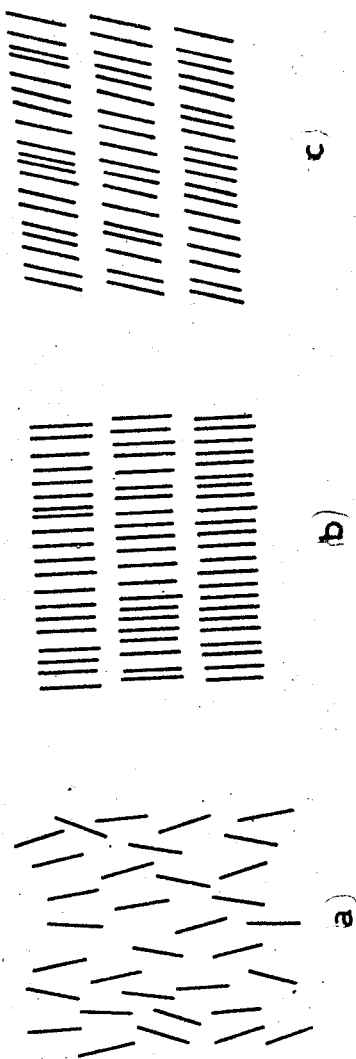


Fig. 1. Schematic representation of molecular order in (a) Nematic, (b) Smectic A and (c) Smectic C phases.

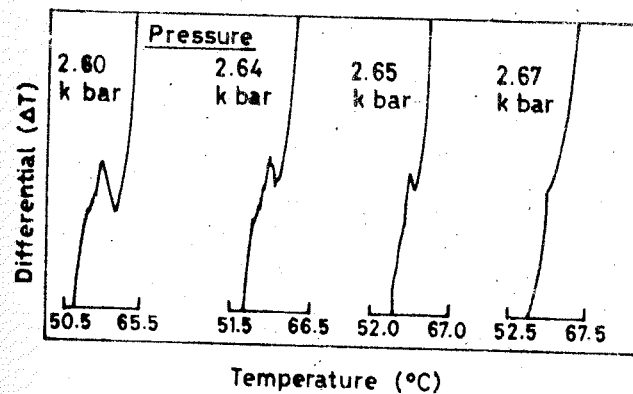
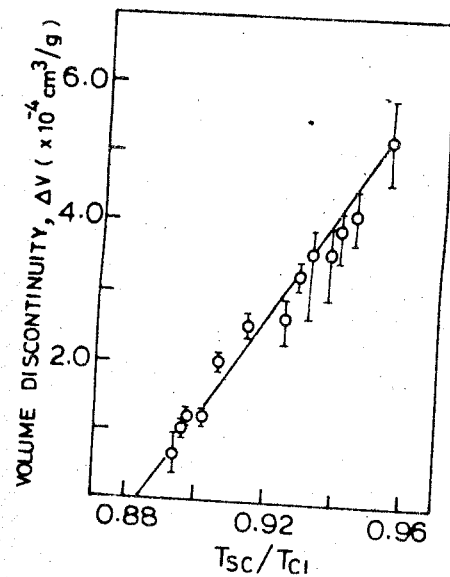


Fig. 2. Raw DTA runs showing the smectic A - cholesteric transition in cholesteryl oleyl carnoate (COC) at different pressures in the vicinity of the tricritical point (From Reference [9])



Volume discontinuity (ΔV) at the smectic A - cholesteric transition in COC as a function of McMillan number (From Reference [10])

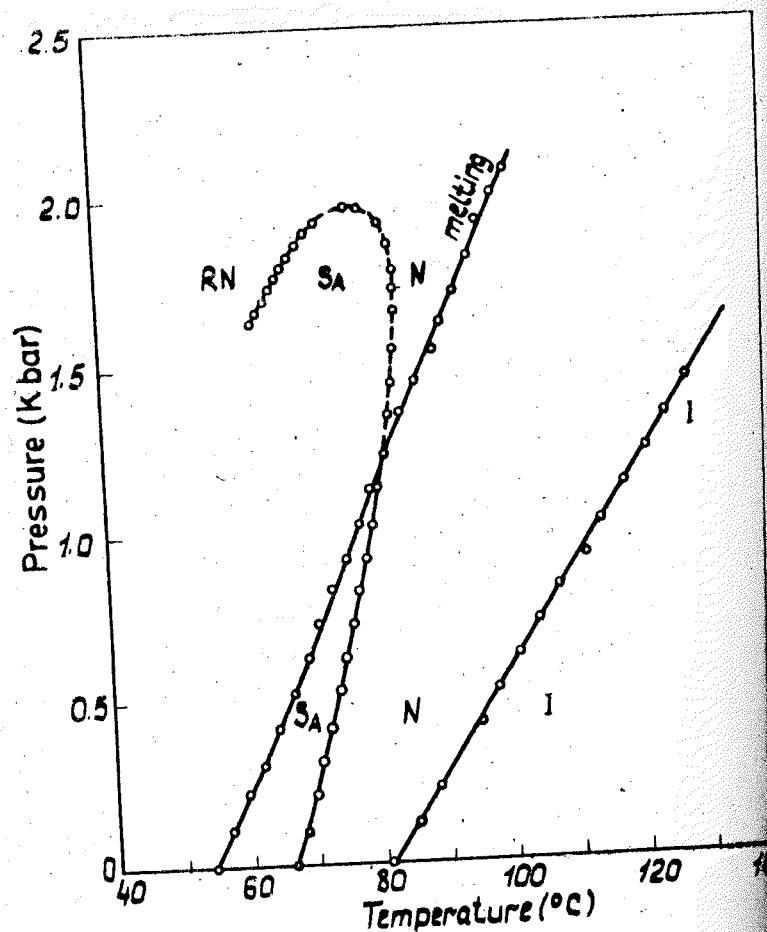


Fig.4. Pressure-temperature (P-T) diagram of 4-n-octyloxy-4'-cyanobiphenyl showing the reentrant nematic phase (RN) between 1.6 and 1.8 kbar. The dashed line indicates that it is a supercooled transition; S_A - smectic A, N-nematic and I-isotropic phases. (From Reference [14])

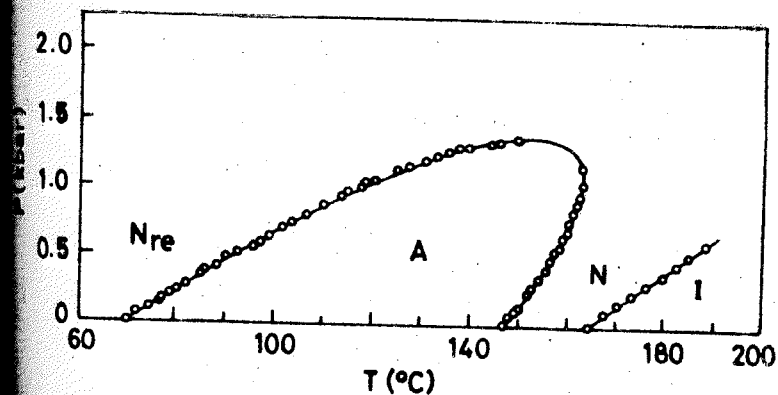
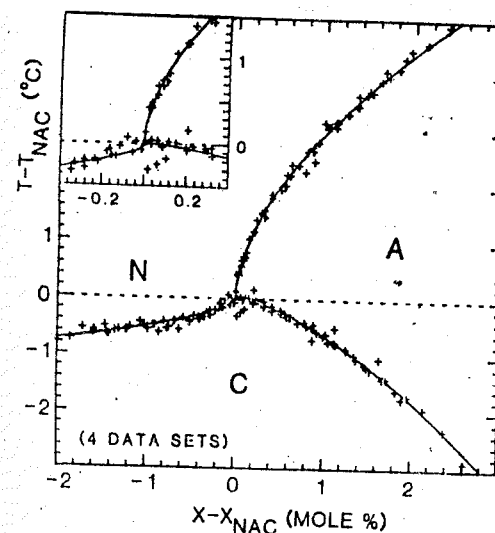


Fig.5. Typical P-T diagram of a substance exhibiting the reentrant nematic phase at atmospheric pressure. (From reference [19]).



The universal temperature-concentration plot of the NAC multicritical point showing the data for four binary liquid crystal system (From Reference [14]).

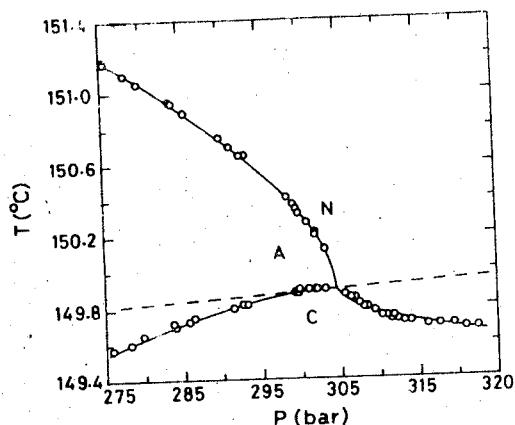


Fig.7. Pressure-temperature diagram of 4-n-heptylphenyl-4'-(4-cyanobenzoyl)benzoate or 7APCBB showing the NAC multicritical point at 304 bar and 149.9°C. The solid lines are guides to the eye. (From reference [24]).

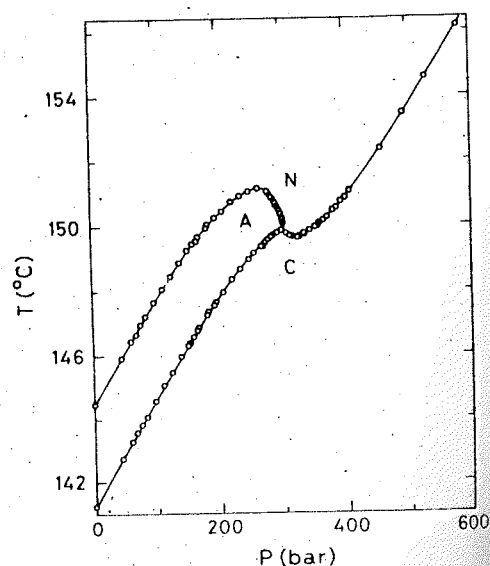


Fig.8. High resolution P-T diagram in the vicinity of the NAC multicritical point. The solid lines are computer fits of the P-T data to expressions given in the text. The dashed line represents the line corresponding to the NAC multicritical point. (From Reference [24]).

References

1. See e.g., Chandrasekhar, S., 'Liquid Crystals', Cambridge University Press, London, New York, Melbourne, 1977, pages 342
2. For a recent review on the current state of understanding of the smectic A-nematic transition, see Lubensky, T.C., 'The nematic-smectic A transition: A theoretical overview', J. Chim. Phys. **80**, 31-44 (1983).
3. Litster, J.D., 'Structural studies of nematic and smectic phases', Phil. Trans. Roy. Soc. A, **309**, 145-153 (1983).
4. Swift, J., 'Fluctuations near the nematic-smectic C phase transition', Phys. Rev. A **14**, 2274-2277 (1976); see also Brazovskii, A., Zh. Eksp. Teor. Fiz. **68**, 175 (1975).
5. Griffiths, R.B., 'Thermodynamics near the two fluid critical mixing point in ^3He - ^4He ', Phys. Rev. Lett., **24**, 715-717 (1970).
6. For an earlier review on pressure studies on liquid crystals, see Chandrasekhar, S. and Shashidhar, R., 'High Pressure Studies of Liquid Crystals', Advances in Liquid Crystals **4**, 83-120 (1979).
7. McMillan, W.L., 'Simple molecular model for the smectic A phase of liquid crystals', Phys. Rev. A, **4**, 1238-1246 (1971).
8. Keyes, P.H., Weston, H.T. and Daniels, W.B., 'Tricritical behavior in liquid crystal systems', Phys. Rev. Lett., **31**, 628-630 (1973).
9. Shashidhar, R. and Chandrasekhar, S., 'Pressure studies on liquid crystalline materials', J. Physique, **36**, C1-49 to C1-53 (1975).
10. Nishijyo, S., Okamoto, T. and Takemura, T., 'Pressure-induced tricritical behavior of smectic A-cholesteric transition in COC', Jap. J. Appl. Phys. **21**, 1260-1261 (1982).
11. Lee, T.J. and McColl, J.R., 'Orientational order measurements near a possible nematic-smectic A tricritical point', Phys. Rev. Lett., **34**, 1076-1079 (1975).
12. Shashidhar, R. and G. Venkatesh, 'High pressure studies on 4-n-allyl-4'-cyanobiphenyls', J. Physique, **40**, C3-396 to C3-399 (1979).
13. Marnissen, H. and Van Dael, W., 'Nematic-smectic A tricritical point in alkyl cyanobiphenyls', Phys. Rev. Lett., **52**, 204-207 (1984).

14. Cladis, P.E., Bogardus, R.K., Daniels, W.B. and Taylor, G.N., 'High pressure investigation of the reentrant nematic-bilayer smectic A transition', *Phys. Rev. Lett.* **39**, 720-723 (1977).
15. E. Muller-Hartmann and J. Zittartz, 'Kondo effect in superconductors', *Phys. Rev. Lett.* **20**, 428-432 (1971).
16. G. Riblet and K. Winzer, 'Vanishing of superconductivity below second order transition temperature in $(La_{1-x}Ce_x)Al_2$ alloys due to the Kondo effect', *Solid State Commun.* **9**, 1663-1665 (1971).
17. Kalkura, A.N., Shashidhar, R. and Urs, M.S., 'High pressure studies on reentrant mesogens', *J. Physique*, **44**, 51-55 (1983).
18. Krishna Prasad, S., Pfeiffer, S., Heppke, G. and Shashidhar, R., 'Effect of pressure on strongly polar liquid crystals', *Z. Naturforsch.* **40a**, 632-635 (1985).
19. Shashidhar, R., Somasekhara, S. and Ratna, B.R., 'Coupling between nematic and smectic ordering in reentrant nematic systems', *Mol. Cryst. Liq. Cryst.* **133**, 19-29 (1986).
20. Shashidhar, R., Ratna, B.R., Surendranath, V., Raja, V.N., Krishna Prasad, S., Nagabhushan, C., 'Experimental studies on a triply reentrant mesogen', *Physique Lett.* **46**, L-445 to L-450 (1985).
21. Chen, J. and Lubensky, T.C., 'Landau-Ginzburg mean field theory for the nematic to smectic C and nematic to smectic A phase transitions', *Phys. Rev. Lett.* **A 14**, 1202-1207 (1976).
22. Johnson, D.L., Allender, D., de Hoff, R., Maze, C., Oppenheim, E. and Reynolds, C., 'Nematic-smectic A-smectic C polycritical point: Experimental evidence and a Landau theory', *Phys. Rev. B* **16**, 470-475 (1977).
23. Brisbin, D., Johnson, D.L., Fellner, H. and Neubert, M.E., 'Universality of phase diagrams near the nematic-smectic A-smectic C multicritical point', *Phys. Rev. Lett.* **50**, 178-181 (1983).
24. Shashidhar, R., Ratna, B.R. and Krishna Prasad, S., 'Nematic-smectic A-smectic C multicritical point in a single component system', *Phys. Rev. Lett.* **52**, 2141-2144 (1984).
25. Somasekhara, S., Shashidhar, R. and Ratna, B.R., 'Universality of the reentrant nematic-smectic C-smectic A and the nematic-smectic A-smectic C multicritical points', *Phys. Rev. (Rapid Commun.) A* **34**, 2561-2564 (1986).
26. Grinstein, G. and Toner, J., 'Dislocation loop theory of the nematic-smectic A-smectic C multicritical point', *Phys. Rev. Lett.* **51**, 2386-2389 (1983).

DISC-LIKE MESOGENS UNDER PRESSURE

J.M. BUISINE

Equipe de Dynamique des Cristaux Moléculaires, U.A. CNRS n° 801
 Université des Sciences et Techniques de Lille Flandres-Artois
 59655 VILLENEUVE D'ASCQ CEDEX - FRANCE

Abstract

A review on the phase behaviour under pressure of disc-like mesogens is presented. The studied compounds and the high pressure technique are reported. The most significant results that emerge from pressure - temperature phase diagrams are reported.

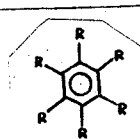
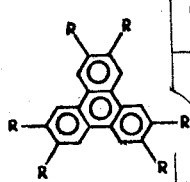
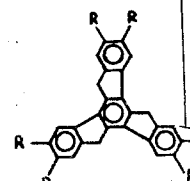
INTRODUCTION

The first experiments on the effect of pressure on disc-like liquid crystals transitions were published in 1979 by Chandrasekhar et al. [1] about two years after their discovery of discotic mesophases [2]. Although, among the several hundred of discotic mesogens synthesized, only a few have been studied under pressure so far [1, 3 - 6], interesting phenomena - previously shown up for mesogens with calamitic (rod-like) molecules [7] - have already been able to be recognised. The aim of this article is to review the studied compounds, the experimental techniques and the most significant results that have emerged from these investigations.

SUBSTANCES

The discotic mesogens studied under pressure are (Table) hexa-n-alkanoylbenzene ($n = 6$: I [1], $n = 8$: II [1]), 2, 3, 6, 7, 10, 11 - hexa-substituted-triphenylene (n-octyloxy : III [3, 4], n-decanoyloxy : IV [4], n-decanoyloxy : V [5], S-(3-methyl) -n-nonanoyloxy : VI [5], n-decyloxy-4-oxyloxy : VII [3]) and 2, 3, 7, 8, 12, 13 - hexa-n-alkanoyloxy-truxenes ($n = 9$: VIII, $n = 11$: IX, $n = 12$: X, $n = 13$: XI, $n = 14$: XII). Phase sequences under atmospheric pressure are reported (Table) according to the now usual classification based on crystallographic criterion [4].

List of disc-like mesogens studied under pressure with their phase sequences (K : crystalline phase ; N_D : lenticular nematic phase ; D_{ho} : hexagonal ordered columnar phase ; D_{hd} : hexagonal disordered columnar phase ; D_{rd} : rectangular disordered columnar phase ; D₀, D₁, D₂ : non identified mesophases ; I : isotropic liquid) and the nature of the pressure study (D.T.A : differential thermal analysis ; O.O. : optical observation, O.T. : optical transmission, T.B.A. : thermo-barometric analysis).

	R	Phase sequence	Nature of Study
	$C_5H_{11}-C(=O)-O-$ (I)	$K D_{rd} I$ [8]	DTA [8]
	$C_7H_{15}-C(=O)-O-$ (II)		
	$C_8H_{17}-O-$ (III)	$K D_{ho} I$ [9]	OO [9] OT [9]
	$C_9H_{19}-C(=O)-O-$ (IV)	$K D_{rd} I$ [9]	OT [9]
	$C_{11}H_{23}-C(=O)-O-$ (V)	$K D_o D_{rd} D_{hd} I$ [10]	TBA [10]
	$C_6H_{13}-CH(CH_3)-C(=O)-O-$ (VI)	$K D_2 D_1 I$ [11]	
	$C_{10}H_{21}-O-C_6H_4-C(=O)-O-$ (VII)	$K D_r N_D I$ [12]	OO [12]
	$C_8H_{17}-C(=O)-O-$ (VIII)	$K [N_D] D_{rd} D_{ho} I$ [13]	TBA [13]
	$C_{10}H_{21}-C(=O)-O-$ (IX)	$K [D_{hd}] N_D D_{rd} D_{hd} I$ [13] ?	
	$C_{11}H_{23}-C(=O)-O-$ (X)		
	$C_{12}H_{15}-C(=O)-O-$ (XI)	$K [D_{hd}] N_D D_{rd} D_{hd} I$ [13]	
	$C_{13}H_{27}-C(=O)-O-$ (XII)		

III - EXPERIMENTAL TECHNIQUES

Three different types of analysis have been used.

Optical analysis

For their high pressure studied on triphenylene derivative (III and VII), Gasparoux et al. used an original set up [3] allowing to detect phase transitions by optical observations (O. O.). The sample was sandwiched between two transparent windows surrounded by a thermo-retractable sheath and placed in a high pressure optical cell. Observations are performed between crossed polarizer and analyzer on using a video camera. Transformations are detected by changes for the textures.

More recently Raja et al. have studied the transitions of two triphenylenes (III and IV) [4] by an optical transmission (O. T.) technique i.e. by monitoring along isobars and versus temperature, the intensity of laser light transmitted by a sample enclosed in a high pressure cell [15]. At the transition an abrupt change in the transmitted light intensity appears.

Differential thermal analysis

By using a high pressure coaxial differential thermal analysis (D.T.A) [16] associated to a 100 ton single acting hydraulic press [17], Prasekhar et al. have studied the phase behaviour under pressure of two derivatives (I and II) and have been the first to determine the diagram of discotic mesogens.

Thermo-barometric analysis

The thermo-barometric analysis (T.B.A) [18] consists by recording, versus temperature, the pressure of a sample enclosed in a weakly dilatable cell. Pressure and temperature are intensive data so very little samples can be used (less than 2 mm³). On thermobarograms, transformations are detected by slope changes for first order transitions [18] and by slope changes for second order ones [19]. Discotic mesogens (V, VI, VIII to XII) exhibit all types of transitions have been investigated by T.B.A. [5-6] on using a pressure meter [18].

IV - PRESSURE - TEMPERATURE PHASE DIAGRAMS

The possibility of inducing a mesophase for a discotic mesogen which is nonmesomorphic under atmospheric pressure, by increasing pressure was pointed out by Chandrasekhar et al. on a benzene derivative (I, [1]). A virtual transition is then induced under atmospheric pressure, the temperature of which is in agreement with miscibility diagram studies [20].

Bounded columnar mesophases was found for a benzene derivative (II: [3]) and for truxene derivatives (III: [3-4], IV: [4], VII: [3]). Raja et al. [4] have pointed out on compounds III and IV the interesting results that first the character of the transition changes from enantiotropic to monotropic by increasing pressure and second $\frac{dT}{dP}$ data for the mesophase - isotropic liquid transitions are nearly equal to zero over the entire range of pressure investigated. However, Gasparoux et al. have not observed, on compound III, such phase behaviours [3].

By studying the influence of pressure on the stability of the different mesophases compared with the effect of increasing chain length on truxene derivatives (VIII to XII), it was shown [6, 2] that the nature of the transition change from monotropic to enantiotropic. For the lower studied term in the series (VIII) the $N_D - D_{rd}$ transition is monotropic over the entire range of pressure investigated. For higher terms (IX to XII) the $N_D - D_{rd}$ transition becomes enantiotropic over the entire range of pressure investigated. More, for a given compound, the nature of the transition can also be changed by pressure from monotropic to enantiotropic (as for rod-like molecules [7, 17]). This is the case for the $D_h - N$ transition of the compounds IX to XII thereby giving rise to a solid-nematic columnar triple point. More the P-T phase diagrams let predict other triple points and perhaps maximums for the equilibrium curves between D_h and N_D or D_{rd} have been already seen for calamitic mesogens [22].

V - THERMODYNAMIC DATA

The study of the P-T diagrams of the truxene homologous series shows that the $\frac{dT}{dP}$ data for the $K - D_h$, $D_h - N_D$ and $N_D - D_{rd}$ transitions alternate with the number of carbon atoms in the alkyl end chain (Figure 1) similar to the well known "odd-even" effect for the temperatures of the transitions [6]. These results are compared to those obtained by Feyz and Kuss [6] for the clearing transitions of some rod-like molecules.

From the slopes of the P-T diagrams, the molar volumes changes under atmospheric pressure can be calculated on using the Clausius - Clapeyron relation $\frac{dT}{dP} = \frac{\Delta S}{\Delta V}$ [24]. Neglecting the cases where the experimental

data for ΔS and $\frac{dT}{dP}$ are too small to be measured, the ΔV data for the melting, clearing and $N_D - D_{rd}$ transitions verify the relations:

$$\begin{aligned} 12.3 &\leq \Delta V_{\text{melting}} \leq 111 \text{ cm}^3/\text{mole} \\ 3.46 &\leq \Delta V_{\text{clearing}} \leq 4.58 \text{ cm}^3/\text{mole} \\ 0.53 &\leq \Delta V_{N_D - D_{rd}} \leq 1.16 \text{ cm}^3/\text{mole} \end{aligned}$$

One data for the $D_{rd} - D_{hd}$ transition is known: $\Delta V_{D_{rd} - D_{hd}} = 0.268 \text{ cm}^3/\text{mole}$.

From thermobarometric analysis, the pressure coefficient B can be deduced for atmospheric pressure [18]; some data are known and verify the relations:

$$\begin{aligned} 8.8 &\leq B^K \leq 16.6 \text{ K}^{-1} \\ 4.2 &\leq B^{D_{rd}} \leq 7.6 \text{ K}^{-1} \\ 4.7 &\leq B^{D_{hd}} \leq 8 \text{ K}^{-1} \\ 4.6 &\leq B^{N_D} \leq 6.8 \text{ K}^{-1} \end{aligned}$$

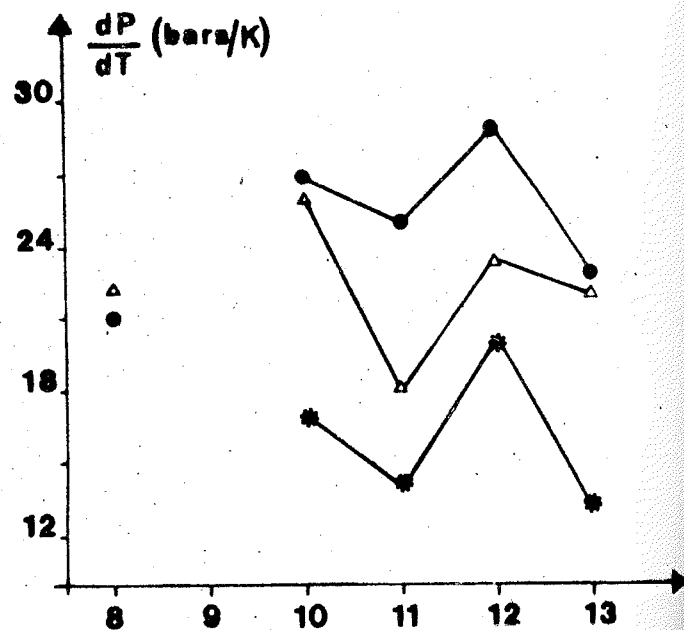
Some data for the isothermal compressibility under atmospheric pressure have been evaluated [6]:

$$\begin{aligned} 0.75 &\leq \chi^{D_{rd}} \leq 1 \cdot 10^{-9} \text{ m}^2/\text{N} \\ 1.1 &\leq \chi^{N_D} \leq 1.47 \cdot 10^{-9} \text{ m}^2/\text{N} \\ \chi^{D_{hd}} &\approx 2.4 \cdot 10^{-9} \text{ m}^2/\text{N} \end{aligned}$$

The magnitude for the ΔV , B and χ data for discotic mesogens are then compared to that for calamitic ones [25].

CONCLUSION

In spite of the weak number of discotic mesogens studied under pressure, the tricritical and multicritical behaviour, all the original properties induced, change from monotropic to enantiotropic and from enantiotropic to monotropic, reentrant mesomorphism, bounded mesophases, that have been already recognised for calamitic mesogens, have also been recognised for discotic mesogens. Thermodynamic data for the phases and transitions have the same magnitude for the two types of mesogens.



Alternation of $\frac{dP}{dT}$ for the $K - D_h$ (•), $D_h - N_D$ (*) and $N_D - D_{rd}$ (Δ) transitions with the number of carbon atoms in the alkyl chains for the alkanoyloxy-truxene homologous serie (compounds VIII to XII).

References

- Chandrasekhar S., Sadashiva B.K., Suresh K.A., Madhusudana N.V., Kumar S., Shashidhar R., Venkatesh G., J. de Phys. (1979) 40, C3, 120-124.
- Chandrasekhar S., Sadashiva B.K., Suresh K.A., Pramana (1977), 9, 471-480.
- Gasparoux H., Achard M.F., Hardouin F., Sigaud G., C.R. Acad. Sc. Paris (1981) 293, Serie II, 1029-1032.
- Raja V.N., Shashidhar R., Chandrasekhar S. Boehm R.E., Martire D.E. Pramana J. Phys. (1985) 25, L119 - L122.
- Buisine J.M., Malthête J., Destrade C., Nguyen Huu Tinh, Physica (1986) 139 and 140 B, 631-635.
- Buisine J.M., Cayuela R., Destrade C., Nguyen Huu Tinh, Mol. Cryst. Liq. Cryst. (1987) 144, 137-160.
- For a review see
Chandrasekhar S., Shashidhar R.
Advances in Liquid Crystals (1979) 4, 83-120.
- Levelut A.M., J. Chem. Phys. (1983) 80, 149-162.
- Destrade C., Mondon M.C., Malthête J., J. de Phys. (1979) 40, C3, 17-22.
- Destrade C., Bernaud M.C., Gasparoux H., Levelut A.M., Proc. Int. Conf. on Liq. Cryst. Bangalore, Heydon London (1980) 29.
- Malthête J., Jacques J., Nguyen Huu Tinh, Destrade C., Nature (1982) 298, 46-48.
- Nguyen Huu Tinh, Gasparoux H., Destrade C., Mol. Cryst. Liq. Cryst. (1981) 68, 101-111.
- Nguyen Huu Tinh, Foucher P., Destrade C., Levelut A.M., Malthête J. Mol. Cryst. Liq. Cryst. (1984) 111, 277-292.

14. Destrade C., Foucher P., Gasparoux H., Nguyen Huu Tinh, Levelut A.M., Malthête J.,
Mol. Cryst. Liq. Cryst. (1984) 106, 121-146.
15. Kalkura A.N., Shashidhar R., Urs M.S.,
J. de Phys. (1983) 44, 51-55.
16. Reshamwala A.S., Shashidhar R.,
J. Phys. E (1977) 10, 180-183.
17. Shashidhar R.,
Mol. Cryst. Liq. Cryst. (1977) 43, 71-81.
18. Buisine J.M., Soulestin B., Billard J.,
Mol. Cryst. Liq. Cryst. (1983) 91, 115-127.
19. Buisine J.M.,
Mol. Cryst. Liq. Cryst. (1984) 109, 143-158.
20. Billard J., Sadashiva B.K.,
Pramana (1979) 13, 309-318.
21. Buisine J.M., Domon M.,
C.R. Acad. Sc. Paris (1986) 303, Serie II, 1769-1772.
22. Cladis P.F., Bogardus R.K., Daniels W.B., Taylor G.N.,
Phys. Rev. Lett. (1977) 39, 720-723.
Lebert L., Daniels W.B.,
J. de Phys. (1977) 38, L 333-L 335.
Kalkura A.N., Shashidhar R., Subramanya, Raj Urs N.,
J. de Phys. (1983) 44, 51-55.
23. Feyz M., Kuss E.,
Ber. Bunsenges. Phys. Chem. (1974) 78, 834-842.
24. Clapeyron E.,
J. Ec. Polytechn. (1834) 14, 153-190.
25. Beguin A., Billard J., Bonamy F., Buisine J.M., Cuvelier P., Dubois Le Barny P.,
Sources of Thermodynamic Data on Mesogens Mol. Cryst. Liq. Cryst. 115. Special Topics XIV.

METASTABLE LIQUID CRYSTAL STATES NEAR THE LIMIT OF STABILITY

A.V.Chalyi¹, V.G.Boyko², H.-J.Mögel³

¹Institute of Medicine, Kiev, USSR

²Institute of Surface Chemistry, the USSR Academy of Sciences, Kiev, USSR

³Martin-Luther Universität, Halle-Wittenberg, DDR

The states of matter sufficiently deep quenched into the metastable region close to the limit of thermodynamical stability (spinodal) are of great interest in various fields of physics and chemistry. Analyzing the properties of the metastable states near the spinodal one must take into account an important effects of the order parameter fluctuations. Theoretical treatment of these effects was carried out in /1-4/, where pseudocritical exponents of metastable fluids were calculated in the mean-field approximation and by means of $\epsilon = 6 - d$ expansion method (d - dimensionality of space) up to the first order in ϵ . The relaxation processes near the spinodal, mechanisms of nucleation of the new phase as well as light scattering effects in the metastable fluids were discussed in /1-4/ too.

The problem of treating metastable states is very important also for liquid crystal systems. It seems clear that various pretransitions occurring in liquid crystals are typical examples of near-spinodal (or pseudocritical) behavior. For instance, the nematic-isotropic (N - I) phase transition is characterised by two temperatures: one (T_C) is the temperature of the N - I transition, while the another (T^*) is associated with the limit of the supercooling of the isotropic phase.

In this note we are going to discuss the order parameter fluctuations and pressure effects in connection with the N - I phase transition.

Pseudocritical exponents. It is well-known that N - I phase transition is a weak first order transition that can be described by the following expansion of the Helmholtz free energy:

$$F(P, T, S) = F_0(P, T) + \int [A S^2 + B S^3 + C S^4 + D(\nabla S)^2 - S \eta] d^3x \quad (1)$$

where $A \sim T - T^*$, as usual in the Landau theory, B, C and D are constants and the value of B is small. We note that for metastable fluids $B \sim V^* - V_C$, where V^* and V_C are specific volumes at the

spinodal and at critical point correspondingly. The last term (1) describes interaction of the order parameter S with the external field h . In general $h = (P - P^*) - b(T - T^*)$, where P^* is pressure at the spinodal, i.e. P^* and T^* are associated with some point at the spinodal line and $b = \partial P / \partial T$ - is an individual for every substance (liquid crystal) constant.

In the mean-field theory one has the following representations for the various physical quantities of the metastable liquid crystal:

- a) heat capacity at constant field $C_h \sim (P - P^*)^{-\alpha}$,
- b) order parameter at the line of constant field in the metastable region $S \sim (P - P^*)^\beta$,
- c) susceptibility at constant field $\chi_h \sim (P - P^*)^{-\gamma}$,
- d) correlation length at the line of constant field

$$\xi \sim (P - P^*)^{-\nu},$$

- e) order parameter at fixed temperature ($T = T^*$)

$$S \sim (P - P^*)^{1/\delta},$$

where $\alpha = \beta = \gamma = 1/2$, $\nu = 1/4$, $\delta = 2$ - are pseudocritical exponents. For metastable fluids these exponents were calculated in

By means of $\varepsilon = 6 - d$ expansion method one can show [4] that at first order in ε $\alpha = \gamma = (1 + \varepsilon/8)/2$, $\beta = (1 - \varepsilon/8)/2$, $\nu = (1 + \varepsilon/8)/4$, $\delta = 2(1 + \varepsilon/8)$, or if $d = \varepsilon + 3$: $\alpha = \gamma = 11/16$, $\beta = 5/16$, $\delta = 11/4$, $\nu = 11/32$.

Basing on the analysis of the Ginzburg criterion one can show that mean-field treatment of the metastable liquid crystals is correct if

$$\frac{B^{5/3}}{|b^* - b_c| \cdot D^2} \ll \frac{(P - P^*)}{P^*} < 1$$

In every case one needs an experimental verification of this last inequality when uses Landau- de Gennes - type theory for the description of the N - I phase transition.

Fractal clusters in metastable liquid crystals. The structure of clusters of the new phase occurring in the metastable liquid crystal state is characterised by the fractal dimension D . Because of well-known result that $D = d - \beta/\nu$ one has that in metastable liquid crystals $D \approx 2.09$. Such a small value of D in this case means that clusters of the new phase are very ramified objects.

References

- Boyko V.G., Chaly A.V., Moegel H.-J. Pseudocritical exponents of metastable fluids//Ukr.Fiz.Zh (USSR) 1986. V.31, N1, p.137-143; v.31, N2, p.299-305 (In Russian)
- Boyko V.G., Chaly A.V., Mögel H.-J. Order parameter relaxation in a metastable liquid//Wiss.Z Univ. Halle. 1986. v.35, N4, p.135-139.
- Boyko V.G., Chaly A.V., Moegel H.-J. Pseudocritical exponents of metastable fluids in the mean-field theory//Prepr. Academy of Sci. Ukr. SSR. 1984.: Kiev. Inst. Theor. Phys., ITP - 84 - 119E. 28 p.
- Mögel H.-J., Chaly A.V. Pseudocritical exponents and the spinodal in metastable fluids//Prepr. Acad.Sci. Ukr.SSR. 1986. Kiev: Inst. Theor. Phys.; ITP - 86 - 96E. 9 pp.

EFFECT OF PRESSURE ON LIQUID CRYSTALS OF AQUEOUS UNSATURATED PHOSPHOLIPIDS

P.T.T. Wong

Division of Chemistry, National Research Council of Canada
Ottawa, Ontario, Canada K1A 0R6

Infrared and Raman spectra of aqueous bilayer dispersions of 1,2-dioleoyl-*sn*-glycero-3-phosphocholine (DOPC) have been measured as a function of pressure. A transformation from a highly disordered liquid crystalline phase to a highly ordered gel phase is induced by external pressure, which is the result of pressure-induced intrachain conformational and interchain reorientational ordering processes. The changes in the configuration of the unsaturated hydrocarbon chains and the interchain packing at the critical pressure are discussed on the basis of the present spectroscopic results.

1. Introduction

Liquid crystals of aqueous unsaturated phospholipids are the major component of biomembranes in most bacterial and mammalian cells. In the present paper, we present the results of an infrared and Raman spectroscopic study of pressure effects on the structural and dynamic properties of a model biomembrane, the liquid crystalline phase of aqueous bilayer dispersions of DOPC in which the *cis* double bond is in the middle of both hydrocarbon chains. These results may help to elucidate the molecular mechanism underlying biomembrane adaption to the stress of pressure in deep-sea marine organisms.

2. Experimental

High purity DOPC was obtained from Avanti Polar Lipids (Birmingham, AL). Fully hydrated lipid dispersions in D₂O (Merck & Dohme, Montreal, Canada) were prepared by vortexing lipid/D₂O mixtures in a closed vial at room temperature. After immediate freezing of the sample in dry ice, the vortex/freeze cycle was repeated twice. Homogeneous dispersions were then placed at temperature together with powdered internal pressure calibrants. A 0.37 mm diameter hole on a 0.23 mm, thick stainless steel piston mounted on a diamond anvil cell as described previously. The internal pressure calibrants are ruby powder and α -quartz. The diamond anvils are made of type Ia diamond for Raman spectroscopic work and type IIA diamond for infrared work [3]. Infrared spectra of the samples were measured at 28 °C on a Bomem Model DA3.02 Fourier transform spectrophotometer and Raman spectra were excited with a Coherent Radiation CRL-12 Ar⁺ ion laser operating at 488.1 nm. The detection system included a Spex Model 1877 TRIPLE-MONOCROMATOR, a Tracor Northern TN-6122 intensified multichannel detector, and a Tracor Northern TN-1710 multichannel analyzer. Details of the high pressure infrared and Raman spectroscopic measurements have been given previously [1,2].

Results and Discussion

The pressure profiles of Raman spectra in the CH stretching region and the infrared spectra in the CH₂ bending region of aqueous dispersions of DOPC are shown in Figs. 1 and 2, respectively. Abrupt changes in both infrared and Raman spectra at 5 kbar indicate a structural phase transition in the liquid crystalline phase of DOPC. This transition is also evident from the discontinuity at 5 kbar in the pressure dependences of all the spectral parameters, for instance, the frequency shift of the infrared bending mode (Fig. 3).

The Raman spectra below 5 kbar are those typical of a reorientationally and conformationally disordered liquid crystalline phase with a large number of gauche bonds in the hydrocarbon chains of the lipid molecules [4,5]. The disordered structure in the liquid crystalline phase is also evident from its Raman spectrum in the C-C skeletal stretching region [4] as shown in Fig. 4. A weak C-C stretching band of the gauche bonds near 1085 cm⁻¹ is clearly observed in the spectra of the liquid crystalline phase. The intensities of the C-C stretching band of the all *trans* isomers at 1121, 1094 and 1063 cm⁻¹ are extremely weak. Above 5 kbar, the intensities of the *trans* C-C stretching bands become very strong whereas the gauche C-C stretching band can be hardly realized in the Raman spectra. Therefore, above 5 kbar the conformation of the hydrocarbon chains in DOPC become highly ordered. The ordered phase of the biomembrane liquid crystal is generally referred to as the gel phase.

Because of the full extension of the methylene chains and the characteristics of the double bond in DOPC, in the gel phase two zig-zag methylene chain segments on both sides of the double bond of each hydrocarbon chain in DOPC form a bent structure. The presence of this bent configuration of the hydrocarbon

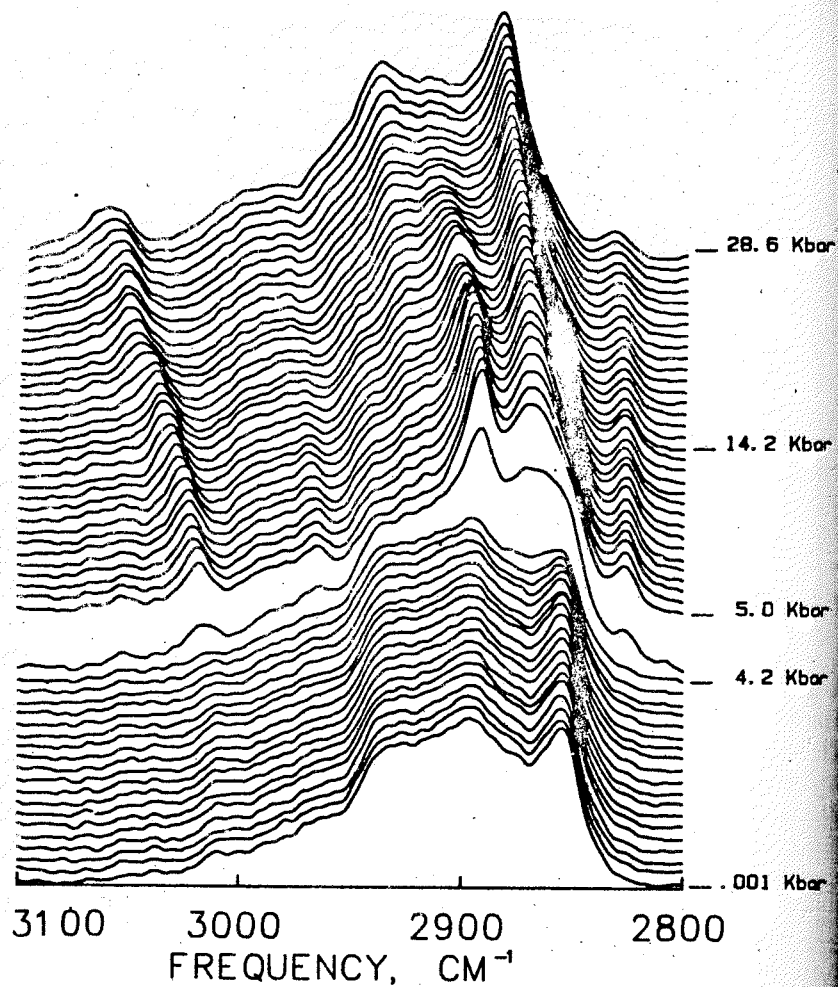


Fig. 1. Stacked contour plots of Raman spectra of aqueous DOPC in the CH stretching region.

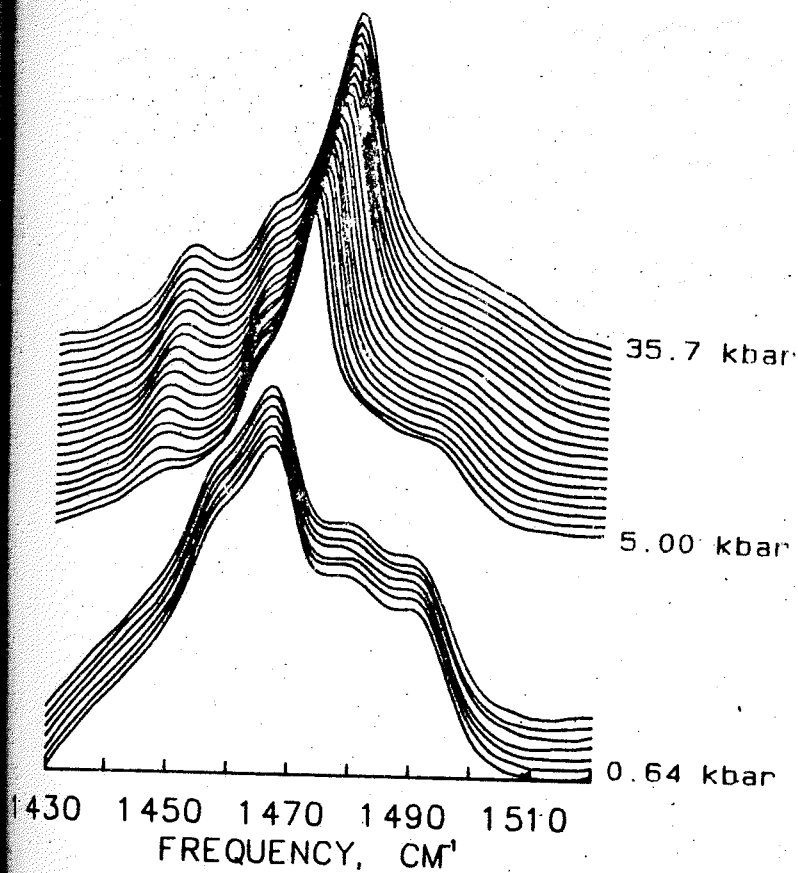


Fig. 2. Stacked contour plots of infrared spectra of aqueous DOPC in the CH_2 bending region.

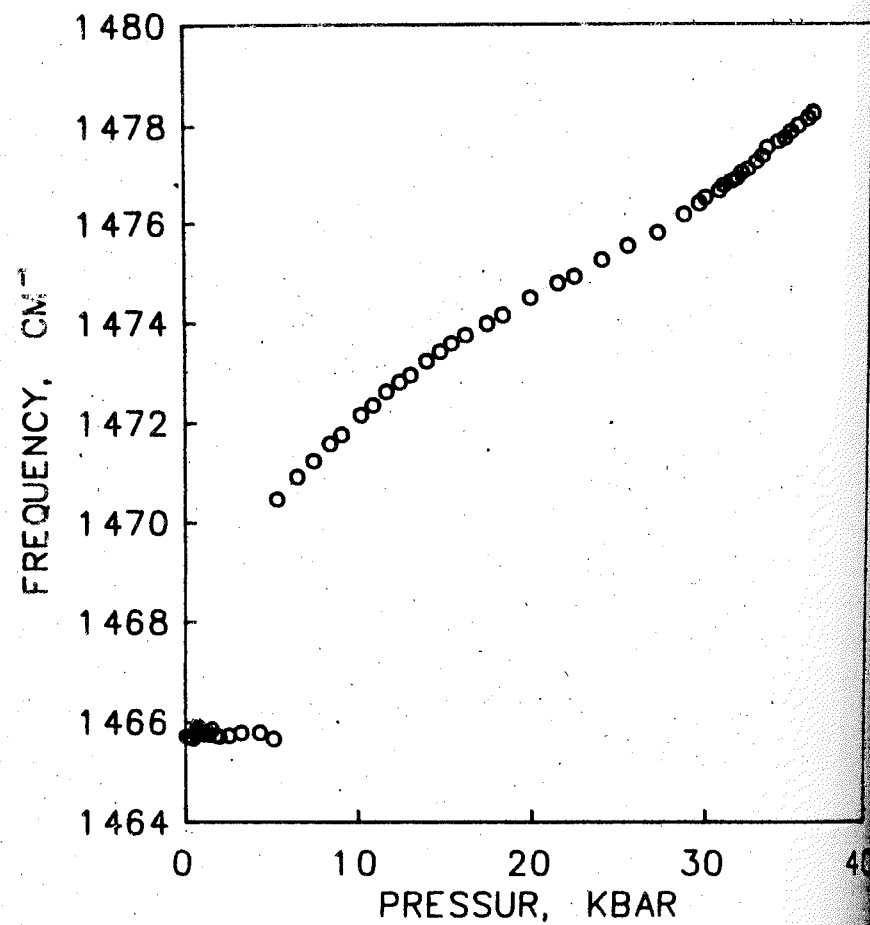


Fig. 3. Pressure dependence of the frequency of the CH₂ bending mode.

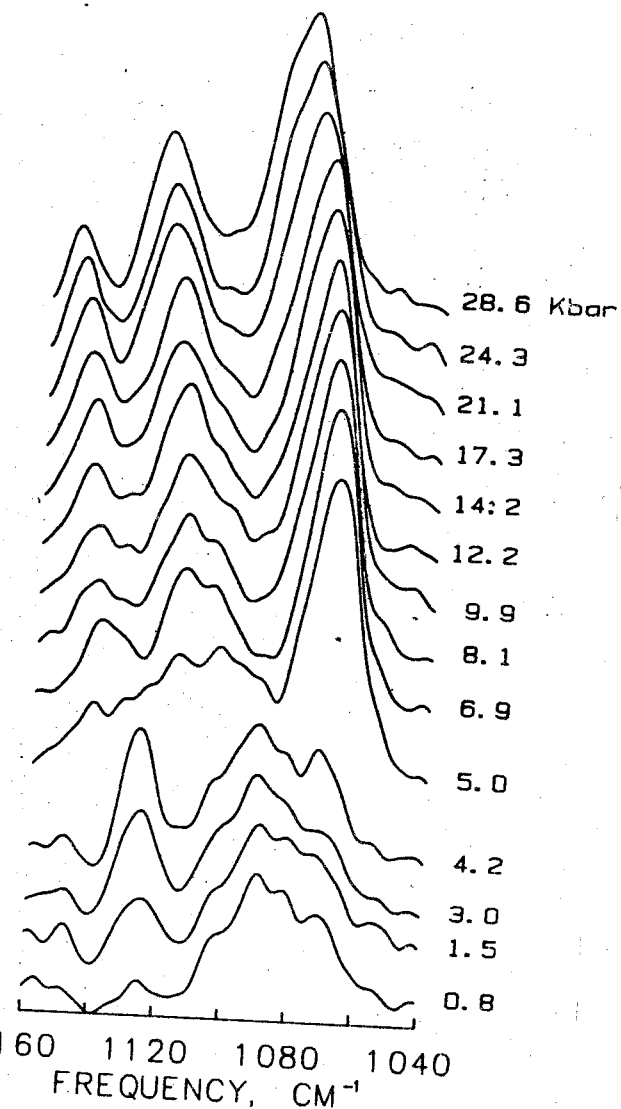


Fig. 4. Raman spectra of aqueous DOPC in the C-C stretching region at several pressures.

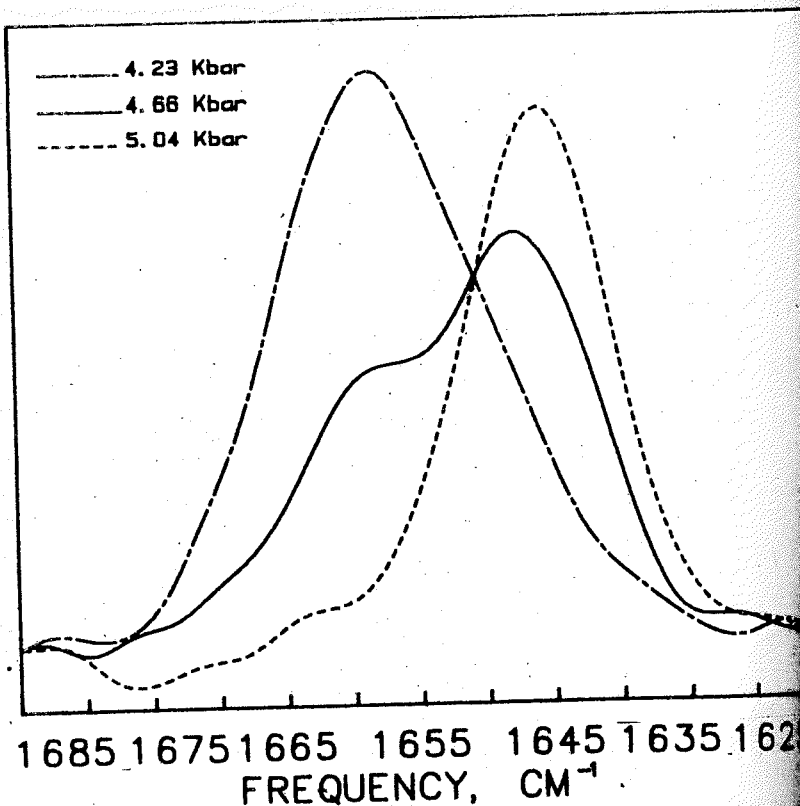


Fig. 5. Raman spectra of aqueous DOPC in the C=C stretching region at three pressures adjacent to the critical pressure.

chains above 5 kbar is also consistent with the dramatic decrease in the frequency of the C=C stretching mode (Fig.5). This decrease in the C=C stretching frequency at 5 kbar is the result of the elongation of the C=C double bond arising from the strong repulsion force between the hydrogen-atoms of the adjacent CH₂ groups on both sides of the double bond in the bent configuration.

Reorientational fluctuations of the hydrocarbon chains and the lipid molecules in the gel phase are completely damped at 5 kbar, since reorientation fluctuations of a bent chain would occupy more space than a straight chain. Thus, reorientational fluctuations are forbidden when the disordered straight chains of DOPC in the liquid crystalline phase transform into the ordered bent chains in the gel phase at 5 kbar.

There is no correlation field splitting of the CH₂ bending mode in the highly ordered gel phase (Fig.2). Therefore, in this phase the orientation of the zig-zag planes of the methylene chain segments, between the neighboring bent hydrocarbon chains must be parallel to each other in the bilayer lattice.

It is clear from the present study that the effect of pressure on the liquid crystal of the unsaturated DOPC is to induce intrachain conformational and interchain reorientational ordering processes which trigger a structural phase transition from the structurally and dynamically disordered liquid crystalline phase to the highly ordered gel phase in which the reorientational fluctuations are completely damped and the hydrocarbon chains are fully extended with a bent configuration at the cis double bond. The packing of all the hydrocarbon chains in the gel phase is parallel to each in the bilayer lattice. These pressure effects on the structural and dynamic properties of the liquid crystal of DOPC are expected to be the same for other dimonounsaturated biomembrane liquid crystals.

References

- Wong, P.T.T., Pressure-induced splitting and collapsing of the CN stretching vibration band in the Raman spectrum of crystalline Hg(CH₂)₂, *J. Chem.Phys.* (1984) **80**, 5937-5941.
- Wong, P.T.T., Moffatt, D.J. and Baudais, F.L., Crystalline quartz as an internal pressure calibrant for high-pressure infrared spectroscopy, *Appl. Spectrosc.* (1985) **39**, 733-735.
- Wong, P.T.T. and Klug, D.D., Reevaluation of type I diamonds for infrared and Raman spectroscopy in high-pressure diamond anvil cells, *Appl. Spectrosc.* (1983) **37**, 284-286.
- Wong, P.T.T., Raman spectroscopy of thermotropic and high-pressure phases of aqueous phospholipid dispersions, *Ann.Rev.Biophys. Bioeng.* (1984) **13**, 1-24.
- Wong, P.T.T., Phase behaviour of phospholipid membranes under high-pressure, *Physica* (1986) **139** and **140B**, 847-852.

PHASE BEHAVIOUR UNDER PRESSURE OF PYRAMIDIC LIQUID CRYSTALS
STUDIED WITH A SCANNING NUMERICAL METABOLEMETER

J.M. BUISINE

Equipe de Dynamique des Cristaux Moléculaires, UA CNRS n° 801
Université des Sciences et Techniques de Lille Flandres-Artois
59655 Villeneuve d'Ascq Cedex - FRANCE

H. ZIMMERMANN

Max-Planck-Institut für medizinische Forschung
Abteilung für Molekulare Physik
D-6900 Heidelberg - FRG

R. POUPKO, Z. LUZ

The Weizmann Institute of Science
Rehovot 76100 - ISRAEL

J. BILLARD

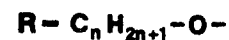
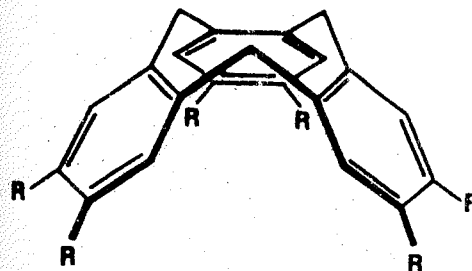
Laboratoire de Physique de la Matière Condensée, UA CNRS n° 542
Collège de France
75231 Paris Cedex 05 - FRANCE

Abstract

The pressure-temperature phase diagrams of four members ($n = 7, 9, 10$ and 11) of the hexaalkyloxytribenzocyclononene homologous series have been determined using a scanning numerical metabolemeter. For $n = 7, 9$ and 10 a new stable phase is detected between a crystalline phase and a pyramidal P_A mesophase; it seems it is a pyramidal P_B mesophase. Details relating to a new pressure-temperature cell ensuring accurate measurements and routine experiments are also reported.

1 - INTRODUCTION

For pyramidal mesogens [1-3], although some X-ray and optical microscopy observations on such pyramidal liquid crystals were published, no experimental results relating to the pressure-temperature dependence of the phase transitions were reported so far. Previous optical microscopy and calorimetric measurements on members of the hexaalkyloxytribenzocyclononene series indicated [1] that the C_6 to C_{12} members exhibit a P_A mesophase, while one member, C_{11} , also has an enantiotropic P_B phase below P_A .



In thermo-barometric experiments [4-7], we have reinvestigated four members of the pyramidal (bowl-like) [8] hexaalkyloxytribenzocyclononene family, i.e. with $n = 7, 9$ and 10 to 11 under various pressures.

1 - SCANNING NUMERICAL METABOLEMETER

The thermo-barometric measurements have been performed with a scanning numerical metabolemeter. The pressure-temperature cell [9] is shown Figure 1. The pressure transducer (1) (HEM 375-20000-Kulite International) is bonded by an epoxy adhesive film on a steel crucible (2) and is used as bottom of the cavity (3) in which the sample is introduced. The cell is closed with a little steel cover (4) and sealed hermetically with a set screw (5). The tightness is ensured by a plan annular joint (tin or zinc) (6). This arrangement cancels the pressure transducer destroying risks during the closing of the cell. Heater (thermocox) (7) are coiled around the crucible (2). A fan (8) allows the cooling experiments. The pressure transducer is compensated for continuous measurements from 25°C to 235°C ; the temperature is measured with a platinum resistance probe. The cell is placed on a steel stand (9) and insulated from outside with a glass housing (10).

The P.T. cell is connected through interfaces to a computer (Goupil 3, configuration 4, S.M.T.) associated to a graphic plotter (DMP 40, Houston Instrument) and a printer (RX 80, Epson). The computer is used to control the heating and the cooling of the cell, for pressure-temperature acquisitions in files and for the delete treatment of the data files.

The temperature range is $+25^\circ\text{C}$ to $+235^\circ\text{C}$; the pressure range is 0 to 10 bar. The maximal volume of the sample is 2 cubic millimeters. The accuracy for the sample temperature is 0.5°C . The sensitivity for the pressure measurements is 0.1 bar. The lower pressure increment that can be detected at order transition is about 5 bar; that corresponds to a transformation

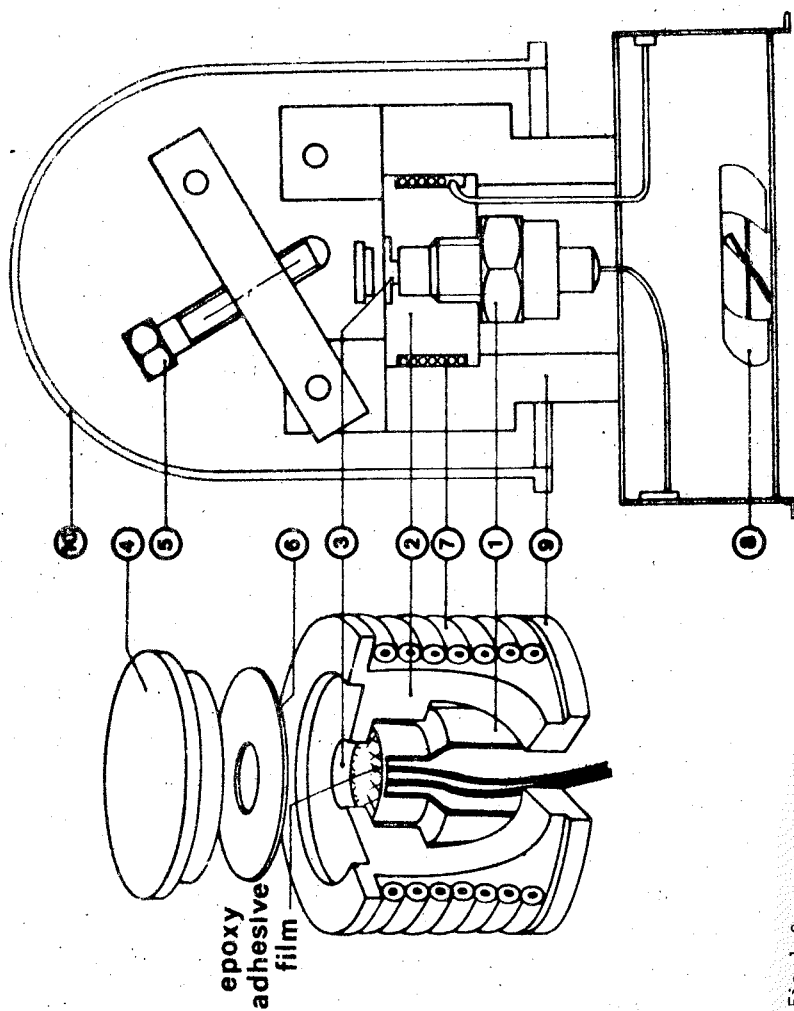


Fig. 1. Cross-sectional drawing of the present pressure-temperature measurement cell of the scanning numerical calorimeter.

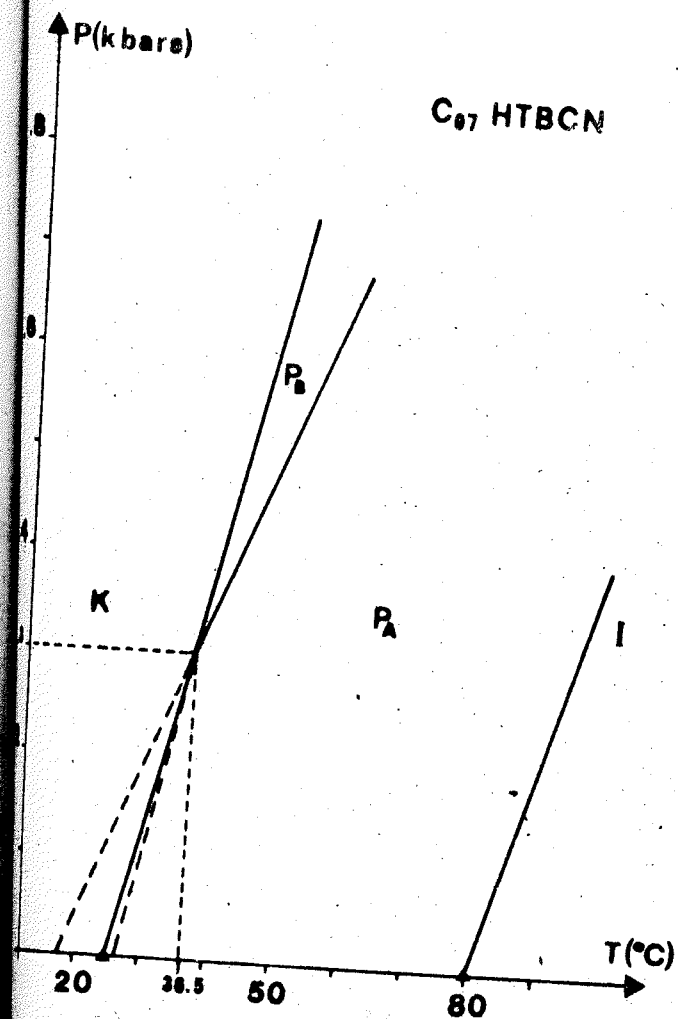
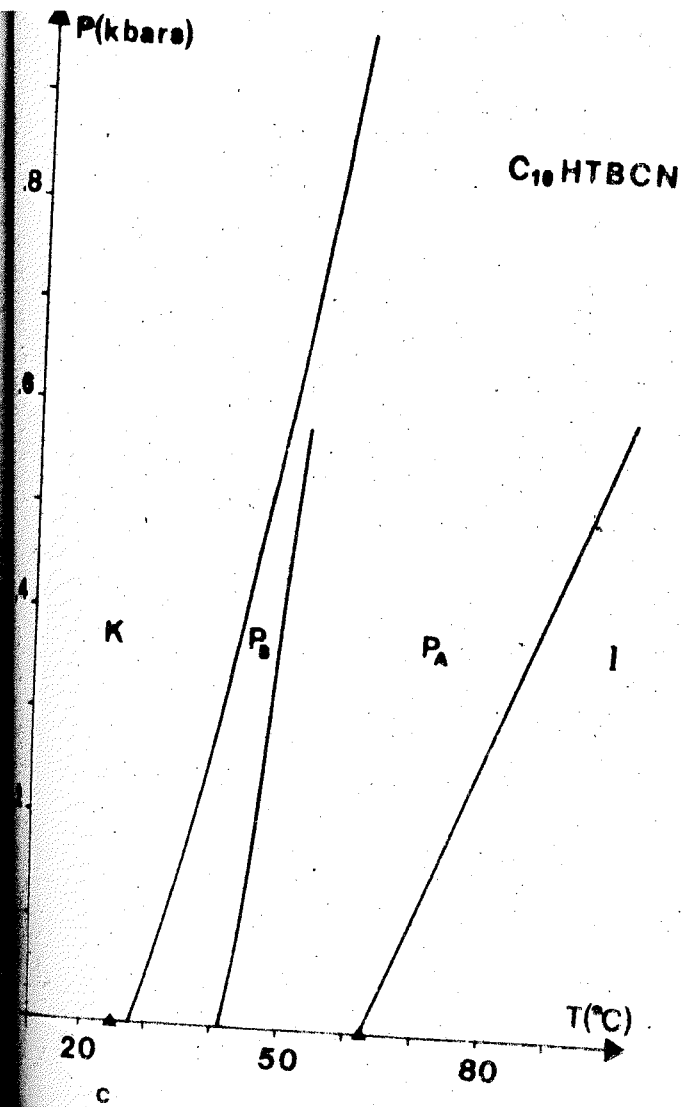
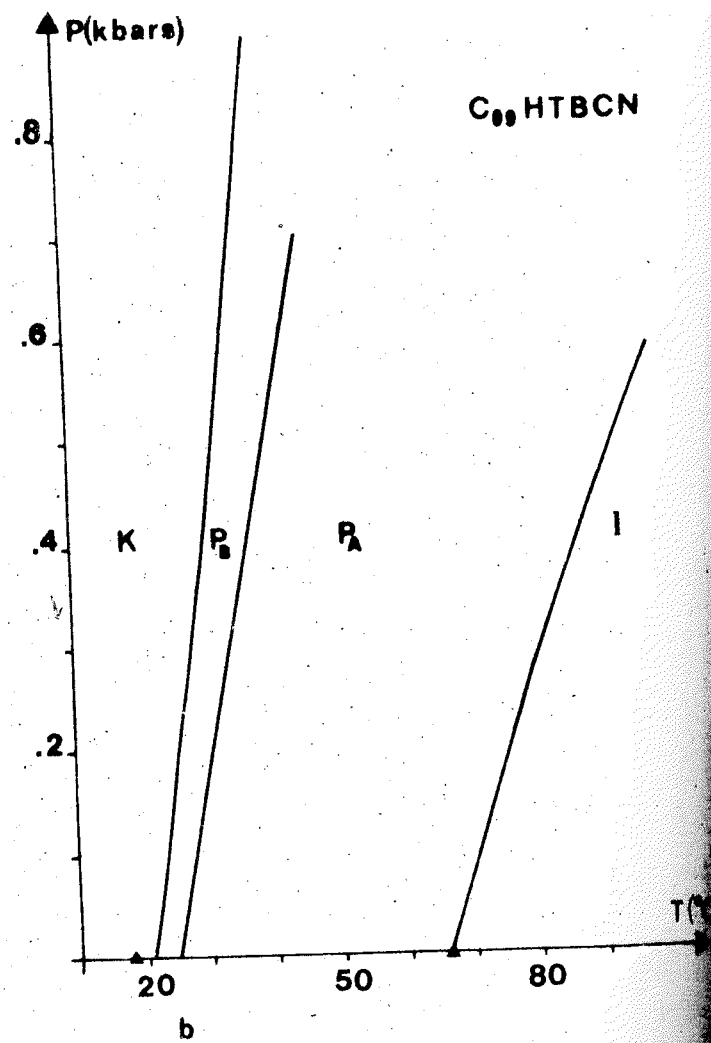
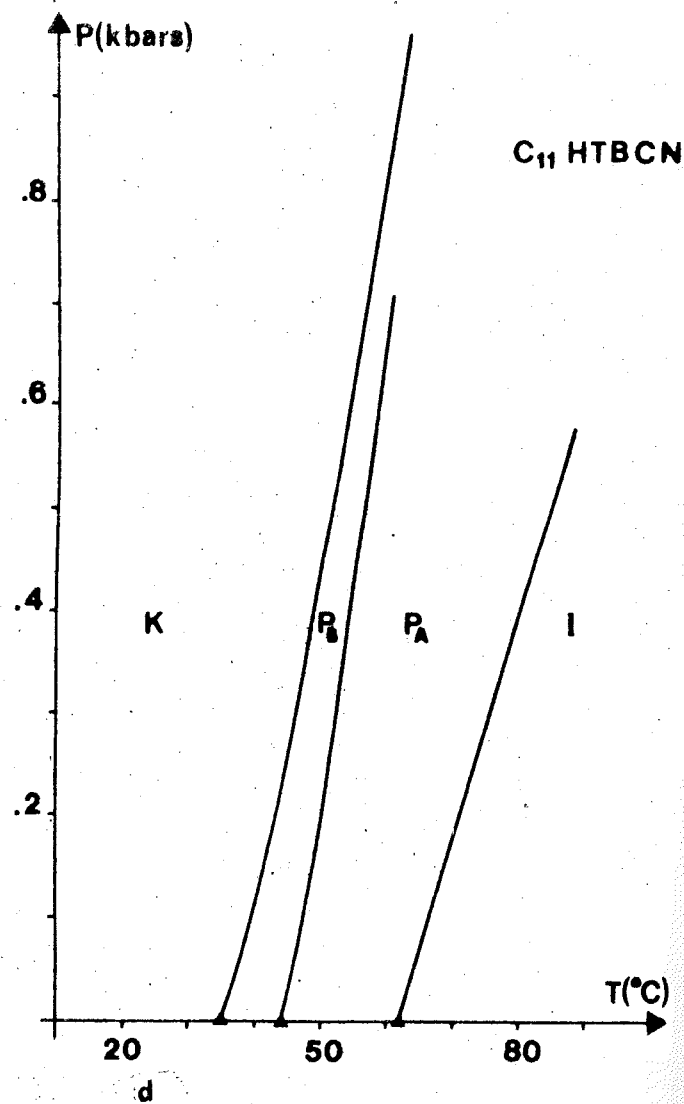


Fig. 2. Pressure-Temperature phase diagram for (see pp.235-238):

a : C_{07} HTBCN , b : C_{09} HTBCN , c : C_{10} HTBCN and
d : C_{11} HTBCN

▲ : Literature data .





with a 0.015 kcal/mole enthalpy change for a 0.5 kg/mole molar mass compound. The lower slope change that can be detected between two phases is 0.8 bar/K.

III - PRESSURE-TEMPERATURE PHASE DIAGRAMS

The pressure-temperature phase diagrams for the studied compounds are plotted in Figures 2 a to d. For $n=7, 9$ and 10 , a phase stable at lower temperature than P_A is observed; comparisons with the P-T phase diagram obtained for $n=11$ (Figure 2d) shows it is probably a P_B mesophase. The P_B phase was not observed in the homologues C_7 , C_9 and C_{10} in the previous work [1]. It is possible that their presence in the present case is due to the use of newly synthesized, purer compound. This is confirmed by the higher melting temperatures obtained in the present work for $n=9$ and 10 using thermo-barometric method (respectively 21 to 28°C) as compared to the initial microscopical results [1] (respectively 18.6 and 25.5°C). The range of thermal stability versus pressure for the P_B phase increases for the $n=7$ and 9 homologues and decreases for $n=10$ and 11 . For $n=7$, the P-T phase diagram (Figure 2a) exhibits a triple point $K-P_A-P_B$ at 36.5°C at 300 bar. Two virtual transitions $K-P_B$ and P_B-P_A can be deduced by extrapolation to atmospheric pressure. For this homologue the P_B-P_A transition is monotropic.

VI - CONCLUSION

Using a scanning numerical metalemmeter equipped with a new pressure-temperature cell ensuring accurate measurements and routine experiments, thermo-barometric measurements have been performed on four members ($n=7, 9, 10$ and 11) of the hexaalkyloxytribenzocyclononene series. The pressure-temperature phase diagrams have been determined. For $n=7, 9$ and 10 , a phase stable at lower temperature than P_A is observed, which is most probably identical to the phase P_B previously identified in $n=11$. For $n=7$, the P_B phase is monotropic and only a virtual transition between the crystalline and this phase is detected at atmospheric pressure.

References

- Zimmermann H., Poupko R., Luz Z., Billard J.
Z. Naturforsch. (1985) 40a, 149-160.
- Z. Naturforsch. (1986) 41a, 1137-1140.
- Malthête J., Collet A.
Nouv. J. Chimie (1985) 9, 151-153.

3. Levelut A.M., Malthête J., Collet A.
J. Phys. (1986) 47, 351-357.
4. Buisine J.M., Soulestin B., Billard J.
Mol. Cryst. Liq. Cryst. (1983) 91, 115-127
Mol. Cryst. Liq. Cryst. (1983) 97, 397-406.
5. Buisine J.M.
Mol. Cryst. Liq. Cryst. (1984) 109, 143-156
C.R. Acad. Sc. Paris (1983) 297 (Série II), 323-326.
6. Buisine J.M., Malthête J., Destrade C., Nguyen Huu Tinh
Physica (1986) 139 and 140 B, 631-635.
7. Buisine J.M., Cayuela R., Destrade C., Nguyen Huu Tinh
Mol. Cryst. Liq. Cryst. (1987) 144, 137-160.
8. Lin Lei
Wuli (1982) 11, 171
9. Buisine J.M., Soulestin B., Billard J.
French Pat. n° 86 05145.

THERMAL CONDUCTIVITY OF POLYMERS UNDER ELEVATED PRESSURES

V.P.Privalko, N.A.Rekhteta

Institute of Macromolecular Chemistry, Academy of Sciences
of the Ukrainian SSR, Kiev, USSR

Polymeric thermoinsulators in practical applications are often subjected to elevated pressures which tend to change their thermophysical properties. A feeling of a probable change in polymer thermal conductivity λ , with pressure P , may be obtained in the framework of Debye equation for solid dielectrics,

$$\lambda = C_V \bar{q} \bar{u} / 3, \quad (1)$$

where C_V is the isochoric specific heat, \bar{q} is density, \bar{u} is the mean velocity of phonon propagation, and l is the corresponding mean free path. It can be assumed that in absence of structural transformations and at sufficiently high (at least, with respect to Debye temperature for interchain vibrations) temperatures the values of C_V and l will be little affected by pressure, so that polymer densification under pressure accompanied by increase of both \bar{q} and \bar{u} , will eventually lead to the rise of thermal conductivity λ .

These simple qualitative arguments are consistent with the results of model analysis of thermal transport in both liquids [1] and polymers [2], according to which the pressure coefficient of thermal conductivity is controlled by coefficient of isothermal compression β_T as

$$(\partial \ln \lambda / \partial P)_T = C_T \beta_T, \quad (2)$$

where C_T is the dimensionless numerical parameter. Thus, equation (2) might have served as a theoretical basis for prediction of thermal conductivity of polymers under elevated pressures using values of β_T from independent measurements, provided that C_T parameter has unique, "universal" value.

Crystallizing polymers are unique in a sense that crystalline (solid-like) and amorphous (liquid-like above the glass transition temperature of amorphous phase T_g) regions coexist below melt-crystal, two-phase equilibrium temperature T_m . Given such structural heterogeneity, pressure application to a crystallizable polymer should have densified, first of all, more compressible, amorphous regions. Generally speaking, in that case C_T parameter

from equation (2) may be expected to depend on the fraction of polymer transformed into crystalline phase (i.e., degree of crystallinity X). Moreover, the pattern of thermal conductivity change with pressure is likely to give additional information about the structure of amorphous phase in a semi-crystalline polymer.

As a typical example, we present in Fig.1 the temperature dependences of isobaric thermal conductivity of the samples of polychlorotrifluoroethylene prepared by crystallization from the melt at pressures of 10 and 100 MPa, respectively (PCTFE-10 and PCTFE-100). One observes on each isobar the characteristic break at the glass transition temperature of amorphous phase T_g and a drastic drop of thermal conductivity on approach to the temperature interval of crystal melting T_m . Lower thermal conductivity of PCTFE-10 as compared to PCTFE-100 might be regarded as a natural consequence of lower crystallinity X (in fact, density ρ and velocity of sound \bar{u}).

As can be seen from Fig.1, thermal conductivity of both samples increases with pressure. In the framework of a concept of structural heterogeneity of crystallizable polymers it was natural to expect that the rate of thermal conductivity rise with pressure would correlate with the fraction of more compressible (amorphous) phase. However, in experiments the reverse was found (Fig.2): both the initial slope of the curve, thermal conductivity increment $\Delta\lambda/\lambda_p$ vs. pressure, and the maximum value of this increment in the region of levelling-off, were higher for more crystalline sample PCTFE-100. Similar data were also obtained for three polyethylenes with different crystallinities X . Evidently, characteristic pattern of λ vs. P dependence is controlled not only by relative content of more compressible phase, but by its microstructure, as well.

As predicted by cell model of polymers [3], increase in thermal conductivity with pressure is a result of decrease in free volume fraction in the amorphous phase, that is

$$\Delta\lambda/\lambda_p = \gamma_L \cdot f(0,T) \cdot [1 - \exp(-PV_0/k \cdot T)],$$

where γ_L is the quasilattice Grüneisen parameter, $f(0,T) = \exp(-E_0/k \cdot T)$ is the free volume fraction at normal pressure, V_0 is the volume of a single cell, and E_0 is the hole energy.

Treatment of a large body of experiments on temperature and pressure dependences of thermal conductivity of many crystalline polymers according to equation (3) has shown that V_0 smoothly increases with temperature, while parameter γ_L , on the contrary, tends to decrease. As can be seen from our data collected in

Table, our suggestion that samples of PCTFE and PE differing in crystallinity, also have amorphous phases with different microstructures, are in line with different values of γ_L and V_0 .

Moreover, quasilattice Grüneisen parameters γ_L calculated by the above equation (3), are higher roughly by an order of magnitude than thermodynamic Grüneisen parameters, $\gamma_L = \alpha/\beta T^3 \cdot C_V$ (see Table). This difference is a consequence of the fact that thermodynamic Grüneisen parameter γ_L is a measure of anharmonicity of all kinds of thermal vibrations (including those of valence bonds with very high values of force constants), whereas quasilattice Grüneisen parameter γ_L accounts only that contribution to anharmonicity which is brought about by weak interchain interactions [3,4].

Properties of semi-crystalline polymers at $P=0.1$ MPa and $T=303$ K^a

Polymer	λ	V_0	γ_L	l	l_c	l_a
Polyethylene						
low density	0.400	0.134	2.75	2.5	4.0	4.0
high density	0.650	0.175	2.72	5.0	12.0	2.4
ultrahigh mol. weight	0.400	0.192	4.72	3.0	8.0	4.0
polypropylene	0.240	0.159	9.4	10.0	22.5	12.1
polybutene-1	0.380	0.134	4.7	10.0	30.0	13.5
poly-4-methylpentene-1	0.160	0.146	4.1	2.0	37.0	68.8
polychlorotrifluoroethylene						
PCTFE-10	0.131	0.142	5.85	10.5	40.0	71.0
PCTFE-100	0.196	0.146	8.4	20.5	50.0	8.0
polyvinyl fluoride	0.238	0.134	7.2	7.5	40.0	29.0
polyvinylidene fluoride	0.208	0.125	5.5	5.0	50.0	52.0
polytetrafluoroethylene	0.260	0.130	4.8	7.0	80.0	47.0

Dimensions: λ in W/m·K; V_0 in nm³/mol; l , l_c , l_a in nm.

Taking this in mind, one may write

$$\gamma_L/\gamma_T = C_V/C^*, \quad (4)$$

where C^* is the contribution of interchain vibrations into the total isochoric specific heat.

The results of theoretical analysis of thermal conductivity of polymer crystals [5] suggest, that experimental values of thermal conductivity of semi-crystalline polymers are about 10³ times

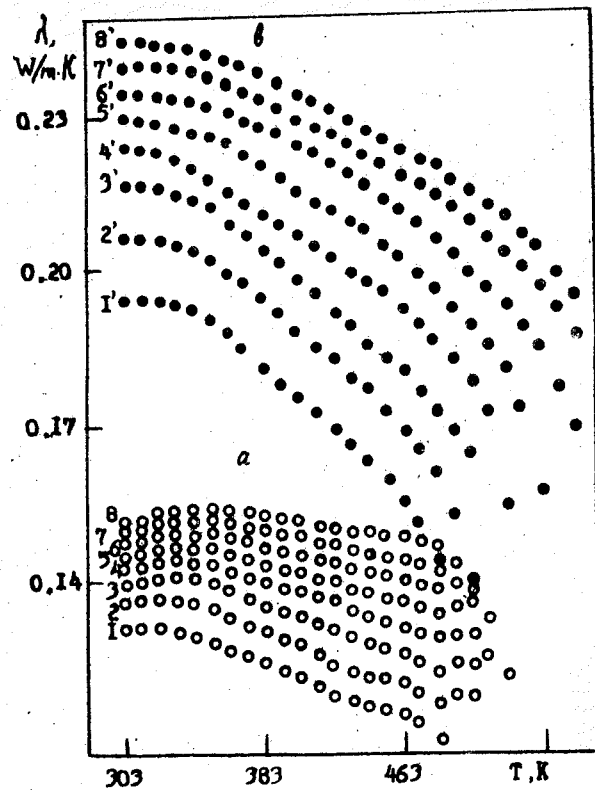


Fig.1. Thermal conductivity of PCTFE-10 (a) and PCTFE-100 (b) at pressures 0.1 (1), 10 (2), 20 (3), 30 (4), 40 (5), 60 (6), 80 (7) and 100 MPa (8).

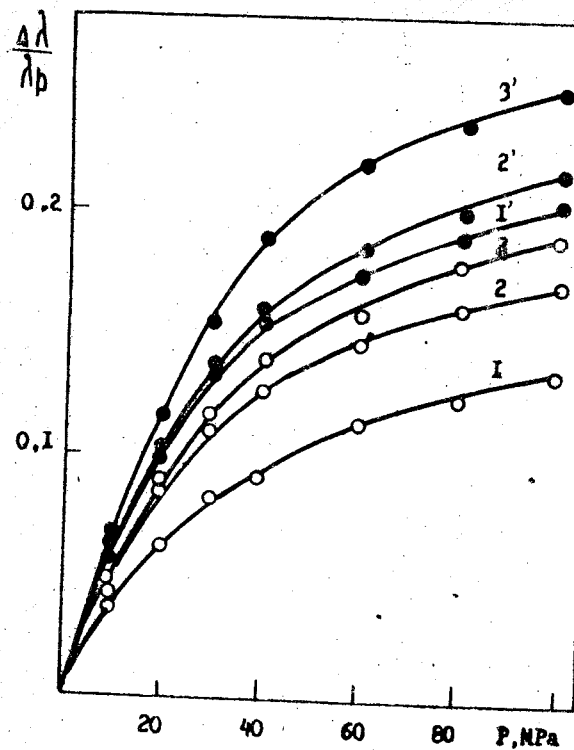


Fig.2. Pressure dependence of thermal conductivity increment for PCTFE-10 (1, 2, 3) and PCTFE-100 (1', 2', 3') at temperatures 303 (1, 1'), 353 (2, 2') and 403 K (3, 3').

lower than thermal conductivity of a crystal in the direction of main chains, while it has roughly the same order of magnitude as thermal conductivity in the transverse direction (i.e., normal to the chain). This means that thermal conductivity of semi-crystalline polymers is dominated by mechanism of interchain heat transfer. Therefore, C_v in equation (1) should be replaced by C^* from equation (4).

Values of the mean phonon free path l calculated by equation (1) with experimental data on λ , ρ , C^* from (4) and assuming $\bar{u} = (\rho_0)^{-1/2}$, are compared in the Table with dimensions of crystalline entities l_c deduced from electron microscopic data, and with linear dimensions of amorphous layers, $l_a = l_c(1-X)/X$.

From this one may draw a general conclusion that thermal conductivity of semi-crystalline polymers is controlled by phonon scattering on structural heterogeneities (i.e., amorphous interlayers between crystalline entities).

References

1. Kamal I., McLaughlin E. Pressure and volume dependence of the thermal conductivity of liquids.-Trans. Faraday Soc., 1964, v.60, No 4, p.809-816.
2. Eiermann K. Modellmässige Deutung der Wärmeleitfähigkeit von Hochpolymeren. - Kolloid Z. u. Z. Polymere, 1965, B.201, No 1, S.3-14.
3. Frost R.S., Chen R.Y.S., Barker R.E., Jr. Pressure dependence of thermal conductivity in polyethylene.- J. Appl. Phys., 1975, v.46, No 10, p.4506-4509.
4. Wada Y., Itani A., Nishi T., Nagai S. Grüneisen constant and thermal properties of crystalline and glassy polymers. - J. Polym. Sci., part A-2, 1969, v.7, No 1, P.201-208.
5. Choy C.L., Wong S.F., Young K. Model calculation of the thermal conductivity of polymer crystals.- J. Polym. Sci.: Polym. Phys. Ed., 1985, v.23, No 8, p.1495-1504.

CRYSTALLIZATION OF POLYMERS FROM THE MELT UNDER ELEVATED PRESSURES

N.L. Rymarenko, V.P. Privalko

Institute of Macromolecular Chemistry, Academy of Sciences of the Ukrainian SSR, Kiev, USSR

Theoretical and practical importance of studies of polymer kinetics of crystallization stems from the fact that it provides information on mechanism of structure formation in the course of phase transformation and thus makes one able to estimate the effect of transformation degree on polymer properties. Kinetic experiments are usually treated according to classical Kolmogorov-Avrami equation /1/, the applicability of which is, however, limited at best to initial stage of transformation.

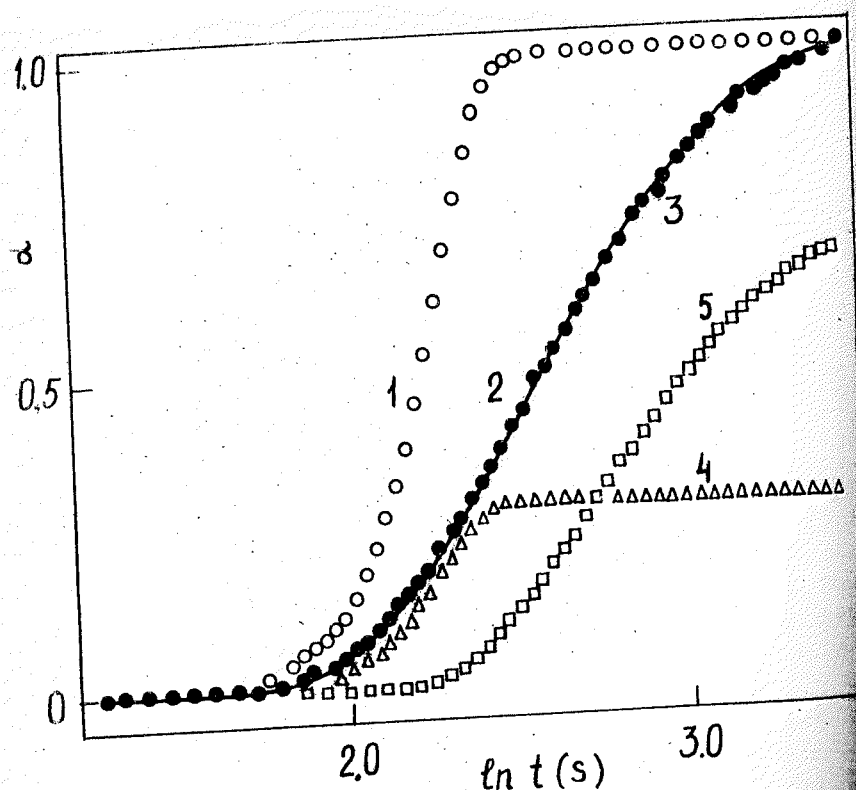
As became evident from analysis of a large amount of experimental data, the crystallization of polymers is controlled by at least two mechanisms /2/, each of which obeys Kolmogorov-Avrami equation but with different set of parameters. Within the framework of this concept, the overall degree of transformation α is expressed as

$$\alpha(t) = \alpha_1(t) + \alpha_2(t),$$

where $\alpha_1(t) = (1-c)[1 - \exp\{-K_1(t + \Delta t)^{n_1}\}]$ is the contribution of the first mechanism, and $\alpha_2(t) = c \int_0^{t+\Delta t} d\tau K_2 n_2 \tau^{n_2-1} \exp\{-K_2(t + \Delta t - \tau)^{n_2}\}$ is the contribution of the second mechanism, K_1 and K_2 are kinetic constants, n_1 and n_2 are parameters dependent on the shape of growing crystalline entities, c is the fraction of material transformed by the second mechanism, t is time, and Δt is an adjustable parameter introduced to account for errors in experimental detection of the onset of transformation.

This approach was used to analyze the dilatometric data on kinetics of melt-crystal phase transformation under elevated pressures in a series of flexible-chain polymers /3/. Optimum values of parameters K_1 , K_2 , n_1 , n_2 , c , and Δt , which assure the best approximation of experimental data were determined by standard methods of regression analysis /3/. Representative results for two high density polyethylenes (HDPE), Lupolen and Sholex, and for polyethylene oxide (PEO), are collected in the Table.

As can be seen from the Figure, the chosen model of isothermal crystallization quite adequately approximates the real process



Crystallization isotherm of HDPE Lupolen at $P = 60$ MPa and $T = 412$ K: 1 - theoretical (standard Kolmogorov-Avrami equation), 2 - theoretical (concept of two mechanisms), 3 - experimental, 4 - contribution of the first mechanism, 5 - contribution of the second mechanism.

in the whole range of transformation degree. Literal analysis of numerical data from the Table suggests that for all polymers the first mechanism corresponds to growth of three-dimensional crystalline entities (most likely, spherulites d_1) on athermal nuclei ($n_1 = 3$), whereas one observes differences in the second mechanism (presumably, crystallization of the melt in the interfibrillar space within spherulites), viz.: $n_2 = 2$ for PEO corresponds to growth of two-dimensional (disc-like) structures, while one-dimensional (needle-like) growth was found for HDPE ($n_1 = 1$).

Kinetic parameters of polymer crystallization

Polymer	P, MPa	T, K	$K_1 \cdot 10^9, s^{-3}$	$K_2 \cdot 10^3, s^{-1}$	n_1	n_2	σ
HDPE Lupolen	80	415	888	2.57	3	1	0.588
	80	418	101	1.461	3	1	0.960
	84	423.9	7.31	3.23	3	1	0.570
	84	436.9	0.01	0.07	3	1	1.0
HDPE Sholex	340	469.1	2441	0.94	3	1	0.200
	340	470.4	18.52	1.504	3	1	0.450
	25.2	332.7	$1.0 \cdot 10^6$	2.22	3	2	0.813
	25.2	333.6	$3.6 \cdot 10^6$	1.45	3	2	0.747
PEO	100.6	339.7	$1.4 \cdot 10^6$	3.45	3	2	0.676
	100.6	340.4	$1.3 \cdot 10^6$	4.97	3	2	0.699
	100.6	340.9	$8.2 \cdot 10^5$	2.26	3	2	0.732

No change of crystallization pattern was observed for HDPE in the whole experimentally studied pressure range (see Table), even above the "critical" pressure where "chain-extension effect" and "extended-chain growth" were postulated [4]. On the other hand, as follows from the analysis of temperature dependence of growth rates, with increasing pressure nucleation barrier to crystallization becomes higher which may be attributed to increasing structural mismatch at the melt-nucleus interface.

References

- Wunderlich B. Macromolecular Physics. Vol. 2. Crystal Nucleation, Growth, Annealing. - New York, Academic Press, 1976.
- Price F.P. A phenomenological theory of spherulitic crystallization: Primary and secondary crystallization processes. - J. Polym. Sci., part A. 1965, v.3, N9, p.3079-3086.
- Kalitkin N.N. Numerical Methods. - Moscow, Nauka, 1973, 512 p.
- Kyotani M., Kanetsuna H. Crystallization kinetics of polyethylene under high pressures. - J. Polym. Sci.: Polym. Phys. Ed., 1974, v.12, N11, p.2331-2345.

A.Ya. Goldman

ONPO "Plastpolymer", Leningrad, USSR

Volume and acoustic studies were carried out for the following polymeric materials: HDPE, LDPE, PTFE, polybenzoxazole (PBO) and composite materials - ABS-plastics in pressure range of 0.1-500 MPa at elevated temperature /1/. Individual tests were done at temperature up to 500 K and pressure up to 800 MPa. Velocity of supersonic oscillations with frequencies of 600 kHz and 1.5 MHz was measured together with measurements of absorption; measurements were also performed for pressure dependent volume changes of the samples at various constant temperatures. The velocity of sound was measured with puls-phase method; volume changes were monitored with supersonic dilatometer. Pressure dependent isometric modulus of uniform compression was calculated for all investigated materials. For PBO it was shown that within pressure range of 200-500 MPa Poisson's ratio is virtually a constant. Such kind of tests were carried out for heat hardened and annealed PTFE samples having the following densities: 2086, 2165 and 2129 kg/m³. DTA method was used for isobar based measurements. As a result, the phase diagram of PTFE was created. Unlike other well known studies, our study revealed a wide area of abnormal behaviour of the velocity of sound, i.e. its increase with temperature, moreover, the border-line of sub-area I' (having a shape of arc rather than straight line) was determined. In /2/ the border-line of areas I-I' under atmospheric pressure was not revealed either. In isobars 400 and 480 MPa after II-I' transition, the velocity of sound increases abnormally with temperature. The coordinates of the triple point were shown to be independent of crystallinity.

The study of II-III phase transition for PTFE showed that the coordinates of the transition depend upon the way how it occurs (Fig.2). At constant temperatures there is a 90 MPa (T=const=326K) difference between pressures under which the transition occurs. Hysteresis is not high for straight and reverse process.

The effect of pressure and temperature on creep and relaxation of polymeric and composite materials was studied. Mechanical state equations with due account of the effect of hydrostatic pressure were derived. Nonlinear equation of viscoelasticity (account-

ing for the effect of pressure on creep deformation at shear) was proposed. The equation was derived with the use of an analogy between the effect of pressure and temperature. This model is based on the assumption that along with the temperature-time analogy (TTA) there exists a baro-time analogy (BTA) /3/. Experimental data were given which supported the existence of BTA for some polymeric materials.

The general model was proposed and studied /4/. Principal assumptions used for this model had been proved experimentally. Analysis of the creep curves of polymers obtained in conditions of simple shear under atmospheric and hydrostatic pressure showed that viscoelastic deformation could be represented as a sum of two terms. The first term accounts for deformation resistance for simple shear and contains both elastic and viscoelastic components. Hydrostatic pressure has an influence on the elastic component only when shear stress, σ_{12} , is changed. The second term characterizes the influence of average stress. The decrease of pressure influence with the increase in creep time was taken into account. It was supposed that viscoelastic deformations are free from the limitations of the principle of simple addition. On the basis of the above mentioned conditions the equation of creep at shear has the following integral form:

$$\epsilon_{12} = f(\sigma_{cp}) f_1[\sigma_{12}(t)] \sigma_{12}(t) + \int_0^t f_1(t-\tau) f_2[\sigma_{12}(\tau)] \sigma_{12}(\tau) d\tau + \int_0^t \psi(t) \Gamma_2(t-\tau) f_3[\sigma_{cp}(\tau)] \sigma_{cp}(\tau) \sigma_{12}(\tau) d\tau \quad (1)$$

Functions, included in (1), are:

$$\begin{aligned} f_1[\sigma_{12}(t)] &= c_1 + c_2 \sigma_{12}(t); \quad f_2[\sigma_{12}(t)] = 1 + c_3 \sigma_{12}(t); \\ f_3[\sigma_{cp}(t)] &= 1 + c_4 \sigma_{cp}(t); \quad \psi = \exp(-\alpha t); \\ \Gamma(\sigma_{cp}) &= \exp(c_5 \sigma_{cp} + c_6 \sigma_{cp}^2) \end{aligned} \quad (2)$$

where $c_1 \dots c_6$ - are unknown factors; $\sigma_{cp} = -p$; $\psi(t)$ - is a function which accounts for the attenuation of the memory from σ_{12} under the effect of hydrostatic pressure. Weak singular nuclei in form of $\lambda \partial \alpha(-\beta, t)$ - Rabotnov's function and in form of the sum of exponential functions are used as creep nuclei. The unknown parameters of the equation (1) were obtained with a computer.

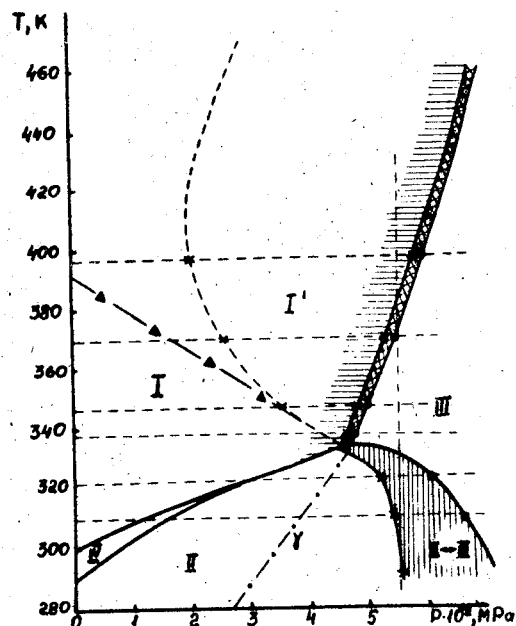


Fig. 1. Pressure-temperature phase diagram for PTFE:
 --- border-line of subarea I; XXX - area of existence
 of hexagonal and orthorhombic crystallites; ≡ - area of
 abnormal behaviour of the velocity of sound; ||| - area
 between II-III and III-II transitions (straight and reverse
 process on isotherm);
 - - - - relaxation transition in phase II;
 ▲▲▲ - border-line of I-I area based on data /4/.

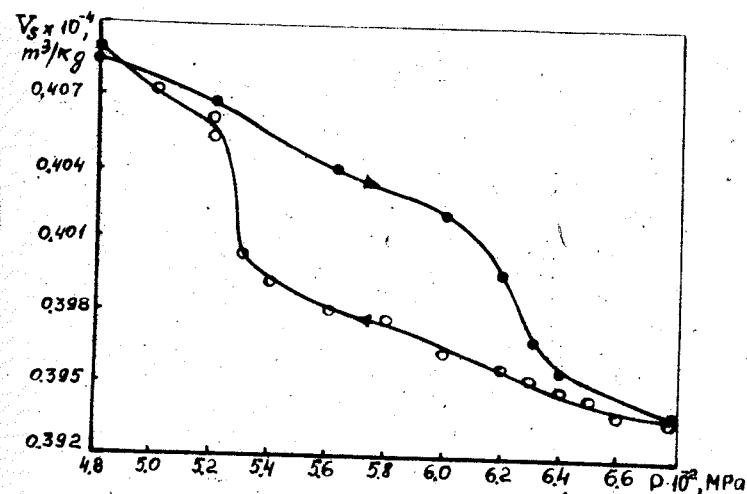


Fig. 2. Specific volume of PTFE vs. pressure at II-III phase transition; (straight and reverse process, $T=326$ K, samples with low crystallinity).

The detailed experimental study was carried out, the theory being compared with the experimental data.

The influence of loading history on the development of viscoelastic deformations was studied under programmed loading. The authors compared the efficiency of the proposed models to describe seven loading programmes with the use of various weak singular and exponential nuclei.

References

1. Goldman A.Ya. Volume deforming of plastics. Leningrad. Mashinostroenie, 1984, 232 p.
2. Matsushige K., Enoshita R., Ide T., Yamauchi N., Takemura T. Fine structure of the III-I transition molecular motion in polytetrafluoroethylene. - Japan J. Appl. Phys., 1977, v.16, N6, p.681-687.
3. Goldman A.Ya. Nonlinear viscoelastic behaviour of polymeric and composite materials with hydrostatic pressure dependent properties. - Mechanics of composite materials, 1984, N1, p.21-34.
4. Goldman A.Ya., Murzakhanov G.K., Demenchuk N.P. Application of nonlinear models of viscoelasticity for study the influence of hydrostatic pressure on shear creep of polymeric materials. - Mechanics of composite materials, 1982, N6, p.965-969.

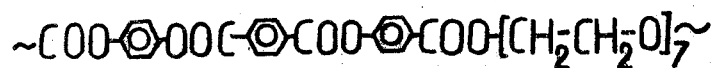
PRESSURE EFFECT ON THE STRUCTURAL ORDER OF LIQUID-CRYSTALLINE POLYMERS

V.V.Shilov, O.A.Lokhonya, V.V.Tsukruk, K.D.Petrenko, V.P.Pri-
valko

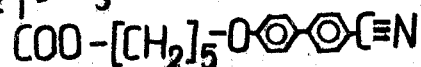
Institute of Macromolecular Chemistry, Academy of Sciences of
the UkrSSR, Kiev, USSR

Liquid-crystalline polymeric materials are characterized by multiple forms of structural order which are subjected to various changes under the action of different (i.e., electric, magnetic and mechanic) external fields [1,2]. Up to present, action of elevated pressures on the structural state of liquid-crystalline (LC) polymeric systems, if fact, was not studied in any detail. Therefore, it is the purpose of the present paper to monitor the pressure effect on the changes of structural order in LC polymers of various nature, and in low-molecular weight LC.

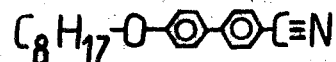
Following substances were chosen for the present study:
linear LC polymer,



comb-like polymer, $\sim \text{CH}_2 \text{---} \text{C}(\text{CH}_3) \sim$



and the low-molecular weight, cyano-biphenyl mesogen,



Polymers were synthesized as outlined in [1,3]. Parameters of structural order, as well as temperatures and heats of transitions are listed in Table.

Samples for the studies were prepared as follows. The initial powder substance was placed into the pressure cell, heated to 150 °C (i.e., to isotropic melt state), isothermally stored for 10 min., pressurized by 1 kbar for half an hour, and then slowly cooled to room temperature under pressure.

Calorimetric studies were carried out with the aid of DSC-1 differential scanning microcalorimeter. X-ray photopatterns were obtained on the plane cassette in vacuo. Wide-angle (5-35°) and low-angle (0.5-5°) X-ray diffraction patterns were recorded with the

aid of X-ray diffractometers, models DRON-2.0 and DRAM-2.0, respectively.

Heating thermograms of initial and pressurized samples are shown in Fig.1. General patterns of heat effects in the temperature ranges of phase transitions are similar: for linear polymer (I) melting of the crystalline phase followed by transition into smectic melt is observed in the temperature interval 110-120 °C, while comb-like polymer (II) exhibits the transition from smectic LC to isotropic melt in the vicinity of 127 °C. Heats of transitions are of the order of 7-8 J/g (see Table). Rather similar pattern of transitions is also observed for pressurized samples (see Fig.1 and Table).

Parameters of structural order, temperatures and heats of transitions

Sample	P, kbar	T _t , °C	ΔH _t , J/g	d	D ₁	D ₂	D ₃
I	0	110, 120	8.4	35	4.6	4.4	3.5
	1	110, 120	8.1	35	4.6	4.3	3.6
II	0	127	7.4	-	4.5	-	-
	1	135	9.7	-	4.6	-	-
III	0	67	-	32	5.6	4.9	4.1
	1	-	-	32	5.6	5.0	4.0

Note: Structural parameters are given in Angstroms; d - interlayer distances for low-angle maxima; D - interlayer distances for wide-angle maxima.

In Fig.2 the schematic representations of X-ray patterns of polymers (I,II) and low-molecular weight LC (III) which were recorded at different directions are shown together with corresponding wide-angle and low-angle diffractograms. One observes a series of sharp wide-angle and low-angle maxima for samples I and III, while only diffuse maximum was found for sample II. The former data are a manifestation of crystallization into perfect crystal lattice during cooling of samples I and III, whereas low-angle maximum is attributed to perfect layer packing of molecules. On the other hand diffuse scattering from sample II suggests that a glassy state was formed on cooling from LC melt. As follows from the analysis of angular distribution of intensity, application of pressure of 1 kbar to sample I makes the planes of layer structures to align along the

direction of piston, while molecular chains are oriented normal to that direction.

References

1. Н.П.Плате, В.П.Шибанов. Гребнеобразные полимеры и жидкие кристаллы - М.: ХИМИЯ, 1980. - 330 с.
2. Finkelmann H. Thermotropic LC polymers//In: Liquid Crystals of One-Two-Dimensional Orders/Eds.W.Helfrich, G.Heppke-Berlin: Springer Verl., 1980. - p.238-252.
3. Молекулярные свойства и фазовые состояния полимера с мезогенными группами в основной цепи/А.И.Григорьев, Н.А.Андреева, А.Ю.Билибин и др. -Высокомолек. соед. Сер.Б, 1983, 25, №5, с.1082-1085.

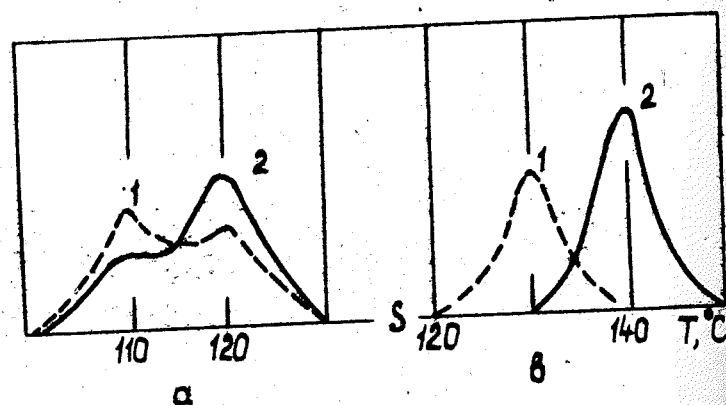


Fig.1. Heating thermograms of samples I (a) and II (b); 1-initial sample, 2-prepared under pressure.

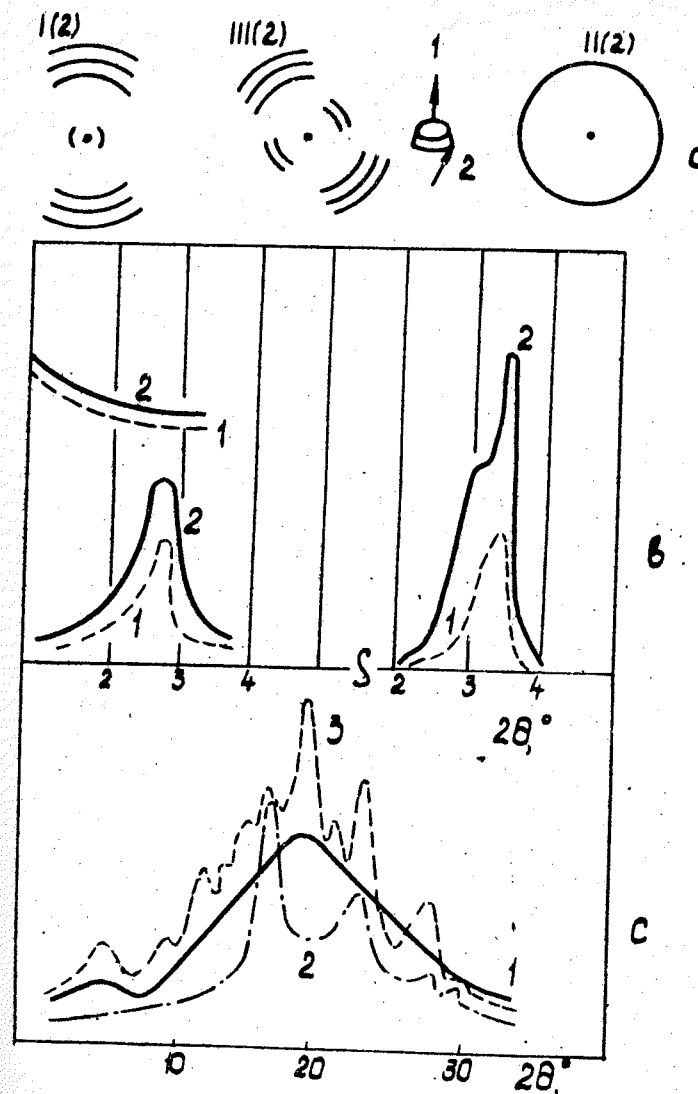


Fig.2. Schematic representation of X-ray photopatterns (a) and diffraction patterns (b, c) of samples prepared under pressure (lowangle and wide-angle records, respectively): position "2", 2 - position "1" (b); sample I (1), sample II (2), sample III (3).

E.V. Slavnov, V.M. Timofeev, A.I. Ostannin
Institute of Continuum Mechanics, Ural Scientific Centre
of the USSR Academy of Sciences, Perm, USSR

This work deals with the process of hydrostatic extrusion which is used to produce highly oriented thermoplastic products. We consider that the preference must be given to materials which are too hard to machine. Further we present experimental hydroextrusion data, show density moulding dependence upon technological parameters, suggest state equation and method for determination of its constants, consider the effect of technology on some material properties.

Hydroextrusion process was performed in order to obtain circular samples in the die with moulding part diameter 6.2 mm, corner $2\alpha = 50^\circ$. The extrusion ratio was set by the sample diameter. The process pressure P_3 dependence on the extrusion ratio K and the temperature T at prescribed extrusion rate was recorded (1.5 mm/s). Relationships $P_3 = f(\ln K, T)$ for different materials are shown in Fig. 1.

In the course of plastic flow calculations the state equation problem appeared. The polymer mechanical properties are strongly depended on temperature, hydrostatic pressure, plastic deformation level and anisotropy that takes place in the process of hydroextrusion. To construct certain equation we need in complex experiments. We set to get these dependences directly from the hydroextrusion process. Let us use now the low estimation method [1] developed in the process of metal hydroextrusion. If the material yield stress in the process of hydroextrusion increases over the axis then, in fact, it does not change in perpendicular direction [2]. We may consider that the yield stress at the entry and the exit of the drawing die equals to the original material yield stress. Under the assumption of low friction ratio we obtain

$$P_3 = 2\sigma_0 \varepsilon_r + \int_{\varepsilon_1}^{\varepsilon_1 + \ln K} \sigma_s(\varepsilon) d\varepsilon$$

We may show that the yield material stress within definite range of values depends linearly on T and P .

$$\sigma_s = \sigma(\varepsilon) + \beta P - \alpha T$$

Let us now take the material hardening in reference to power law:

$$\sigma = \sigma_0 + A \varepsilon^q \quad (3)$$

where σ_0 - yield stress, α, β, A, q - material constants. We substitute (3) and (2) in (1) and, assuming that the hydrodynamic pressure over the drawing die equals to the extrusion pressure, get

$$P_3 = aT + b$$

$$a = \alpha \frac{\ln K}{1 - \beta \ln K},$$

$$b = \sigma_0 \frac{2\varepsilon_r + \ln K}{1 - \beta \ln K} + A \frac{(\ln K)^{q+1}}{(q+1)(1 - \beta \ln K)}$$

If we have a set of experimental points P_3^n and T_3^n with general number of them N , then we may find values a and b by the use of method of least squares. Physical constant values α and β are determined under the minimum of quadratic error for the description of the ratio $a = f(\ln K)$ and σ_0, A, q are defined under the same condition for the ratio $b = f(\ln K)$. Comparing the values of constants we can note that the highest temperature belongs to compound 3-6-3 and the lowest one to $\phi-4$, whereas the latter shows one of the most strong pressure dependences.

One would think that the material obtained under the high hydrostatic pressure with well pronounced orientation had to have density as high as the original one. At the same time all extrudates had the cross-section integral density which was 2-8% lower (Fig. 2, a) and therefore the filled polyethylene ratio $\rho = f(P_3)$ is minimum. This can be attributed to the fact that the material densification in the course of deformation under low extrusion ratios goes intensively than the process of material densification due to orientation and contraction which take place in the presence of low hydrostatic pressure. With the increased extrusion ratio the orientation degree and the developed pressure which lead up appearing microvoids increase as well. The experimental absorption dependences which have the character of curves with reflection $\rho = f(P_3)$ confirm the presence of microvoids in the samples.

Cross-section density distribution of polycaprolamide samples shown in Fig. 2, b. We observe essential density inhomogeneity with the radius and it grows the higher K and the lower T .

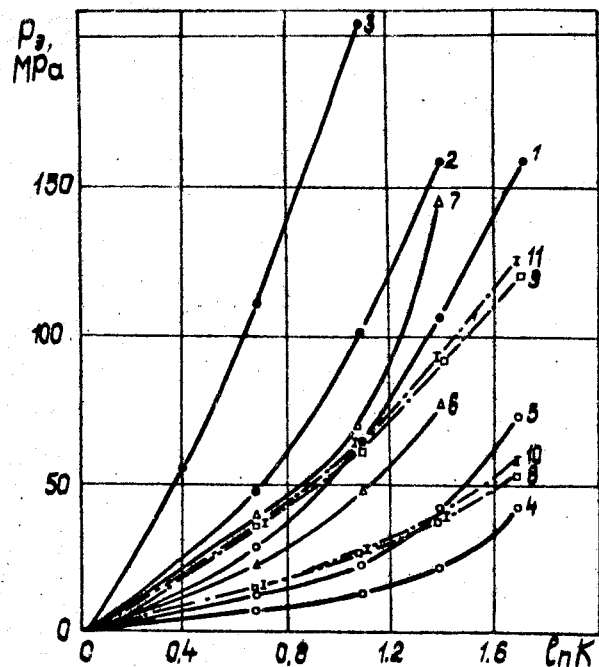
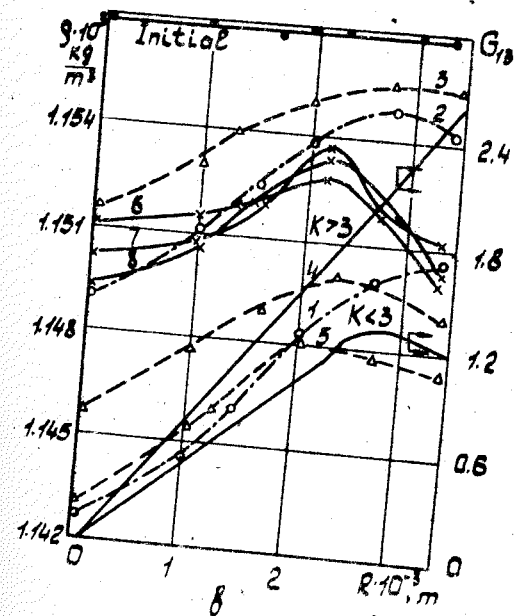
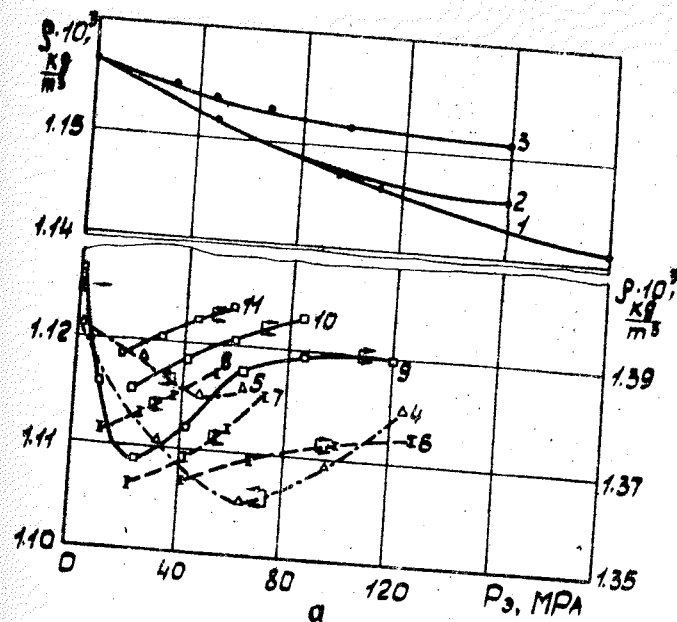


Fig. 1. Extrusion pressure versus $\ln K$ for different T :
 \circ - poly-E-caproamide; \square - polytetrafluoroethylene;
 Δ - Π , I - comonomer 3-6-3, 1-1-7-50, 1-1-1-50; $T(^{\circ}K)$ = 1, 6, 8,
 10 - 298; 7, 9, 11 - 363; 2-383; 4-403; 3-433; 5-453.

Fig. 2. Cross-section integral density versus moulding pressure (a) and polycapraamide sample density distribution and shear component distribution of deformation tensor of Green's measure over radius (b):
 a) \circ, Δ, Π - Fig. 1; $T(K)$ = 1, 4, 6, 9-298; 2-383; 7, 10-333;
 5, 8, 11-363; 3-433; b) $T(K)$ = 0-298; Δ - 383; \times - 433; 1, 3- $K=2$;
 2, 4, 6- $K=3$; 5, 7- $K=4$; 8- $K=5$.



With increasing temperature the homogeneous nucleus with density which hardly depended on K appears in the center of the sample. We observe density maximum in all samples $0.8 \div 0.92 R$. Comparing these data with the cross-section deformation picture obtained on cutting samples (Fig.2,b) we can conclude that if the integral density is caused by deformation elongation level, pressure and temperature then its cross-section inhomogeneity is defined by the deformation shear component and more over this limited shear gives the increase of the material density.

References

1. Pae K.D. High Pressure Material Mechanical Characteristics. Moscow: Mir, 1973, 521 p.
2. Clifferri A., Ward I.M. Ultra-High Modulus Polymers. Leningrad: Chimija, 1983, p. 270.

МЕЖДУНАРОДНАЯ АССОЦИАЦИЯ ПО РАЗВИТИЮ ИССЛЕДОВАНИЙ В ОБЛАСТИ ВЫСОКИХ ДАВЛЕНИЙ

ВЫСОКИЕ ДАВЛЕНИЯ В НАУКЕ И ТЕХНИКЕ

ТРУДЫ

XI МЕЖДУНАРОДНОЙ КОНФЕРЕНЦИИ МАРИЦ

В 4 томах

Том 4

Ответственный редактор Н.В.Ноников

На английском языке

Киев, издательство "Наукова думка"

Художник обложки В.С.Мельничук

Художественный редактор И.Е.Писарева

Технические редакторы Т.М.Зубрицкая, Т.К.Валыцкая

Д. в печ. 13.07.88. Формат 60x84/16. Бум. офо. № 2. Офо. печ.
печ. л. 15.81. Усл.кр.-отт. 16.04. Уч.-изд.л. 14,76+вкл.0,39
14. Тираж 720 экз. Заказ 9-3. Цена 85 к.

Издательство "Наукова думка". 252601 Киев 4, ул. Рейкина, 3.
Киевская книжно-журнальная типография научной книги. 252004
4, ул. Рейкина, 4.

FOR NOTES

To the paper: Beresnev B. I., Getmanskii A. P., Efros B. M., Beigelzimer Yu. E., Loladze L. V. «Investigation of pressure distribution in working space between diamond anvils by change of properties of a deformable spacer».

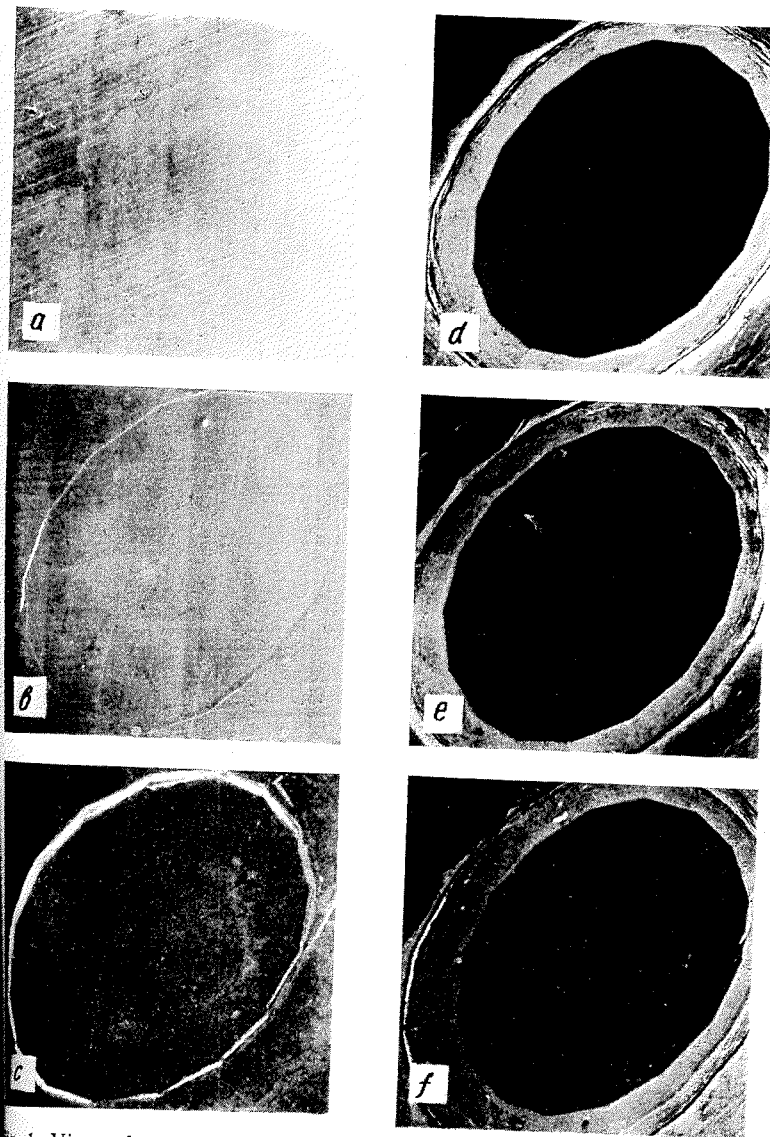


Fig. 1. View of a deformed spacer from T-301 stainless steel after loading in a pressure device with different loads (GPa): a — 6.5; b — 8.5; c — 14.5; d — 40; e — 45.5; f — 65.

To the paper: Ruoff A. L., Brister K. E., Weir S. T., Vohra Y. K. «Megabar pressures with synthetic diamonds».

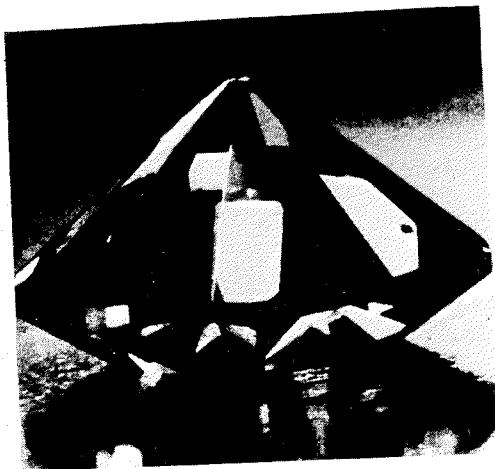


Fig. 1. Photograph of the synthetic gray-blue diamond used in the present experiment. This diamond survived the static high pressures exceeding 125 GPa. The tip of the diamond is 200 μm in diameter and has a bevel of 5 degrees approaching a central flat of 70 μm .

To the paper: Borisevitch V. K., Isaenko V. I. «Automatic press for sheet-metal explosive stamping».

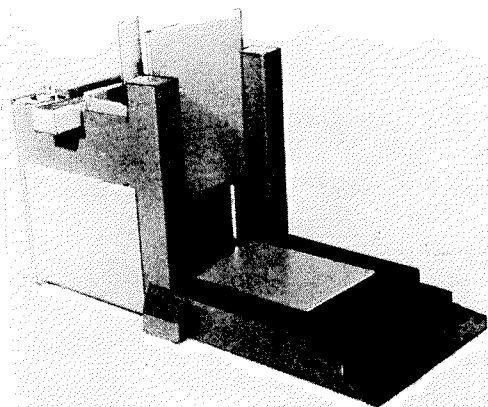


Fig. 1. Automatic explosive stamp.

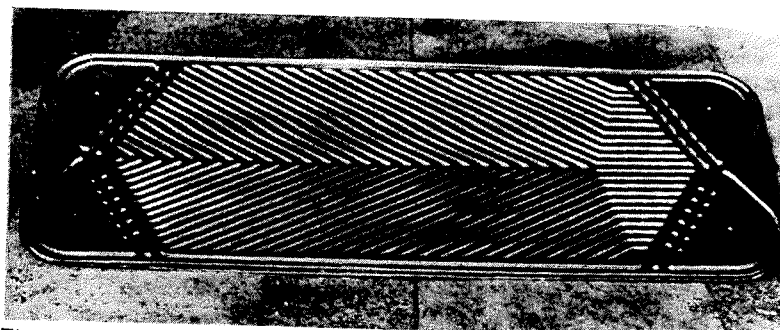


Fig. 2. Heat exchanger plate 500 \times 1450 mm, $\delta=1$ mm, 12X18H10T material.

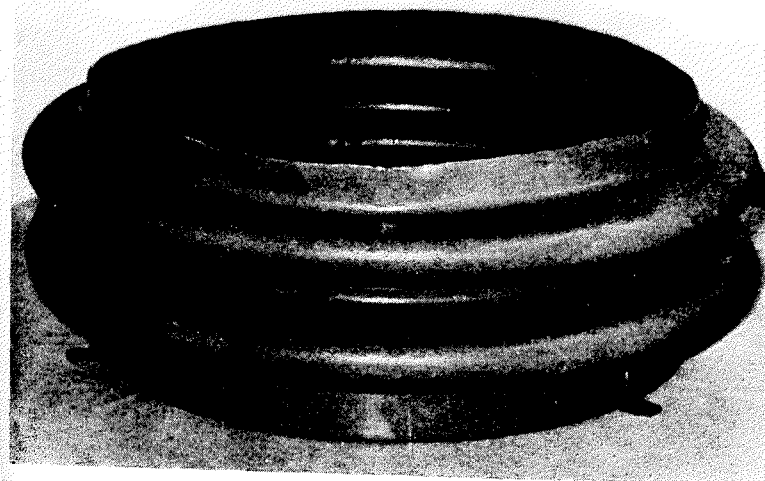


Fig. 3. Compensator $\varnothing=730$ mm, H=260 mm, $\delta=4$ mm, AD-1 material.

To the paper: Nesterenko V. F., Pershin S. A. «The shear localization at explosive compaction of rapidly solidified metal powders».

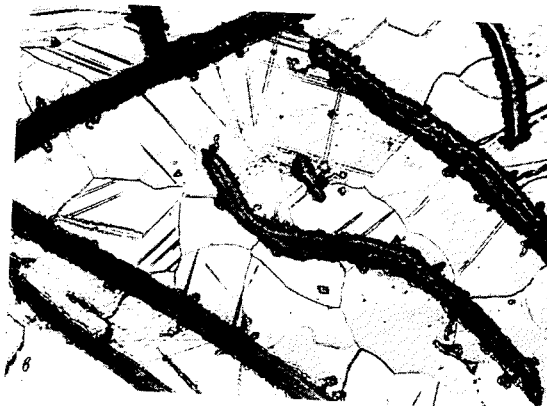


Fig. 1. Inter-particle shear in 71KHCP particle, mixture with Cu (weight content 40 %) ($\times 300$).



Fig. 2. Trans-particle shear in 71KHCP alloy ($\times 50$).

To the paper: Voloshin M. N. «The peculiarities of structural and phase transformations in cast iron under shock — wave loading».



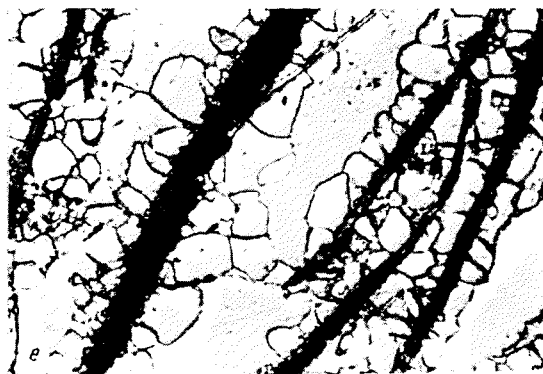


Fig. 1. Microstructures of the grey cast iron specimens: a) initial; b) to e) after the different amplitude shock wave action.

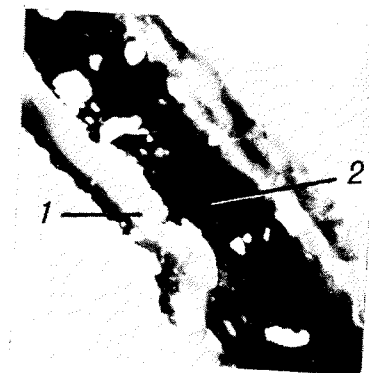


Fig. 3. The view of a diamond-graphite aggregate: 1 — diamond; 2 — graphite.

To the paper: Chistyakov E. M., Vinnichenko V. N., Belostotskiy A. V., Mukha I. M. «Alternating pressure — induced phase transformation in hardmetals».

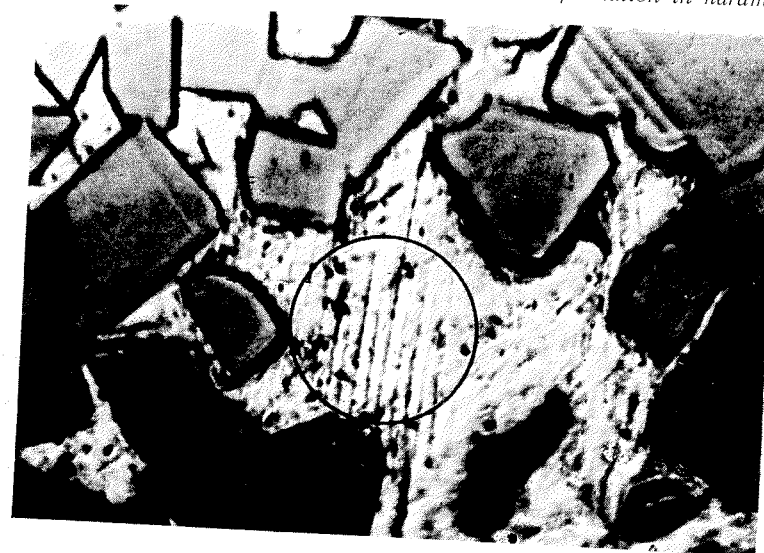


Fig. 2. A relief of some portions of the binder phase of ultrasonically treated BK20K hardmetal.

To the paper: Jach K. «Numerical modelling of two-dimensional elastic/visco — plastic deformation of materials at dynamic loads».

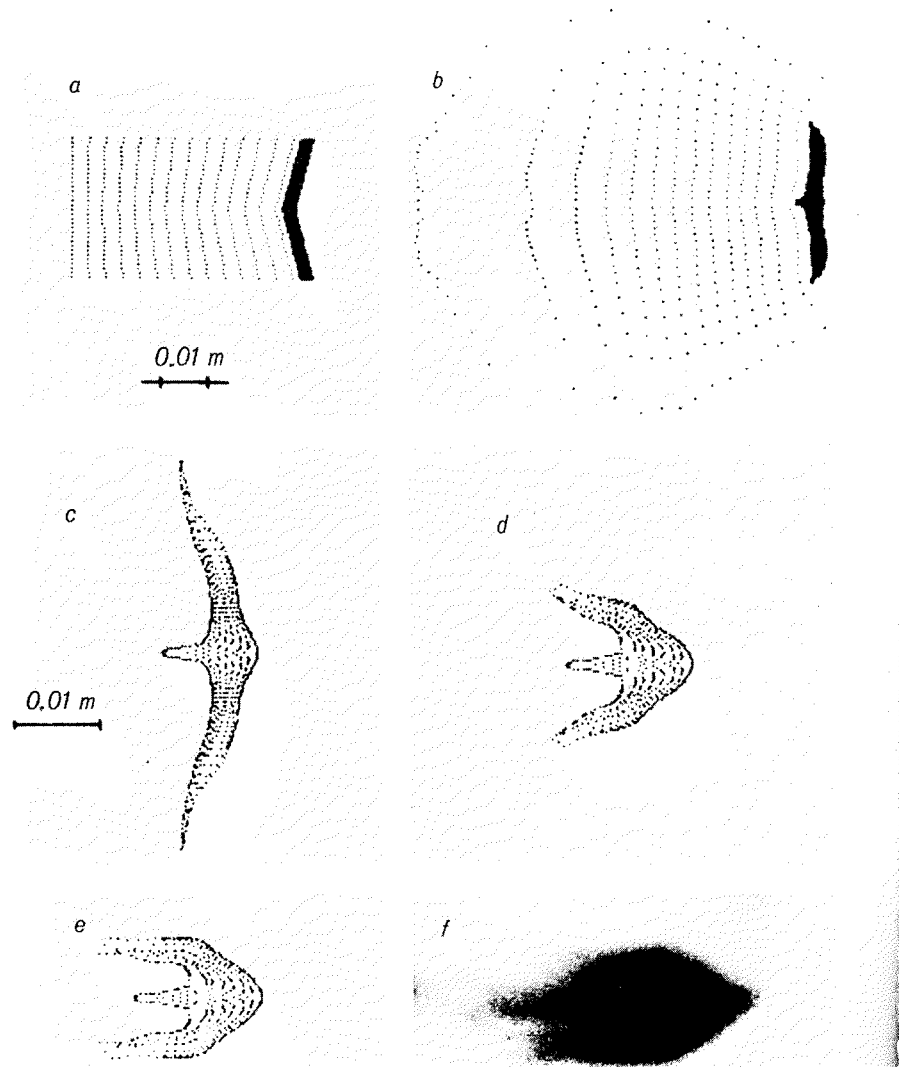


Fig. 1. Reverse cumulation — $\alpha=150^\circ$, cylindrical symmetry: a) $t=0$; b) $t=10\text{ }\mu\text{s}$; c) $t=16\text{ }\mu\text{s}$; d) $t=48\text{ }\mu\text{s}$; e) $t=70\text{ }\mu\text{s}$; f) shadow photograph.